Towards A Systems-Level Understanding of Battery Systems: Modeling and Simulation Approaches for Design, Control, and Analysis

Akshay Subramaniam

A dissertation

submitted in partial fulfilment of the

requirements for the degree of

Doctor of Philosophy

University of Washington
2021

Submitted to the Supervisory Committee

Venkat R. Subramanian, Committee Chair

Daniel T. Schwartz, Committee Chair

Stuart Adler, Committee Member

Mehran Mesbahi, Graduate School Representative

Program Authorized to Offer Degree:

Chemical Engineering

University of Washington

Abstract

Towards A Systems-Level Understanding of Battery Systems: Modeling and Simulation Approaches for Design, Control, and Analysis

Chair(s) of the Supervisory Committee: Prof. Daniel T. Schwartz and Prof. Venkat R. Subramanian

Department of Chemical Engineering

Current imperatives of electrification and decarbonization entail significant improvements in energy density, performance, and cost metrics for battery technology. This has motivated active research into new materials, cell designs, and external controls to ensure safe and efficient operation. Modeling and simulation approaches have a powerful complementary function in this regard, most notably exemplified by the models for Lithium-ion batteries by Newman and co-workers. The overarching theme of this dissertation is thus the development and application of electrochemical modeling approaches at multiple scales in problems relevant to the abovementioned contexts.

At the systems level, the development of more intelligent and powerful Battery Management Systems is enabled by fast electrochemical models, which must balance competing considerations of accuracy, computational efficiency, and ease of parameterization. To this end, we report a rigorous and generalized methodology for ‘upscaling’ continuum electrochemical models. This approach, based on the visualization of a battery as Tanks-in-Series, has been demonstrated for

both Lithium-ion and more complex Lithium-sulfur batteries. With respect to full models, voltage prediction errors below 20 mV are achieved for high-energy cells in most practical cases. <30 mV errors are achieved for aggressive conditions of high-rate operation at sub-zero ambient temperatures, illustrating their practical utility. This approach results in improved computational speed since each conservation law is replaced by a relatively simple volume-averaged differential or algebraic equation. For examples of large-scale problems, this leads to >10x savings in computation time over fast implementations of conventional models, illustrating competitiveness for real-time applications.

In the development of next-generation chemistries, continuum models can serve as a framework for the analysis and interpretation of experimental data, while providing design guidance and helping determine desirable operating regimes. Electrochemical phenomena at different length and time scales are manifested during operation through voltage and temperature signatures, cycle life, and coulombic efficiency. Optimization of cell-level metrics is thus predicated on their correlation with the internal electrochemistry. This entails the integration of electrochemical models at different levels of detail in a computationally efficient and robust manner. To this end, the second half of this dissertation describes our efforts to develop a simulation framework for the modeling of Lithium-metal systems. We first describe a robust computational method to simulate Poisson Nernst Planck (PNP) models for Lithium symmetric cells characterized by thin double layers. This can be leveraged in applications where computational efficiency is of salience, such as cycling simulations and parameterization by coupling kinetic models of interest. This is demonstrated by a systems level method, enabling the quick evaluation of candidate mechanisms appropriately expressed as time-varying rate constants, making it useful for understanding the phenomena underpinning voltage transitions in Lithium symmetric cells. This is followed by a description of

a preliminary electrochemical-mechanical model for Li metal interfaces, which is expected to serve as basis for more sophisticated electrochemical-mechanical models for Li metal systems operating under external pressure. We expect these approaches to advance fundamental understanding and design of Li-metal batteries, while creating accessible computational tools to complement experimental studies.

Taken together, these contributions are envisaged to advance the knowledge base for model-based design as well as Battery Management Systems, particularly in anticipation of the commercialization of emerging battery chemistries.

Table of Contents

List of Figures

List of Tables

Acknowledgements

The past few years have been quite the remarkable and enriching experience, and I owe an immense debt of gratitude to a number of individuals who made it happen. I would like to express my gratitude towards my advisor, Prof. Venkat Subramanian. Despite being a relatively late entrant to the group, he went out of his way to make sure I felt welcomed and an integral part of the group. Always eager to share his vast knowledge, he goes out of his way to help us with modeling and simulation difficulties, sometimes working with us late into the night. His constant enthusiasm, dedication, and work-ethic has been an inspiration that I strive to emulate. Despite my junior status as a graduate student, he always encouraged me to chart my own path during my PhD, giving me ample freedom to explore my own interests and formulate my own research plans. His investment in my journey continued even after his move to Texas, and he remained just as communicative and helpful. His technical inputs in my projects have greatly improved the quality of my work. I continue to try and learn his knack of identifying approaches that always work, despite their seeming implausibility and my argumentative nature, which he has always graciously indulged.

Thanks are also due to my co-advisor, Prof. Dan Schwartz, who was of great help in the latter half of my PhD. After the group's move to Texas, he ensured that I felt at home in his group and provided invaluable insight and guidance. Several stimulating discussions and feedback played an important role in better defining and communicating my research, and in better interpreting and contextualizing my findings. I would also like to extend my thanks to Prof. Stu Adler and Prof. Mehran Mesbahi for serving on my committee and providing useful feedback. Prof. Adler has been a great mentor outside research as well, and I learnt a lot serving as his Teaching Assistant,

where I got to learn from his vast knowledge and enthusiasm for the subject. I would also like to thank Prof. Martin Bazant for his kind recommendations and valuable discussions. Dr. Diptarka Majumdar is another collaborator I would like to humbly acknowledge. I learnt immensely from his technical and managerial expertise, and his feedback provided a critical, industry-oriented dimension to our work. I would also like to thank other members of the UW ChemE faculty, especially Prof. Jim Pfaendtner who provided valuable guidance and support during the particularly tough transition phase in my first year.

I would like to express thanks to all past and current members of the M.A.P.L.E. and EMI labs. I had the privilege of being part of not one but two amazing research groups, and I consider this one of the best aspects of my entire experience. This work would not have been possible without the constant encouragement, support, and myriad forms of assistance from all my fellow members. I would like to thank Dr. Yanbo Qi, Dr. Seong Beom Lee, Dr. Manan Pathak, and Dr. Neal Dawson-Elli for loads and loads of initial guidance and support. I would also like to acknowledge Dr. Suryanarayana Kolluri for his constant and invaluable assistance in every respect, from the nitty-gritties of computer codes to guidance on future career goals. Taejin has also been a constant support, not shying from pulling all-nighters to help with troubleshooting codes. I remain forever indebted for such invaluable assistance. I would like to thank my fellow lab members Caitlin Parke, Jerry Chen, Maitri Uppaluri, Dr. Krishna Shah, and Dr. Lubhani Mishra for valuable collaboration experiences and insightful discussions. In addition, I would like to acknowledge all my group mates without whose curious questions and constructive criticism this would never have been possible, particularly Chintan, Linnette, Victor, Erica, Mihyun, Varun, Maitri, and Kirutiga.

I would also like to thank all my friends and batchmates who made my stay in Seattle enjoyable, and who took the edge off the stresses and frustrations that accompany a PhD program. I would like to acknowledge the members of my PhD cohort and all past roommates. Particular thanks are due to Prabhleen. Without her unwavering support and selfless encouragement I would never have made through the stressful transition phase and completed my degree.

I would also like to take this opportunity to acknowledge the amazing teachers who inspired me during my formative years and had substantial contributions towards where I am today. I would like to thank Prof. Vishwanath Dalvi for instilling in me a passion for chemical engineering with his innovative teaching methods and constant mentorship. Prof. Sunil Bhagwat was another amazing teacher I had the privilege to learn from, particularly the principles of rigorous engineering analyses and problem solving. My Masters' advisor Prof. Santosh Noronha helped me augment these skills by impressing upon me the need to be versatile and constantly update one's skills as a researcher.

Lastly, I thank my family, particularly my grandfather who inspired me to do a PhD, and who continues to guide and mentor me even at his advanced age. My parents and sister have been a constant source of support and encouragement. I am grateful to them for their patience and understanding, and apologize for the times I wasn't there. To them I dedicate all my achievements.

Akshay Subramaniam

University of Washington, June 2021

Chapters 1-4 are reproduced with permission from journal articles published by The Electrochemical Society.

For my parents

1. Introduction

1.1. Role of Modeling and Simulation – Systems-Level Models of Lithium-ion Batteries

Lithium-ion (Li-ion) batteries are achieving increasing ubiquity as Electric Vehicle (EV) adoption continues to grow.[1] Material and manufacturing innovations, coupled with market pressures and economies of scale, have led to declines in battery pack costs of nearly 85% in the period 2010-18.[2] In this context, further improvement in competitiveness relative to internal combustion engines entails extracting the maximum possible value out of battery systems by ensuring their safe and efficient operation. This entails maximizing utilization, reducing overdesign, enabling fast charging, and mitigating degradation phenomena. Thermal runaway and the resulting likelihood of fires and explosions is another critical consideration, and it is essential to ensure battery operation in the safe temperature range. The performance and safety issues of Li-ion batteries are well-known, and problems such as Lithium plating[3],chemomechanical degradation[4] and thermal runaways[5] are exacerbated under practical conditions such as fast charging, low ambient temperatures, and dynamic operation.[6–9] In multi-cell stacks, large format cells and large battery packs, spatial non-uniformities in temperature greatly influence the electrochemical performance of individual cells, with significant implications for overall utilization, temperature, safety and system lifetime.[10–12]. The Battery Management System (BMS) is the combination of hardware and software components that performs the requisite functions to ensure safe and efficient operation.[13] An accurate and robust mathematical model is essential for BMS, which

estimates battery state variables such as State of Charge (SoC), State of Health (SoH), and temperature.[13,14] . Advanced BMS and Thermal Management Systems (TMS) designed to ensure optimal operation have access to a limited number of measurements, and rely on the predictions of key quantities, voltage-current trends, and temperature distributions.[14] To this end, mathematical models play a critical role in predicting battery state and dynamics, which in turn informs estimation, optimization and real-time control strategies.[15–19] Prediction of thermal dynamics is particularly critical in view of deleterious phenomena such as overheating, non-uniform capacity degradation, and potential thermal runaways.[11,20,21]

In addition to design and analysis applications, we can also use the electrochemical information provided by such models to compute cell-level quantities that are of salience in real-time BMS and TMS applications. As mentioned previously, cell-balancing is a critical function of BMS. The performance of multi-cell stacks and large battery packs consisting of series-parallel combinations of cells is often limited by the 'weakest' cell in the array.[10,20] The BMS must be able to ensure that individual cells are not over-charged or over-discharged and ensure that individual cells are not over or under-loaded, thereby mitigating the effects of non-uniform degradation rates.[17] This requires the monitoring of the State of Charge (SoC) of individual cells and estimates of the current flowing through each cell. In real-time applications, this is often done by assuming empirical circuit models for each cell[17], in which the temperature also thought to affect individual cell resistances and heat generation rates, which in turn alters the effective resistance of each cell and thus the dynamic current distribution.[11] In contrast to ad-hoc empirical models, physics-based models can leverage the full electrochemical state to directly compute instantaneous SoC and current in individual cells, thereby capturing the complex interplay of various electrochemical

phenomena that influence the dynamic behavior of cell resistance. In most cases, the p2D model is far too computationally expensive to simulate multiple cells in real-time, not including the additional computational overhead of using the simulation results to compute emergent cell-level quantities. However, a simplified model which still retains adequate electrochemical information can potentially help balance this trade-off.

1.2. Role of Modeling and Simulation – Lithium Metal Batteries

There is significant interest in lithium metal anodes to increase the energy density of lithium batteries, and thus achieve the metrics required to hasten the progress of electric transportation and grid-scale energy storage.[22] Lithium is the most electropositive element, and lithium anodes have a higher theoretical specific capacity (3860 $mAh \cdot g^{-1}$) compared to the graphite (372 $mAh \cdot g^{-1}$) used in conventional lithium-ion batteries.[23] Several failure modes and performance limitations hinder wider adoption, including low coulombic efficiency, reduced cycle life, and potentially unsafe internal short circuits during operation.[24–26] These issues are a result of the high reactivity, large volume changes, and poor electrodeposition properties of lithium, characterized by parasitic side reactions, dendrite formation, inactive lithium, and other undesirable deposition phenomena. Lithium metal tends to plate in an non-uniform fashion, leading to the formation of protrusions which increase in size and density during repeated cycling, increasing the surface area for parasitic side reactions associated with the formation of the Solid Electrolyte Interphase (SEI). The concentration of electric currents at protrusions leads to non-uniform reactions across the deposit surface, which can lead to the electrochemical disconnection of certain regions of the metal anode,

leading to the formation of 'dead lithium', which, in recent studies has been identified as the dominant mechanism of lithium loss and eventual capacity degradation.[27] Minimizing these issues entails a rigorous understanding of the complex interplay among electrodeposition dynamics, transport phenomena, and mechanical effects. This is essential in order to enable the identification of desirable material attributes and external controls to achieve safe and efficient battery operation.

The application of mechanical pressure is receiving interest for controlling the deposition morphology of lithium metal (Li metal) anodes.[28] Pressure has been observed to induce constrained Li growth and result in more uniform deposition, in contrast to the high surface-area, 'mossy' Li deposits that are typically observed.[29,30] The prevention mossy or dendritic Li can result in significant increases in the cycle life of high-energy Li metal cells.

In further rationalizing these observations, continuum-scale physics-based models can provide useful mechanistic insight grounded in thermodynamics, electrochemical transport and kinetics. This can serve as a framework for the analysis and interpretation of experimental data, while providing useful design guidance and determining desirable operating regimes. In particular, these phenomena occur at different length and time scales, and are manifested during battery operation through voltage and temperature signatures, cycle life, and coulombic efficiency. [26,31,32]

Past modeling work has focused on a subset of the above phenomena, delivering useful insights. Localized electrochemical-mechanical models have studied the influence of the mechanical deformation of electrolyte-electrode interfaces on electrodeposition kinetics.[33–35] Transport models have focused on simulating the spatiotemporal evolution of interfaces and for evaluating the impact of kinetic and transport limitations on morphological evolution and cell-level voltage.[36–

[39] Further insights can thus be obtained by the study of coupled electrochemical-mechanical effects during the dynamic evolution of the electrode-electrolyte interface, and similar correlation with cell-level measurements, e.g. voltage evolution during extended cycling.[40] The importance of correlating cell voltage with trends in deposition phenomena and internal electrochemistry, as a means of identifying key signatures and transitions, has been highlighted.[26] There is thus substantial value in coupling these models to electrochemical engineering models that can predict cell-level quantities during cycling. This integration requires multiscale approach that combines the three sets of models in a computationally efficient manner.

1.3. Scope and Organization of Dissertation

This document is thus divided into two parts, each corresponding to the research thrusts described in the previous section. Chapters 2 and 3 thus deal with the development of a computationally efficient, 'upscaled' physics-based models for Li-ion batteries.[41,42] The second part deals with our attempts to develop a multiscale continuum simulation framework for Li metal batteries. In Chapter 4, the envisaged systems-level approach is illustrated for Li Symmetric Cells. An electrochemical engineering model in the form of a robust fast code, was combined with modified kinetic models and a parameterization approach to attempt to rationalize key voltage signatures in experimental data.[43] Important takeaways and directions for future research are then outlined in the concluding Chapter 5, which also introduces a preliminary electrochemical-mechanical model developed as the first step towards a localized coupled electrochemical-mechanical model for Li metal cells. The localized electrochemical-mechanical model is able to predict the extent of enhancement of electrochemical reactions as a result of interfacial deformation[44], with rigorous solution techniques facilitating more accurate determination of profiles. Extensions, refinements,

and next steps are discussed for both sets of research efforts detailed herein.

2. The Tanks-in-Series Methodology for 'Upscaling' Lithium-ion Batteries

2.1. Reformulated and Simplified Electrochemical Models

The incorporation of sophisticated electrochemical models has the potential to enable more powerful and intelligent BMS. In addition to improved prediction of battery states, variables internal to battery electrochemistry allow the formulation of more complete optimization and control problems than would be possible by simple circuit models.[19] Achieving this integration requires the reduction of the computational demands of complex models, such as the macro-homogeneous 'p2D' models of Newman and co-workers.[45] In addition to model reformulation techniques that exploit the underlying mathematical structure of the equations to achieve fast simulation[46,47], the tradeoff between accuracy and computational efficiency has spurred active investigation into simplifications of the p2D model subject to limiting assumptions.[48]

In our past work, we extensively used model reformulation techniques. Millisecond computation times were achieved using coordinate transformation, spectral methods and reformulation enabled by analytical solution[46,49–51], and successfully demonstrated in applications for parameter estimation, optimal control, and BMS.[52–54] Despite detailed analysis and comparisons of efficient simulations of SPM-like models in past work from our group[55], the two and three-parameter models have been arguably the most widely used for control, optimization and BMS by the community at large.[49] This motivates the development of efficient models for the electrolyte phase in lithium-ion batteries.

2.2. Current Landscape of Simplified Electrochemical Models – Advantages and Limitations

2.2.1. *Single Particle Model (SPM)*

Since its introduction by Atlung et al.[56], the Single Particle Model (SPM) has been extensively used for efficient simulation, estimation, optimal charging and life-cycle modeling.[16,18,52,57] The SPM visualizes the electrodes in a lithium-ion battery as two representative spherical particles and considers the electrode reactions and transport through the active particle. SPM is particularly attractive since the largest reduction in the number of equations is achieved via simplifications of the solid phase, given that the corresponding equation is solved at each point in the electrode computational grid (see section on Model Development).[49,55] Importantly however, it neglects potential and concentration variations in the electrolyte phase, which limits its predictive ability to low-current scenarios and relatively thin electrodes, where liquid phase polarizations can be neglected.[48] In addition, SPM assumes a uniform reaction distribution throughout each electrode, which is only attained at moderate currents in which kinetic resistances dominate ohmic effects, and in electrodes which possess a monotonic dependence of equilibrium potential with degree of lithiation.[58,59] SPM has been recovered in the limits of fast diffusion dynamics with respect to characteristic discharge time.[60] The p2D model also returns SPM in the limit of large changes in characteristic overpotential upon Li intercalation, which results in uniform reaction distributions.[61] These limitations have led to efforts to expand the applicability of SPM by introducing simplified descriptions of electrolyte dynamics and non-uniform reaction distributions.

2.2.2. *Extensions to SPM – Non-uniform reaction distributions*

A common approach for the inclusion of non-uniform reaction distributions is to directly assume a polynomial profile for pore-wall flux. Alternatively, polynomial profiles for both electrolyte concentration and potential may be assumed and used to determine the spatial variation of the pore-wall flux.[62–64] In addition, some workers have derived closed-form analytical solutions for the pore-wall flux distribution. However, these solutions are only valid under certain assumptions, such as linear kinetics, or by neglecting the diffusional contribution to the electrolyte current, and also neglect the concentration-dependence of one or more electrolyte transport properties.[65] Still other approaches assume a polynomial or exponential dependence for the equilibrium electrode potential in space. These assumed profiles are often combined with polynomial spatial dependence for other electrochemical variables, converting the original Partial Differential Equations (PDEs) of the p2D model into a system of Differential Algebraic Equations (DAEs). The simplifications require assumptions to achieve closure, while also assuming constant electrolyte transport properties for tractability.[66,67] For both types of approaches, the use of higher-order polynomial profiles for increased accuracy is expected to increase the DAE system size, with the attendant penalty for computational efficiency.

2.2.3. *Extensions to SPM – Electrolyte dynamics (SPMe)*

Extensions of SPM to electrolyte dynamics are often termed 'SPM*e*' , where *e* denotes electrolyte. A common approach begins with the assumption of a uniform reaction in the electrodes.[50,60,68] This results in simplified PDEs for electrolyte concentration. For constant electrolyte diffusivity, SPM*e* results in linear PDEs, which are computationally simple to solve. Indeed, it is possible to derive

closed-form analytical solutions for the constant diffusivity case.[58,69] Alternatively, instead of constant reaction distributions, polynomial spatial dependence for concentration can also be assumed, resulting in a system of DAEs.[70–72] With the knowledge of electrolyte concentrations, the electrolyte current equation is usually integrated, or volume-averaged quantities are used to obtain the liquid-phase potential drop. In some cases, polynomial profiles are assumed for the liquid-phase potential as well. This information is then used in conjunction with the electrode-kinetics equation to estimate the cell voltage. The uniform-reaction SPM*e*[50,68] is rigorously derived from the scaled p2D model in the limit of fast electrolyte diffusion dynamics.[60] This perturbation approach yields simplified algebraic expressions for the various polarization contributions to the cell voltage. These expressions can be evaluated at negligible computational cost. In addition, the cell voltage equation is expressed in terms of electrode-averaged quantities to obviate the need for assumptions on the pore-wall flux at the terminals.

The PDE system in SPM*e* becomes non-linear in the case of variable diffusion coefficient, which might compromise computational efficiency. When solving numerically, the non-linearities are likely to entail finer spatial discretization in both the electrode and the solid particle to ensure numerical convergence, which will increase the DAE system size. The stiffness of the resulting system is also likely to increase for the non-linear case, especially at high current densities. The effect of increased computational cost may become more significant in real-time environments, both due to stringent accuracy requirements and hardware limitations.[54] In addition, even in situations where the non-linear equation is solved numerically, simplifications of the electrolyte current equation, such as constant electrolyte conductivity[68], are necessary to allow tractable integration for calculating electrolyte ohmic drop. This can be a requirement even if polynomial

profiles for electrolyte concentration are assumed for the non-linear equation.[73,74] The perturbation approach results in expressions in which the transport properties are evaluated at a given representative concentration.[60] This may result in errors in estimating concentration overpotentials at high discharge rates, where substantial spatial variations are expected to arise. Additionally, it is not clear whether the algebraic expressions for electrolyte ohmic drop are valid for variable concentration properties and may have to be rederived. Using a constant value may lead to errors in estimating ohmic drops and concentration overpotentials at high current-densities.

2.3. Motivation for the Tanks-in-Series Approach

In this work, we use a Tanks-in-Series approach to reduce the p2D model. The electrolyte conservation equations are written in volume-averaged form, without resorting to any direct assumptions on the spatial dependence, unlike in polynomial profile methods. The proposed Tanks-in-Series approach also does not assume uniform reaction rates to predict concentration profiles, since we deal in average quantities. The key approximations are (a) in the interfacial fluxes and (b) using the electrode-averaged pore-wall flux to estimate the electrode-averaged overpotential. The second assumption is analogous to some SPM*e* models.[60] For problem closure, we make reasonable approximations for the flux variables at the interface. Mass and charge conservation are imposed at the domain interfaces in order to determine the unknown interfacial values. The cell-voltage is then calculated from the known electrode-averaged pore-wall flux. This formulation allows for the inclusion of concentration-dependent transport properties, since terminal-to-terminal integration is not required, and the properties are only evaluated at the domain interfaces. In addition, it reduces the full p2D model into a fixed-size system of < 20 DAEs and no PDEs need be solved.

2.4. Model Development – Systematic Derivation from the p2D Model

2.4.1. *The pseudo-2-dimensional (p2D) Model*

The pseudo 2-dimensional (p2D) model of Newman and co-workers is a continuum electrochemical model that has found substantial application for simulation of Li-ion battery performance.[52] **Figure 2.1** illustrates the computational schematic of the model.[45,59] The typical p2D model is written for a single 'cathode-separator-anode' sandwich. Each domain is modeled using porous electrode theory, in which the two solid and electrolyte phases are regarded as superimposed continua.[75] The model is a set of coupled partial differential equations (PDEs) based on one-dimensional conservation laws for charge and mass in each domain. The individual domain equations are coupled through the specification of appropriate interfacial boundary conditions, which also ensure mathematical well-posedness. In the p2D representation of the battery, the active material is regarded as composed of spherical particles of uniform radii. Lithium intercalation and de-intercalation occurs through electron-transfer reactions at the particle surface and transport through the solid particle, modeled by conservation laws in the 'pseudo' r-dimension. The complete mathematical model and parameter values may be found in **Table 2-I - Table 2-IV**.

Table 2-I. Governing PDEs for the p2D model.

Equations	Boundary Conditions
Positive Electrode (Region 1)	
$\varepsilon_1 \frac{\partial c_1}{\partial t} = \frac{\partial}{\partial x}\left[D(c_1)\varepsilon_1^{b_1} \frac{\partial c_1}{\partial x} \right] + a_1(1-t_+) j_1$	$\left.\frac{\partial c_1}{\partial x}\right\|_{x=0} = 0$
	$\left.\varepsilon_1^{b_1} \frac{\partial c_1}{\partial x}\right\|_{x=l_1} = \left.\varepsilon_2^{b_2} \frac{\partial c_2}{\partial x}\right\|_{x=l_1}$
$i_{l,1} = -\kappa(c_1)\varepsilon_1^{b_1} \frac{\partial \phi_{l,1}}{\partial x} + \frac{2RT(1-t_+^0)}{F}\left(1+\frac{\partial \ln f}{\partial \ln c_1}\right)\kappa(c_1)\varepsilon_1^{b_1} \frac{1}{c_1}\frac{\partial c_1}{\partial x}$	$\left.\frac{\partial \phi_{l,1}}{\partial x}\right\|_{1,x=0} = 0$
	$\left.\varepsilon_1^{b_1} \frac{\partial \phi_{l,1}}{\partial x}\right\|_{x=l_1} = \left.\varepsilon_2^{b_2} \frac{\partial \phi_{l,2}}{\partial x}\right\|_{x=l_1}$
$\frac{\partial}{\partial x}\left[\sigma_{eff,1} \frac{\partial \phi_{s,1}}{\partial x} \right] = a_1 F j_1$	$\left.\frac{\partial \phi_{l,1}}{\partial x}\right\|_{x=0} = -\frac{i_{app}}{\sigma_{eff,1}}$
	$\left.\frac{\partial \phi_{l,1}}{\partial x}\right\|_{x=l_1} = 0$
$\frac{\partial c_1^s}{\partial t} = \frac{1}{r^2}\frac{\partial}{\partial r}\left[r^2 D_1^s \frac{\partial c_1^s}{\partial x} \right]$	$\left.\frac{\partial c_1^s}{\partial r}\right\|_{r=0} = 0$
	$\left.\frac{\partial c_1^s}{\partial r}\right\|_{r=R_1} = -\frac{j_1}{D_1^s}$
Separator (Region 2)	
$\varepsilon_2 \frac{\partial c_2}{\partial t} = \frac{\partial}{\partial x}\left[D(c_2) \frac{\partial c_2}{\partial x} \right]$	$c_1\|_{x=l_1} = c_2\|_{x=l_1}$
	$c_2\|_{x=l_1+l_2} = c_3\|_{x=l_1+l_2}$
$i_{l,2} = -\kappa(c_2)\varepsilon_2^{b_2} \frac{\partial \phi_{l,2}}{\partial x} + \frac{2RT(1-t_+^0)}{F}\left(1+\frac{\partial \ln f}{\partial \ln c_2}\right)\kappa(c_2)\varepsilon_2^{b_2} \frac{1}{c_2}\frac{\partial c_2}{\partial x}$	$\phi_{l,1}\|_{x=l_1} = \phi_{l,2}\|_{x=l_1}$
	$\phi_{l,2}\|_{x=l_1+l_2} = \phi_{l,3}\|_{x=l_1+l_2}$
Negative Electrode (Region 3)	
$\varepsilon_3 \frac{\partial c_3}{\partial t} = \frac{\partial}{\partial x}\left[D(c_3) \frac{\partial c_3}{\partial x} \right] + a_3(1-t_+) j_3$	$\left.\frac{\partial c_3}{\partial x}\right\|_{x=l_1+l_2+l_3} = 0$
	$\left.\varepsilon_2^{b_2} \frac{\partial c_2}{\partial x}\right\|_{x=l_1+l_2} = \left.\varepsilon_3^{b_3} \frac{\partial c_3}{\partial x}\right\|_{x=l_1+l_2}$
$i_{l,3} = -\kappa(c_3)\varepsilon_3^{b_3} \frac{\partial \phi_{l,3}}{\partial x} + \frac{2RT(1-t_+^0)}{F}\left(1+\frac{\partial \ln f}{\partial \ln c_3}\right)\kappa(c_3)\varepsilon_3^{b_3} \frac{1}{c_3}\frac{\partial c_3}{\partial x}$	$\phi_{l,3}\|_{x=l_1+l_2+l_3} = 0$
	$\left.\varepsilon_2^{b_2} \frac{\partial \phi_{l,2}}{\partial x}\right\|_{x=l_1+l_2} = \left.\varepsilon_3^{b_3} \frac{\partial \phi_{l,3}}{\partial x}\right\|_{x=l_1+l_2}$
$\frac{\partial}{\partial x}\left[\sigma_{eff,3} \frac{\partial \phi_{s,3}}{\partial x} \right] = a_3 F j_3$	$\left.\frac{\partial \phi_{s,3}}{\partial x}\right\|_{x=l_1+l_2} = 0$
	$\left.\frac{\partial \phi_{s,3}}{\partial x}\right\|_{x=l_1+l_2+l_3} = -\frac{i_{app}}{\sigma_{eff,3}}$
$\frac{\partial c_3^s}{\partial t} = \frac{1}{r^2}\frac{\partial}{\partial r}\left[r^2 D_3^s \frac{\partial c_3^s}{\partial r} \right]$	$\left.\frac{\partial c_3^s}{\partial r}\right\|_{r=0} = 0$
	$\left.\frac{\partial c_3^s}{\partial r}\right\|_{r=R_3} = -\frac{j_3}{D_3^s}$

Table 2-II. Additional constitutive equations for the p2D model.

$$j_1 = k_1 c_1^{\alpha_{a,1}} (c_1^{s,\max} - c_1^{s,surf})^{\alpha_{a,1}} (c_1^{s,surf})^{\alpha_{c,1}} \left(\exp\left(\frac{\alpha_{a,1} F \eta_1}{RT} \right) - \exp\left(\frac{-\alpha_{c,1} F \eta_1}{RT} \right) \right)$$

$$j_3 = k_3 c_3^{\alpha_{a,3}} (c_3^{s,\max} - c_3^{s,surf})^{\alpha_{a,3}} (c_3^{s,surf})^{\alpha_{c,3}} \left(\exp\left(\frac{\alpha_{a,3} F \eta_3}{RT} \right) - \exp\left(\frac{-\alpha_{c,3} F \eta_3}{RT} \right) \right)$$

$$\kappa(c_i) = 1\times10^{-4} c_i \left[\begin{array}{l} \left(-10.5 + 0.0740T - 6.96\times10^{-5}T^2\right) \\ +c_i(0.668 - 0.0178T + 2.8\times10^{-5}T^2) \\ +c_i^2(0.494 - 8.86\times10^{-4}T^2) \end{array} \right]^2, i \in \{1,2,3\}$$

$$\sigma_{eff,i} = \sigma_i \left(1 - \varepsilon_i - \varepsilon_{f,i}\right), i \in \{1,3\}$$

$$D\left(c_i\right) = 0.0001\times10^{-\left[4.43 + \frac{54}{T - 229 - 0.005c_i}\right] - 0.00022c_i}, i \in \{1,2,3\}$$

$$a_i = \frac{3}{R_i}\left(1 - \varepsilon_i - \varepsilon_{f,i}\right), i = 1,2,3$$

$$U_p = -10.72\theta_p^{\,4} + 23.88\theta_p^{\,3} - 16.77\theta_p^{\,2} + 2.595\theta_p + 4.563$$

$$\theta_p = \frac{c_1^{s,surf}}{c_1^{s,\max}}$$

$$U_n = 0.1493 + 0.8493\mathrm{e}^{-61.79\theta_n} + 0.3824\mathrm{e}^{-665.8\theta_n} - \mathrm{e}^{39.42\theta_n - 41.92} -$$
$$0.03131\tan^{-1}\left(25.59\theta_n - 4.099\right) - 0.009434\tan^{-1}\left(32.49\theta_n - 15.74\right)$$

$$\theta_p = \frac{c_3^{s,surf}}{c_3^{s,\max}}$$

$$\left(1 - t_+^0\right)\left(1 + \frac{\partial \ln f}{\partial \ln c_i}\right) = 0.601 - 7.5894\times10^{-3} c_i^{\,0.5} + 3.1053\times10^{-5}\left(2.5236 - 0.0052T\right)c_i^{\,1.5},\ i \in \{1,2,3\}$$

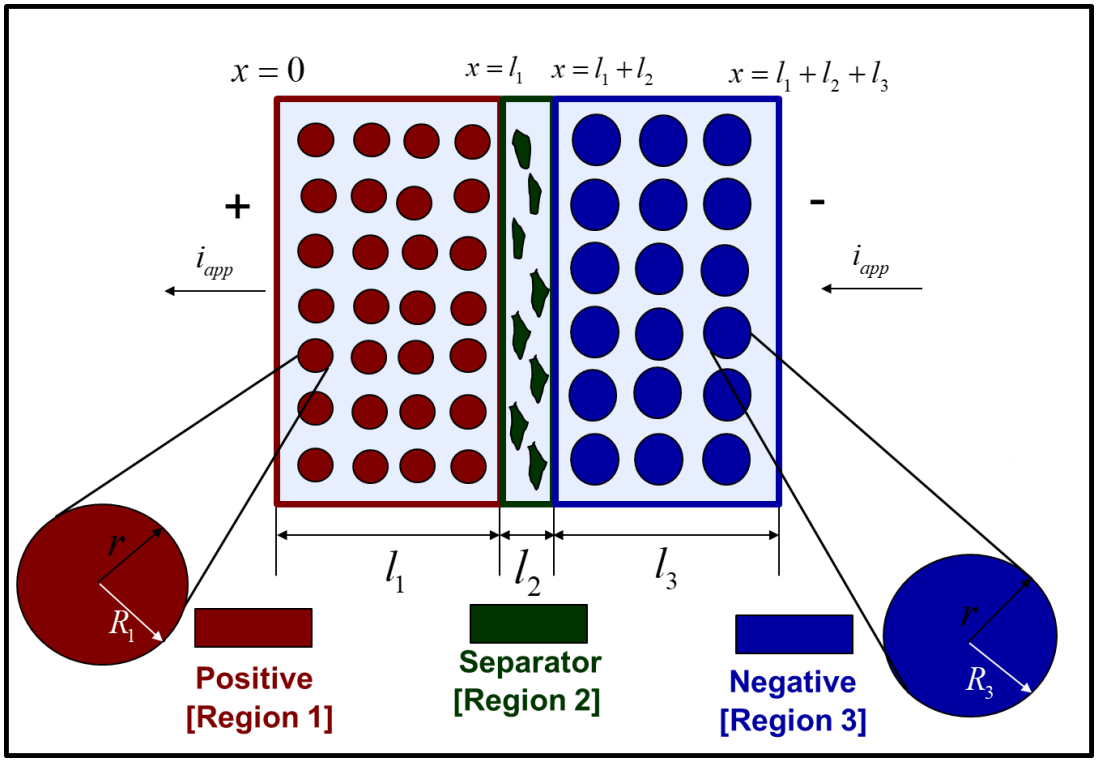

Figure 2.1. Schematic representation of the computational domain in the p2D model for a dual insertion lithium-ion cell. The active material in both electrodes is modeled as spherical particles. Electron-transfer reactions are modeled at the particle-electrolyte interface, as is the transport of intercalated lithium through the active particle. Liquid phase mass and charge transport through the thickness l_i of each domain also modeled using concentrated solution theory. Electron transport through the solid phase is also considered, with electronic current entering and leaving the cell at the current collectors (not shown). The color codes for the three porous domains are used throughout this chapter, i.e. positive (dark red), separator (dark green), negative (dark blue).

In deriving the Tanks-in-Series model, the volume-averaging procedure is applied first to the solid phase conservation equations, illustrating how SPM is recovered under certain assumptions. The concept is then applied to the electrolyte transport equations, thereby resulting in averaged equations for the liquid phase 'Tanks' of **Figure 2.2**.

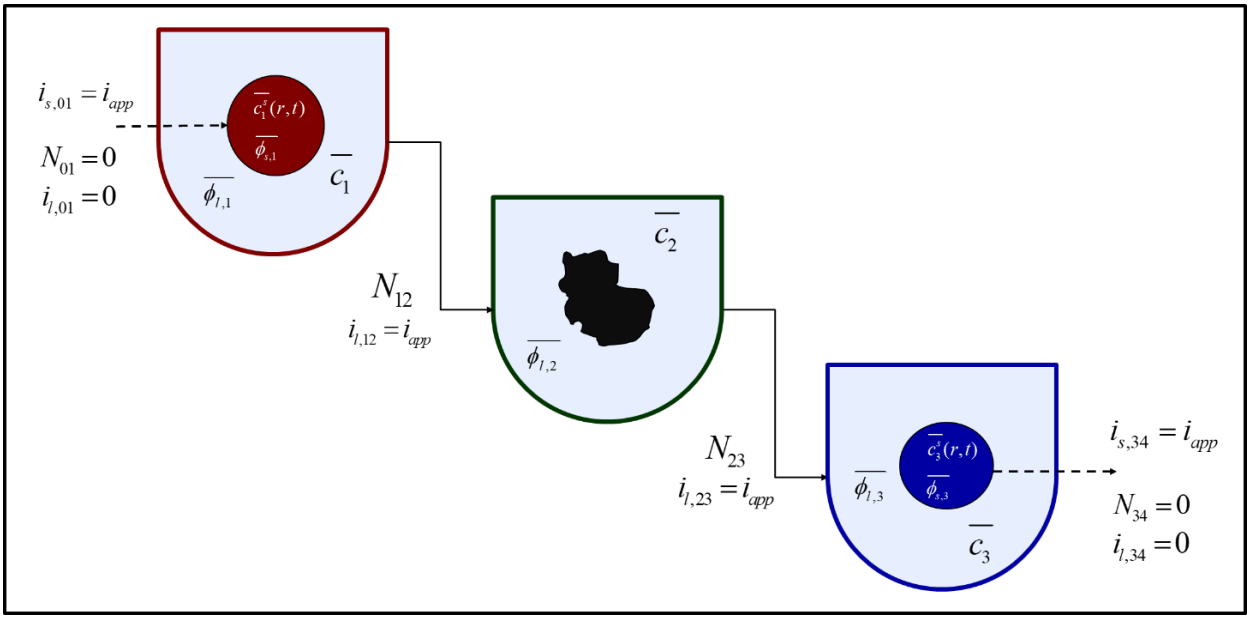

Figure 2.2. A visualization of the Tank Model approach depicting the mass and charge flows in to and out of each 'tank'. Since both the electrolyte flux and liquid phase current density are zero at the current collectors, net flows into the liquid phase of the positive 'tank' and out of the negative 'tank' are zero. The interfacial boundary conditions at the separator define the mass and charge flows for the middle separator 'tank'. The electronic current carried by the solid phase at the current collectors is denoted by dotted lines. The solid and liquid phases exchange mass and charge at a rate determined by the pore-wall flux $\overline{j_i}$, an internal exchange which is not shown here. The sign convention is so adopted that i_{app} is negative during discharge.

2.4.2. *Solid Particle Transport*

In the absence of complexities such as phase-separation or concentrated solution effects[76,77], solid phase transport is modeled by Fick's second law in spherical coordinates. For the positive electrode particle, we have

$$\frac{\partial c_1^s}{\partial t} = \frac{1}{r^2}\frac{\partial}{\partial r}\left(r^2 D_1^s \frac{\partial c_1^s}{\partial r}\right) \quad [0 < x < l_1] \tag{1}$$

Where the r coordinate denotes the radial distance within the particle and is thus the second

'pseudo-dimension'. The subscript *1* denotes variables and parameters pertinent to the positive electrode (region 1).

In porous electrode theory, equation (1) is valid at each point along the electrode thickness x. The superscript s is used to denote the solid phase. D_1^s is the diffusion coefficient in the positive particle. The second-order problem in r requires the specification of two boundary conditions. At the surface of the solid particle, the diffusive flux is related to the local rate of electrode reaction or pore-wall flux as

$$-D_1^s \frac{\partial c_1^s}{\partial r} = j_1 \quad [r = R_1, 0 < x < l_1] \tag{2}$$

A symmetry boundary condition is applied at the center of the positive particle

$$\frac{\partial c_1^s}{\partial r} = 0 \quad [r = 0, 0 < x < l_1] \tag{3}$$

The analogous set of equations are written for the negative electrode (region *3*)

$$\frac{\partial c_3^s}{\partial t} = \frac{1}{r^2}\frac{\partial}{\partial r}\left(r^2 D_3^s \frac{\partial c_3^s}{\partial r} \right) \quad [l_1 + l_2 < x < l_1 + l_2 + l_3] \tag{4}$$

With the boundary conditions given by

$$-D_3^s \frac{\partial c_3^s}{\partial r} = j_3 \quad [r = R_3, l_2 + l_3 < x < l_1 + l_2 + l_3] \tag{5}$$

$$\frac{\partial c_3^s}{\partial r} = 0 \quad [r = 0, l_1 + l_2 < x < l_1 + l_2 + l_3] \tag{6}$$

The Butler-Volmer equation is a common constitutive relation for the pore-wall flux in each

electrode as follows

$$j_1 = k_1 c_1^{\alpha_{a,1}} (c_1^{s,\max} - c_1^{s,surf})^{\alpha_{a,1}} (c_1^{s,surf})^{\alpha_{c,1}} \left(\exp\left(\frac{\alpha_{a,1} F \eta_1}{RT} \right) - \exp\left(\frac{-\alpha_{c,1} F \eta_1}{RT} \right) \right) \quad (7)$$

Where k_1 is the rate constant for the positive electrode reaction, and $c_1^{s,\max}$ denotes the maximum concentration of Li in the positive electrode particle. F and R denote Faraday's constant and the gas constant respectively. α 's are the charge transfer coefficients for each electrode reaction. The quantity $\eta = \phi_{s,1} - \phi_{l,1} - U_1(c_1^{s.surf})$ is the surface overpotential, expressed as the difference between the solid and liquid phase potentials minus the electrode open circuit potential $U_1(c_1^{s,surf})$ vs. a Li/Li^+ reference electrode. $c_1^{s,surf}$ is the solid particle concentration evaluated at the surface of the particle, i.e.

$$c_1^{s,surf} = c_1^s(r = R_1, x, t) \quad (8)$$

The dependence of open circuit potential (OCP) on the surface concentration is indicated accordingly. The equivalent expression for the negative electrode is given by

$$j_3 = k_3 c_3^{\alpha_{a,3}} (c_3^{s,\max} - c_3^{s,surf})^{\alpha_{a,3}} (c_3^{s,surf})^{\alpha_{c,3}} \left(\exp\left(\frac{\alpha_{a,3} F \eta_3}{RT} \right) - \exp\left(\frac{-\alpha_{c,3} F \eta_3}{RT} \right) \right) \quad (9)$$

Equations (1) and (4) can be volume-averaged over their respective electrode volumes. For the positive electrode, we obtain

$$\frac{\partial \int_{x=0}^{x=l_1} c_1^s dx}{\partial t} = \frac{1}{r^2}\frac{\partial}{\partial r}\left(r^2 D_1^s \frac{\partial \int_{x=0}^{x=l_1} c_1^s dx}{\partial r} \right) \tag{10}$$

The volume-averaged form becomes

$$\frac{\partial \overline{c_1^s}}{\partial t} = \frac{1}{r^2}\frac{\partial}{\partial r}\left(r^2 D_1^s \frac{\partial \overline{c_1^s}}{\partial r} \right) \tag{11}$$

Similarly, for the negative electrode, we have

$$\frac{\partial \overline{c_3^s}}{\partial t} = \frac{1}{r^2}\frac{\partial}{\partial r}\left(r^2 D_3^s \frac{\partial \overline{c_3^s}}{\partial r} \right) \tag{12}$$

The corresponding boundary conditions can also be expressed in volume-averaged form.

$$\begin{aligned} &\frac{\partial \overline{c_i^s}}{\partial r} = -\frac{\overline{j_i}}{D_i^s}, r = R_i \\ &\frac{\partial \overline{c_i^s}}{\partial r} = 0, r = 0 \qquad\qquad i \in \{1,3\} \end{aligned} \tag{13}$$

Numerical solution of these equations entails spatial discretization in the spherical dimension. Discretization of equations (11) and (12) results in a system of Differential Algebraic Equations (DAEs), with a convenient linear form for constant D_i^s . For discretization, we employ an efficient three-parameter model based on a biquadratic profile for the radial dependence of c_i^s .[49,78] This approximation is expected to ensure higher accuracy than a two-parameter parabolic profile even at relatively high rates of discharge. The discretized system of equations is therefore

$$\frac{d\overline{c_i^{s,avg}}}{dt} = -3\frac{\overline{j_i}}{R_i} \tag{14}$$

$$\frac{d\overline{q_i^{avg}}}{dt} = -30\frac{D_i^s}{R_i^2}\overline{q_i^{avg}} - \frac{45}{2}\frac{\overline{j_i}}{R_i^2} \tag{15}$$

$$35\frac{D_i^s}{R_i}[\overline{c_i^{s,surf}} - \overline{c_i^{s,avg}}] - 8D_i^s\overline{q_i^{avg}} = -\overline{j_i} \qquad i \in \{1,3\} \tag{16}$$

Where the three-parameter model has been expressed in terms of the particle-averaged solid phase concentration $\overline{c_i^{s,avg}}$, the particle-averaged concentration gradient $\overline{q_i^{avg}}$, and the particle surface concentration $\overline{c_i^{s,surf}}$. The particle average concentrations are related to the State of Charge (SoC) at the cell level and is directly obtained from the simulation results in the above formulation.

As mentioned earlier, the focus of this work is the development of efficient equations for the electrolyte phase, and therefore the most commonly adopted solid-phase approximation is used in this work. While other reformulation and approximation techniques may be more suitable at higher discharge rates and parameter combinations, we chose this approximation to (a) explain the concepts with a simpler approximation for brevity and easier adoption of current work (b) to alert users the importance of more detailed and relevant approximations published elsewhere.[55] Importantly, the accuracy of the quartic profile approximation was quantitatively verified against nearly error-free numerical methods (collocation, finite difference) for the cases considered in this work.

2.4.3. ***Solid Phase Charge Transport***

For charge transport in the solid phase, the governing equation may be written as a conservation law for charge as follows[75,79]

$$-\frac{\partial i_{s,1}}{\partial x} - a_1 F j_1 = 0 \quad [0 < x < l_1] \tag{17}$$

The time-derivative for charge density is ignored due to electroneutrality.

Similarly, we have, for the negative electrode

$$-\frac{\partial i_{s,3}}{\partial x} - a_3 F j_3 = 0 \qquad [l_1 + l_2 < x < l_1 + l_2 + l_3] \tag{18}$$

Here, are $i_{s,1}$ and $i_{s,3}$ denote the solid phase current densities. The constitutive equation for the solid phase current density is an Ohm's law expression based on the effective electronic conductivity and local potential gradient as follows

$$\begin{aligned} i_{s,1} &= -\sigma_1 \left(1 - \varepsilon_1 - \varepsilon_{f,1}\right) \frac{\partial \phi_{s,1}}{\partial x} \\ i_{s,3} &= -\sigma_3 \left(1 - \varepsilon_3 - \varepsilon_{f,3}\right) \frac{\partial \phi_{s,3}}{\partial x} \end{aligned} \tag{19}$$

Where $1 - \varepsilon_i - \varepsilon_{f,i}$ is the fraction of solid phase in electrode *i*, after subtracting the liquid and inert volume fractions. This factor corrects for the actual conduction pathways in the electrode material. More detailed correction factors may also be applied. The solid phase volume fraction also appears

in the specific interfacial area, which for perfectly spherical particles is given by $a_i = \frac{3}{R_i}\left(1-\varepsilon_i-\varepsilon_{fi}\right)$.

Volume-averaging gives us

$$\frac{i_{1,x=0}-i_{1,x=l_1}}{l_1} = a_1 F \overline{j_1} \tag{20}$$

Using the boundary conditions that impose the solid phase current density at the interfaces, one can simplify equation (20) as

$$\frac{i_{app}}{l_1} = a_1 F \overline{j_1} \tag{21}$$

Volume averaging thus connects the applied cell current density i_{app} and average pore-wall flux. The sign convention for the model is so adopted that i_{app} is negative during discharge.

$$\overline{j_1} = \frac{i_{app}}{a_1 F l_1} \tag{22}$$

Similarly, for the negative electrode, we have

$$\overline{j_3} = -\frac{i_{app}}{a_3 F l_3} \tag{23}$$

Equations (21) and (22) can be used in conjunction with the volume - averaged forms of equations (1) - (6) to determine the temporal evolution of average solid-phase concentrations for a given i_{app}. In effect, the active material in each electrode is now modeled by a single representative

particle[60], the Li concentration profiles through which will be influenced by factors such as the applied current density i_{app} , solid phase diffusion coefficients D_i^s and the characteristic particle radius R_i . This set of equations also determines the evolution of the averaged surface particle concentration, which in turn affects the surface overpotentials and thus the cell voltage response through constitutive equations (7) and (9). These equations are volume-averaged in order to obtain a relationship between the average pore-wall fluxes $\overline{j_i}$ and the average potentials $\overline{\phi_{s,i}}$ and $\overline{\phi_{e,i}}$. This is illustrated for the positive electrode in equation (24) below

$$\overline{j_1} = \frac{\int_{x=0}^{x=l_1} j_1 dx}{\int_{x=0}^{x=l_1} dx} = \frac{\int_{x=0}^{x=l_1} k_1 {c_1}^{\alpha_{a,1}} (c_{1,\max}^s - c_1^{s,surf})^{\alpha_{a,1}} (c_1^{s,surf})^{\alpha_{c,1}} \left(\exp\left(\frac{\alpha_{a,1} F \eta_1}{RT} \right) - \exp\left(\frac{-\alpha_{c,1} F \eta_1}{RT} \right) \right) dx}{\int_{x=0}^{x=l_1} dx} \tag{24}$$

Unlike the equations for electrolyte concentration, the highly non-linear nature of the constitutive equation renders evaluation of equation (24) cumbersome and likely impossible without the use of a full-order solution that gives the actual spatial dependence of the variables. To this end, averages of non-linear quantities are approximated by their value at the average values of the variables on which they depend (i.e. $\overline{f(X)} \approx f\left(\overline{X}\right)$).

Mathematically, this can be stated as

$$\begin{aligned} \overline{j_i} &\simeq k_i (\overline{c_i})^{\alpha_{a,i}} (c_i^{s,\max} - \overline{c_i^{s,surf}})^{\alpha_{a,i}} (\overline{c_i^{s,surf}})^{\alpha_{c,i}} \left(\exp\left(\frac{\alpha_{a,i} F \overline{\eta_i}}{RT} \right) - \exp\left(\frac{-\alpha_{c,i} F \overline{\eta_i}}{RT} \right) \right) \\ \overline{\eta_i} &= \overline{\phi_{s,i}} - \overline{\phi_{l,i}} - U_i(\overline{c_i^{s,surf}}) \qquad i \in \{1,3\} \end{aligned} \tag{25}$$

The classic Single Particle Model (SPM) employs an additional simplification by ignoring the

dynamics of the electrolyte phase. Therefore, $\overline{c_i} = c_0$, implying that the electrolyte concentration is always equal to its initial value. Neglecting liquid phase variations also means that $\overline{\phi_{2,i}}$ is often set to a constant reference, .e.g. $\overline{\phi_{2,i}} = 0$ for all i .

Neglect of ohmic and electrolyte concentration effects restricts the accuracy of SPM to operating regimes characterized by low ohmic losses, low currents, and kinetically limited electrodes, which usually result in spatially uniform pore-wall flux distributions.[58,68] To this end, the Tanks-in-Series descriptions of electrolyte dynamics are expected to augment and improve the practical applicability of SPM.

2.4.4. *Electrolyte Mass Balance: Volume-Averaging*

We begin with the governing equation for electrolyte concentration for an isothermal model in one spatial dimension. The equations for c based on porous electrode theory may be expressed in the form of conservation laws[75]

In the positive electrode,

$$\varepsilon_1 \frac{\partial c_1}{\partial t} = -\frac{\partial N_1}{\partial x} + a_1\left(1 - t_+^0\right) j_1 \qquad [0 < x < l_1] \tag{26}$$

Due to the absence of solid active material, the conservation equation for c in the separator is characterized by a lack of a source term as

$$\varepsilon_2 \frac{\partial c_2}{\partial t} = -\frac{\partial N_2}{\partial x} \qquad [l_1 < x < l_1 + l_2] \tag{27}$$

The subscript *2* is used to denote the variables in the separator domain.

The equation for the negative electrode is identical in form to that of the positive electrode

$$\varepsilon_3 \frac{\partial c_3}{\partial t} = -\frac{\partial N_3}{\partial x} + a_3\left(1-t_+^0\right) j_3 \quad [l_1 + l_2 < x < l_1 + l_2 + l_3] \tag{28}$$

N_1, N_2, N_3 may regarded as electrolyte fluxes, which need to be related to local concentration gradients. Noting the similarity of the governing equations to Fick's second law, we have the following constitutive equations[79]

$$\begin{aligned} \mathrm{N}_1 &= -D(c_1)\varepsilon_1^{b_1}\frac{\partial c_1}{\partial x} \\ \mathrm{N}_2 &= -D(c_2)\varepsilon_2^{b_2}\frac{\partial c_2}{\partial x} \\ \mathrm{N}_3 &= -D(c_3)\varepsilon_3^{b_3}\frac{\partial c_3}{\partial x} \end{aligned} \tag{29}$$

In the above equations, $D(c)$ denotes the concentration-dependent electrolyte diffusion coefficient, corrected by a Bruggemann-type factor to account for porous medium tortuosity.

The governing equations for electrolyte concentration are second-order in space, which entails the specification of two boundary conditions for c_1, c_2 and c_3. The boundary conditions are defined at the extremities of each domain. The positive and negative current collectors are physical barriers to the transport of Li^+ ions, and thus the electrolyte flux at these locations is set to zero. These boundary conditions are thus given by

$$N_{1,x=0} = N_{01} = 0 \tag{30}$$

And,

$$N_{3,x=l_p+l_s+l_n} = N_{34} = 0 \tag{31}$$

In addition, electrolyte concentrations and their fluxes must be continuous at the interface between the separator and electrodes. At the positive electrode-separator interface, this is expressed as

$$\begin{aligned} c_{1,x=l_1} &= c_{2,x=l_1} \\ N_{1,x=l_1} &= N_{2,x=l_1} = N_{12} \end{aligned} \tag{32}$$

In general N_{ij} is used to denote the flux at the interface of regions i and j.

Similarly, at the interface between the separator and negative electrode, we have

$$\begin{aligned} c_{2,x=l_1+l_2} &= c_{3,x=l_1+l_2} \\ N_{2,x=l_1+l_2} &= N_{3,x=l_1+l_2} = N_{23} \end{aligned} \tag{33}$$

Now, equation (26) is integrated over the volume of the positive electrode V_1 as

$$\frac{\partial \int_{V_1} \varepsilon_1 c_1 dV}{\partial t} = -\int_{V_1} \frac{\partial N_1}{\partial x} dV + \int_{V_1} a_1 \left(1 - t_+^0\right) j_1 dV \tag{34}$$

For the one-dimensional model in cartesian coordinates, the differential volume dV is given by $dV = Adx$, where A is a constant that may be considered a cross-sectional area. In addition, we express the integrals in terms of average quantities as $\overline{c_1} = \frac{\int_{V_1} c_1 dV}{\int_{V_1} dV}$, and $\overline{j_1} = \frac{\int_{V_1} j_1 dV}{\int_{V_1} dV}$, with $\overline{\nu}$ denoting the volume average of variable ν in a given 'tank'. Substituting these relations converts the volume integral into a one-dimensional integral over electrode thickness, i.e. from $x = 0$ to

$x = l_1$.

Equation (34) thus becomes

$$\varepsilon_1 \frac{d\overline{c_1}}{dt} = -\frac{\int_{x=0}^{x=l_1} \frac{\partial N_1}{\partial x} dx}{l_1} + a_1\left(1-t_+^0\right)\overline{j_1} = \frac{N_{1,x=0} - N_{1,x=l_1}}{l_1} + a_1\left(1-t_+^0\right)\overline{j_1} \tag{35}$$

Here, we make the reasonable assumption that the electrode porosity ε_1, specific interfacial area a_1 and Li^+ transport number t_+^0 in the electrolyte phase are constant in both space and time.[80]

Using equation (30), equation (35) reduces to

$$\varepsilon_1 \frac{d\overline{c_1}}{dt} = \frac{-N_{1,x=l_1}}{l_1} + a_1\left(1-t_+^0\right)\overline{j_1} \tag{36}$$

The same sequence of operations gives us the volume-averaged equations for the separator and negative electrode as follows

$$\varepsilon_2 \frac{d\overline{c_2}}{dt} = \frac{N_{2,x=l_1} - N_{2,x=l_1+l_2}}{l_2} \tag{37}$$

$$\varepsilon_3 \frac{d\overline{c_3}}{dt} = \frac{N_{3,x=l_1+l_2}}{l_3} + a_3\left(1-t_+^0\right)\overline{j_3} \tag{38}$$

It is worth noting that the steps applied so far represent a rigorous volume-averaging of the equations in each porous domain, followed by the use of the boundary conditions to eliminate interfacial flux terms where possible. No approximations have been made up to this point.

2.4.5. *Electrolyte Mass Balance: Approximating Interfacial Fluxes*

In order to track the average concentrations in each 'tank', we begin with the volume-averaged concentration equations (36) - (38). Inspection of these equations reveals the presence of the unknown interfacial flux terms that require suitable approximations to achieve closure. In doing so, we can exploit the flux boundary conditions (32) and (33), which establish the mass flow coupling between adjacent tanks in series.

A simple approximation for the interfacial diffusive flux is in terms of a 'driving force' Δc and a 'length scale' approximation $\delta_{i,ij}$ within domain i for the interface between domains i and j. The concept is depicted in **Figure 2.3**. This is analogous to the 'diffusion-length' approach attempted previously, but we dispense with assumptions on the spatial profiles for c.[70,81] The 'driving force' Δc is expressed in terms of a difference between the average concentration and the unknown interfacial concentration $\Delta c_1 = \overline{c_1} - c_{1,x=l_1}$, and we use $\delta_{1,12} = \frac{l_1}{2}$ as a first approximation. We therefore have, using the constitutive equations (29)

$$\mathrm{N}_{1,x=l_1} = -D(c_{1,x=l_1})\varepsilon_1^{b_1}\left.\frac{\partial c_1}{\partial x}\right|_{x=l_1} \approx D(c_{1,x=l_1})\varepsilon_1^{b_1}\left(\frac{\Delta c_1}{\delta_{1,12}}\right) = D(c_{1,x=l_1})\varepsilon_1^{b_1}\left(\frac{\overline{c_1} - c_{1,x=l_1}}{\frac{l_1}{2}}\right) \qquad (39)$$

On the separator side of the interface, we assume $\delta_{2,12} = \frac{l_2}{2}$, which we use for the flux approximation

$$\mathrm{N}_{2,x=l_1} = -D(c_{2,x=l_1})\varepsilon_2^{b_2}\left.\frac{\partial c_2}{\partial x}\right|_{x=l_2} \approx D(c_{2,x=l_1})\varepsilon_2^{b_2}\left(\frac{\Delta c_2}{\delta_{2,12}}\right) = D(c_{2,x=l_1})\varepsilon_2^{b_2}\left(\frac{-\overline{c_2}+c_{2,x=l_1}}{\frac{l_2}{2}}\right) \quad (40)$$

An equivalent interpretation of the above flux approximations is that we have assumed that the concentration at the midpoint of the porous domain equal to the volume average. This approximation is mathematically equivalent to Gaussian integration with one point, accurate to l_1^2

.

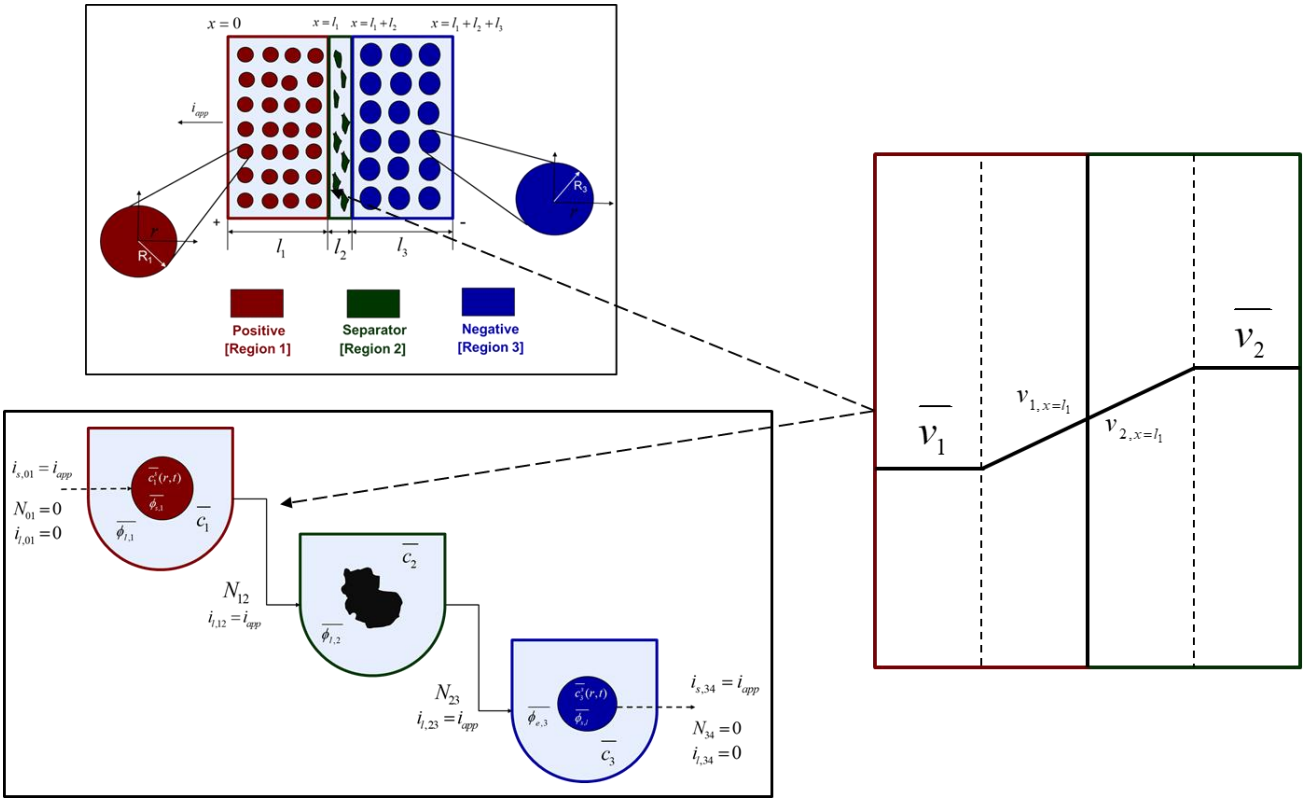

Figure 2.3. Representing the flux approximations at the interface of two regions. The example is illustrated for the positive electrode-separator interface.

Substitution of the above approximations into the continuity conditions of equations (32) gives us

$$D(c_{1,x=l_1})\varepsilon_1^{b_1}\left(\frac{\overline{c_1}-c_{1,x=l_1}}{\frac{l_1}{2}}\right)=D(c_{2,x=l_1})\varepsilon_2^{b_2}\left(\frac{-\overline{c_2}+c_{2,x=l_1}}{\frac{l_2}{2}}\right) \tag{41}$$

The interfacial concentration is now expressed in terms of tank averages as

$$c_{12}=c_{1,x=l_1}=c_{2,x=l_1}=\left(\frac{\frac{\varepsilon_1^{b_1}}{l_1}\overline{c_1}+\frac{\varepsilon_2^{b_2}}{l_2}\overline{c_2}}{\frac{\varepsilon_1^{b_1}}{l_1}+\frac{\varepsilon_2^{b_2}}{l_2}}\right) \tag{42}$$

In general, we use the notation v_{ij} to denote the value of a given variable v at the interface of domains i and j. An identical sequence of steps yields the concentration at the separator-negative interface as

$$c_{23}=c_{2,x=l_1+l_2}=c_{3,x=l_1+l_2}=\left(\frac{\frac{\varepsilon_3^{b_3}}{l_3}\overline{c_3}+\frac{\varepsilon_2^{b_2}}{l_2}\overline{c_2}}{\frac{\varepsilon_3^{b_3}}{l_3}+\frac{\varepsilon_2^{b_2}}{l_2}}\right) \tag{43}$$

Substituting the values of interfacial concentrations back into the flux approximations allows us to express the interfacial fluxes in terms of tank-average variables. Thus, we have

$$N_{12}=\frac{-2D\left(c_{12}\right)(\overline{c_2}-\overline{c_1})}{\frac{l_1}{\varepsilon_1^{b_1}}+\frac{l_2}{\varepsilon_2^{b_2}}} \tag{44}$$

$$N_{23} = \frac{-2D(c_{23})(\overline{c_3} - \overline{c_2})}{\frac{l_2}{\varepsilon_2^{b_2}} + \frac{l_3}{\varepsilon_3^{b_3}}} \tag{45}$$

Equations (44) and (45) can thus be inserted into the volume-averaged forms (36) - (38) to obtain a system of Ordinary Differential Equations (ODEs). It is important to equate the approximations for the *total flux*, and not just the driving forces.[82] This ensures true mass conservation.

In the three 'tanks', after substituting the known values of average pore-wall fluxes, we have

$$\frac{d\overline{c_1}}{dt} = \frac{\frac{2D(c_{12})(\overline{c_2} - \overline{c_1})}{\frac{l_1}{\varepsilon_1^{b_1}} + \frac{l_2}{\varepsilon_2^{b_2}}}}{\varepsilon_1 l_1} + \left(1 - t_+^0\right)\frac{i_{app}}{\mathrm{F}\varepsilon_1 l_1} \tag{46}$$

$$\frac{d\overline{c_2}}{dt} = \frac{\frac{-2D(c_{12})(\overline{c_2} - \overline{c_1})}{\frac{l_1}{\varepsilon_1^{b_1}} + \frac{l_2}{\varepsilon_2^{b_2}}} + \frac{2D(c_{23})(\overline{c_3} - \overline{c_2})}{\frac{l_2}{\varepsilon_2^{b_2}} + \frac{l_3}{\varepsilon_3^{b_3}}}}{\varepsilon_2 l_2} \tag{47}$$

$$\frac{d\overline{c_3}}{dt} = \frac{\frac{-2D(c_{23})(\overline{c_3} - \overline{c_2})}{\frac{l_2}{\varepsilon_2^{b_2}} + \frac{l_3}{\varepsilon_3^{b_3}}}}{\varepsilon_3 l_3} - \left(1 - t_+^0\right)\frac{i_{app}}{\mathrm{F}\varepsilon_3 l_3} \tag{48}$$

As specified previously, a slight difference between this approach and others in literature[60,68,74,83] is that it avoids the assumption of uniform reaction rate (given by the pore-wall flux) to solve the PDEs for concentration, but instead deals in average quantities. This allows the prediction of average concentration trends even when the constant pore-wall flux assumption is not applicable, with the flux approximations as the sole source of error. Inspection of equations (46) - (48) also

suggests their decoupling from those for other electrochemical variables, indicating that they may be solved independently as an ODE system, the solutions of which may be used to compute other relevant quantities during post-processing. While all model equations are simulated simultaneously throughout this work, such a segregated approach may be computationally efficient in real-time control or resource-constrained environments and is enabled by the Tanks-in-Series model. Leaving the model in this form allows for the incorporation of nonlinear diffusivities.

2.4.6. *Liquid Phase Charge Transport*

The governing equation for electrolyte current is related to charge conservation in the electrolyte phase. Thus, we have

$$\begin{aligned} -\frac{\partial i_{l,1}}{\partial x} &= -Fa_1 j_1 \\ -\frac{\partial i_{l,2}}{\partial x} &= 0 \\ -\frac{\partial i_{l,3}}{\partial x} &= -Fa_3 j_3 \end{aligned} \tag{49}$$

Where the constitutive equation for electrolyte current is given by a modified Ohm's law based on concentrated solution theory. Thus

$$\begin{aligned} i_{l,1} &= -\kappa(c_1)\varepsilon_1^{b_1}\frac{\partial \phi_{l,1}}{\partial x} + \frac{2RT(1-t_+^0)}{F}\left(1+\frac{\partial \ln f}{\partial \ln c_1}\right)\kappa(c_1)\varepsilon_1^{b_1}\frac{1}{c_1}\frac{\partial c_1}{\partial x} \\ i_{l,2} &= -\kappa(c_2)\varepsilon_2^{b_2}\frac{\partial \phi_{l,2}}{\partial x} + \frac{2RT(1-t_+^0)}{F}\left(1+\frac{\partial \ln f}{\partial \ln c_2}\right)\kappa(c_2)\varepsilon_2^{b_2}\frac{1}{c_2}\frac{\partial c_2}{\partial x} \\ i_{l,3} &= -\kappa(c_3)\varepsilon_3^{b_3}\frac{\partial \phi_{l,3}}{\partial x} + \frac{2RT(1-t_+^0)}{F}\left(1+\frac{\partial \ln f}{\partial \ln c_3}\right)\kappa(c_3)\varepsilon_3^{b_3}\frac{1}{c_3}\frac{\partial c_3}{\partial x} \end{aligned} \tag{50}$$

The concentration-dependent ionic conductivity $\kappa(c)$ is corrected by a tortuosity factor specific to

each region.

Now, volume-averaging equation (49) is redundant, ultimately resulting in equation (21) due to the overall charge balance imposed by porous electrode theory. However, the interfacial boundary conditions for $i_{2,i}$ provide for the estimation of liquid phase ohmic effects. At the interface between the electrodes and separator, the entire current i_{app} is carried by the liquid phase, and the solid-phase current density is zero. Using the constitutive equations (50), we therefore have, at the positive electrode-separator interface

$$\begin{aligned} i_{l,1,x=l_1} &= -\kappa(c_{1,x=l_1})\varepsilon_1^{b_1}\frac{\partial\phi_{l,1}}{\partial x} + \frac{2RT(1-t_+^0)}{F}\nu(c_{1,x=l_1})\kappa(c_{1,x=l_1})\varepsilon_1^{b_1}\frac{1}{c_{1,x=l_1}}\frac{\partial c_1}{\partial x} = i_{app} \\ i_{l,2,x=l_1} &= -\kappa(c_{2,x=l_1})\varepsilon_2^{b_2}\frac{\partial\phi_{l,2}}{\partial x} + \frac{2RT(1-t_+^0)}{F}\nu(c_{2,x=l_1})\kappa(c_{2,x=l_1})\varepsilon_2^{b_2}\frac{1}{c_{2,x=l_1}}\frac{\partial c_2}{\partial x} = i_{app} \end{aligned} \tag{51}$$

Where we have defined the thermodynamic factor as $\nu(c_i) = 1 + \frac{\partial \ln f}{\partial \ln c_i}$. The tank-averaged equations for the electrolyte potential are now written as

$$\begin{aligned} i_{l,1,x=l_1} &= -\kappa(c_{1,x=l_1})\varepsilon_1^{b_1}\left(\frac{\phi_{l,x=l_1} - \overline{\phi_{l,1}}}{\frac{l_p}{2}}\right) + \frac{2RT(1-t_+^0)}{F}\nu(c_{1,x=l_1})\kappa(c_{1,x=l_1})\varepsilon_1^{b_1}\frac{1}{c_{1,x=l_1}}\left(\frac{c_{1,x=l_1} - \overline{c_1}}{\frac{l_p}{2}}\right) = i_{app} \\ i_{l,2,x=l_1} &= -\kappa(c_{2,x=l_1})\varepsilon_2^{b_2}\left(\frac{\overline{\phi_{l,2}} - \phi_{l,x=l_1}}{\frac{l_s}{2}}\right) + \frac{2RT(1-t_+^0)}{F}\nu(c_{2,x=l_1})\kappa(c_{2,x=l_1})\varepsilon_2^{b_2}\frac{1}{c_{2,x=l_1}}\left(\frac{\overline{c_2} - c_{2,x=l_1}}{\frac{l_s}{2}}\right) = i_{app} \end{aligned} \tag{52}$$

Where an approximation $\frac{\partial\phi_{l,1}}{\partial x} \approx \frac{(\phi_{l,1,x=l_p} - \overline{\phi_{l,1}})}{\frac{l_p}{2}}$ and $\frac{\partial\phi_{l,2}}{\partial x} \approx \frac{(\phi_{l,2,x=l_p} - \overline{\phi_{l,2}})}{\frac{l_s}{2}}$, analogous to

equations (39) and (40) is made for the gradients of $\phi_{l,i}$, in terms of tank-average and interfacial values. Equating the interfacial current density results in equation (53) , which can be solved in conjunction with continuity conditions to obtain the interfacial electrolyte potential.

$$-\varepsilon_1^{b_1}\left(\frac{\phi_{l,1,x=l_1}-\overline{\phi_{l,1}}}{\frac{l_1}{2}}\right)=-\varepsilon_2^{b_2}\left(\frac{\overline{\phi_{l,2}}-\phi_{l,2,x=l_1}}{\frac{l_2}{2}}\right) \tag{53}$$

Solving for $\phi_{l,12}$ gives us

$$\phi_{l,12}=\phi_{l,1,x=l_1}=\phi_{l,2,x=l_1}=\left(\frac{\frac{\varepsilon_1^{b_1}}{l_1}\overline{\phi_{l,1}}+\frac{\varepsilon_2^{b_2}}{l_2}\overline{\phi_{l,2}}}{\frac{\varepsilon_1^{b_1}}{l_1}+\frac{\varepsilon_2^{b_2}}{l_2}}\right) \tag{54}$$

A similar form is obtained at the separator-negative electrode interface

$$\phi_{l,23}=\phi_{l,2,x=l_1+l_2}=\phi_{l,3,x=l_1+l_2}=\left(\frac{\frac{\varepsilon_3^{b_3}}{l_3}\overline{\phi_{l,3}}+\frac{\varepsilon_2^{b_2}}{l_2}\overline{\phi_{l,2}}}{\frac{\varepsilon_3^{b_3}}{l_3}+\frac{\varepsilon_2^{b_2}}{l_2}}\right) \tag{55}$$

Equations (39) - (43) can now be combined with equations (51) - (55) to give us the algebraic equations governing electrolyte potential

$$
\begin{aligned}
i_{app} &= -2\kappa(c_{12})\left(\frac{\overline{\phi_{l,2}}-\overline{\phi_{l,1}}}{\frac{l_1}{\varepsilon_1^{b_1}}+\frac{l_2}{\varepsilon_2^{b_2}}}\right)+\frac{4RT(1-t_+^0)}{F}\nu(c_{12})\kappa(c_{12})\frac{1}{c_{12}}\left(\frac{\overline{c_2}-\overline{c_1}}{\frac{l_1}{\varepsilon_1^{b_1}}+\frac{l_2}{\varepsilon_2^{b_2}}}\right)=i_{l,1,x=l_1} \\
i_{app} &= -2\kappa(c_{23})\left(\frac{\overline{\phi_{l,3}}-\overline{\phi_{l,2}}}{\frac{l_3}{\varepsilon_3^{b_3}}+\frac{l_2}{\varepsilon_2^{b_2}}}\right)+\frac{4RT(1-t_+^0)}{F}\nu(c_{23})\kappa(c_{23})\frac{1}{c_{23}}\left(\frac{\overline{c_3}-\overline{c_2}}{\frac{l_2}{\varepsilon_2^{b_2}}+\frac{l_3}{\varepsilon_3^{b_3}}}\right)=i_{l,3,x=l_1+l_2}
\end{aligned}
\tag{56}
$$

The final step in the model formulation is the specification of a reference potential. A convenient reference is the electrolyte potential at the interface between the separator and positive electrode. We thus set $\phi_{l,12}=0$. This modifies equation (54), and completes the DAE system for the Tank Model.

$$
\phi_{l,12}=\left(\frac{\frac{\varepsilon_1^{b_1}}{l_1}\overline{\phi_{l,1}}+\frac{\varepsilon_2^{b_2}}{l_2}\overline{\phi_{l,2}}}{\frac{\varepsilon_1^{b_1}}{l_1}+\frac{\varepsilon_2^{b_2}}{l_2}}\right)=0 \tag{57}
$$

We can now assemble the complete Tanks-in-Series Model in **Table 2-III**.

Table 2-III. Governing Equations of the Tanks-in-Series Model.

Positive Electrode (Region 1)	Separator (Region 2)	Negative Electrode (Region 3)
$\frac{d\bar{c}_1}{dt} = \frac{\frac{2D(c_{12})(\bar{c}_2-\bar{c}_1)}{\frac{l_1}{\varepsilon_1^{b_1}}+\frac{l_2}{\varepsilon_2^{b_2}}}}{\varepsilon_1 l_1} + \left(1-t_+^0\right)\frac{i_{app}}{F\varepsilon_1 l_1}$	$\frac{d\bar{c}_2}{dt} = \frac{\frac{-2D(c_{12})(\bar{c}_2-\bar{c}_1)}{\frac{l_1}{\varepsilon_1^{b_1}}+\frac{l_2}{\varepsilon_2^{b_2}}} + \frac{2D(c_{23})(\bar{c}_3-\bar{c}_2)}{\frac{l_2}{\varepsilon_2^{b_2}}+\frac{l_3}{\varepsilon_3^{b_3}}}}{\varepsilon_2 l_2}$	$\frac{d\bar{c}_3}{dt} = \frac{\frac{-2D(c_{23})(\bar{c}_3-\bar{c}_2)}{\frac{l_2}{\varepsilon_2^{b_2}}+\frac{l_3}{\varepsilon_3^{b_3}}}}{\varepsilon_3 l_3} - \left(1-t_+^0\right)\frac{i_{app}}{\varepsilon_3 l_3}$
$i_{app} = -2\kappa(c_{12})\left(\frac{\bar{\phi}_{l,2}-\bar{\phi}_{l,1}}{\frac{l_1}{\varepsilon_1^{b_1}}+\frac{l_2}{\varepsilon_2^{b_2}}}\right) + \frac{4RT(1-t_+^0)}{F}\nu(c_{12})\kappa(c_{12})\frac{1}{c_{12}}\left(\frac{\bar{c}_2-\bar{c}_1}{\frac{l_1}{\varepsilon_1^{b_1}}+\frac{l_2}{\varepsilon_2^{b_2}}}\right)$	$\phi_{l,12} = \left(\frac{\frac{\varepsilon_1^{b_1}}{l_1}\bar{\phi}_{l,1}+\frac{\varepsilon_2^{b_2}}{l_2}\bar{\phi}_{l,2}}{\frac{\varepsilon_1^{b_1}}{l_1}+\frac{\varepsilon_2^{b_2}}{l_2}}\right) = 0$	$i_{app} = -2\kappa(c_{23})\left(\frac{\bar{\phi}_{l,3}-\bar{\phi}_{l,2}}{\frac{l_3}{\varepsilon_3^{b_3}}+\frac{l_2}{\varepsilon_2^{b_2}}}\right) + \frac{4RT(1-t_+^0)}{F}\nu(c_{23})\kappa(c_{23})\frac{1}{c_{23}}\left(\frac{\bar{c}_3-\bar{c}_2}{\frac{l_2}{\varepsilon_2^{b_2}}+\frac{l_3}{\varepsilon_3^{b_3}}}\right)$
$\frac{d\overline{c_1^{s,avg}}}{dt} = -3\frac{\bar{j}_1}{R_1}$		$\frac{d\overline{c_3^{s,avg}}}{dt} = -3\frac{\bar{j}_3}{R_3}$
$\frac{d\overline{q_1^{avg}}}{dt} = -30\frac{D_1^s}{R_1^2}\overline{q_1^{avg}} - \frac{45}{2}\frac{\bar{j}_1}{R_1^2}$		$\frac{d\overline{q_3^{avg}}}{dt} = -30\frac{D_3^s}{R_3^2}\overline{q_3^{avg}} - \frac{45}{2}\frac{\bar{j}_3}{R_3^2}$
$35\frac{D_1^s}{R_1}[\overline{c_1^{s,surf}} - \overline{c_1^{s,avg}}] - 8D_1^s\overline{q_1^{avg}} = -\bar{j}_1$		$35\frac{D_3^s}{R_1}[\overline{c_3^{s,surf}} - \overline{c_3^{s,avg}}] - 8D_3^s\overline{q_3^{avg}} = -\bar{j}_3$
$\frac{i_{app}}{Fa_1l_1} = k_1\left(\bar{c}_1\right)^{\alpha_{c,1}}{}_1(c_1^{s,\max}-\overline{c_1^{s,surf}})^{\alpha_{a,1}}(\overline{c_1^{s,surf}})^{\alpha_{c,1}}\left(\exp\left(\frac{\alpha_{a,1}F\bar{\eta}_1}{RT}\right)-\exp\left(\frac{-\alpha_{c,1}F\bar{\eta}_1}{RT}\right)\right)$		$\frac{-i_{app}}{Fa_3l_3} = k_3\left(\bar{c}_3\right)^{\alpha_{a,3}}(c_3^{s,\max}-\overline{c_3^{s,surf}})^{\alpha_{a,3}}(\overline{c_3^{s,surf}})^{\alpha_{c,3}}\left(\exp\left(\frac{\alpha_{a,3}F\bar{\eta}_3}{RT}\right)-\exp\left(\frac{-\alpha_{c,3}F\bar{\eta}_3}{RT}\right)\right)$
$\bar{\eta}_1 = \bar{\phi}_{s,1} - \bar{\phi}_{l,1} - U(\overline{c_1^{s,surf}})$		$\bar{\eta}_3 = \bar{\phi}_{s,3} - \bar{\phi}_{l,3} - U(\overline{c_3^{s,surf}})$

2.4.7. *Cell Voltage*

Solving the system of **Table 2-III** now allows the prediction of the cell voltage as

$$V_{cell} = \overline{\phi_{s,1}} - \overline{\phi_{s,3}} \tag{58}$$

In using equation (58) to calculate cell voltage for the Tanks-in-Series Model, it is implicitly assumed that the solid phase potentials at the cell termini may be approximated by their respective electrode averages. In reality, the terminal potentials must be determined via interfacial approximations for the constitutive equations (19) analogous to equations (52) for $\phi_{l,i}$. Accounting for this potential drop may be necessitated at high current densities, or for electrodes with poor electronic conductivity. In practice, σ_{eff} ~ 50 S/m and the $\phi_{s,i}$ gradients within the electrode are negligible . This can be seen by the following rough estimation for an aggressive $\left|i_{app}\right| = 100 \ \ {}^{A}\!/_{m^2}$ and $\sigma_{eff} = 1 \ \ {}^{S}\!/_{m}$, and electrode thickness $l_1 = 100 \ \mu m$. We therefore have

$$\begin{aligned} i_{app} &\simeq -\sigma_{eff} \frac{\overline{\phi_{s,1}} - \phi_{s,01}}{l_1 / 2} \\ \overline{\phi_{s,1}} - \phi_{s,01} &= \left| -l_1 i_{app} / (2\sigma_{eff}) \right| = 10^{-2} / 2 \sim 0.005V \end{aligned} \tag{59}$$

Thus, the upper limit of this solid phase ohmic drop is ~5 mV per electrode. This justifies the assumption of uniform $\phi_{s,i}$ for most situations of practical salience.

2.5. Model Parameters

Table 2-IV lists the parameter values for a 1.78 Ah Nickel-Cobalt-Manganese (NCM)/graphite power cell, collated from various sources by Tanim et al.[71] Electrolyte transport property correlations were taken from the work of Valøen and Reimers, and are listed in **Table 2-II**.[80] A modified value of $R_i = 1 \ \mu m$ was used for the particle radii, in order to ensure rapid diffusion with negligible gradients. The absence of solid phase diffusion limitations serves the practical purpose of ensuring the accuracy of our three-parameter model for solid phase transport even at relatively high discharge rates, based on the quantitative guidelines of Subramanian et al.[78] This prevents numerical errors for solid phase discretization from confounding our analysis, which is focused on examining the accuracy of our Tanks-in-Series equations for the liquid phase.

Table 2-IV. Base case model parameters (constant values).

Symbol	Parameter	Negative Electrode	Separator	Positive Electrode	Units
ε_i	Porosity	0.3	0.4	0.3	
ε_{fi}	Electrode filler fraction	0.038		0.12	
b_i	Brugemann tortuosity correction	1.5	1.5	1.5	
a_i	Particle surface area per unit volume	1740000		1986000	m^2/m^3
$c_i^{s,\max}$	Maximum particle phase concentration	31080		51830	mol/m^3
$c_i^{s,0}$	Initial particle phase concentration	24578		18645	mol/m^3
c_0	Initial electrolyte concentration		1200		mol/m^3
D_i^s	Solid phase diffusivity	1.4×10^{-14}		2.0×10^{-14}	m^2/s
k_i	Electrode reaction rate	6.626×10^{-10}		2.405×10^{-10}	$m^{2.5}/(mol^{0.5}s)$

	constant				
$\alpha_{a,i}$	Electrode reaction anodic coefficient	0.5		0.5	
$\alpha_{c,i}$	Electrode reaction cathodic coefficient	0.5		0.5	
l_i	Electrode thickness	40 x 10^{-6}	25 x 10^{-6}	36.55 x 10^{-6}	m
R_i	Characteristic particle radius	10^{-6}		10^{-6}	m
t_+^0	Li+ transference number		0.38		
σ_i	Electronic conductivity	100		100	S/m
T	Temperature		298.15		K
i_{app}	Current Density (1C)		-17.54		A/m^2

2.6. Computational Details

The full p2D model is used as the benchmark in evaluating the predictions of the Tanks-in-Series model. The p2D model was discretized and solved using coordinate transformation, model

reformulation and orthogonal collocation techniques described in previous work.[46] The number of collocation points in each region were adjusted to achieve numerical convergence of discharge curves at different current densities, ultimately selecting n=(7,3,7) Gauss-Legendre collocation points. Comparisons of the Tank Model with SPM are also reported, for which a Finite-Difference discretization with n=256 internal node points were employed. All DAE systems were consistently initialized [84], and solved using the *dsolve* function in *Maple 2018*.[85] An absolute solver tolerance $abserr = 10^{-8}$ was specified.

For evaluating computational performance, the discretized equations were solved in time using IDA, an Implicit Differential-Algebraic solver in ANSI-standard C language under BSD license. IDA is an efficient solver for initial value problems (IVP) for systems of DAEs, which is part of the SUNDIALS (SUite of Nonlinear and DIfferential/ALgebraic equation Solvers) package.[86] The absolute solver tolerance was set to $atol = 10^{-8}$ and a relative tolerance of $rtol = 10^{-7}$ was specified.

All computations were performed on an Intel ® Core ™ i7-7700K processor with a clock speed of 4.2 GHz, 8 logical cores and 64 GB RAM.

2.7. Results and Discussion – Base Case Model Comparisons

In this section, the Tanks-in-Series model is simulated for galvanostatic discharge at C-rates of 1C, 2C, and 5C. In comparing the model predictions to the full p2D model, we seek to ascertain the accuracy of the Tanks-in-Series approximations, and to quantify its deviation from p2D as a function of applied current density. The results are also compared against curves from SPM,

chiefly to illustrate improvement over commonly used fast physics-based models.

2.7.1. *Galvanostatic Discharge Curves*

Figure 2.4 compares the cell voltage-time predictions of our Tanks-in-Series model (hereafter termed the 'Tank Model') with SPM and the full p2D model. The agreement of all three models at 1C and 2C indicates relatively low liquid phase polarizations compared to other overpotentials, possibly due to the values of the Base Case parameters, which are those of a power-cell rated for higher discharge rates. Even so, there is a discernible improvement with the Tank Model. The improved accuracy of the tank model at 5C discharge is substantially more pronounced, particularly during the intermediate phase of the discharge process. This is further illustrated in **Figure 2.5**, which depicts the instantaneous error for V_{cell}. The qualitative trends are identical for both the Tank Model and SPM, but the curves for the Tank Model appear shifted by nearly a constant value compared to SPM. This difference is due to the Tank Model's estimates of liquid phase ohmic drops and concentration overpotentials, which reduces error. The magnitude of these overpotentials increases with current density as characterized by the C-rate.

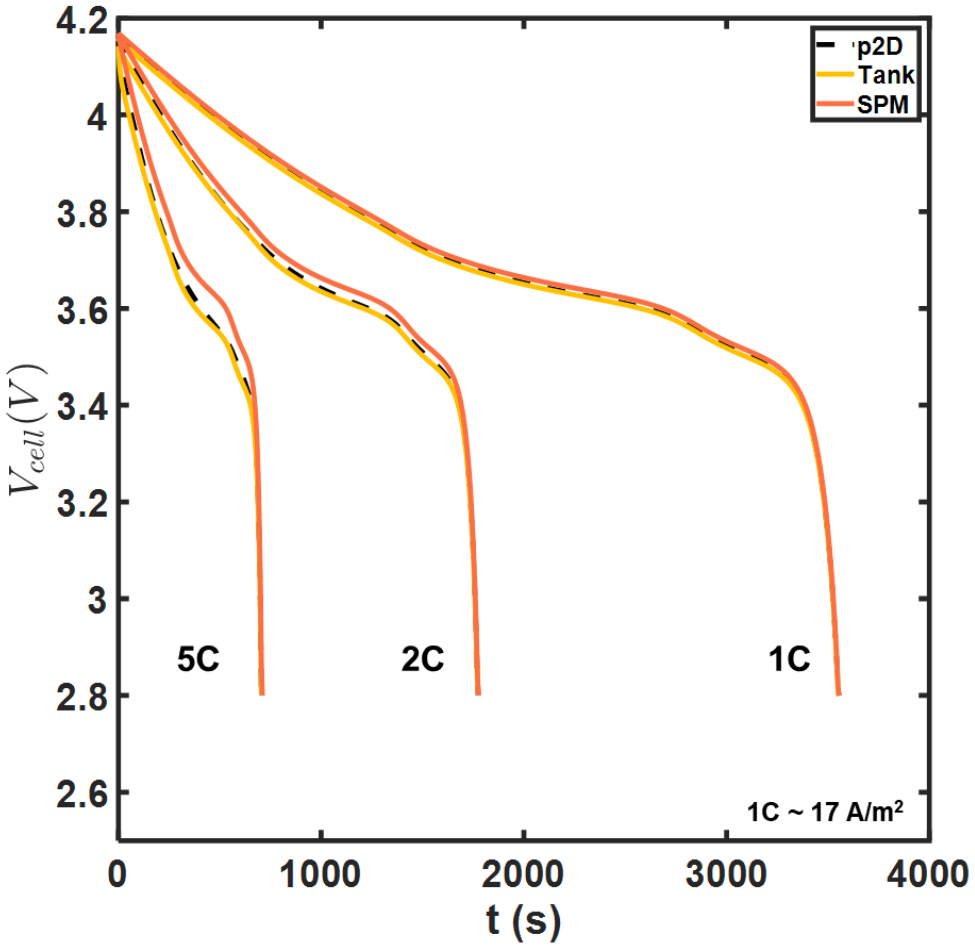

Figure 2.4. Model comparisons for cell voltage at different rates of discharge. The tank model (gold) coincides almost exactly with the p2D model, obscuring the black dashed curves of the latter. This color code is used throughout the chapter in all model comparisons involving SPM.

The increased accuracy of the Tank Model at 5C is illustrated in **Figure 2.5 (c)** , and **(d)**, with the absolute error only slightly exceeding 20 mV, in contrast to >60 mV for SPM. A more than threefold reduction in RMSE is obtained at 5C due to the incorporation of the lumped equations for the electrolyte.

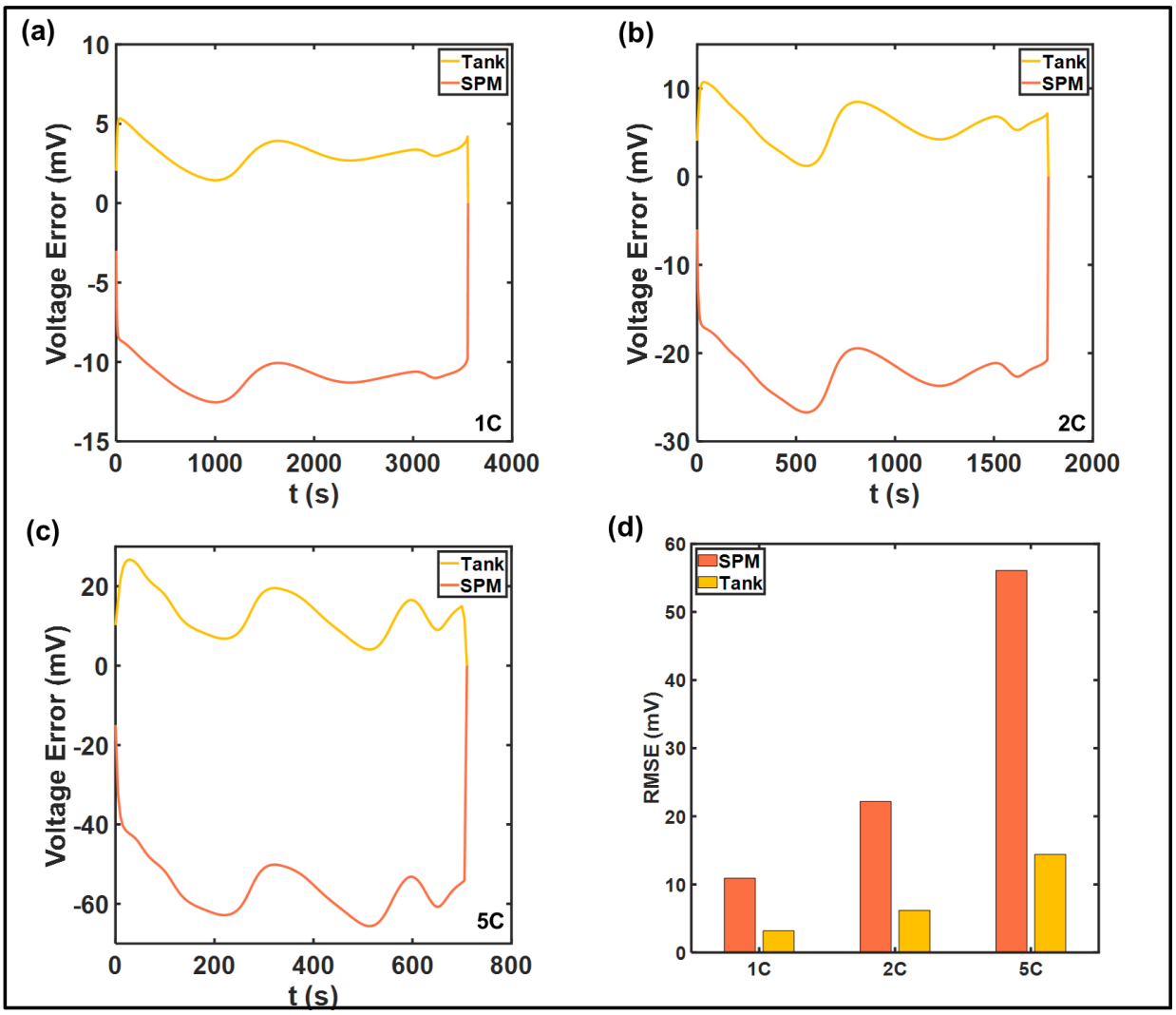

Figure 2.5. Instantaneous voltage errors with respect to the p2D model at **(a)** 1C **(b)** 2C **(c)** 5C discharge. **(d)** compares the overall Root Mean Square Errors (RMSE). The error profiles exhibit oscillations.

The oscillatory instantaneous error profiles in **Figure 2.5** can be observed in other reduced-order models.[60,63,64] The maximum amplitude of the oscillations, corresponding to the maximum absolute error, expectedly increases with discharge rates. Sources of this error may be in the liquid phase approximations of the Tank Model, and in the estimation of electrode averaged overpotential from the electrode averaged current as in equation (25). In this case, the contribution of errors from

the solid phase concentration is expected to be negligible given the choice of particle size R_i , which ensures rapid diffusion dynamics and attainment of steady state in ~50 s. This can also be seen in **Figure 2.6**, in which the averaged particle surface concentrations $\overline{c_i^{s,surf}}$ across the three models at 1C are compared. The close agreement of the Tank Model to the finely discretized SPM and p2D models indicates the accuracy of the biquadratic profile approximations (14) - (16).

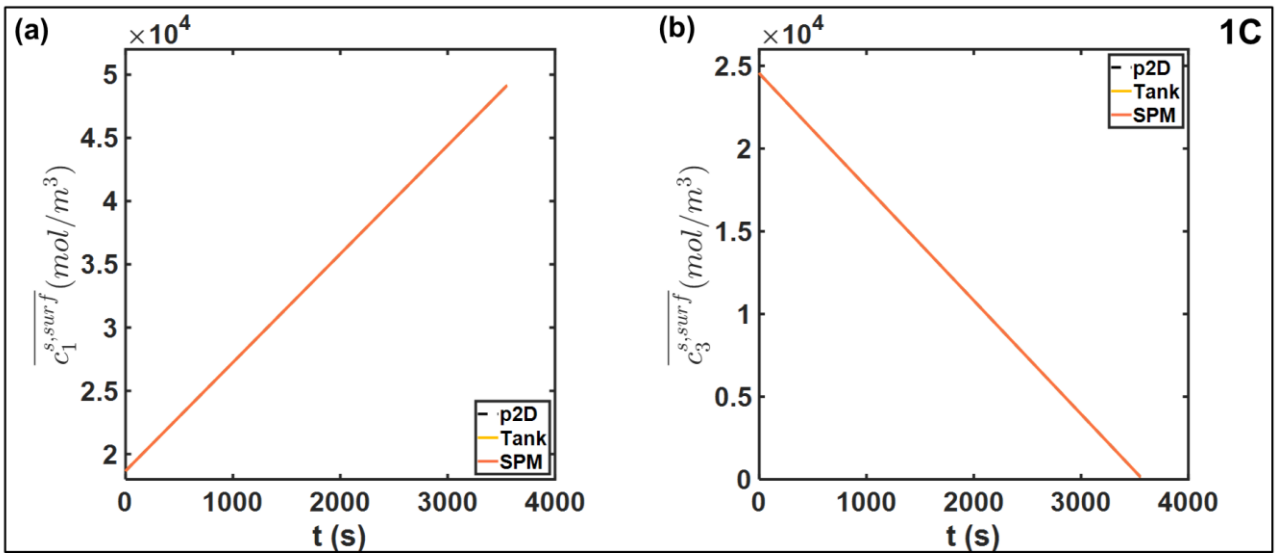

Figure 2.6. Comparison of electrode-averaged particle surface concentrations at 1C discharge for (a) positive electrode and (b) negative electrode. The close agreement between the three models means the curves are nearly on top of each other.

Even at a higher current density of 5C, agreement is ensured in both electrode particles, as depicted in **Figure 2.7**. However, the average values may still obscure variations across the electrode thickness due to a non-uniform reaction distribution. In particular, the particle surface concentration at the termini will also deviate from its electrode average due to variations in local pore-wall flux j_i. Such deviation from the average values of equations (22) and (23) results in

errors in reaction overpotentials, which contributes to errors in V_{cell}.

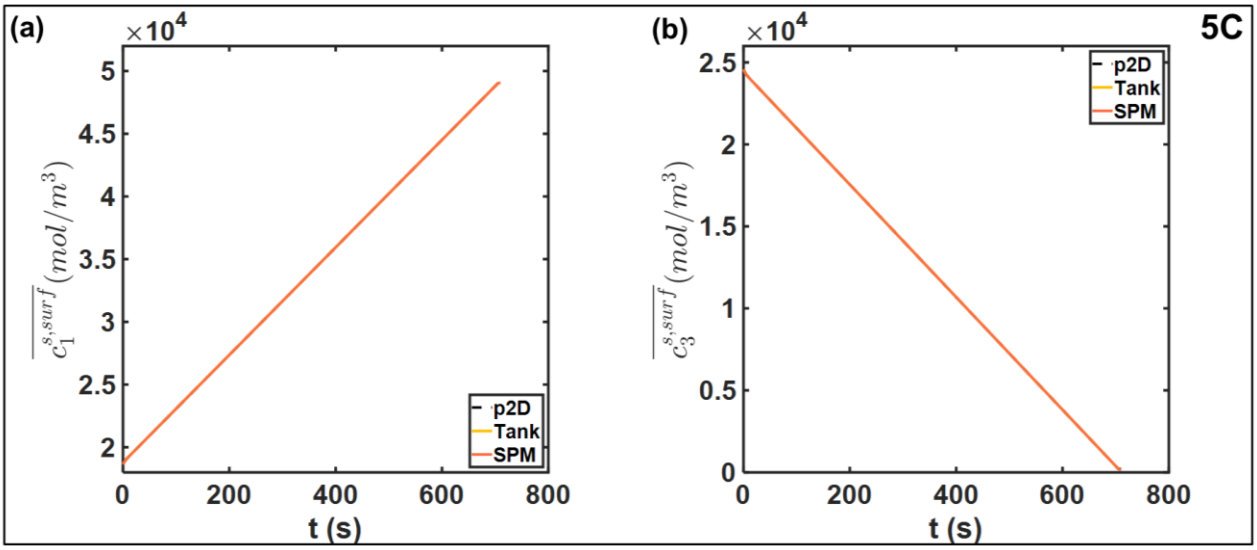

Figure 2.7. Comparison of electrode-averaged particle surface concentrations at 5C discharge rate for (a) positive electrode and (b) negative electrode. The close agreement between the three models means the curves are nearly on top of each other.

Figure 2.8 compares the spatial distribution of pore-wall fluxes at 1C. The positive electrode j_1 achieves rapid uniformity, even though the reaction is initially confined near the separator interface at $t = 0$. Minor oscillations and deviations from the average are observed towards the end of discharge, but the relative change is negligible compared to that for the negative electrode j_3. The local value near the separator is six times higher than the Tank Model average at the beginning of the discharge, whereas $j_3 \sim 0$ near the negative collector. The maxima shift towards the negative collector as the discharge progresses. The reaction 'front' propagates through the electrode, and successive peaks are observed at the two points. Throughout the discharge, the local intercalation rate near the terminal deviates substantially from the Tank Model, sometimes by a factor of two,

approaching the average $\overline{j_3}$ only towards the end of discharge. The reaction distribution in a porous electrode is the result of the relative balance between reaction kinetics, ohmic resistances, and the functional dependence of the open circuit potential $U(c_i^{s,surf})$. Non-uniform reaction distributions are observed in electrodes with faster kinetics with respect to ionic or electronic transport, and flat OCP curves.[59,87] The $U(c_i^{s,surf})$ curve for graphite has a substantially flat section corresponding to multiple phase transitions at different degrees of lithiation.[88] In contrast, $U(c_i^{s,surf})$ for the NCM positive electrode exhibits a more monotonic dependence with a larger (in magnitude) average slope over the full lithiation range. The non-uniform reaction distribution thus contributes to the error in the Tank Model, in addition to the approximations for liquid phase.[61]

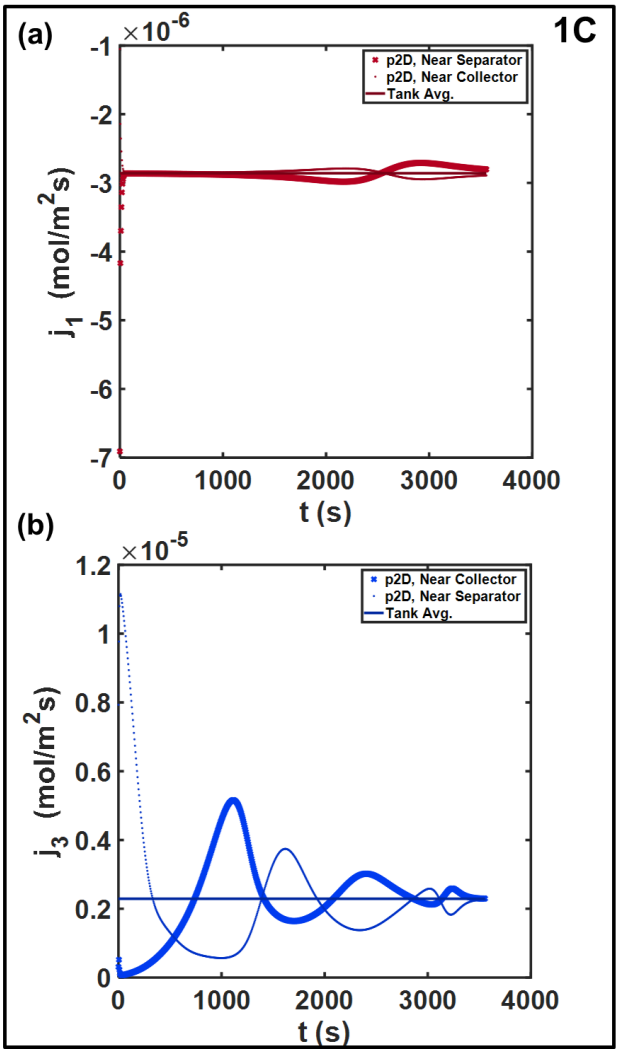

Figure 2.8. Spatial distribution of pore-wall flux in (a) positive electrode and (b) negative electrode at 1C. The error due to the use of the average pore-wall flux to estimate the cell voltage is expected to be larger in magnitude for the spike-shaped profile for the negative electrode.

These effects are even more pronounced in **Figure 2.9**, which examines these trends at 5C. The larger relative deviation close to the negative collector is expected at the higher overall current density. Additionally, oscillatory trends are also observed for the positive electrode beyond t ~ 300 s, with the deviations about the average increasing to ~20%.

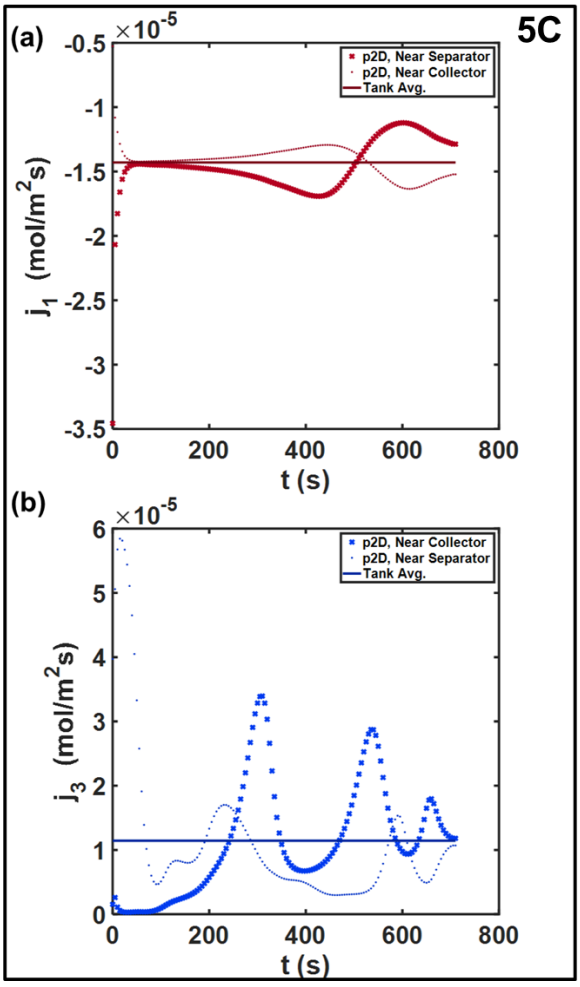

Figure 2.9. Spatial distribution of pore-wall flux in (a) positive electrode and (b) negative electrode at 5C . The non-uniformities in both electrodes are more prominent relative to the 1C rate.

Despite the chemistry-specific considerations and limitations of the Tank Model equations, the Tank Model results in an RMSE of 14.3 mV even at 5C discharge rate, making it competitive in terms of error metrics for online applications. This error is expected to reduce even further based on the specific battery chemistries being considered, such as in the case of a negative electrode with slower kinetics and a more monotonic $U(c_i^{s,surf})$ curve[59], which is expected to result in an inherently more uniform reaction profile. This would further bolster the case for the Tank Model with its substantially improved computational efficiency.

Given the approximate nature of the Tank Model equations, it is also expected that errors in estimating the liquid phase overpotentials will contribute to the error. In order to characterize the extent of this error, we now examine the liquid phase variable predictions. The next section evaluates the Tank Model predictions of liquid phase quantities.

2.7.2. *Electrolyte Phase Variables - Concentration*

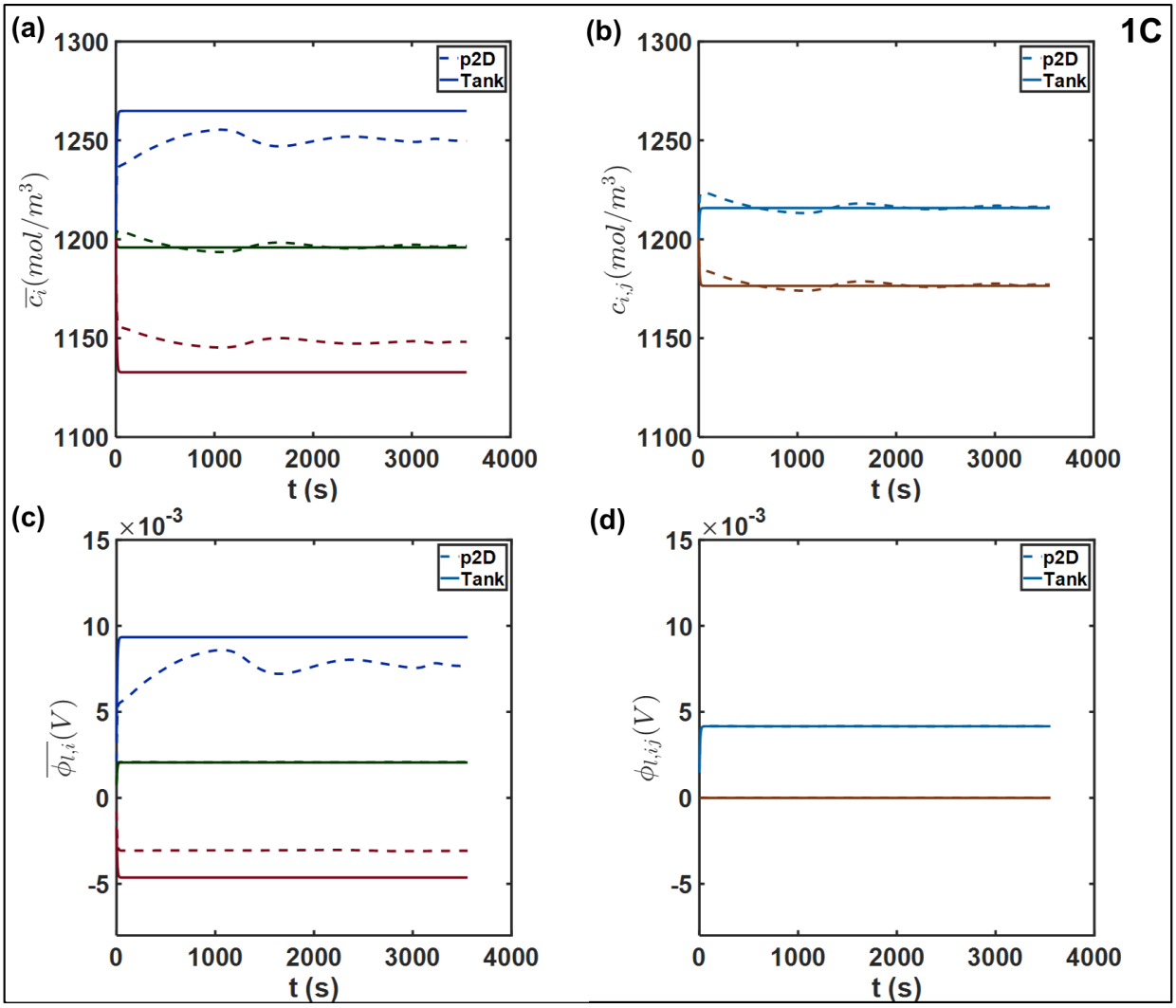

Figure 2.10. Comparison of liquid phase variables at 1C, namely (a) average concentrations $\overline{c_i}$ (b) interfacial electrolyte concentrations c_{ij} (c) average electrolyte phase potential $\overline{\phi_{l,i}}$ and (d) interfacial potential $\phi_{l,ij}$. The separator-positive electrode interface is the potential reference, hence $\phi_{l,ij} = 0$. The negative-separator interface is indicated by the light blue and positive-separator interface by maroon. The average and interfacial values are plotted on identical scale to aid interpretation of the respective concentration and potential drops.

Figure 2.10 (a) and **(b)** compares the average and interfacial concentrations from the Tank Model and the p2D models, at 1C discharge rate. While there is a disagreement in the steady state values of $\overline{c_i}$ attained, the deviation from the p2D model is ~2% in the two electrodes. On the other hand, there is near perfect agreement for the average electrolyte concentration in the separator $\overline{c_2}$. The interfacial concentrations also exhibit agreement, despite the somewhat naïve approximations used for interfacial flux. This is likely due to the smaller thickness of the separator relative to the electrodes (25 μm vs. ~40 μm) which improves the validity of our two-point flux approximations in equation (44) and (45). The Tank Model predicts different dynamics for $\overline{c_i}$ compared to the p2D model. An approach to a constant steady state value compared is indicated, in contrast to the p2D model, which shows small fluctuations. The establishment of this steady state occurs on the characteristic electrolyte diffusion timescale, given by $\tau_D = \frac{l_i^2}{D_{eff,i}} \sim 30s$ in the electrodes.

The concentration drop across the separator is ~ 40 mol/m^3 given its smaller thickness relative to the electrodes. Therefore, the diffusion coefficient at both interfaces is comparable in magnitude, since the concentration change is within 4%. Coupled with the comparable thicknesses of both electrodes (**Table 2-IV**), this results in similar magnitudes of interfacial concentration drops in both electrodes due to the imposition of flux continuity by the Tank Model as in equation (41).

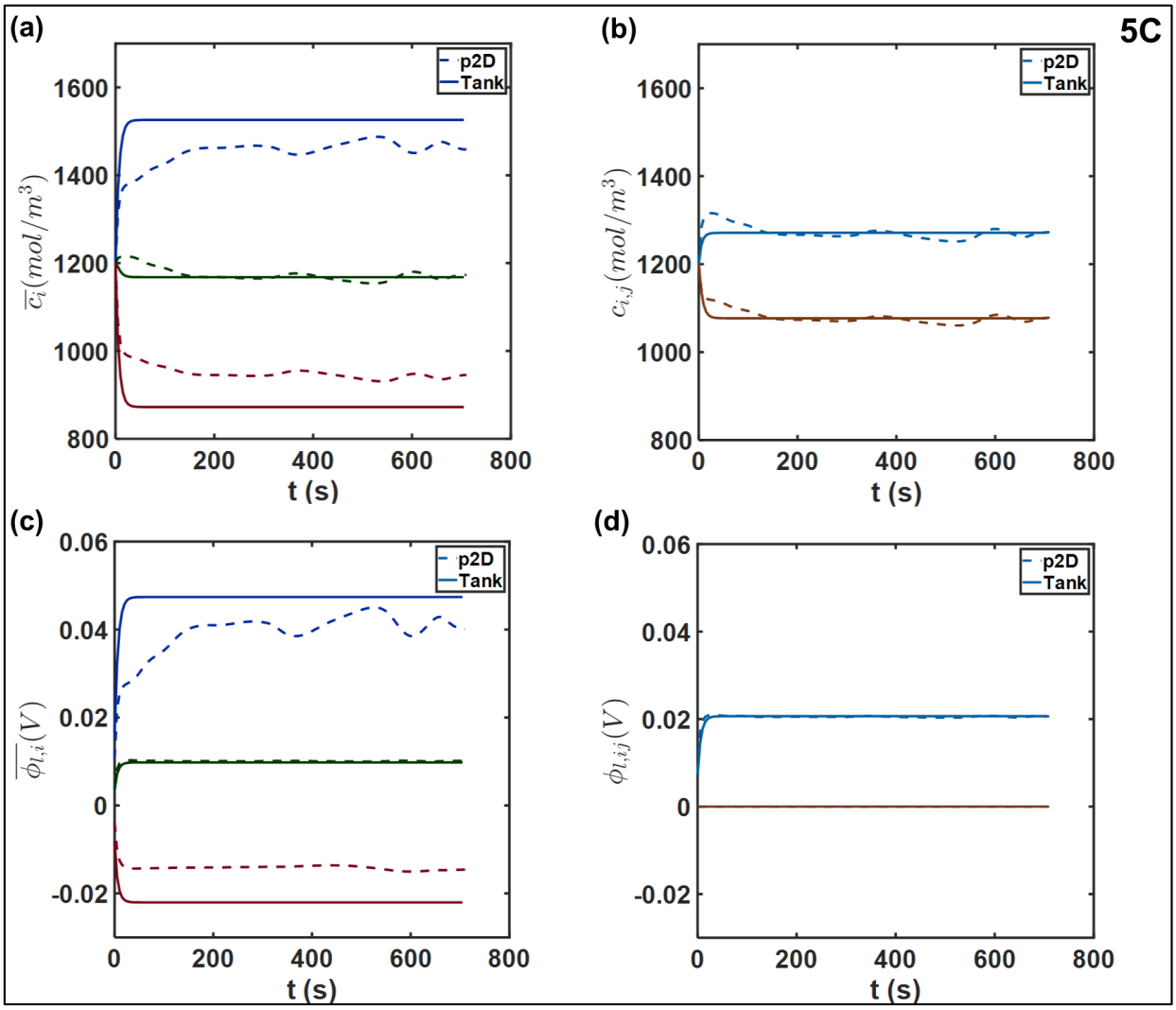

Figure 2.11. Comparison of liquid phase variables at 5C, namely (a) average concentrations $\overline{c_i}$ (b) interfacial electrolyte concentrations c_{ij} (c) average electrolyte phase potential $\overline{\phi_{l,i}}$ and (d) interfacial potential $\phi_{l,ij}$. The separator-positive electrode interface is the potential reference, hence $\phi_{l,ij} = 0$. The values at the negative-separator interface are indicated by light blue curves and positive-separator interface by maroon curves. The average and interfacial values are plotted on identical scales to aid interpretation of the respective concentration and potential differences.

Figure 2.11 (a) and **(b)** compares the concentrations at 5C discharge rate. The close agreement between the concentrations is notable, indicating the ability of the Tank Model equations to capture the concentration variations. The average concentrations in the electrodes agree within 5%, with near-exact agreement for the values in the separator, and at the interfaces. The transient dynamics and concentration drop in the electrodes for both models are qualitatively similar to the 1C case, though the magnitude of the concentration drop has increased to sustain the higher flux at 5C. The close agreement between the concentrations profiles suggests that the contribution of concentration overpotential errors to V_{cell} is not significant up to 5C for the cell parameters considered here. It also indicates the accuracy of the $\frac{l_i}{2}$ approximation, likely due to the electrode thicknesses considered. It may be possible to refine these flux approximations by altering the diffusion lengths $\delta_{i,ij}$. This can be used to in order to match the concentration profiles with attendant benefits for the accuracy of prediction of V_{cell} through the concentration overpotentials. For example, it is common in literature to assume a parabolic or cubic spatial dependence for c_i in the electrodes.[62,63,65,72,83] Applying volume-averaging on a parabolic profile in a given domain returns a value of $\delta_{i,ij} = \frac{l_i}{3}$, the use of which may result in more accurate predictions.[70,72] It is worth noting however that the $\delta_{i,ij}$ value can be treated as an adjustable parameter that can be estimated, providing a representative measure of the diffusion length scales for a given operating situation. This allows more flexibility, in that different values may be adjusted for different domains without altering the model formulation, in contrast to assuming spatial profiles in a somewhat heuristic fashion, which entails rederiving the DAE system each time a spatial profile is changed.

2.7.3. *Electrolyte Phase Variables - Electrolyte Potential*

Figure 2.10 (c) and **(d)** depict the average and interfacial values of the electrolyte potential ϕ_l over a 1C discharge. Of note, the average values $\overline{\phi_{l,i}}$ rapidly reach a steady state for the Tank Model. We observe excellent agreement in the separator $\overline{\phi_{l,2}}$. This indicates the validity of the chosen flux approximations in the relatively thin separator, which also ensure agreement between the interfacial values $\phi_{l,ij}$. This is a likely consequence of the charge conservation imposed by the Tank Model through equation (56), which adjusts the values of interfacial potential to maintain the total liquid phase current i_{app}.

More significant differences are observed in the electrodes. In particular, the $\overline{\phi_{l,3}}$ value predicted by the p2D model exhibits substantial fluctuations, whereas the Tank Model predicts a steady state within ~30 s of the discharge process. This qualitative difference is likely due to the errors in the prediction of average potential from the average pore-wall flux, owing to the non-uniform reaction distribution in the negative electrode, as discussed previously. The errors due to approximating the terminal overpotential based on the average $\overline{j_3}$ in the Tank Model is thus manifested in $\overline{\phi_{l,3}}$, with the instantaneous deviation from the p2D model tracking the time-varying local reaction rates. In addition, substantial errors are observed at shorter timescales, where the Tank Model predicts the attainment of steady state. The maximum absolute value of this deviation is ~ 3 mV, corresponding to approximately 40%. The choice of flux approximation is also likely to affect the deviation of the average value from that at the terminal, in addition to producing mismatches in ohmic drop.

In contrast, the uniform reaction distribution in the positive electrode results in a more spatially uniform overpotential profile over the discharge process, which is also reflected in the nature of the $\overline{\phi_{l,1}}$ profiles. The average values reach quasi-steady values differing by ~1.5 mV. The sum of the average errors in both electrodes value is ~3 mV, which is comparable in magnitude to the voltage errors in **Figure 2.5 (a)** and **(d)**. The main contributions to the error V_{cell} are thus the liquid-phase potentials in the electrodes.

These effects are further accentuated at 5C, as illustrated in **Figure 2.11 (c) and (d)**. In particular, the initial deviation in $\overline{\phi_{l,3}}$ has increased beyond 10 mV, with a commensurate increase in average errors in both electrodes. The deviations in both electrodes are ~ 7 mV, indicating comparable errors in ohmic drops. Interestingly, the profile for $\overline{\phi_{l,1}}$ from the p2D model also shows a slight fluctuation at t ~ 300 s, corresponding to the non-uniformities in j_1 at 5C as seen in **Figure 2.9 (a)**. The total average error in electrolyte potentials is comparable to the values of **Figure 2.5 (c)** and **(d)**. This indicates a contribution of errors in $\overline{\eta_i}$ to V_{cell} through $\overline{\phi_{l,i}}$. The separator $\overline{\phi_{l,2}}$ and interfacial values $\phi_{l,ij}$ are in close agreement even at 5C, except for relatively small errors in $\phi_{l,23}$ during the approach to steady state.

Refinement of the gradient approximation for $\overline{\phi_{l,i}}$ may help reduce errors by matching the ohmic drops across the electrodes, and by improving predictions of reaction overpotential. As with electrolyte concentration, it is common to assume polynomial profiles for the spatial variation of ϕ_l.[64,70] Similar adjustments of the analogous length-scale approximations may help improve

estimates of the migration contribution to ionic current, helping reduce errors in the estimation of both ohmic drops and reaction overpotentials. Preliminary studies suggest that altering gradient approximations marginally increases the errors for $\overline{\phi_{l,1}}$ and $\overline{\phi_{l,2}}$, and thus for the positive overpotential $\overline{\eta_1}$, but this error is more than balanced by the reduction in errors for $\overline{\phi_{l,3}}$, $\overline{\eta_3}$ and the overall electrolyte ohmic drop.

2.7.4. *Interfacial Fluxes*

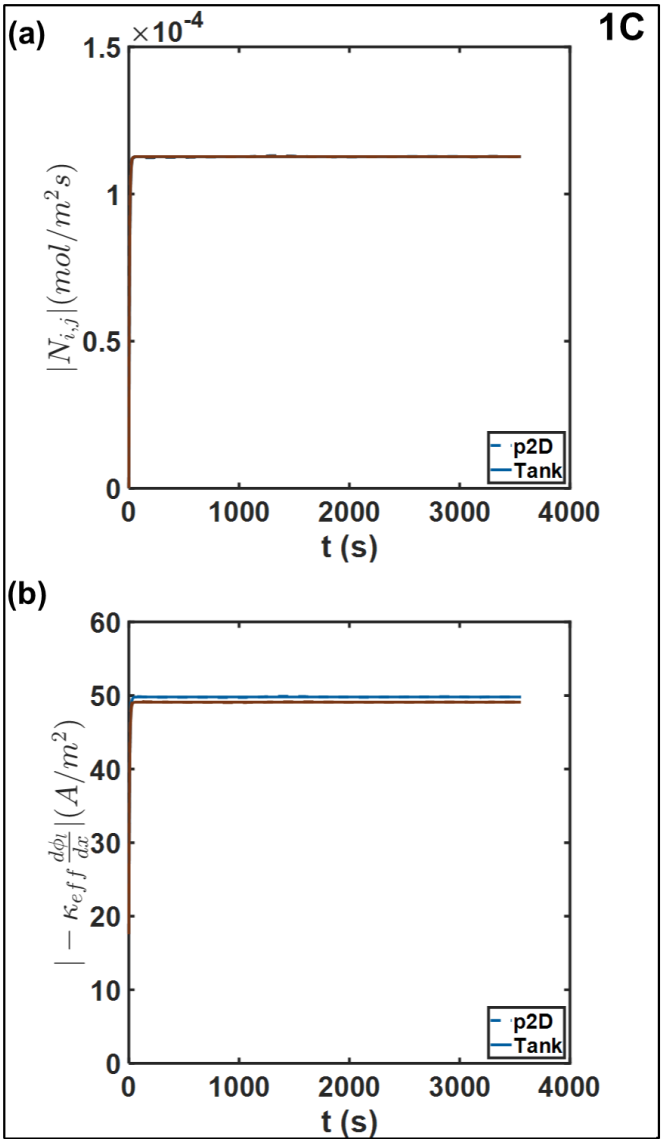

Figure 2.12. Comparison of (a) interfacial molar flux $N_{i,j}$ and the (b) ohmic contribution to liquid phase current density at the positive-separator interface (maroon) and negative-separator negative (blue), at 1C. The operating current density i_{app} is ~17.5 A/m^2.

Figure 2.12 (a) depicts the comparison of the Tank Model approximations $N_{i,j}$ with the actual interfacial values from the p2D model. The interfacial fluxes exhibit excellent agreement even with the somewhat simple approximations for the Tank Model. Discrepancies in the temporal profiles are observed at relatively short timescales, where the full model predicts a different trajectory for the approach to steady state and subsequent minor fluctuations (not shown). However, this error is less than 1% even for 5C discharge, as in **Figure 2.13 (a)**. The close match between fluxes is observed once the steady state gradients have been established at approximately 30 s, which, expectedly, is of the order of the diffusion timescale for the electrolyte. For the Tank Model, the match between the fluxes at the two interfaces is also consistent with the observation of nearly equal interfacial concentration drops and comparable electrode thicknesses, as discussed in the section on electrolyte concentration. There is a rapid establishment of steady state. We expect the approximations to reduce in validity as the current density is increased further. Errors will also arise if the characteristic timescales for different processes are increased, which will result in significant spatial gradients (analogous to the reaction distribution). This in turn is expected to result in errors of concentration overpotentials, with its manifestation in errors in V_{cell} .

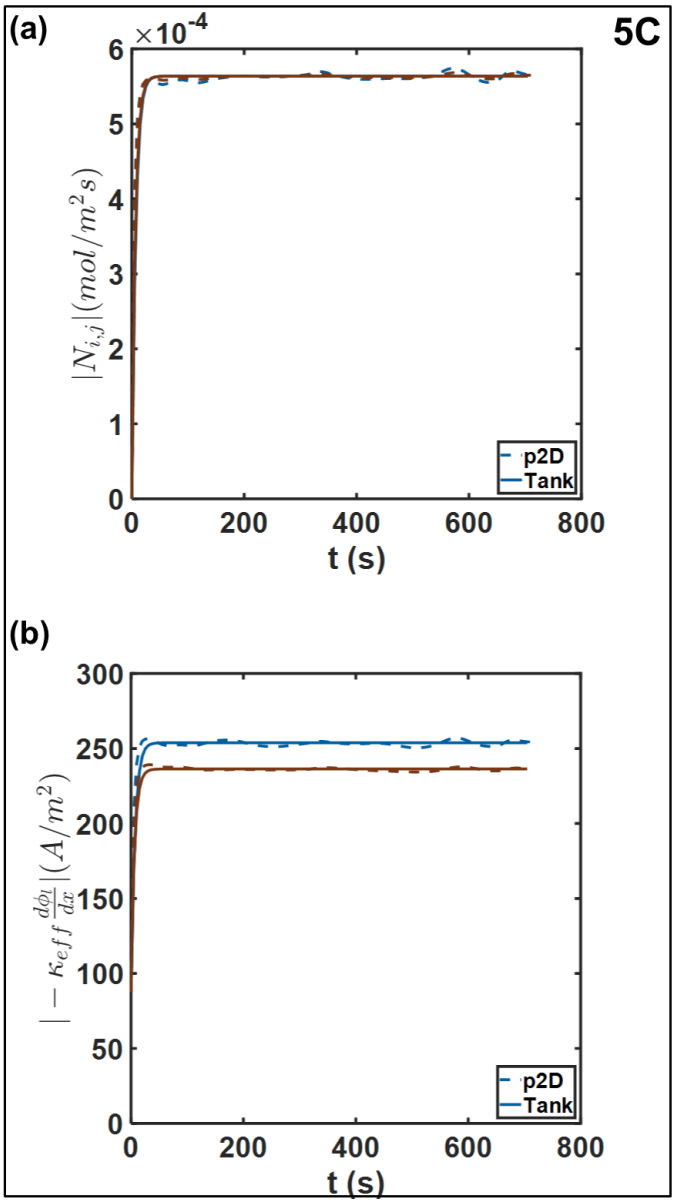

Figure 2.13. Comparison of (a) interfacial molar flux and the (b) ohmic contribution to liquid phase current density at the positive-separator interface (maroon) and negative-separator negative (blue), at 5C. For reference, the operating current density is ~87 A/m^2.

Figure 2.12 (b) compares the approximations for the ohmic contribution to the electrolyte current density at 1C, to evaluate the approximations for the electrolyte potential gradients. Here too we observe substantial agreement with respect to the p2D model. This is expected given the match in the interfacial mass flux predictions above. The Tank Model ensures charge conservation at the interface through equations (52). Agreement between the diffusional contributions forces the equality of the ohmic contributions to maintain the current density at the interfaces. The relative error is comparable even at 5C, as depicted in **Figure 2.13 (b).** There is a slight discrepancy in values during the approach to the quasi-steady value and in subsequent fluctuations, which tracks the errors in electrolyte potentials discussed previously.

Given the close agreements in predicted concentrations and concentration overpotentials, the flux approximations for may be modified to reduce errors in $\overline{\phi_{l,1}}$ and $\overline{\phi_{l,3}}$. One easy way to achieve this could be to use a length scale approximation corresponding to a higher order polynomial profile. For the cell and current densities considered in this work both concentration overpotentials and liquid phase ohmic drops are small relative to the 'thermal voltage' RT/F.[45,60] However, the errors in ohmic potential drop and concentrations could cause errors in V_{cell} at higher current densities, which will be reflected in systematic errors in both $|N_{i,j}|$ and $\left|-\kappa_{eff}\frac{\partial \phi_l}{\partial x}\right|$.

2.7.5. *Case Study – Thick Electrodes*

The tanks-in-series model needs to be examined in light of different limiting performance scenarios, especially for situations in which significant spatial gradients can arise across the electrodes, giving rise to polarizations that are underestimated – e.g. extremely high rates of discharge, or very thick electrodes. This is related to the key assumptions in the Tank Model, namely the interfacial fluxes, which determines the accuracy of the corrections for liquid phase effects.

The impacts of these approximations are now studied in a special case, by the comparison of the Tank Model for the case of a cell with relatively thick electrodes, which may be of salience for high-energy density batteries.[89,90] For this case study, the electrode thicknesses l_1 and l_3 were increased by a factor of 6 while holding all other parameters constant. Thus, the individual capacities of each electrode increase by a factor of 6, while their ratio is held constant. For a consistent comparison with the Base Case, the model was compared at a 5C/6 C-rate, corresponding to the current density i_{app} equivalent to the 5C discharge for the Base Case. The modified parameter values are listed in **Table 2-V**.

For this '6x case', significant electrolyte diffusion limitations and ohmic drops are expected to arise compared to the Base Case. A modified parameter S_e based on Doyle et al. can be used as a measure of expected diffusion limitation.[45,91]

Table 2-V. Modified Parameters for the 'thick electrode' case.

Parameter	Base Case Value	Modified Value
Positive Electrode Thickness (μm)	36.55	219.3
Negative Electrode Thickness (μm)	40	240
1C Discharge Current Density (A/m^2)	-17.54	-105.24
C-rate	5	5/6
S_e	0.1	0.53

Thus

$$S_e = \frac{\left(\frac{l_1^2}{\varepsilon_1^{b_1}} + \frac{l_2^2}{\varepsilon_2^{b_2}} + \frac{l_3^2}{\varepsilon_3^{b_3}} \right)}{\frac{D(c_0)}{t_{dis}}} \tag{60}$$

This factor is thus the ratio of the characteristic time for electrolyte diffusion to the total discharge time, higher values suggesting exacerbated diffusion resistances.

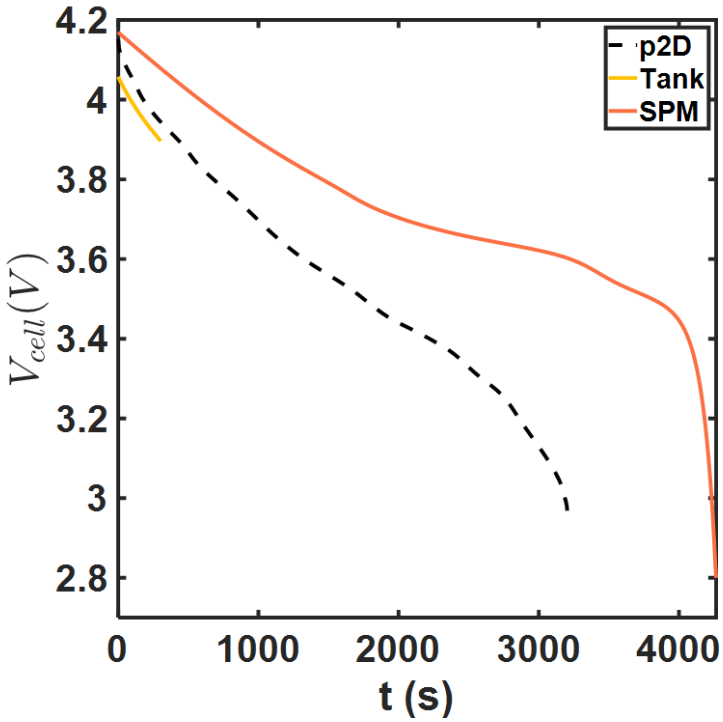

Figure 2.14. Discharge curve comparisons for the thick electrode case.

The voltage-time discharge curve for this case is depicted in **Figure 2.14**. Here we can observe the large liquid phase polarization and spatial non-uniformities that SPM is clearly unable to capture, and instead predicts near-complete cell utilization. The p2D model predicts termination of discharge at an intermediate time point, likely owing to severe electrolyte depletion in the positive electrode. What is noteworthy however is the prediction of the Tank Model, which predicts a premature termination but within 5 minutes of the discharge process. This is despite substantially improved agreement compared to SPM over the small portion of its operation. This suggests substantial error in the prediction of c_i and $\phi_{l,i}$. This can now be seen in **Figure 2.15**, which compares the average concentration predictions from the two models.

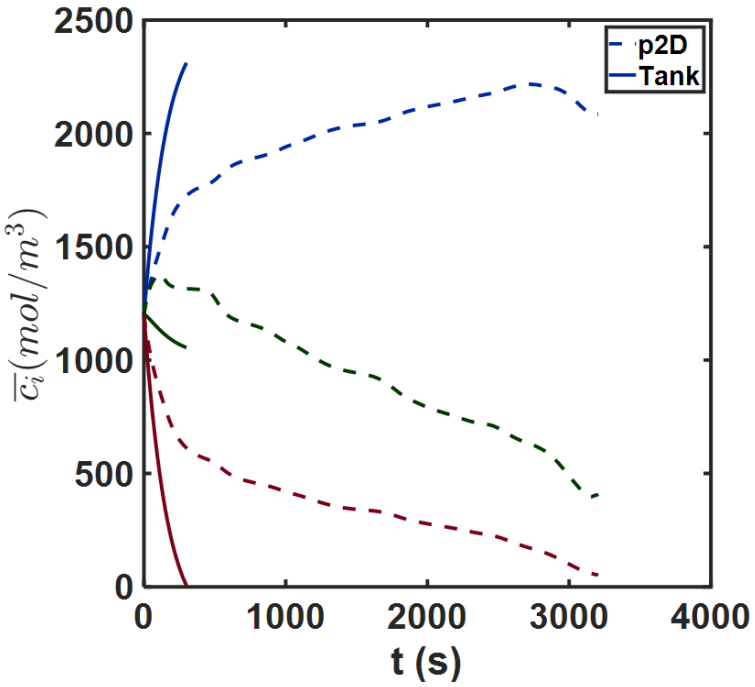

Figure 2.15. Average concentration $\overline{c_i}$ comparison for the thick electrode case. The approximate Tank Model predicts zero electrolyte concentration in the positive electrode at a relatively short time (t~300 s).

In particular, the Tank Model predicts the $\overline{c_i}$ being driven to zero at t ~ 5 minutes, which coincides with the termination of discharge. The $\overline{c_3}$ values disagree by more than 20%, while the Tank Model predicts $\overline{c_1} \sim 0$ at t ~ 300 s, in contrast to the actual value of ~500 mol/m^3. This discrepancy thus suggests the limitation of the diffusive flux approximations, which substantially overestimate the concentration gradients. One possible reason for this error is that the diffusion layers have not built up to their steady state value, as also indicated by the diffusivity parameter S_e . The errors due to the resulting flux approximations may be circumvented by refining the same, or by the use of a time-dependent exponential correction for the length approximation as suggested by some

workers.[70,92] The time constants for this exponential change may be defined based on characteristic diffusion timescales.

This example thus demonstrates a combination of design and operating parameters in which the Tank Model has reduced performance and necessitates improved approximations. In particular, the large polarizations considered in this example may be encountered for the Base Case cell as well, such as during high-current dynamic and pulsed operation. A more comprehensive analysis is useful to establish the parameter combinations at the cell level that deem the Tank Model useful. The limits of a BMS that uses such a model can also be defined through such an analysis.

2.7.6. *Comparison with a version of SPMe*

In this work, the Tank Model is compared against SPM because of its substantial ubiquity in advanced BMS applications, as it continues to be the model of choice when physical detail is desired. In introducing the Tank Model, we seek to propose an alternative for various applications where SPM is substantially common. However, for additional perspective, this section discusses the error metrics of the Tank Model relative to a recent version of the SPM*e*, which corrects SPM with electrolyte dynamics as mentioned previously.[60] For this study, the electrode parameters from Ref. 18 were chosen, in addition to electrolyte transport correlations from Ref. 42. The representative values of electrolyte transport properties required by the SPMe formulation were evaluated at the initial electrolyte concentration.

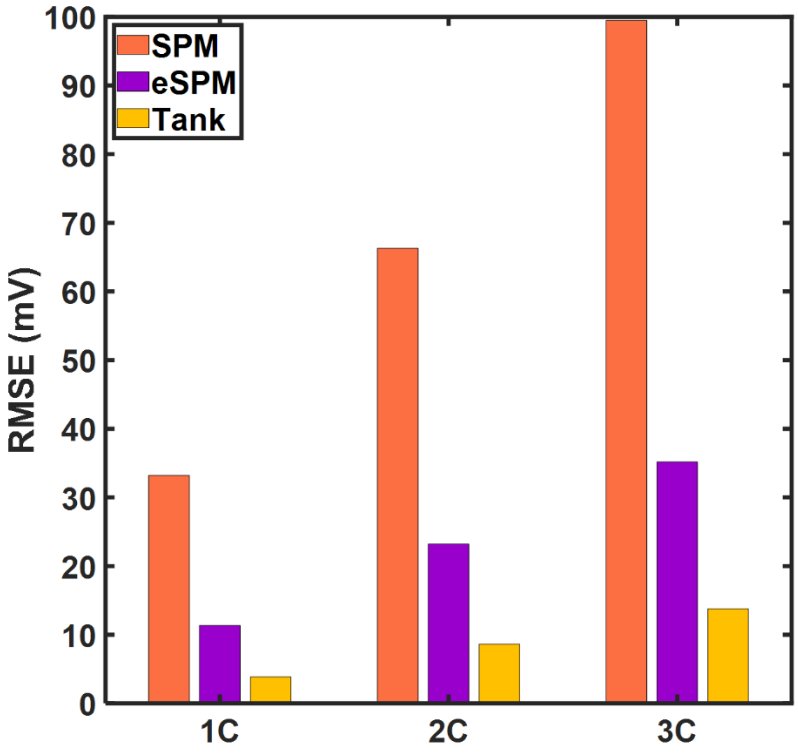

Figure 2.16. Representative comparisons of SPM (peach) , SPM*e* (purple), and the Tank Model (gold). The p2D model is used as the benchmark.

The error metrics up to 3C discharge rate are illustrated in **Figure 2.16**. The substantial improvement in error in going from SPM to lumped electrolyte models is evident, particularly at 3C, where the RMSE reduction is nearly three-fold for SPM*e*. However, the Tank Model exhibits even lower error (13 mV vs. 35 mV). This suggests more accurate estimation of concentration overpotentials and liquid phase ohmic drops for the chosen parameters. The SPM*e* uses representative values, whereas the Tank Model only requires the evaluation of electrolyte transport properties at the interfaces. Consequently, the concentration-dependent transport properties can be

included in an efficient manner. The expressions in SPM*e* may need to be rederived to account for these variations.

2.7.7. *Computational Performance*

Table 2-VI. Representative computational performance metrics for the Tank Model.

Model and Implementation	Number of DAEs	Computation time (ms)*
p2D – Finite Difference (50,35,50)	986	1493
p2D - Reformulated	30 - 150	5 - 20
Tank Model	15**	2.1

*Average of N=3 simulation runs for a 1C discharge. It must be noted that the simulation time and memory consumption is a strong function of the computing environment as well as error tolerances for both initialization and simulation.

**Including the equation for cell voltage

Computational times for the Tank Model are listed in **Table 2-VI**. For the Tank Model, each conservation law in the electrolyte phase is replaced by its volume-averaged form, while the solid phase in each electrode is replaced by 3 linear DAEs. The original ~ 200 – 1000 DAEs are thus replaced by 14 average conservation equations. This results in a 1C discharge curve being simulated in ~ 2 ms, in contrast to >1000 ms for a standard Finite Difference implementation. The computational speed of this model is comparable to fast SPM implementations. The Tank Model

is also competitive with the state-of-the-art reformulated p2D model from our group, achieving up to an order of magnitude reduction in computation time. The mathematical similarity of the Tank Model to the reformulated model with n = (1,1,1) collocation prompts the question as to why the (1,1,1) reformulated model is not used instead of developing the Tank Model. This is because the proposed model is conservative and exhibited higher accuracy. In addition, it can be rewritten so as to contain fewer adjustable parameters compared to reformulated models. Increasing the accuracy and numerical convergence of reformulated models requires using its ability to guarantee convergence for different chemistries, parameters and operating conditions by increasing the number of collocation points.

2.8. Conclusions

An efficient, conservative model for lithium-ion batteries is presented, which uses a Tanks-in-Series approach to generate approximate equations for electrolyte dynamics. Despite the loss of information due to volume-averaging, the additional equations result in a nearly four-fold reduction in error compared to typical SPM at high (5C) discharge rates. While the Tank Model achieves excellent accuracy with respect to the full p2D model for the cell considered in this work (<0.4% error), even better performance is expected for electrodes with inherently more uniform reaction distributions. The model formulation provides for the convenient refinement of flux approximations and estimation to increase accuracy for more aggressive parameter combinations. The model retains the computational simplicity of SPM-like models, with the ~millisecond computation time making it a candidate for a replacement of SPM in the simulation of large series-parallel configurations of cells. The model may also be used for long cycle simulation and parameter estimation towards modeling capacity degradation, and the evaluation of models for the

same.

2.9. List of Symbols

2.9.1. *Dependent Variables*

c Electrolyte Concentration

c^s Solid Phase Concentration

ϕ_l Liquid Phase Potential

ϕ_s Solid Phase Potential

V_{cell} Cell Voltage

j Pore-wall flux

N Electrolyte molar flux

2.9.2. *Other Superscripts*

surf Pertaining to the surface of the particle in the solid phase

$\bar{}$ Pertaining to the average over the volume of a porous domain

s, avg Pertaining to the average over the volume of the solid particle

2.9.3. *Other Subscripts*

i Pertaining to region *i* where $i \in \{1,2,3\}$

ij Pertaining to the interface between regions *i* and *j*, where $i, j \in \{1,2,3\}$

i,ij Pertaining to the interface between regions *i* and *j* on the side of region *i* where $i, j \in \{1,2,3\}$

3. Extending the Tanks-in-Series Methodology to Thermal Effects, Large-Scale Simulations, and Cell-Level Monitoring

3.1. Limitations of SPM-like Thermal Models

The choice of battery model is typically a trade-off between physical detail and computational speed. Various approximation and reformulation techniques have been applied to enable the practicability of complex electrochemical models by reducing their computational demands.[48] A relatively simple method for the generation of efficient electrochemical-thermal models is to couple the classic Single Particle Model (SPM) with a lumped description of thermal dynamics. Simple thermal models are generated based on the form-factor of the cell, and approximations made for the various contributions to the electrochemical heat generation rates. These methods have been demonstrated for various systems-level applications.[16,93] Often the thermal model computes heat source from more complex electrochemical model while using a simple series-resistor model for thermal transport.[94] While these models have significantly improved computational efficiency, they are only valid for specific operating regimes and parameter combinations, and are unable to account for subtle electrochemical aspects that impact battery state. Additionally, while SPM-like models can neglect electrolyte dynamics in isothermal situations, the non-linear dependence of electrolyte transport on temperature necessitates incorporation of equations for the electrolyte, which can often require ad-hoc simplifications, such as empirical equations[93], uniform reaction distributions[16] or polynomial spatial profiles.[70] Analytical solutions for the temperature profiles can also be derived under certain limiting conditions, but their accuracy is also similarly restricted and relies on simplifying assumptions on

either the electrochemical or thermal model components.

3.2. Implications of Electrochemical-Thermal Models for Models of Large Format Cells

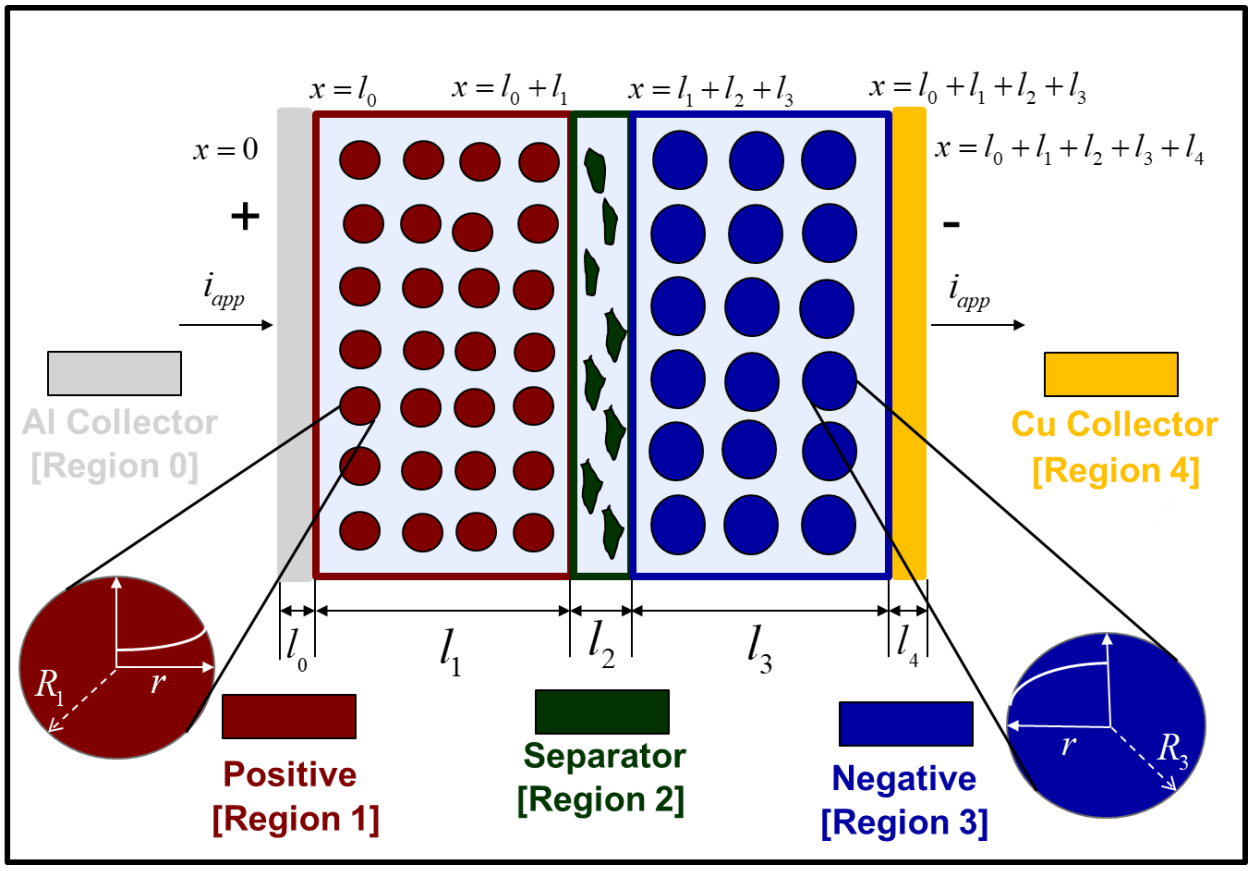

Figure 3.1. Computational domain for the p2D representation of a single Li-ion cell sandwich, including current collectors, Aluminum (Al) for the positive electrode, and Copper (Cu) collectors for the negative electrode.

In addition to the spatial variations along the electrode thickness predicted by p2D models (**Figure 3.1**), large format cells such as those considered for EVs exhibit spatial non-uniformities in the plane of their current collectors ($y-z$ plane).[95] These effects depend on design factors such as the

location of collector tabs, cooling conditions, and contact and thermal resistances.[95–98] A realistic model for design and safety entails computing the temperature and current distributions in the collectors, which in turn affects the local electrochemical behavior within the electrode thickness. This requires a coupled modeling approach in which the local potential, temperature, and current density is used as input to an electrochemical model in the x-direction at each point in the collector plane. Given the computational complexity of such a Multi-Scale Multi-Domain (MSMD) framework where the electrochemical model is evaluated at every point in a 2 or 3-dimensional computational grid, efficient electrochemical models for the 'electrode subdomains' have received significant attention.[96,99] While examples of efficient reformulated MSMD models exist[96],usually reduced order models are employed. Various approaches such as equivalent circuit models[95], extended SPM[70], Pade approximation models[100], and series expansions[101] have been applied. While these approaches significantly reduce the computational footprint of coupled MSMD models, several works use a volume-averaged approach in which temperature variations along the x thickness dimension are neglected.[95,101–104] Lumped thermal models are used even when standard and reformulated implementations of the p2D models are used for the electrochemical submodels[96,105], and even when the p2D model is used to model full cells.[21,106] For a single cathode – separator – anode representation, the ambient heat transfer coefficients and length scales for thermal conduction are low enough that the Biot numbers Bi satisfy the thresholds ($Bi<0.1$) for uniform temperature.[107] However, these assumptions may not hold if the Biot number exceeds the threshold, as is possible with large cell stacks and multiple cell layers.[108] Significant temperature gradients may also result for aggressive convective heat transfer conditions and due to the presence of interfacial thermal resistances.[98,106] A common approach to account for gradients in a multi-cell

stack is to assume a uniform temperature within each individual cell and make suitable approximations for the flux at intercell interfaces[100,108], but this approach may also be error-prone if intra-cell gradients are significant. To circumvent the need for p2D models for multi-cell stacks, efficient analytical solutions have been developed using rigorous asymptotic analyses[109], but their accuracy is similarly restricted to low *Bi* regimes.

3.3. Motivation for an Electrochemical-Thermal Tanks-in-Series Model

The Tanks-in-Series approach involves the rigorous volume-averaging of each conservation law in a given domain, followed by suitable approximations of interfacial fluxes for closure. Such an approach thus obviates the need for uniform temperature assumptions by way of physically meaningful approximations for the gradients, which can capture temperature drops due to thermal resistances and in multi-cell stacks. Additionally, the flux approximations may be easily refined by variation of the corresponding diffusion lengths, providing a flexible way for tuning the gradients within each domain, and suggesting applications in parameter estimation. Since each partial differential equation (PDE) in the p2D model is replaced by its volume-averaged form, a single cell can be represented by <20 Differential Algebraic Equations (DAEs). Based the results in Chapter 2, this suggests substantial gains in computational efficiency (~1 s computation time) for a multi-cell stack featuring ~500 DAEs[54], and makes the Tanks-in-Series method worthy of consideration.

3.4. Model Development

3.4.1. *Single Cell Model*

In this section, we apply the Tanks-in-Series methodology to the governing equations for

temperature in the p2D thermal model. The modeling schematic of a single repeat cell 'sandwich', also called a 'single cell', is depicted in **Figure 3.1**. The complete set of equations and boundary conditions used in this study may be found in **Table 3-I**. The full-order model used as the benchmark in this study is based on the extensions to the isothermal p2D model by Newman and others.[104,110–112]

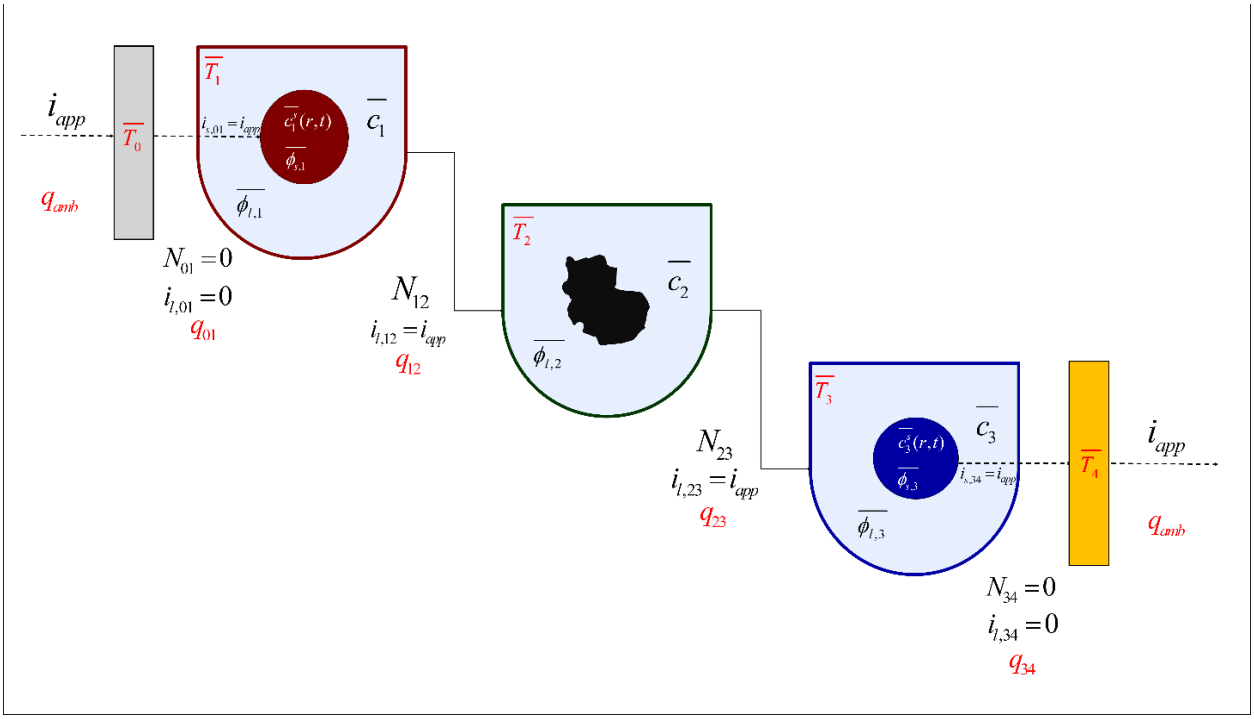

Figure 3.2. The extended Tanks-in-Series model for thermal effects. Additional variables introduced due to the consideration of thermal effects are highlighted in red. In particular, the average temperature $\overline{T}_i$ is introduced in each 'Tank' by way of the heat conservation equations. The volume-averaged form of the equations also includes the interfacial heat fluxes $\overline{q}_{ij}$. The Thermal Tank Model also considers volume-averaged forms of the heat equations in two additional domains, namely the positive and negative electrode current collectors. The cell as a whole exchanges heat with the ambient surroundings via the external heat flux q_{amb}.

Table 3-I. Governing Equations for the electrochemical-thermal p2D model.

Equations	Boundary Conditions
Positive Current Collector (Region 0)	
$\rho_0 C_{p,0} \frac{\partial T_0}{\partial t} = \frac{\partial}{\partial x}\left[\lambda_0 \frac{\partial T_0}{\partial x}\right] + \frac{i_{app}^2}{\sigma_0}$	$\lambda_0 \frac{\partial T_0}{\partial x}\Big\|_{x=l_0} = -h_{amb}\left(T_0 - T_{amb}\right)$
Positive Electrode (Region 1)	
$\varepsilon_1 \frac{\partial c_1}{\partial t} = \frac{\partial}{\partial x}\left[D(c_1)\varepsilon_1^{b_1} \frac{\partial c_1}{\partial x}\right] + a_1(1-t_+)\, j_1$	$\frac{\partial c_1}{\partial x}\Big\|_{x=l_0} = 0$
	$\varepsilon_1^{b_1} \frac{\partial c_1}{\partial x}\Big\|_{x=l_0+l_1} = \varepsilon_2^{b_2} \frac{\partial c_2}{\partial x}\Big\|_{x=l_0+l_1}$
$i_{l,1} = -\kappa(c_1)\varepsilon_1^{b_1} \frac{\partial \phi_{l,1}}{\partial x} + \frac{2RT(1-t_+^0)}{F}\left(1+\frac{\partial \ln f}{\partial \ln c_1}\right)\kappa(c_1)\varepsilon_1^{b_1} \frac{1}{c_1}\frac{\partial c_1}{\partial x}$	$\frac{\partial \phi_{l,1}}{\partial x}\Big\|_{x=l_0} = 0$
	$\varepsilon_1^{b_1} \frac{\partial \phi_{l,1}}{\partial x}\Big\|_{x=l_0+l_1} = \varepsilon_2^{b_2} \frac{\partial \phi_{l,2}}{\partial x}\Big\|_{x=l_0+l_1}$
$\frac{\partial}{\partial x}\left[\sigma_{eff,1} \frac{\partial \phi_{s,1}}{\partial x}\right] = a_1 F j_1$	$\frac{\partial \phi_{s,1}}{\partial x}\Big\|_{x=l_0} = -\frac{i_{app}}{\sigma_{eff,1}}$
	$\frac{\partial \phi_{s,1}}{\partial x}\Big\|_{x=l_0+l_1} = 0$
$\frac{\partial c_1^s}{\partial t} = \frac{1}{r^2}\frac{\partial}{\partial r}\left[r^2 D_1^s \frac{\partial c_1^s}{\partial x}\right]$	$\frac{\partial c_1^s}{\partial r}\Big\|_{r=0} = 0$
	$\frac{\partial c_1^s}{\partial r}\Big\|_{r=R_1} = -\frac{j_1}{D_1^s}$
$\rho_1 C_{p,1} \frac{\partial T_1}{\partial t} = \frac{\partial}{\partial x}\left[\lambda_1 \frac{\partial T_1}{\partial x}\right] + Q_{rxn,1} + Q_{rev,1} + Q_{ohm,1}$	$\lambda_0 \frac{\partial T_0}{\partial x}\Big\|_{x=l_0} = \lambda_1 \frac{\partial T_1}{\partial x}\Big\|_{x=l_0}$
	$T_0\big\|_{x=l_0} = T_1\big\|_{x=l_0}$
Separator (Region 2)	
$\varepsilon_2 \frac{\partial c_2}{\partial t} = \frac{\partial}{\partial x}\left[D(c_2) \frac{\partial c_2}{\partial x}\right]$	$c_1\big\|_{x=l_0+l_1} = c_2\big\|_{x=l_0+l_1}$
	$c_2\big\|_{x=l_0+l_1+l_2} = c_3\big\|_{x=l_0+l_1+l_2}$
$i_{l,2} = -\kappa(c_2)\varepsilon_2^{b_2} \frac{\partial \phi_{l,2}}{\partial x} + \frac{2RT(1-t_+^0)}{F}\left(1+\frac{\partial \ln f}{\partial \ln c_2}\right)\kappa(c_2)\varepsilon_2^{b_2} \frac{1}{c_2}\frac{\partial c_2}{\partial x}$	$\phi_{l,1}\big\|_{x=l_0+l_1} = \phi_{l,2}\big\|_{x=l_0+l_1}$
	$\phi_{l,2}\big\|_{x=l_0+l_1+l_2} = \phi_{l,3}\big\|_{x=l_0+l_1+l_2}$
$\rho_2 C_{p,2} \frac{\partial T_2}{\partial t} = \frac{\partial}{\partial x}\left[\lambda_2 \frac{\partial T_2}{\partial x}\right] + Q_{ohm,2}$	$\lambda_1 \frac{\partial T_1}{\partial x}\Big\|_{x=l_0+l_1} = \lambda_2 \frac{\partial T_2}{\partial x}\Big\|_{x=l_0+l_1}$
	$T_3\big\|_{x=l_0+l_1+l_2} = T_2\big\|_{x=l_0+l_1+l_2}$
Negative Electrode (Region 3)	

$$\varepsilon_3 \frac{\partial c_3}{\partial t} = \frac{\partial}{\partial x}\left[D(c_3) \frac{\partial c_3}{\partial x} \right] + a_3 (1 - t_+) j_3$$

$$i_{l,3} = -\kappa(c_3)\varepsilon_3^{b_3} \frac{\partial \phi_{l,3}}{\partial x} + \frac{2RT(1-t_+^0)}{F}\left(1 + \frac{\partial \ln f}{\partial \ln c_3}\right)\kappa(c_3)\varepsilon_3^{b_3} \frac{1}{c_3}\frac{\partial c_3}{\partial x}$$

$$\frac{\partial}{\partial x}\left[\sigma_{eff,3} \frac{\partial \phi_{s,3}}{\partial x} \right] = a_3 F j_3$$

$$\frac{\partial c_3^s}{\partial t} = \frac{1}{r^2}\frac{\partial}{\partial r}\left[r^2 D_3^s \frac{\partial c_3^s}{\partial r} \right]$$

$$\rho_3 C_{p,3} \frac{\partial T_3}{\partial t} = \frac{\partial}{\partial x}\left[\lambda_3 \frac{\partial T_3}{\partial x} \right] + Q_{rxn,3} + Q_{rev,3} + Q_{ohm,3}$$

Negative Current Collector (Region 4)

$$\rho_4 C_{p,4} \frac{\partial T_4}{\partial t} = \frac{\partial}{\partial x}\left[\lambda_4 \frac{\partial T_4}{\partial x} \right] + \frac{i_{app}^2}{\sigma_4}$$

$$\left.\frac{\partial c_3}{\partial x}\right|_{x=l_1+l_2+l_3} = 0$$

$$\left.\varepsilon_2^{b_2}\frac{\partial c_2}{\partial x}\right|_{x=l_1+l_2} = \left.\varepsilon_3^{b_3}\frac{\partial c_3}{\partial x}\right|_{x=l_1+l_2}$$

$$\left.\phi_{l,3}\right|_{x=l_0+l_1+l_2+l_3} = 0$$

$$\left.\varepsilon_2^{b_2}\frac{\partial \phi_{l,2}}{\partial x}\right|_{x=l_0+l_1+l_2} = \left.\varepsilon_3^{b_3}\frac{\partial \phi_{l,3}}{\partial x}\right|_{x=l_0+l_1+l_2}$$

$$\left.\frac{\partial \phi_{s,3}}{\partial x}\right|_{x=l_0+l_1+l_2} = 0$$

$$\left.\frac{\partial \phi_{s,3}}{\partial x}\right|_{x=l_0+l_1+l_2+l_3} = -\frac{i_{app}}{\sigma_{eff,3}}$$

$$\left.\frac{\partial c_3^s}{\partial r}\right|_{r=0} = 0$$

$$\left.\frac{\partial c_3^s}{\partial r}\right|_{r=R_3} = -\frac{j_3}{D_3^s}$$

$$\left.\lambda_2\frac{\partial T_2}{\partial x}\right|_{x=l_0+l_1+l_2+l_3} = \left.\lambda_3\frac{\partial T_3}{\partial x}\right|_{x=l_0+l_1+l_2+l_3}$$

$$\left.T_3\right|_{x=l_0+l_1+l_2+l_3+l_4} = \left.T_4\right|_{x=l_0+l_1+l_2+l_3+l_4}$$

$$\left.\lambda_4\frac{\partial T_4}{\partial x}\right|_{x=l_0+l_1+l_2+l_3+l_4} = h_{amb}\left(T_4 - T_{amb}\right)$$

Table 3-II. Additional constitutive equations for the isothermal p2D and Tank models.

$$j_1 = k_1 c_1^{\alpha_{a,1}} (c_1^{s,\max} - c_1^{s,surf})^{\alpha_{a,1}} (c_1^{s,surf})^{\alpha_{c,1}} \left(\exp\left(\frac{\alpha_{a,1} F \eta_1}{RT_1} \right) - \exp\left(\frac{-\alpha_{c,1} F \eta_1}{RT_1} \right) \right)$$

$$j_3 = k_3 c_3^{\alpha_{a,3}} (c_3^{s,\max} - c_3^{s,surf})^{\alpha_{a,3}} (c_3^{s,surf})^{\alpha_{c,3}} \left(\exp\left(\frac{\alpha_{a,3} F \eta_3}{RT_i} \right) - \exp\left(\frac{-\alpha_{c,3} F \eta_3}{RT_i} \right) \right)$$

$$\sigma_{eff,i} = \sigma_i \left(1 - \varepsilon_i - \varepsilon_{f,i}\right), i \in \{1,3\}$$

$$a_i = \frac{3}{R_i}\left(1 - \varepsilon_i - \varepsilon_{f,i}\right), i \in \{1,2,3\}$$

$$U_p = \frac{\left[-4.656 + 88.669\theta_p^2 - 401.119\theta_p^4 + 342.909\theta_p^6 - 462.471\theta_p^8 + 433.434\theta_p^{10}\right]}{-1.0 + 18.933\theta_p^2 - 79.532\theta_p^4 + 37.311\theta_p^6 - 73.083\theta_p^8 + 95.96\theta_p^{10}}$$

$$\theta_p = \frac{c_1^{s,surf}}{c_1^{s,\max}}$$

$$U_n = 0.7222 + 0.1387\theta_n + 0.029\theta_n^{0.5} - \frac{0.0172}{\theta_n} + \frac{0.0019}{\theta_n^{1.5}} +$$
$$0.2808\exp\left(0.90 - 15\theta_n\right) - 0.7984\exp\left(0.4465\theta_n - 0.4108\right)$$

$$\theta_n = \frac{c_3^{s,surf}}{c_3^{s,\max}}$$

$$\left(1 + \frac{\partial \ln f}{\partial \ln c_i}\right) = \nu(c_t, T_i) = 0.601 - 7.5894 \times 10^{-3} c_i^{0.5} + 3.1053 \times 10^{-5}\left(2.5236 - 0.0052T\right) c_i^{1.5}, \; i \in \{1,2,3\}$$

Table 3-III. Additional constitutive equations for the p2D and Tank thermal models.

$$Q_{irrev,i} = Fa_i j_i \left[\phi_{s,i} - \phi_{l,i} - U\left(c_i^{s,surf}\right) \right], \ i \in \{1,3\}$$

$$Q_{rev,i} = Fa_i j_i T_i \left[\frac{\partial U\left(c_i^{s,surf}\right)}{\partial T} \right], i \in \{1,3\}$$

$$Q_{ohm,i} = \sigma_{eff,i} \left(\frac{1}{l_i} \frac{\partial \phi_{s,i}}{\partial x} \right)^2 + \left(\kappa_{eff,i} \left(\frac{1}{l_i} \frac{\partial \phi_{l,i}}{\partial x} \right) - \frac{2\kappa_{eff,i} RT_i}{F} \left(1 - t_+^0\right) \left(1 + \frac{\partial \ln f}{\partial \ln c_i} \right) \frac{1}{l_i^2} \frac{1}{c_i} \frac{\partial c_i}{\partial x} \right) \frac{\partial \phi_{l,i}}{\partial x}, \ i \in \{1,3\}$$

$$Q_{ohm,2} = \left(\kappa_{eff,2} \left(\frac{1}{l_2} \frac{\partial \phi_{l,2}}{\partial x} \right) - \frac{2\kappa_{eff,2} RT_2}{F} \left(1 - t_+^0\right) \left(1 + \frac{\partial \ln f}{\partial \ln c_2} \right) \frac{1}{l_2^2} \frac{1}{c_2} \frac{\partial c_2}{\partial x} \right) \frac{\partial \phi_{l,2}}{\partial x}$$

$$D\left(c_i, T_i\right) = 0.0001 \times 10^{-\left[4.43 + \frac{54}{T_i - 229 - 0.005 c_i}\right] - 0.00022 c_i}, i \in \{1,2,3\}$$

$$\kappa(c_i) = 1 \times 10^{-4} c_i \left[\begin{array}{l} \left(-10.5 + 0.0740 T_i - 6.96 \times 10^{-5} T_i^2\right) \\ + c_i (0.668 - 0.0178 T_i + 2.8 \times 10^{-5} T_i^2) \\ + c_i^2 (0.494 - 8.86 \times 10^{-4} T_i^2) \end{array} \right]^2, i \in \{1,2,3\}$$

$$\left(1 + \frac{\partial \ln f}{\partial \ln c_i} \right) = \nu(c_i, T_i) = 0.601 - 7.5894 \times 10^{-3} c_i^{0.5} + 3.1053 \times 10^{-5} \left(2.5236 - 0.0052 T_i\right) c_i^{1.5}, \ i \in \{1,2,3\}$$

$$U_i\left(T_i, \theta_i\right) = U_{i,ref}\left(T_{ref}, \theta_i\right) + \left(T_i - T_{ref}\right) \left[\frac{dU_i}{dT} \right]_{T_{ref}}, \ i \in \{1,3\}$$

$$\frac{dU_1}{dT} = -0.001 \frac{\left[\begin{array}{l} 0.199521039 - 0.928373822 \theta_p + \\ 1.3645506890000003 \theta_p^2 - 0.61154489399999998 \theta_p^3 \end{array} \right]}{\left[\begin{array}{l} 1 - 5.6614798869999997 \theta_p + 11.476361910 \theta_p^2 - \\ 9.824312135999998 \theta_p^3 + 3.048755063 \theta_p^4 \end{array} \right]}$$

$$\frac{dU_3}{dT} = 0.001 \frac{\left[\begin{array}{l} 0.005269056 + 3.299265709 \theta_n - 91.7932579 \theta_n^2 + \\ 1004.911008 \theta_n^3 - 5812.278127 \theta_n^4 + 19329.7549 \theta_n^5 - \\ 37147.8947 \theta_n^6 - 38379.18127 \theta_n^7 - 16515.05308 \theta_n^8 \end{array} \right]}{\left[\begin{array}{l} 1 - 48.09287227 \theta_n + 1017.234804 \theta_n^2 - \\ 10481.80419 \theta_n^3 + 59431.3 \theta_n^4 - 195881.6488 \theta_n^5 + \\ 374577.3152 \theta_n^6 - 385821.1607 \theta_n^7 + 165705.8597 \theta_n^8 \end{array} \right]}$$

$$D_{i,eff}^s = D_i^s \exp\left(-\frac{E_a^{D_i^s}}{R} \left[\frac{1}{T_i} - \frac{1}{T_{ref}} \right] \right), \ i \in \{1,3\}$$

3.4.2. ***Energy Balance Equation: Volume-Averaging***

In the positive electrode, the governing PDE for the temperature T_1 is given by

$$\rho_1 C_{p1} \frac{\partial T_1}{\partial t} = -\frac{\partial q_1}{\partial x} + Q_{irrev,1} + Q_{rev,1} + Q_{ohmic,1} \quad [l_0 < x < l_0 + l_1] \tag{61}$$

For one spatial dimension in cartesian coordinates. q_1 denotes the local heat flux, and $Q_{rev,1}$, $Q_{irrev,1}$ and $Q_{ohmic,1}$ denote the volumetric source terms corresponding to reversible and irreversible components of the heat of reaction, and joule heating resulting from ohmic effects. [104,112] ρ_i and C_{pi} respectively denote the density and heat capacity of the material in domain i.

Due to the absence of solid active material, the conservation equation for T in the separator is characterized by a lack of heat of reaction terms as

$$\rho_2 C_{p2} \frac{\partial T_2}{\partial t} = -\frac{\partial q_2}{\partial x} + Q_{ohmic,2} \quad [l_0 + l_1 < x < l_0 + l_1 + l_2] \tag{62}$$

The subscript *2* is used to denote the variables in the separator domain.

The equation for the negative electrode is identical in form to that of the positive electrode

$$\rho_3 C_{p3} \frac{\partial T_3}{\partial t} = -\frac{\partial q_3}{\partial x} + Q_{irrev,3} + Q_{rev,3} + Q_{ohmic,3} \quad [l_0 + l_1 + l_2 < x < l_0 + l_1 + l_2 + l_3] \tag{63}$$

q_1, q_2, q_3 are local thermal fluxes which may be defined using standard constitutive equations. Thus we have[79]

$$q_i = -\lambda_i \frac{\partial T_i}{\partial x} \tag{64}$$

In the above equations, λ_i denotes the (assumed isotropic) thermal conductivity of the domain i.

For the thermal model, we also consider the temperature distribution through the current collectors. For the positive electrode, the governing equation for the Aluminum current collector (Region 0 in **Figure 3.1**) may be written as

$$\rho_0 C_{p0} \frac{\partial T_0}{\partial t} = -\frac{\partial q_0}{\partial x} + \frac{i_{app}^2}{\sigma_0} \quad [0 < x < l_0] \tag{65}$$

Similarly, for the negative Copper (Cu) collector, Region 4 (**Figure 3.1**) may be written as

$$\rho_4 C_{p4} \frac{\partial T_4}{\partial t} = -\frac{\partial q_4}{\partial x} + \frac{i_{app}^2}{\sigma_4} \quad [l_0 + l_1 + l_2 + l_3 < x < l_0 + l_1 + l_2 + l_3 + l_4] \tag{66}$$

Note that the only source term in the current collectors is ohmic heating due to the passage of current.

For the base case, the boundary conditions are imposed at the surface of the current collectors as

$$\begin{aligned} q_{0,x=0} &= q_{-10} = q_{amb} = -h(T_0 - T_{amb}) \\ q_{4,x=l_4} &= q_{45} = q_{amb} = -h(T_4 - T_{amb}) \end{aligned} \tag{67}$$

In addition, we also impose continuity conditions for temperature and heat fluxes at the interfaces

between the separator and electrodes, and the electrodes and collectors. At the positive electrode-separator interface, this is expressed as

$$\begin{aligned} T_{1,x=l_0+l_1} &= T_{2,x=l_0+l_1} \\ q_{1,x=l_0+l_1} &= q_{2,x=l_0+l_1} = q_{12} \end{aligned} \tag{68}$$

Similarly, at the interface between the separator and negative electrode, we have

$$\begin{aligned} T_{2,x=l_0+l_1} &= T_{3,x=l_0+l_1} \\ q_{2,x=l_0+l_1} &= q_{3,x=l_0+l_1} = q_{23} \end{aligned} \tag{69}$$

At the collector-electrode interfaces, we have

$$\begin{aligned} T_{0,x=l_1} &= T_{1,x=l_1} \\ q_{0,x=l_1} &= q_{1,x=l_1} = q_{01} \\ T_{3,x=l_0+l_1+l_2+l_3} &= T_{4,x=l_0+l_1+l_2+l_3} \\ q_{3,x=l_0+l_1+l_2+l_3} &= q_{4,x=l_0+l_1+l_2+l_3} = q_{34} \end{aligned} \tag{70}$$

Note that in the above equations we neglect any interfacial thermal resistances at the separator-electrode interfaces.

Within the porous domains, the volumetric heat generation terms are defined as[104,112]

$$Q_{irrev,i} = Fa_i j_i \left(\phi_{s,i} - \phi_{l,i} - U\left(c_i^{s,surf} \right) \right) \quad i \in \{1,3\} \tag{71}$$

$$Q_{rev,i} = Fa_i j_i T_i \frac{\partial U\left(c_i^{s,surf} \right)}{\partial T} \quad i \in \{1,3\} \tag{72}$$

For the ohmic heating term, we have, using the constitutive equations (19) and (50) from Ref. 41

$$Q_{ohmic,i} = \sigma_i \left(1-\varepsilon_i-\varepsilon_{fi}\right)\left(\frac{\partial \phi_{s,i}}{\partial x}\right)^2 + \left(\kappa(c_i)\varepsilon_i^{b_i}\left(\frac{\partial \phi_{l,i}}{\partial x}\right)^2 - \frac{2\kappa(c_i)\varepsilon_i^{b_i}(1-t_+^0)RT_i}{F}\left(\frac{\partial \phi_{l,i}}{\partial x}\right)\left(1+\frac{\partial \ln f}{\partial \ln c_i}\right)\left(\frac{\partial \ln c_i}{\partial x}\right)\right)$$

$$i \in \{1,2,3\} \qquad (73)$$

Now, assuming constant density and heat capacities, equation (26) is integrated over the volume of the positive electrode V_1 as

$$\frac{\rho_1 C_{p1} d\int_{V_1} T_1 dV}{dt} = -\int_{V_1} \frac{\partial q_1}{\partial x} dV + \int_{V_1} Q_{irrev,i} dV + \int_{V_1} Q_{rev,i} dV + \int_{V_1} Q_{ohmic,i} dV \qquad (74)$$

For the one-dimensional model in cartesian coordinates, the differential volume dV is given by $dV = Adx$, where A is a constant that may be considered a cross-sectional area. In addition, we express the integrals in terms of average quantities such as, $\overline{T_1} = \frac{\int_{V_1} T_1 dV}{\int_{V_1} dV}$, and $\overline{Q_{rev,1}} = \frac{\int_{V_1} Q_{rev,1} dV}{\int_{V_1} dV}$, with $\bar{v}$ denoting the volume average of variable v in a given 'tank'. Substituting these relations converts the volume integral into a one-dimensional integral over electrode thickness, i.e. from $x = 0$ to $x = l_1$.

Equation (34) thus becomes

$$\rho_1 C_{p1} \frac{d\overline{T_1}}{dt} = -\frac{\int_{x=0}^{x=l_1} \frac{\partial q_1}{\partial x} dx}{l_1} + \overline{Q_{irrev,1}} + \overline{Q_{ohmic,1}} + \overline{Q_{rev,1}} \qquad (75)$$

$$\rho_1 C_{p1} \frac{d\overline{T_1}}{dt} = -\left(\frac{q_{1,x=l_1} - q_{1,x=0}}{l_1}\right) + \overline{Q_{irrev,1}} + \overline{Q_{ohmic,1}} + \overline{Q_{rev,1}} \qquad (76)$$

Similar equations may be derived for the other domains as follows

$$\rho_2 C_{p2} \frac{d\overline{T_2}}{dt} = -\left(\frac{q_{2,x=l_0+l_1+l_2} - q_{2,x=l_0+l_1}}{l_2} \right) + \overline{Q_{ohmic,2}} \tag{77}$$

$$\rho_3 C_{p3} \frac{d\overline{T_3}}{dt} = -\left(\frac{q_{3,x=l_0+l_1+l_2+l_3} - q_{3,x=l_0+l_1+l_2}}{l_3} \right) + \overline{Q_{irrev,3}} + \overline{Q_{ohmic,3}} + \overline{Q_{rev,3}} \tag{78}$$

3.4.3. ***Source Term Approximations***

The volume-averaged heat generation terms due to electrochemical reaction are defined using standard approximations of the Tanks-in-Series approach as

$$\overline{Q_{irrev,i}} = \left(\frac{i_{app,i}}{l_i} \right) \left(\overline{\phi_{s,i}} - \overline{\phi_{l,i}} - U\left(\overline{c_i^{s,surf}} \right) \right) \quad i \in \{1,3\} \tag{79}$$

$$\overline{Q_{rev,i}} = \left(\frac{i_{app,i}}{l_i} \right) \left(\overline{T_i} \frac{\partial U\left(\overline{c_i^{s,surf}} \right)}{\partial T} \right) \quad i \in \{1,3\} \tag{80}$$

The averaged form of the ohmic contributions is given by

$$\overline{Q_{ohmic,i}} = \left(\frac{\left| i_{app} \left(\phi_{l,ij} - \overline{\phi_{l,i}} \right) \right|}{l_i} \right) \quad i \in \{1,3\} \tag{81}$$

$$\overline{Q_{ohmic,2}} = \left(\frac{\left| i_{app} \left(\phi_{l,12} - \phi_{l,23} \right) \right|}{l_2} \right) \tag{82}$$

A detailed derivation of the $\overline{Q_{ohmic,i}}$ terms may be found in the Appendix A (**Section 6**).

Recalling the standard flux approximations introduced in previous work[41,108], we have

$$q_{ij} = -\lambda_i \frac{\partial T_i}{\partial x}_{x=l_i} \approx \lambda_i \left(\frac{\Delta T_i}{\delta_{Ti,ij}} \right) = \lambda_i \left(\frac{\overline{T_i} - T_{ij}}{\frac{l_i}{2}} \right)$$
$$q_{ij} = -\lambda_j \frac{\partial T_j}{\partial x}_{x=l_i} \approx \lambda_j \left(\frac{\Delta T_j}{\delta_{Tj,ij}} \right) = -\lambda_j \left(\frac{\overline{T_j} - T_{ij}}{\frac{l_j}{2}} \right) \tag{83}$$

Here we have implicitly used the flux continuity conditions of equations (32) - (70), which then allows us to estimate the unknown interfacial value as

$$\lambda_i \left(\frac{\overline{T_i} - T_{ij}}{\frac{l_i}{2}} \right) = -\lambda_j \left(\frac{\overline{T_j} - T_{ij}}{\frac{l_j}{2}} \right)$$
$$T_{ij} = \frac{\left(\frac{\lambda_i}{l_i} \right) \overline{T_i} + \left(\frac{\lambda_j}{l_j} \right) \overline{T_j}}{\left(\frac{\lambda_i}{l_i} + \frac{\lambda_j}{l_j} \right)} \tag{84}$$

Now, after substituting equation (84) into the volume-averaged equations (36) - (38), we obtain the final form of the temperature equations. These equations constitute the thermal augmentation to the isothermal Tank Model equations of Ref. 41. Taken together, the combined set of equations is termed the 'Thermal Tank Model'. The complete set of equations for the porous domains may be found in **Table 3-V**. **Figure 3.2** represents the modeling schematic of the Tanks-in-Series representation of a single cell.

3.4.4. *Multi-cell Stack Model*

We now briefly describe the extension of the single cell models of the previous section to a simplified multi-cell stack depicted in **Figure 3.3** . The modeling schematic may be representative of a multi-layer pouch cell, in which the individual layers are connected in parallel. Each individual layer may be regarded a 'repeat unit', itself represented by an electrochemical model for a single cell.[96,105,108,109] Given that a single domain consists of five domains, the volume-averaged Tanks-in-Series model results in five such Tanks. Thus a 10-cell stack may thus be regarded as '50 Tanks-in-Series'. **Figure 3.3** indicates that adjacent cells are in thermal contact and can exchange heat by conduction. Appropriate coupling boundary conditions need to be defined to account for this thermal interaction.[46,105] In addition, the cell draws a total current which is distributed among the individual layers, which are connected electrically in parallel and thus experience the same voltage V_{cell} .

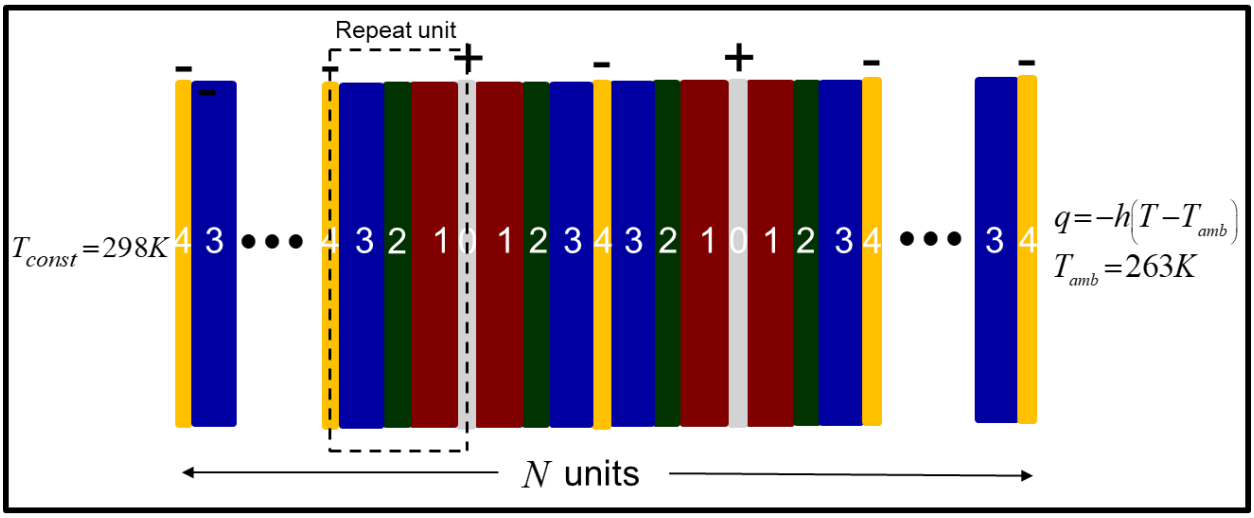

Figure 3.3. Schematic of an *N-cell* stack. An instance of the p2D model (**Figure 3.1**) is used to represent each individual sandwich (termed the 'cell' in this work) in the stack. The N repeat units are connected in parallel and experience the same voltage V_{cell}. The current densities from individual cells add up to the total value. The asymmetric temperature boundary conditions considered in this work are also indicated. The collector plate for the cell at the left extreme, is held at a constant temperature. The negative collector for the right extreme cell, on the other hand, is free to exchange heat with the surroundings. In the remainder of this document, the left cell is referred to as either the 'leftmost' cell or the 'hot' cell. The right extreme cell is similarly termed the 'rightmost' or 'cold cell'.

For the positive collector, the temperature coupling boundary conditions between successive cells, thermally in series, are given by

$$T_{4,k,x=l_0+l_1+l_2+l_3+l_4/2} = T_{4,k+1,x=l_0+l_1+l_2+l_3+l_4/2,}$$
$$\left.\frac{\partial T_{4,k}}{\partial x}\right|_{x=l_0+l_1+l_2+l_3+l_4/2} = -\left.\frac{\partial T_{4,k+1}}{\partial x}\right|_{x=l_0+l_1+l_2+l_3+l_4/2} \quad [1 \le k \le N_{cell}] \tag{85}$$

Here we note that each 'repeat unit' includes one half of each current collector, as indicated in **Figure 3.4**.

Similarly, at the negative Cu collectors in the interior layers, we have

$$T_{0,k,x=0} = T_{0,k+1,x=0}$$
$$\left.\frac{\partial T_{0,k}}{\partial x}\right|_{x=0} = -\left.\frac{\partial T_{0,k+1}}{\partial x}\right|_{x=0} \qquad [2 \le k \le N_{cell} - 1] \tag{86}$$

Where the gradient boundary condition is required based on the modeling approach described above. This is essentially a flux continuity condition, with the negative sign required by the coordinate transformation approach.[46] For the Cu collectors for the end cells in **Figure 3.3**, for the leftmost 'hot' cell, we have the following boundary conditions for T_0

$$T_{0,1,x=0} = T_{const} \tag{87}$$

This denotes the constant temperature boundary condition at the left end, as indicated in . In this case, the subscript $k = 1$ denotes for the first cell.

Similarly, we apply the convection boundary condition at the rightmost cell ($k = N_{cell}$)

$$\lambda_0 \left.\frac{\partial T_{0,N_{cell}}}{\partial x}\right|_{x=0} = h(T_{0,N_{cell}} - T_{amb}) \tag{88}$$

These equations thus establish the coupling between temperatures in adjacent cells.

In the single cell models, we must specify a current density boundary condition for the solid phase potentials $\phi_{s,i}$ (**Table 3-I**). In addition, a reference potential is specified as a Dirichlet condition to obtain a well-posed problem formulation. Similar relations must be specified for each cell in a stack model. For the stack model, the equality of terminal potentials $\phi_{s,i}$ between the cells gives rise to $N_{cell} - 1$ unique coupling conditions for each cell terminal. Thus, at the negative electrode, we have

$$\phi_{s,3,k,x=l_0} = \phi_{s,3,k+1,x=l_0} = 0 \quad [1 \le k \le N_{cell} - 1] \tag{89}$$

Where we specify a reference potential as above.

Similarly, at the positive electrode, we have

$$\phi_{s,1,k,x=l_0+l_1+l_2+l_3} = \phi_{s,1,k+1,x=l_0+l_1+l_2+l_3} \quad [1 \le k \le N_{cell} - 1] \tag{90}$$

Now, analogous to the single cell models, we must specify an overall current condition. For a parallel configuration, the current density $i_{app,k}$ through cell *k* may be defined using the boundary conditions of **Table 3-I** as

$$i_{app,k} = -\sigma_{eff,1} \left. \frac{\partial \phi_{s,1,k}}{\partial x} \right|_{x=l_0+l_1+l_2+l_3} \tag{91}$$

Now, the currents drawn from the individual layers must sum to the total stack value. This overall charge conservation is expressed in terms of the per-unit-area quantities as

$$i_{app,stack} = \sum_{k=1}^{N_{cell}} i_{app,k} \tag{92}$$

Here, it is worth mentioning that for a parallel configuration, even during galvanostatic operation characterized by a constant total current $i_{app,stack}$, inhomogeneities in the temperature profiles in individual cells may lead to variations in the individual $i_{app,k}$ as a function of time. This model formulation predicts the instantaneous values of current densities and electrochemical variables simultaneously. This is in contrast to other approaches which first solve for electrochemical variables at a given time step, and then subsequently solve a circuit-level system of equations to

compute current distributions.[10,113]

Equations (85) - (92) thus establish the additional boundary conditions and overall relations required to model an N-cell stack. This is in addition to the equation set of **Table 3-I** for each individual cell. The equivalent Tanks-in-Series model can be generated by applying the standard volume-averaging and flux-approximation methodology to the equations of the individual cells (analogous to those in **Table 3-III**) as well as the additional constraints of equations (85) - (92). The Tanks-in-Series modeling approach for the stack is illustrated in **Figure 3.4**.

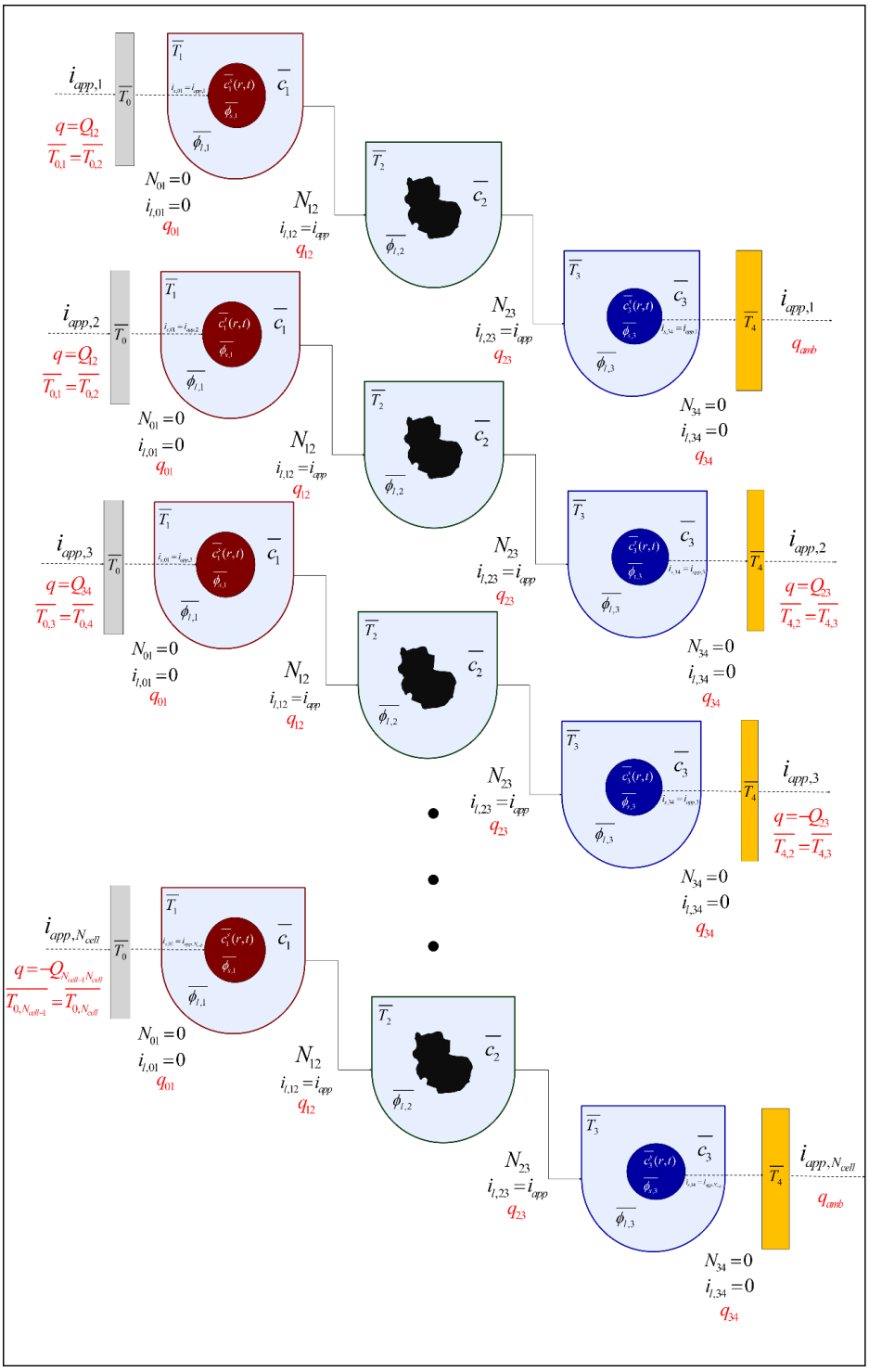

Figure 3.4. Computational schematic of the Tanks-in-Series representation of a cell stack. Individual layers are represented as Tanks-in-Series. The internal repeat unit includes one-half of each current collector, while the end cells consist of the entirety of the Cu collectors. This is illustrated by the relative sizes of the Cu collectors in the end and internal cells. The coordinate transformation strategy requires the temperature

and flux relations highlighted in red, which are approximated using the Tanks-in-Series methodology.

The balance between internal conduction and external heat transfer can often be expressed in terms of the Biot Number, given by

$$Bi = hR_t \tag{93}$$

Where the quantity R_t denotes the net thermal resistance of the cell stack given by

$$R_t = \sum_{i=1}^{N_{cell}} \sum_{j=0}^{4} \frac{l_{i,j}}{\lambda_{i,j}} \tag{94}$$

A range of *Bi* numbers can thus be generated by varying both the value of h and the thermal resistance R_t by way of N_{cell}. The Thermal Tank Model can then be evaluated under different operating current densities, with a view to establishing the limits of operation, which can help provide guidance for the incorporation of the Stack Model in practical applications.

3.5. Model and Simulation Details

3.5.1. *Single Cell Simulations*

Table 3-I - **Table 3-IV** list the parameter values and constitutive equations for a $LiCO_2$ positive electrode and graphite negative electrode, taken from past work.[46,93,112] Modified values for the high capacity case with electrolyte transport limitations may be found in **Table 3-VI**. Electrolyte transport property correlations were adapted from the work of Valøen and Reimers.[80] In the isothermal Tank Model, these properties are evaluated at the interfacial values of electrolyte concentration c_{ij}. In extending these models to thermal effects, the electrolyte transport properties

also depend on the interfacial value of temperature T_{ij}. Other interfacial conditions that feature temperature, such as equation (56) in Ref. 41, are also evaluated at the interfacial T_{ij}. For the equations solved within the interior of a domain, relevant kinetic, transport and thermodynamic quantities were calculated at the average value $\overline{T_i}$. The particle radii R_i, the current densities i_{app}, and the solid diffusion coefficients D_i^s were so chosen that the three-parameter model for solid phase transport is within the range of validity.[78]

Table 3-IV. Base case model parameters (constant values).

Symbol	Parameter	Aluminum Current Collector	Positive Electrode	Separator	Negative Electrode	Copper Current Collector	Units
ε_i	Porosity		0.385	0.724	0.485		
ε_{fi}	Electrode filler fraction		0.025		0.0326		
b_i	Brugemann tortuosity correction		1.5	1.5	1.5		
a_i	Particle surface area per unit volume		885000		723600		m^2/m^3
$c_i^{s,\max}$	Maximum particle phase concentration		51554		30555		mol/m^3
$c_i^{s,0}$	Initial particle phase concentration		25751		26128		mol/m^3
c_0	Initial electrolyte concentration			1000			mol/m^3
D_i^s	Solid phase diffusivity		1.0×10^{-14}		3.9×10^{-14}		m^2/s
k_i	Electrode reaction rate constant		2.334×10^{-11}		5.031×10^{-11}		$m^{2.5}/(mol^{0.5}s)$
$\alpha_{a,i}$	Electrode reaction anodic coefficient		0.5		0.5		
$\alpha_{c,i}$	Electrode reaction cathodic coefficient		0.5		0.5		
l_i	Electrode thickness	10×10^{-6}	80×10^{-6}	25×10^{-6}	88×10^{-6}	10×10^{-6}	m
R_i	Characteristic particle radius		2×10^{-6}		2×10^{-6}		m
t_+^0	Li^+ transference number			0.364			
σ_i	Electronic conductivity	3.55×10^7	100		100	5.96×10^7	S/m
T_{ref}	Temperature			298.15			K
i_{app}	1C Current Density			30			A/m^2
C_p	Specific heat	897	700	700	700	385	J/(kg K)
$E_a^{D_i^s}$	Activation energy for temperature dependent solid phase diffusion		5000		5000		J/mol
$E_a^{D_i^s}$	Activation energy for temperature dependent for kinetic rate constant		5000		5000		J/mol
λ	Thermal conductivity	237	2.1	0.16	1.7	401	W/(m K)
ρ	Density	2700	2500	1100	2500	8940	Kg/m^3
F	Faraday's constant			96487			C/mol
R	Gas constant			8.314			J/(mol K)

Table 3-V. Governing Equations of the Thermal Tanks-in-Series Model for the porous domains.

Positive Electrode (Region 1)

$$\frac{d\overline{c_1}}{dt} = \frac{\frac{3D(c_{12},T_{12})(\overline{c_2}-\overline{c_1})}{\frac{l_1}{\varepsilon_1^{b_1}}+\frac{l_2}{\varepsilon_2^{b_2}}}}{\varepsilon_1 l_1} + \left(1-t_+^0\right)\frac{i_{app}}{\mathrm{F}\varepsilon_1 l_1}$$

$$i_{app} = -3\kappa(c_{12},T_{12})\left(\frac{\overline{\phi_{l,2}}-\overline{\phi_{l,1}}}{\frac{l_1}{\varepsilon_1^{b_1}}+\frac{l_2}{\varepsilon_2^{b_2}}}\right) + \frac{6RT_{12}(1-t_+^0)}{F}\nu(c_{12},T_{12})\kappa(c_{12},T_{12})\frac{1}{c_{12}}\left(\frac{\overline{c_2}-\overline{c_1}}{\frac{l_1}{\varepsilon_1^{b_1}}+\frac{l_2}{\varepsilon_2^{b_2}}}\right)$$

$$\frac{d\overline{T_1}}{dt} = \frac{-\frac{2(\overline{T_1}-\overline{T_0})}{\frac{l_1}{\lambda_1}+\frac{l_0}{\lambda_0}} + \frac{2(\overline{T_2}-\overline{T_1})}{\frac{l_1}{\lambda_1}+\frac{l_2}{\lambda_2}}}{l_1} + \overline{Q_{rev,1}} + \overline{Q_{irrev,1}} + \overline{Q_{ohmic,1}}$$

$$\frac{d\overline{c_1^{s,avg}}}{dt} = -3\frac{\overline{j_1}}{R_1}$$

$$\frac{d\overline{q_1^{avg}}}{dt} = -30\frac{D_1^s}{R_1^2}\overline{q_1^{avg}} - \frac{45}{2}\frac{\overline{j_1}}{R_1^2}$$

$$35\frac{D_1^s}{R_1}[\overline{c_1^{s,surf}} - \overline{c_1^{s,avg}}] - 8D_1^s\overline{q_1^{avg}} = -\overline{j_1}$$

$$\frac{i_{app}}{Fa_1l_1} = k_1\left(\overline{c_1}\right)^{\alpha_{c,1}}{}_1(c_1^{s,\max}-\overline{c_1^{s,surf}})^{\alpha_{a,1}}(\overline{c_1^{s,surf}})^{\alpha_{c,1}}\left(\exp\left(\frac{\alpha_{a,1}F\overline{\eta_1}}{R\overline{T_1}}\right)-\exp\left(\frac{-\alpha_{c,1}F\overline{\eta_1}}{R\overline{T_1}}\right)\right)$$

$$\overline{\eta_1} = \overline{\phi_{s,1}} - \overline{\phi_{l,1}} - U(\overline{c_1^{s,surf}})$$

Separator (Region 2)

$$\frac{d\overline{c_2}}{dt} = \frac{\frac{-3D(c_{12},T_{12})(\overline{c_2}-\overline{c_1})}{\frac{l_1}{\varepsilon_1^{b_1}}+\frac{l_2}{\varepsilon_2^{b_2}}} + \frac{3D(c_{23},T_{23})(\overline{c_3}-\overline{c_2})}{\frac{l_2}{\varepsilon_2^{b_2}}+\frac{l_3}{\varepsilon_3^{b_3}}}}{\varepsilon_2 l_2}$$

$$\phi_{l,12} = \left(\frac{\frac{\varepsilon_1^{b_1}}{l_1}\overline{\phi_{l,1}} + \frac{\varepsilon_2^{b_2}}{l_2}\overline{\phi_{l,2}}}{\frac{\varepsilon_1^{b_1}}{l_1}+\frac{\varepsilon_2^{b_2}}{l_2}}\right) = 0$$

$$\frac{d\overline{T_2}}{dt} = \frac{-\frac{2(\overline{T_2}-\overline{T_1})}{\frac{l_1}{\lambda_1}+\frac{l_2}{\lambda_2}} + \frac{2(\overline{T_3}-\overline{T_2})}{\frac{l_3}{\lambda_3}+\frac{l_2}{\lambda_2}}}{l_2} + \overline{Q_{ohmic,2}}$$

Negative Electrode (Region 3)

$$\frac{d\overline{c_3}}{dt} = \frac{\frac{-3D(c_{23},T_{23})(\overline{c_3}-\overline{c_2})}{\frac{l_2}{\varepsilon_2^{b_2}}+\frac{l_3}{\varepsilon_3^{b_3}}}}{\varepsilon_3 l_3} - \left(1-t_+^0\right)\frac{i_{app}}{\varepsilon_3 l_3}$$

$$i_{app} = -3\kappa(c_{23},T_{23})\left(\frac{\overline{\phi_{l,3}}-\overline{\phi_{l,2}}}{\frac{l_3}{\varepsilon_3^{b_3}}+\frac{l_2}{\varepsilon_2^{b_2}}}\right) + \frac{6RT_{23}(1-t_+^0)}{F}\nu(c_{23})\kappa(c_{23},T_{23})\frac{1}{c_{23}}\left(\frac{\overline{c_3}-\overline{c_2}}{\frac{l_2}{\varepsilon_2^{b_2}}+\frac{l_3}{\varepsilon_3^{b_3}}}\right)$$

$$\frac{d\overline{T_3}}{dt} = \frac{-\frac{2(\overline{T_3}-\overline{T_2})}{\frac{l_2}{\lambda_2}+\frac{l_3}{\lambda_3}} + \frac{2(\overline{T_4}-\overline{T_3})}{\frac{l_4}{\lambda_4}+\frac{l_3}{\lambda_3}}}{l_3} + \overline{Q_{rev,3}} + \overline{Q_{irrev,3}} + \overline{Q_{ohmic,3}}$$

$$\frac{d\overline{c_3^{s,avg}}}{dt} = -3\frac{\overline{j_3}}{R_3}$$

$$\frac{d\overline{q_3^{avg}}}{dt} = -30\frac{D_3^s}{R_3^2}\overline{q_3^{avg}} - \frac{45}{2}\frac{\overline{j_3}}{R_3^2}$$

$$35\frac{D_3^s}{R_1}[\overline{c_3^{s,surf}} - \overline{c_3^{s,avg}}] - 8D_3^s\overline{q_3^{avg}} = -\overline{j_3}$$

$$\frac{-i_{app}}{Fa_3l_3} = k_3\left(\overline{c_3}\right)^{\alpha_{a,3}}(c_3^{s,\max}-\overline{c_3^{s,surf}})^{\alpha_{a,3}}(\overline{c_3^{s,surf}})^{\alpha_{c,3}}\left(\exp\left(\frac{\alpha_{a,3}F\overline{\eta_3}}{R\overline{T_3}}\right)-\exp\left(\frac{-\alpha_{c,3}F\overline{\eta_3}}{R\overline{T_3}}\right)\right)$$

$$\overline{\eta_3} = \overline{\phi_{s,3}} - \overline{\phi_{l,3}} - U(\overline{c_3^{s,surf}})$$

Table 3-VI. Modified parameters for the electrolyte-limited case.

Symbol	Description	Base Case Value	Modified Value	Units
l_1	Positive Electrode Thickness	80	160	μm
l_3	Negative Electrode Thickness	88	176	μm
ε_1	Positive Electrode Porosity	0.385	0.3	
ε_3	Negative Electrode Porosity	0.485	0.35	
i_{app}	Current Densities Studied (C-rates)	30,60,150 (1C,2C,5C)	30,60,150 (0.4C,0.8C,2C)	A/m^2

3.5.2. *Multi- Cell Stack Simulations*

For the stack study, the electrode and electrolyte properties for the base case were used. The temperature boundary conditions at the ends of the stack for this study are depicted **Figure 3.3**. One end is maintained at a constant temperature (298 K), while the other extremity exchanges heat with the ambient surroundings by convection. An ambient temperature $T_{amb} = 263K$ (-10ºC) was used. Additionally, the cell was assumed to be at a uniform temperature of 298 K at the beginning of discharge. These conditions may be regarded as representing practical scenarios corresponding to a preheated battery operating under low-temperatures, such as for electric vehicles in cold weather, or electric aircraft applications.[114] The study of the low-temperature performance of Li-ion batteries has significant practical value due to the increased capacity loss due to the enhanced thermodynamic favorability of lithium deposition reactions, and model-based studies and optimal charging strategies are actively explored.[6,19] The variation of the ambient heat transfer coefficient h in conjunction with ambient temperature T_{amb} has been explored as a means to study the resulting deterioration in energy and power density.[106] In addition, such a parametric study may

have practical utility in guidance for preventing heat loss and insulation design for Li-ion cells under cold ambient conditions.[115] The asymmetric boundary conditions impose a temperature gradient across the cell stack, which provides a relevant scenario to evaluate the Tanks-in-Series approach applied to multi-cell stacks.[46,51] **Table 3-VII** lists the parameter values used for the stack simulation studies.

Table 3-VII. Relevant Parameters for the Cell Stack simulations.

Symbol	Parameter	Value
N_{cell}	No. of cells in the stack	2 - 10
$i_{app,stack} = N_{cell} i_{app}$	1C current density in the stack	60 – 300 A/m^2
T_{const}	Temperature condition at the leftmost collector in the stack	298 K
h	Ambient heat transfer coefficient	4 – 4000 $\frac{W}{m^2 K}$
T_{amb}	Ambient Temperature	263 K

3.5.3. *Computational Details*

The full electrochemical-thermal p2D model is used as the benchmark in evaluating the predictions of the Tanks-in-Series model. The p2D model was discretized and solved using coordinate transformation, model reformulation and orthogonal collocation techniques.[46] The number of collocation points in each region were adjusted to achieve numerical convergence of discharge curves at different current densities up to 5C, ultimately selecting n=(2,7,3,7,2) Gauss-Legendre collocation points. This discretization scheme was also used for the component cell models in the stack simulation studies.

The discretized equation systems were solved in time using IDA, an Implicit Differential-

Algebraic solver in ANSI-standard C language under BSD license. IDA is an efficient solver for initial value problems (IVP) for systems of DAEs, which is part of the SUNDIALS (SUite of Nonlinear and DIfferential/ALgebraic equation Solvers) package.[86] The absolute solver tolerance was set to $atol = 10^{-8}$ and a relative tolerance of $rtol = 10^{-7}$ was specified. All computations were performed on an Intel ® Core ™ i7-7700K processor with a clock speed of 4.2 GHz, 8 logical cores and 64 GB RAM.

3.6. Single Cell Results : Base Case

In this section, we evaluate the thermally augmented the Tanks-in-Series model for representative cases of galvanostatic discharge. In particular, we consider two values of the convective heat transfer coefficient corresponding to practically relevant scenarios. In the first instance, we assume $h = 0$, implying a completely insulated cell operating adiabatically. The second case uses a relatively high $h = 1000 W/m^2K$ corresponding to fast convective heat transfer. These cases are termed as 'adiabatic operation' and 'fast heat transfer' respectively. A particular focus is the comparison of internal electrochemical variables and the accuracy of individual terms in the energy balances. The solid phase concentration ($\overline{c_i^{s,surf}}$) and potential variables ($\overline{\phi_{s,i}}$) were compared and found to exhibit close agreement for the cases considered herein, and are not shown here.

3.6.1. *Discharge Curves*

Comparisons of the cell voltage from the thermally augmented Tanks-in-Series Model, hereafter termed the 'Thermal Tank Model', versus the full-order p2D model are depicted in **Figure 3.5.** Comparisons of the Thermal Tank Model with the full-order p2D model for **(a)** adiabatic **(b)** fast

external heat transfer scenarios.. The agreement of the two models even for the relatively aggressive 5C discharge rate is quite remarkable. Upon inspecting the instantaneous error profiles in **Figure 3.6**, it is observed that the cell voltage error does not exceed 6 mV for adiabatic operation, and 15 mV for the fast heat transfer case. These metrics point to the competitiveness of the Tank Model in real-time frameworks and advanced BMS. As in the isothermal case, the errors arise primarily due to the approximate nature of the flux equations, and the assumption of uniform reaction distribution in the electrodes.[41]

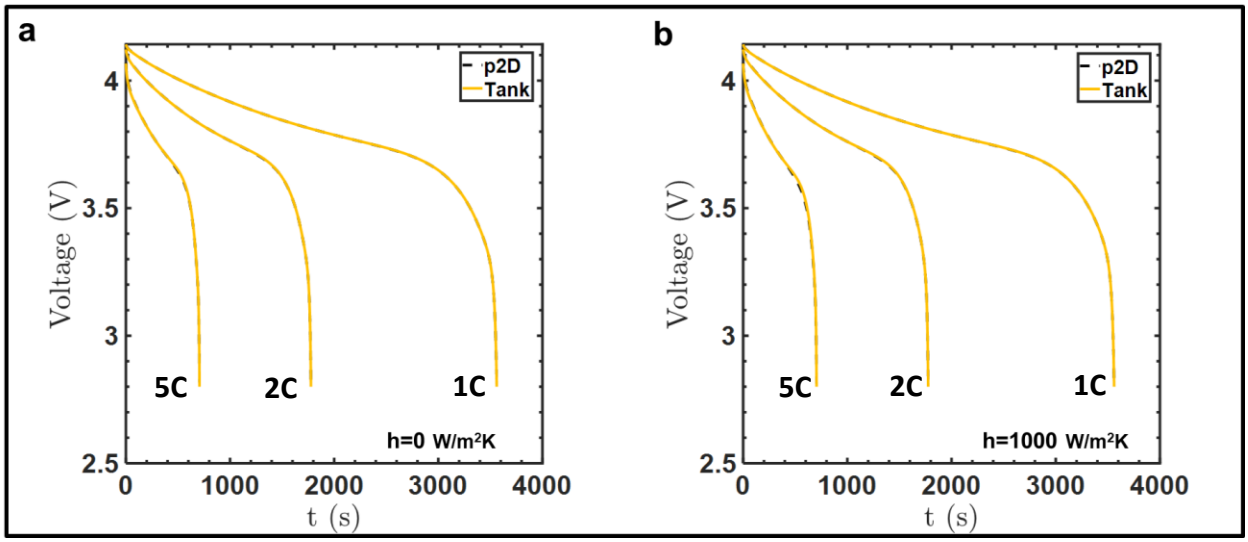

Figure 3.5. Comparisons of the Thermal Tank Model with the full-order p2D model for **(a)** adiabatic **(b)** fast external heat transfer scenarios.

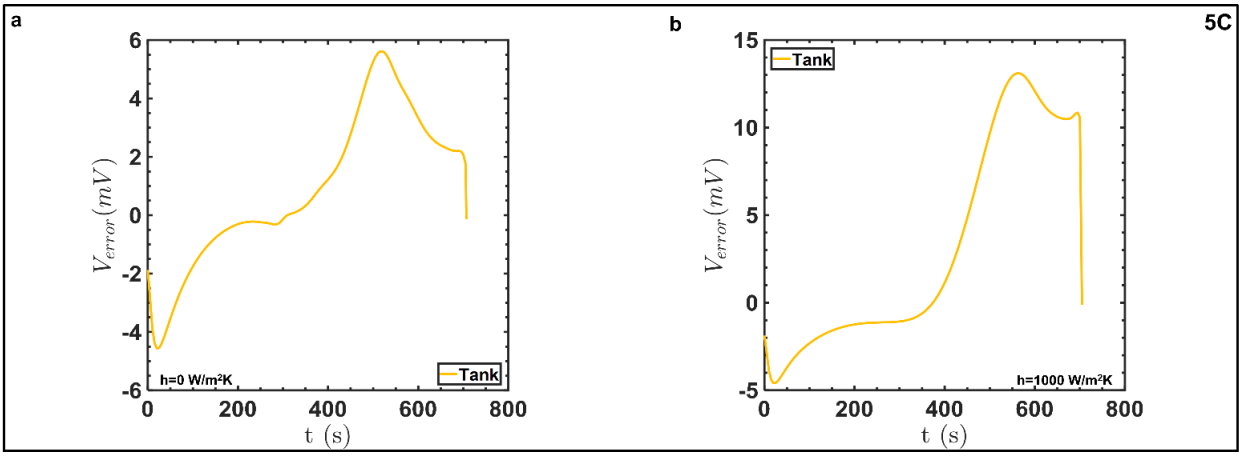

Figure 3.6. Representative voltage error profiles at 5C discharge for the (a) adiabatic and (b) fast external heat transfer scenarios.

The coupling of temperature with electrochemical transport phenomena helps understand the differences in errors between the adiabatic and fast heat transfer scenarios. In the adiabatic case, the heat generated during operation is expected to produce a rise in cell temperature, enhancing reaction kinetics and transport rates. Consequently, the polarization of the cell is reducing with time, dissipating gradients in both solid and liquid phases. This is in contrast to the fast heat transfer case, where the large external cooling rate results in near-isothermal operation for which the average cell polarization is higher. This explains the improved performance for the Tank Model for the adiabatic case.

3.6.2. *Electrolyte Phase Variables*

As discussed in the previous chapter[41], the use of a diffusion length $\delta_{i,ij} = \frac{1}{3}$ for electrolyte phase variables, corresponding to a parabolic spatial profile, substantially improves estimates of ohmic potential drop and concentration overpotential relative to the standard $\delta_{i,ij} = \frac{1}{2}$ value. The

agreement of the Tank Model is illustrated in **Figure 3.7**, which compares the concentration profiles for the two scenarios. For both the adiabatic and fast heat transfer cases, the maximum error in concentration is about 50 mol/m^3, corresponding to an error of less than 1% even for a 5C discharge rate. In examining the concentration trends for the p2D model, we can notice pronounced fluctuations for the fast heat transfer case (**Figure 3.7 (b)**), which may be attributed to local variations in the reaction rate. Expectedly, the Tank Model predicts a rapid attainment of steady state at t~50 s due to the uniform reaction assumption. The fluctuations for the adiabatic case are not as pronounced due to the rising temperature as the discharge progresses, which tends to enhance both kinetics and transport, homogenizing the reaction distributions (**Figure 3.7 (a)**). The effect of temperature is also reflected in the temporal variation of the concentration. While the concentrations rapidly attain a steady state during near-isothermal operation, during adiabatic operation the concentrations first reach the same value on a comparable timescale (~50 s), but one then notices a gradual depletion of electrolyte in the negative electrode, accompanied by a corresponding increase in the positive electrode. These trends reflect the increase in diffusivities $D(\overline{c_i},\overline{T_i})$ with temperature, which leads to a reduction in the concentration gradients required to sustain a given electrolyte flux.

Similar qualitative trends are seen for $\phi_{l,i}$ as well (**Figure 3.8**). The Tank Model exhibits close agreement for both average and interfacial values, with the maximum error not exceeding 3 mV for the adiabatic case, and 5 mV for the fast heat transfer scenario. The instantaneous fluctuations for $\overline{\phi_{l,3}}$ in the negative electrode appear more pronounced than that in the positive electrode $\overline{\phi_{l,1}}$, likely due to the faster kinetics in the negative electrode, and the more non-uniform reaction

distribution that results. Expectedly, this is more discernible during near-isothermal operation, as in **Figure 3.8 (b)**.

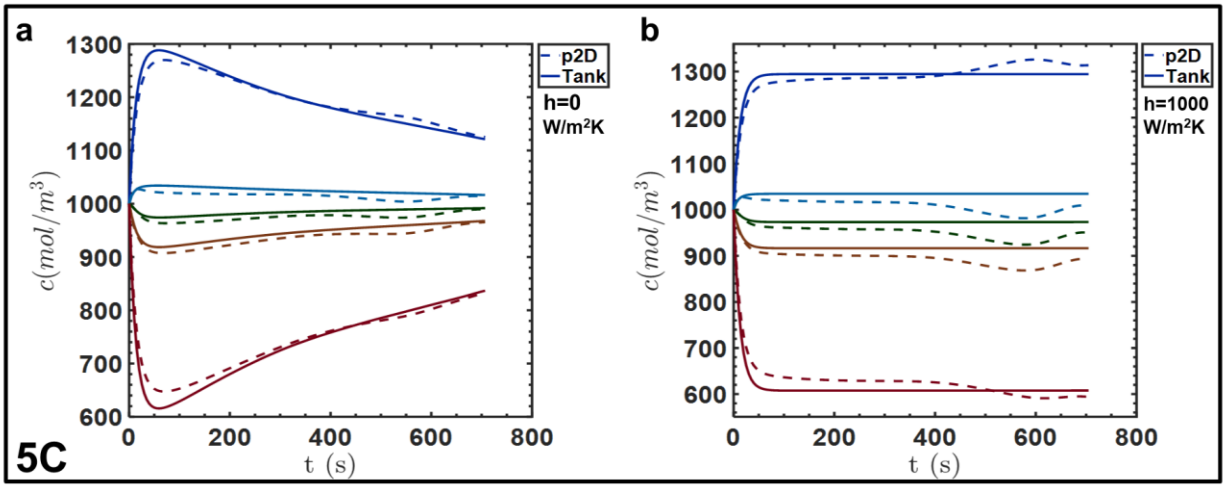

Figure 3.7. Representative concentration profiles at 5C discharge for **(a)** adiabatic operation **(b)** fast heat transfer. The color convention of **Figure 3.1** is used, i.e. (i) Positive Electrode (Dark Red), (ii) Positive-Separator Interface (Light Red), (iii) Separator (Forest Green), (iv) Separator-Negative Interface (Light Green), and (v) Negative Electrode (Dark Blue).

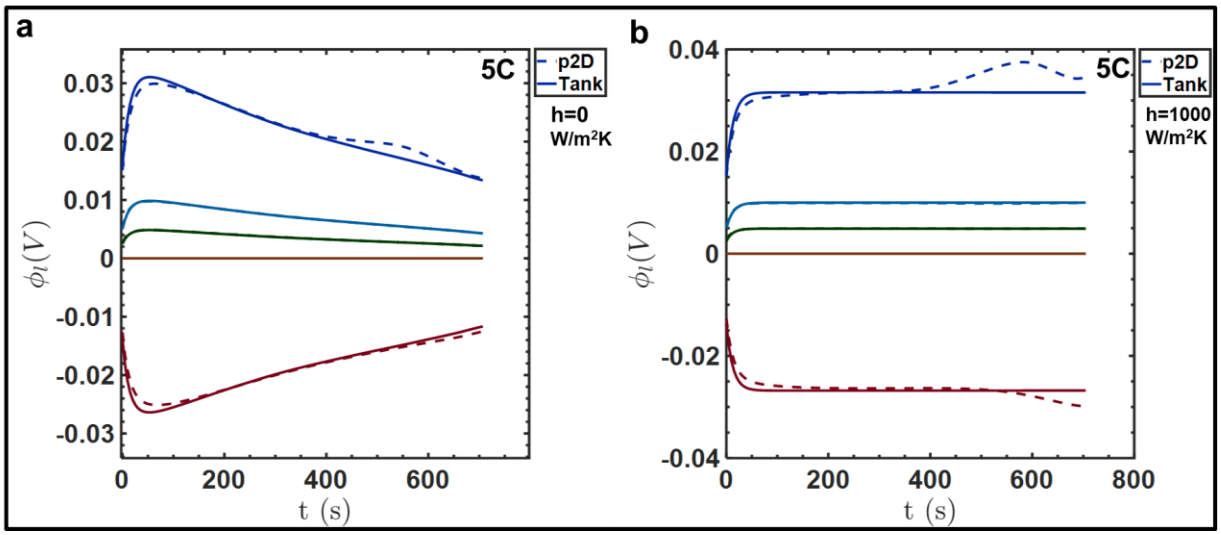

Figure 3.8. Representative electrolyte potential profiles at 5C discharge for (a) adiabatic operation (b) fast

heat transfer. As done elsewhere, the color convention of **Figure 3.1** is used.

The base case temperature boundary conditions, which define the heat fluxes at the collector surfaces, impose a near-symmetric temperature profile due to the comparable thicknesses and thermal conductivities of the electrodes and respective collector materials. In addition, the inherently low thermal resistance ensures near-uniform temperature for all operating conditions. While a simple lumped model is thus applicable for this case[107,111], these simulations represent the initial check for the accuracy of the Tank Model prior to use for stack simulations. The temperature trends for the two scenarios are illustrated in **Figure 3.9**. As expected, the cell temperature exhibits a near-monotonic increase beyond t=50 s during adiabatic operation, reaching approximately 356 K at ~700 s. The Thermal Tank Model is able to ensure agreement with the p2D model even with the simple averaging procedure combined with the naïve approximations for 'thermal diffusion length'. A caveat in interpreting the adiabatic results is that the transport property correlations used in this work are only valid up to a temperature of 333 K, beyond which they are extrapolated.[80] However, the same property correlations are used in comparing both models, so the evaluation of the Thermal Tank Model holds. In contrast to the adiabatic case, using a value $h = 1000$ W/m^{2}K results in a near-constant temperature throughout the cell, as depicted in **Figure 3.9 (b)**, indicating the establishment of a steady-state value of temperature corresponding to the balance between the net internal heat generation rate and the rate of convective heat dissipation. For this case, it is interesting also to note an extremely small but finite internal temperature gradient in the cell. From **Figure 3.9 (b)**, it can be seen that the temperature at the surface of the Al collector (peach) is marginally higher (~ 3 mK) compared to the Cu collector (purple). This may be attributed to

variations in the local heat generation rates and the conduction resistances of the materials. In practice, degradation and thermal decomposition reactions of the electrodes, electrolyte and other components, are likely to be triggered above a temperature threshold, leading to accelerated capacity degradation and potential thermal runaway. These reactions are not considered in our models, but the temperature prediction from the Thermal Tank Model could be used as rough threshold guidelines by a BMS to define safe operating limits for a given battery. Further, the Thermal Tank Model represents a simplified framework for the integration of explicit models for deleterious side reactions.

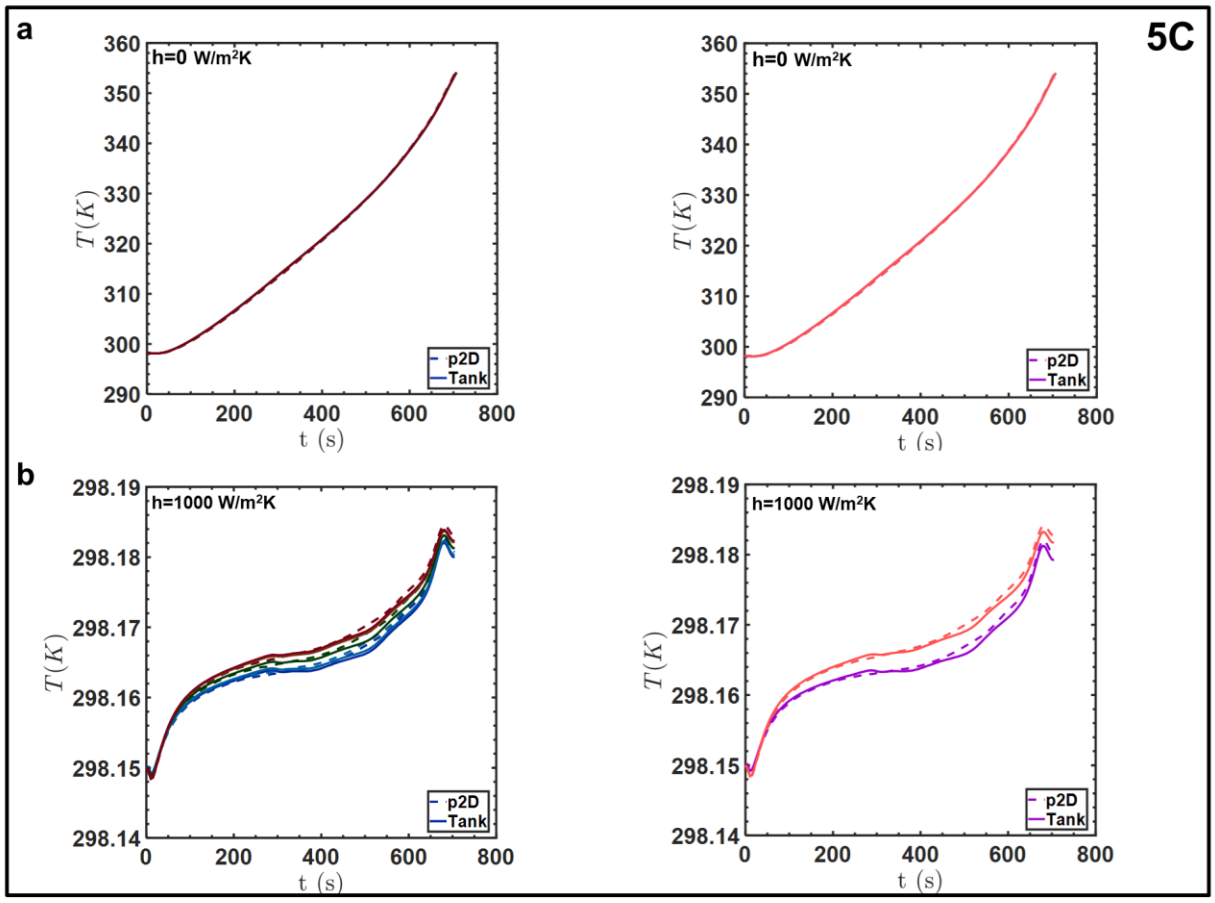

Figure 3.9. Internal Temperature (left) and Surface Temperature profiles at Aluminum (peach) and Copper

(purple) collectors at 5C discharge rate for the **(a)** adiabatic and **(b)** fast heat transfer scenarios. The color convention of **Figure 3.1** is used.

3.6.3. *Thermal Variables*

The results thus far indicate the ability of the approximate Thermal Tank Model, with its substantially reduced computational footprint, to predict the temperature variation of a single Li-ion cell under practically relevant conditions. Increasing the value of the heat transfer coefficients tends to increase the magnitude of temperature gradients within the cell by altering the balance between conduction and convection resistances. Typically, this is expressed in the form of a dimensionless group such as the Biot number (*Bi*).[14] For the parameters considered for a single cell, the value of *Bi* number is low enough to ensure the validity of lumped thermal approximations.[107,109]. For a cell consisting of several layers of these Li-ion 'sandwiches', the length scales for conduction and thus the corresponding resistances are expected to be substantially higher, leading to higher values of *Bi* for a given value of *h*. The limit of applicability of the Tanks-in-Series methodology is tackled in subsequent sections studying the performance of the Thermal Tank Model over a range of *Bi* values.

While the agreement in temperature profiles indicates the validity of the Thermal Tank Model approximation for the heat balance, it is important to examine its ability to predict individual terms therein, the relative contributions of which change according to cell parameters and operating conditions. This is especially true for the various heat generation rates[110], errors in prediction of which can produce erroneous temperature predictions, potentially compromising the ability of BMS and TMS to ensure safe operation in practical scenarios. **Figure 3.10** illustrates the comparisons of reversible and irreversible heat generation rates in the positive electrode. It can be

seen that the Thermal Tank Model matches closely with the average value from the p2D model. The local generation rates at the extremities of the electrode domain

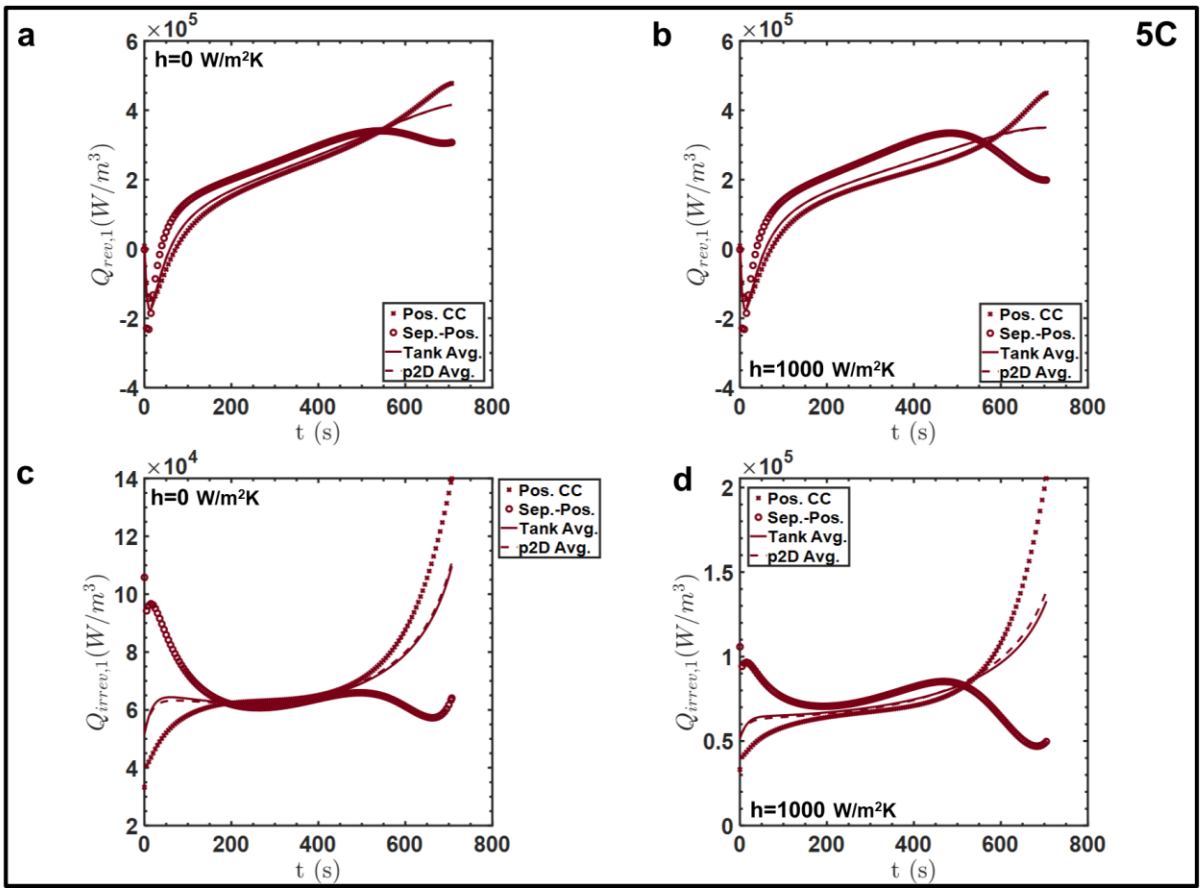

Figure 3.10. Representative heat generation rates in the positive electrode at a typical 5C discharge rate for the two cases. **(a)** and **(b)** compare the reversible component $Q_{rev,1}$, while **(c)** and **(d)** illustrate the irreversible heat $Q_{irrev,1}$ for the adiabatic and fast heat transfer cases respectively.

are also shown to indicate the spatial distribution. It is interesting to note that the reversible heating rate exhibits only slight variation across the electrode thickness (**Figure 3.10 (a)** and **(b)**). Greater spatial non-uniformity (between ~200 – 400 s) is obtained for the fast heat transfer case, consistent with the more non-uniform reaction distribution. Additionally, $Q_{rev,1}$ is initially higher near the separator-interface, but the maximum shifts towards the current collector as the active material

saturates. $Q_{rev,1}$ values are comparable for the two cases, which indicates the effect of local pore-wall flux and the entropic coefficient $\frac{\partial U\left(c_1^{s,surf}\right)}{\partial T}$ (equation (80)). A noteworthy feature is the relatively large negative value of $Q_{rev,1}$ at short times (t~50 s), which has implications for the resulting cell temperature trends, and will be discussed presently.

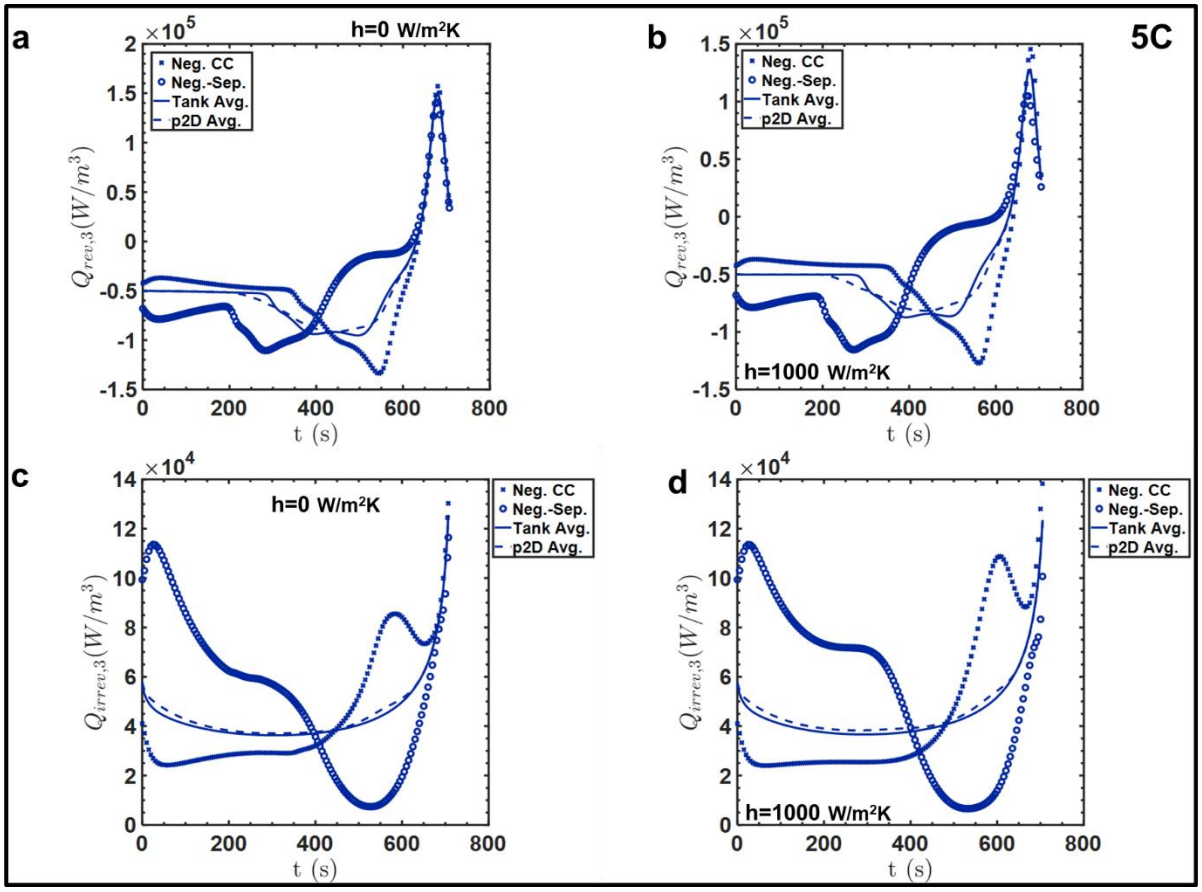

Figure 3.11. Heat generation terms in the negative electrode. **(a)** and **(b)** compare the reversible component $Q_{rev,3}$, while **(c)** and **(d)** illustrate the irreversible heat $Q_{irrev,3}$ for the adiabatic and fast heat transfer cases respectively.

Figure 3.10 (c) and **(d)** compare the variation of the irreversible electrochemical heat $Q_{irrev,1}$. The agreement of the Thermal Tank Model approximation with the averages obtained from the p2D

model is quite noteworthy, with very marginal errors of ~1% observed for the fast heat transfer case towards the end of discharge. This may be related to the accuracy in predicting the average potential quantities, and thus the reaction overpotentials. The spike in $Q_{irrev,1}$ at the collector towards the end of discharge may be explained by equation (79), likely due to the sharp increase in overpotential towards the end of discharge due to local exhaustion of active material, in addition to the large local reaction rate at the collector. **Figure 3.10 (c)** indicates a slightly lower generation than the fast heat transfer case, and this may be due to the lower average polarization during adiabatic operation. This difference is more pronounced towards the end of the discharge process at t ~ 500 s, particularly at the current collector. Greater non-uniformity in $Q_{irrev,1}$ is observed for the fast heat transfer case, in line with expectations. The marginal error observed for the fast heat transfer case may thus be attributed to the limitations of the Tank average expression.

The same set of variables are now plotted for the negative electrode in **Figure 3.11**. Here too, we observe the close agreement of the Thermal Tank average with the p2D model. In the profiles for $Q_{rev,3}$, one notices greater non-uniformities in **Figure 3.11 (b)** compared to the adiabatic case, as expected for less uniform reaction distributions. The assumptions of uniform pore-wall flux by the Thermal Tank Model also result in certain fluctuations in the Thermal Tank average $Q_{rev,3}$ about the p2D average after the initial constant portion at t~300 s. The overall trends are in line with the $\frac{\partial U\left(c_3^{s,surf}\right)}{\partial T}$ profile for the graphite electrode. The higher value of $\overline{T_3}$ for the adiabatic case may explain the marginally higher value of $Q_{rev,3}$ towards the end of discharge. As with the positive electrode, there is a substantial 'endothermic' portion characterized by negative values of $Q_{rev,3}$,

though the magnitude of $Q_{rev,3}$ is substantially lower than the corresponding $Q_{rev,1}$.

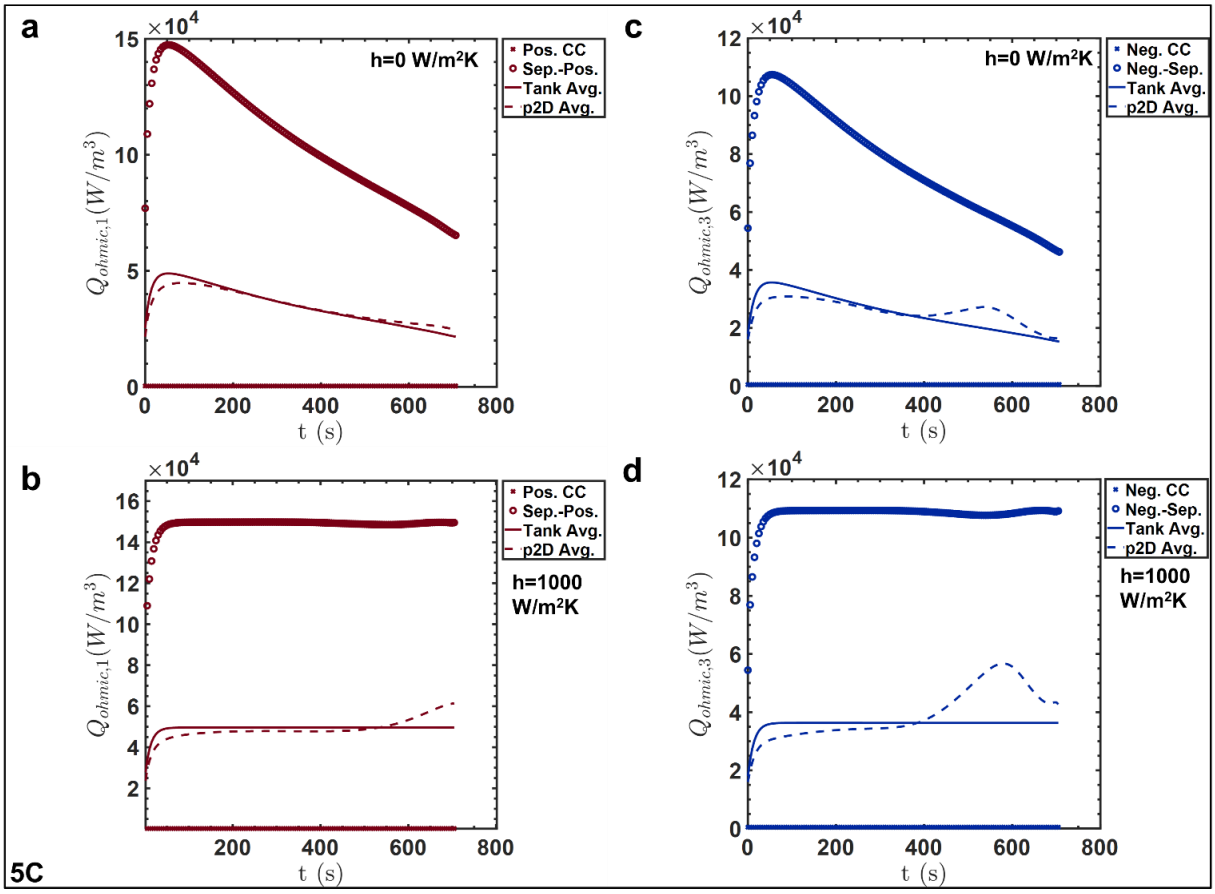

Figure 3.12. Representative contributions to the ohmic heating terms in the electrodes at 5C discharge for positive electrode (**(a) and (b))**, and negative electrode (**(c)** and **(d))** for the two respective cases.

The agreement of the irreversible heating averages in **Figure 3.11 (c)** and **(d)** may be related to the accuracies in predicting the average potential quantities. The spike in the heat generation rate at the end of discharge may be related to the exhaustion of Li in the negative electrode particles, and the corresponding increase in polarization. The reaction rate non-uniformity may explain the

differences in heat generation rates, especially at the collectors at the end of discharge in **Figure 3.11 (d)** . Of note, while both $Q_{rev,3}$ and $Q_{irrev,3}$ initially exhibit significant spatial non-uniformities, beyond t~600 s, the local values rapidly converge to the average value given by $\frac{i_{app}}{Fa_3 l_3}$. This may be explained by the pore-wall flux profiles j_3 in **Figure 9 (b)** of Ref. 41. As the fraction of Li in the graphite particle ($\frac{c_3^{s,surf}}{c_3^{s,\max}}$) reduces during discharge, below a certain degree of lithiation the equilibrium potential exhibits a sharp and monotonic variation coinciding with the presence of a single intercalant phase.[88] This in turn rapidly homogenizes the reaction distribution as argued in past work[41,87,116], which is manifested in the electrochemical heat generation terms.

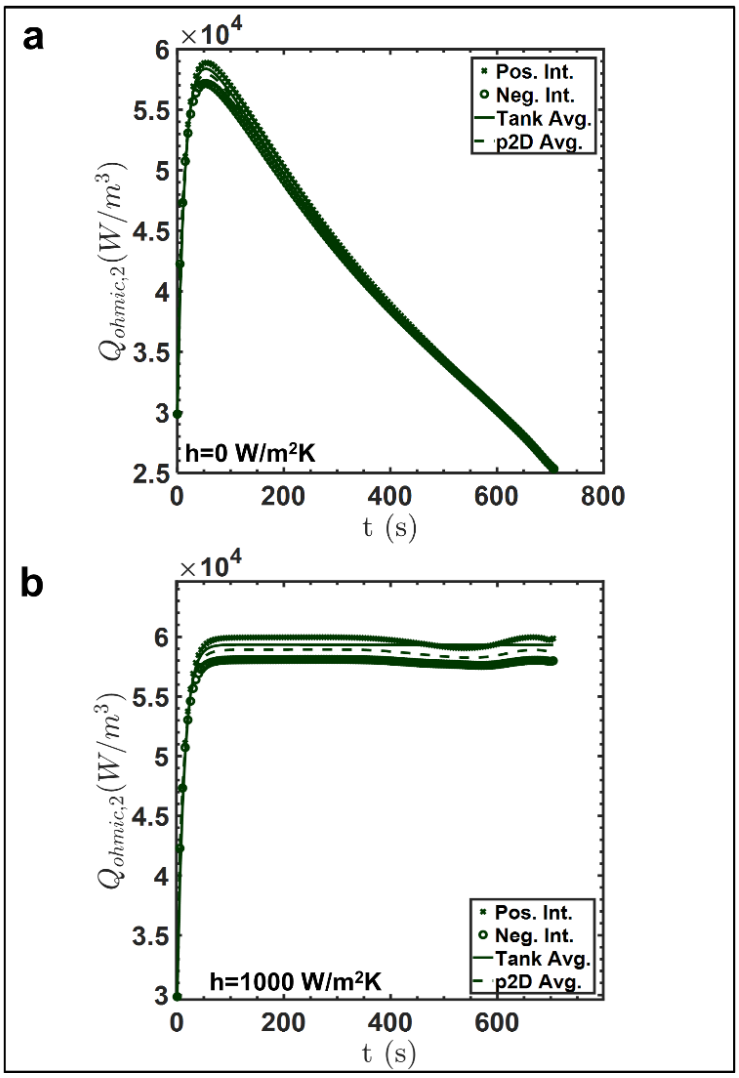

Figure 3.13. Comparison of ohmic heating terms in the separator for a representative 5C discharge and **(a)** adiabatic operation **(b)** fast heat transfer.

The ohmic heat generation terms $Q_{ohmic,i}$ in the electrodes are now depicted in **Figure 3.12**. Notably, the local heat generation at the current collector interface is at least an order of magnitude lower than at the electrode-separator interface. An additional feature is the gradually reducing instantaneous $Q_{ohmic,i}$ with discharge time during adiabatic operation, as observed in **Figure 3.12**

(a) and **(c)**. For both scenarios, the Thermal Tank Model approximations of equations (191) and (192) is able to achieve substantial agreement with the p2D model. As with other volumetric terms, we expect the chief source of qualitative differences to be the non-uniformities in the reaction distribution, which in turn result in oscillations in electrochemical variables, as observed in **Figure 3.8 (b)** and **Figure 3.7 (b)**. For all cases, discernible fluctuations may be observed for the p2D average $\overline{Q_{ohmic,i}}$ at approximately t~400 s in the negative electrode, and towards the end of discharge in the positive electrode (t~700 s). These features closely track similar fluctuations observed in the profiles for both $\overline{c_i}$ and $\overline{\phi_{l,i}}$. Oscillations are observed even for adiabatic operation in the negative electrode, and this may again be attributed to the less uniform pore-wall flux distribution on account of the inherently faster kinetics and flatter equilibrium potential curves vis-à-vis the positive electrode.

The large difference in $Q_{ohmic,i}$ at the separator and current collector interfaces may be explained in terms of equation (184). For most practical batteries, the electronic conductivity of the electrodes is about an order of magnitude higher than the ionic conductivity of the electrolyte. This means that the ionic current contribution to the ohmic heat generation is higher than that due to electronic resistances. At the electrode-separator interfaces, the total current density is carried in the form of ionic current based on the boundary conditions (**Table 3-I** and **Table 3-III**), leading to a maximum in $Q_{ohmic,i}$ given the gradients in $\phi_{l,i}$ required to drive the current. The situation is reversed at the current collector, where the ionic current is zero, and the entire applied current i_{app}

exists in the form of electrons. The reduced electronic resistance vis-à-vis the ionic term means that substantially smaller gradients of $\phi_{s,i}$ are required to sustain the applied current i_{app} at the current collector. Indeed, we neglect this contribution in the Thermal Tank Model approximations of equations (191) - (193).

In **Figure 3.12 (a)** and **(c)** for the adiabatic case, the instantaneous average $\overline{Q_{ohmic,i}}$ first attains a maximum, and then gradually reduces with time. These trends mirror those for the electrolyte phase variables $\overline{c_i}$ and $\overline{\phi_{l,i}}$. In contrast, for the fast heat transfer case, $\overline{Q_{ohmic,i}}$ rapidly reaches a near-constant maximum value at relatively short times. The discussion on the electrolyte phase variables indicates that these trends are expected. For adiabatic operation, the uniform cell temperature, which increases with time, gradually equalizes the reaction distribution and dissipates the spatial gradients of the electrolyte variables. The reducing concentration and potential gradients in turn lead to a reduction in instantaneous $\overline{Q_{ohmic,i}}$. The downward trend during adiabatic operation and the near-constant generation rate for the near-isothermal scenario is also observed for the separator $\overline{Q_{ohmic,2}}$ (**Figure 3.13**). However, the spatial distribution of heats is nearly uniform since the current density is carried as ions throughout the domain. The relatively smaller thickness of the domain also means that it is easier to match ohmic heating rates compared to the electrodes, where the gradients are higher in magnitude. It is also worth noting that, unlike the approximations for the electrodes, equation (193) is an exact relation obtained by a rigorous volume-averaging. Therefore the accuracy of the $\overline{Q_{ohmic,2}}$ by the Thermal Tank Model is directly dependent on the accuracy of the predictions for $\overline{\phi_{l,i}}$. For the parameters considered here, the polarizations in the

electrolyte phase are sufficiently captured by the Tank Model approximations. However, significant spatial gradients arise can introduce substantial mismatches in predictions of electrolyte potential, with attendant implications for the accuracy of predicted heat generation rates, ultimately affecting the accuracy of cell-level voltage and temperature predictions. The accuracy of $\overline{Q_{ohmic,1}}$ and $\overline{Q_{ohmic,3}}$ is limited by errors in not just $\overline{\phi_{l,i}}$, but also mismatches in reaction overpotential due to the uniform pore-wall flux assumption.

To provide an sense of the relative magnitudes of the various heat generation rates, **Figure 3.14** plots the values of $\overline{Q_{rev,i}}$, $\overline{Q_{irrev,i}}$ and $\overline{Q_{ohmic,i}}$ on the same scale. Upon inspection of the figure, it can be seen that the endothermic $\overline{Q_{rev,i}}$ for both electrodes dominate the net heat generation rate at short times till about t ~ 150 s. The magnitude of $\overline{Q_{rev,1}}$, for instance, is ~200,000 W/m^3, about four times the values of other terms. This explains the slight initial fall in cell temperatures for both cases, as noted in **Figure 3.9**. Beyond t~ 200 s, $\overline{Q_{rev,1}}$ far dominates the other sources for the cell parameters and operating conditions considered here. It is worth noting that $\overline{Q_{rev,1}}$ is higher for the adiabatic case than the fast heat transfer case, where the cell is nearly isothermal. The increase in temperature increases the instantaneous generation rate due to its dependence on temperature via equation (80). This also explains the increased generation rate for the negative electrode as well, towards the end of discharge when the $\frac{\partial U\left(c_3^{s,surf}\right)}{\partial T}$ profile for graphite begins to increase. [46,112]

The increase of $\overline{Q_{irrev,i}}$ towards the end of discharge is consistent with the sudden spike in cell

polarization due to the saturation of the solid particles in the positive electrode, and the depletion of Li in the negative electrode particles. The heat generation trends reported herein are consistent with predictions from other workers.[105,109,117]

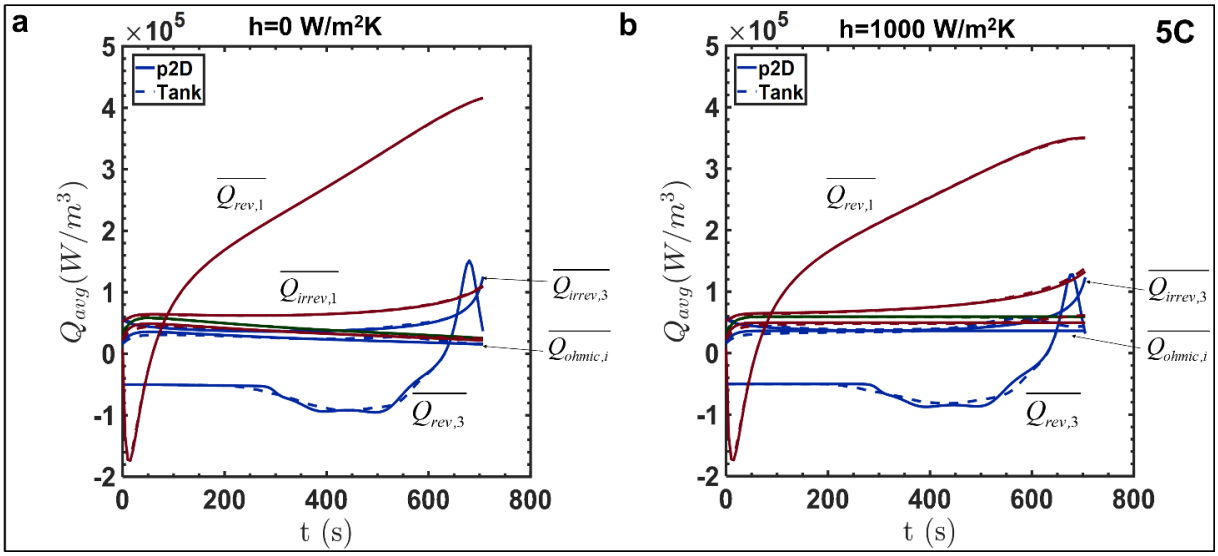

Figure 3.14. Comparison of relative contributions to the various heating terms. The same color convention as in previous plots is used. The plots for **(a)** adiabatic operation and **(b)** fast heat transfer are plotted on the same scale to aid comparison. Given the depiction of the heating terms on the same scale, the ohmic heating terms in three domains are not easily distinguishable, and are generally indicated by $\overline{Q_{ohmic,i}}$.

Figure 3.14 indicates that while the relative contribution of $\overline{Q_{ohmic,i}}$ may be only a fraction of the total generation rate[109], the instantaneous generation rates are comparable over certain portions of discharge. Ohmic heating plays an important role up to t~50 s. This indicates that this contribution may be important during short timescales, especially in scenarios of dynamic variations in applied current, as seen in other works.[105] While the total magnitude of these rates is much lower than electrochemical heats, it could also become significant in high current-density regimes or cells in which significant electrolyte phase limitations can exist, such as ultra-thick electrodes. Having a simplified yet physically meaningful expression for the various contributions is thus more valuable

than the use of empirical expressions given the clear connection to battery electrochemistry, information of which can be incorporated into algorithms of BMS and TMS. A detailed analysis is required to quantify the relative contribution of the different heat generation terms under a range of parameter combinations and operating conditions, while also quantifying the resulting accuracy of the Thermal Tank Model.

3.7.Single Cell Results: Electrolyte Phase Limitations

Representative results for the thick electrode case are shown in **Figure 3.15**. The reduced accuracy of the Tank Model flux approximations for the thick electrodes is evidenced in the concentration profiles of **Figure 3.15 (a)**, with resulting errors in concentration overpotentials leading to increased Root Mean Square Errors (RMSE). For the adiabatic case with $h = 0$, the concentration profiles gradually converge as the temperature increases with discharge. Thus, even for such transport-limited situations, internal heating serves to reduce transport resistances, improving the validity of the approximations. For the fast heat transfer case, the Thermal Tank Model greatly overpredicts the electrolyte depletion in the positive electrode and consequent termination of discharge at t~300 s. This suggests a mismatch in estimating the liquid phase gradients in the thick electrodes, since the average electrolyte transport resistances are substantially higher for this near-isothermal case. Despite this limitation, the RMSE values are <30 mV for adiabatic operation up to an aggressive 150 A/m^2. For $h = 1000\ W/m^2K$, acceptable errors <20 mV are achieved up to 60 A/m^2, which is still a high operating current for the high-energy cell parameters considered herein. This study illustrates the ability of the Thermal Tank Model to match the full model over a wide range of parameters. The error comparisons of **Figure 3.15 (b)** suggests a threshold current density at which

severe electrolyte phase resistances cause a breakdown of the Tank Model approximations, and the resulting mismatch in concentration overpotentials sharply increases voltage errors. This effect is further discussed in subsequent sections. Of note, while the simulated temperatures are higher than the threshold of validity of transport property correlations, identical expressions are used in evaluating both models.

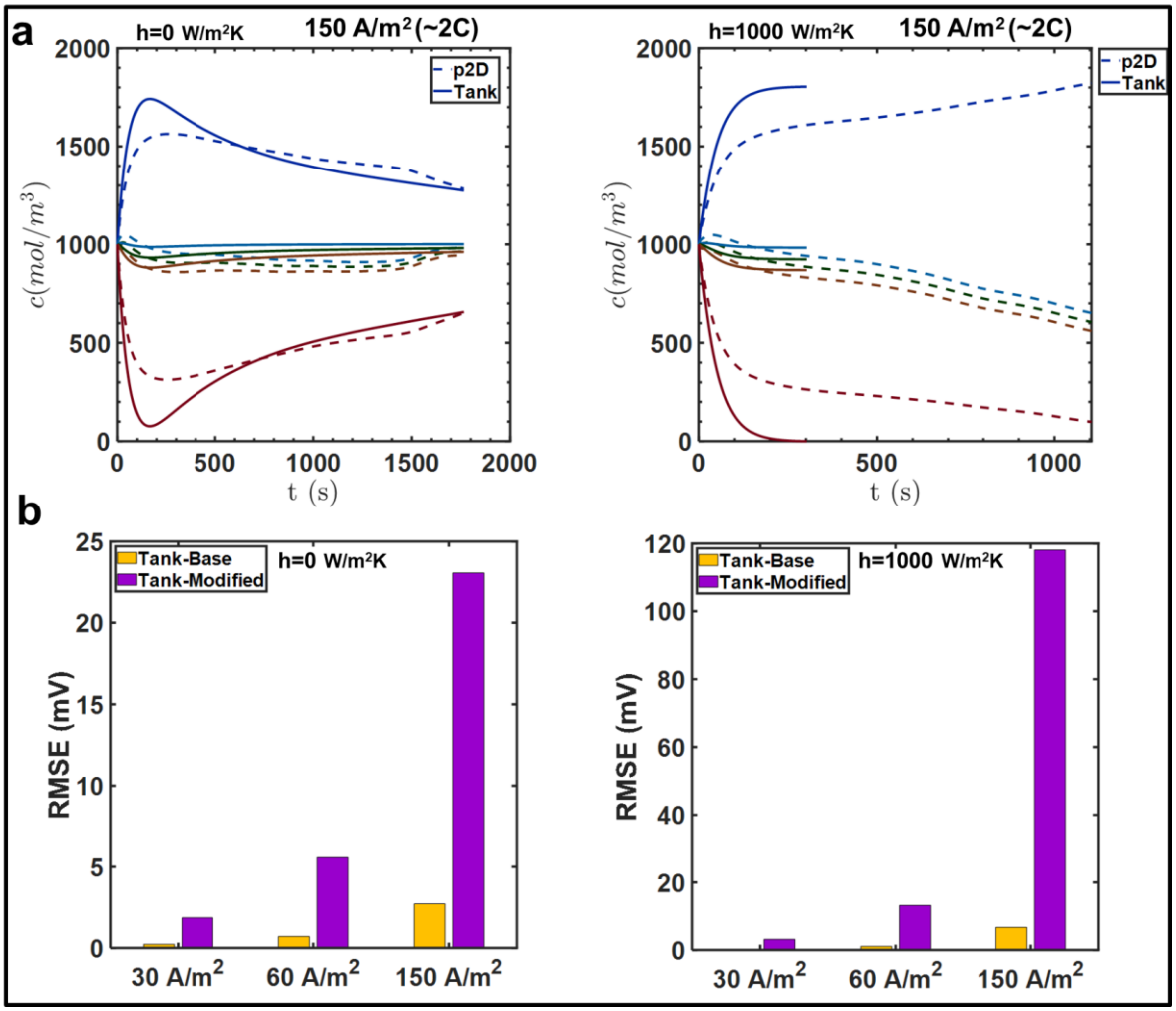

Figure 3.15. (a) Representative concentration profiles and **(b)** Root Mean Square Error (RMSE) comparisons for the electrolyte-limited case in adiabatic and fast heat transfer scenarios, respectively. The thermal p2D model is used as benchmark. For consistent comparison, the models are evaluated at the current densities studied for the base case. This corresponds to C-rates of 1C, 2C and 5C for the base case, and 2C/5, 4C/5 and 2C for the modified high capacity case.

3.8. Results for Multi-cell Stacks

The following subsections thus detail the comparison of the Stack Thermal Tank Model (sTTM) with the Stack p2D model (hereafter termed the sp2D model), with a particular focus on cell voltage, temperature, and current distribution predictions. The focus of this study is to examine the effect of effective thermal resistances and discharge rates on the accuracy of the Thermal Tank Model for a practical case of a multi-cell stack. An important aspect of the study is evaluating the performance of the Thermal Tank Model as the effective length scale for thermal transport increases with the number of cells.

3.8.1. *Representative Discharge Curves*

Figure 3.16 depicts representative discharge curves for a 10-cell stack for two representative values of the Biot number. In this study, the *Bi* numbers are varied through different values of the ambient heat-transfer coefficient h. The agreement of the sTTM for *Bi*=0.01 is remarkable, even up to an 8C discharge rate. In contrast, the sTTM exhibits substantial error beyond 1C for the high Bi case. This indicates the limitation of the Tank Model flux approximations, especially beyond 4C discharge rates. While the sTTM is able to predict the increased polarization at higher rates, the full model predicts a premature termination of discharge relative to the Tank Model. The end-of-discharge discrepancy is likely due to the prediction of a sudden drop in V_{cell}, corresponding to a sharp increase in polarization. While this feature is captured by both models, the much larger DAE system size of the sp2D model leads to a numerical singularity at t~50 s for the 8C curve in **Figure 3.16 (b)** due to increased numerical stiffness relative to the sTTM, which reaches a singularity at marginally longer times (t~80 s for the same case). The premature termination of discharge under

aggressive diffusion-limited operating conditions has been observed in other works.[7,45,118]

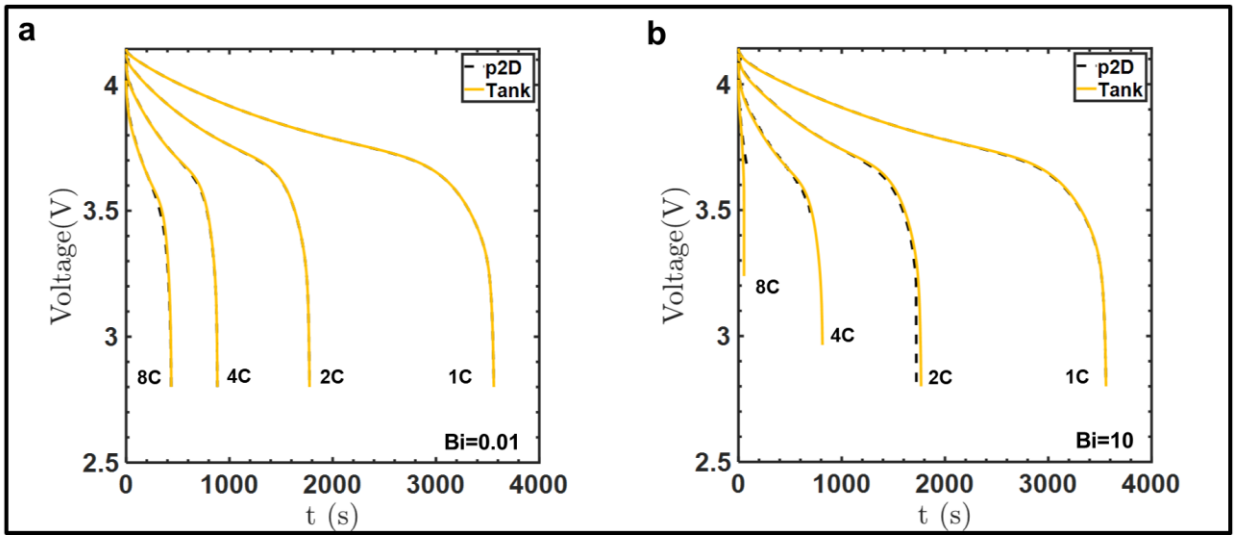

Figure 3.16. Representative discharge curves for 10-cell stack at representative values of low and high Biot numbers, namely **(a)** *Bi*=0.01 **(b)** *Bi* =10.

An examination of the electrochemical and temperature profiles is now conducted in order to determine the chief source of error. In particular, the temperature drop across the cell is likely to be substantially higher for *Bi=10* than *Bi=0.01*. The coupling between temperature and the electrochemical variables will increase errors due to both the thermal and electrochemical approximations. An additional source of error is the three-parameter model used for simplifying solid-phase diffusion, which may introduce numerical errors in solid phase concentrations at high discharge rates and low temperatures, affecting the estimation of reaction overpotentials. However, this error was determined to be negligible for the cases considered in this study.

3.8.2. *Representative Concentration and Temperature Profiles*

Figure 3.17 depicts representative electrolyte concentration profiles as a function of distance at t=300 s. A nearly symmetric profile is observed for the Bi=0 case. In addition, there is close agreement between the sp2D average value and those predicted by the sTTM. Beginning from the leftmost porous domain in **Figure 3.3**, each 'point' may be mapped to the corresponding porous domain (ignoring the collectors, where the equations for c_i are not applicable). Thus the first average point corresponds to the negative electrode $\overline{c_3}$ for the leftmost cell , followed by the separator $\overline{c_2}$, and so on. The near-symmetric concentration profile suggests a near-uniform temperature distribution across the cell stack, consistent with zero heat transfer from the cold end, and thus the stack temperature rapidly attains a uniform 298 K. The concentration drop across each cell is nearly equal, suggesting near-identical polarization in each cell. The error in average concentration is marginally higher in the positive electrode domain relative to the negative electrode and separator domains. The profiles of **Figure 3.17 (b)** represent an interesting contrast, on the other hand. It can be seen that, for high *Bi*=10, the concentration drop across each cell increases in magnitude as we move right from the leftmost cell which is held at a constant temperature. The increasing concentration drop as we approach the 'cold' end, suggests a progressive decrease in cell temperature with x. The consequent decrease in diffusion coefficient leads to the increased concentration gradients required to drive the electrolyte flux. It is also expected that the non-uniform temperature distribution across the stack will lead to non-uniformities in the effective cell resistances, and thus in the current distribution across the individual cells, which will also influence concentration profiles. Additionally, the positive

electrode concentration $\overline{c_1}$ in the leftmost cell is ~500 mol/m^3 but reduces to < 100 mol/m^3 at the rightmost cells. This severe electrolyte depletion in the 'colder' cells is then the reason for the termination of the 4C discharge observed in **Figure 3.16 (b)**. Of particular relevance, the agreement with the sTTM and the sp2D averages is close near $x = 0$, but the errors in $\overline{c_i}$ increase as we move towards the colder end. The mismatch is most pronounced towards the rightmost cells, reaching a maximum of ~200 mol/m^3, which is a substantial 20% of the initial concentration c_0. There are two factors that can potentially contribute to this error – the limitations of the Tank Model flux approximations in capturing the large Δc at low $\overline{T_i}$, and errors in prediction of the $\overline{T_i}$ themselves, which affects the estimates of transport properties such diffusion coefficients $D(\overline{c_i}, \overline{T_i})$.

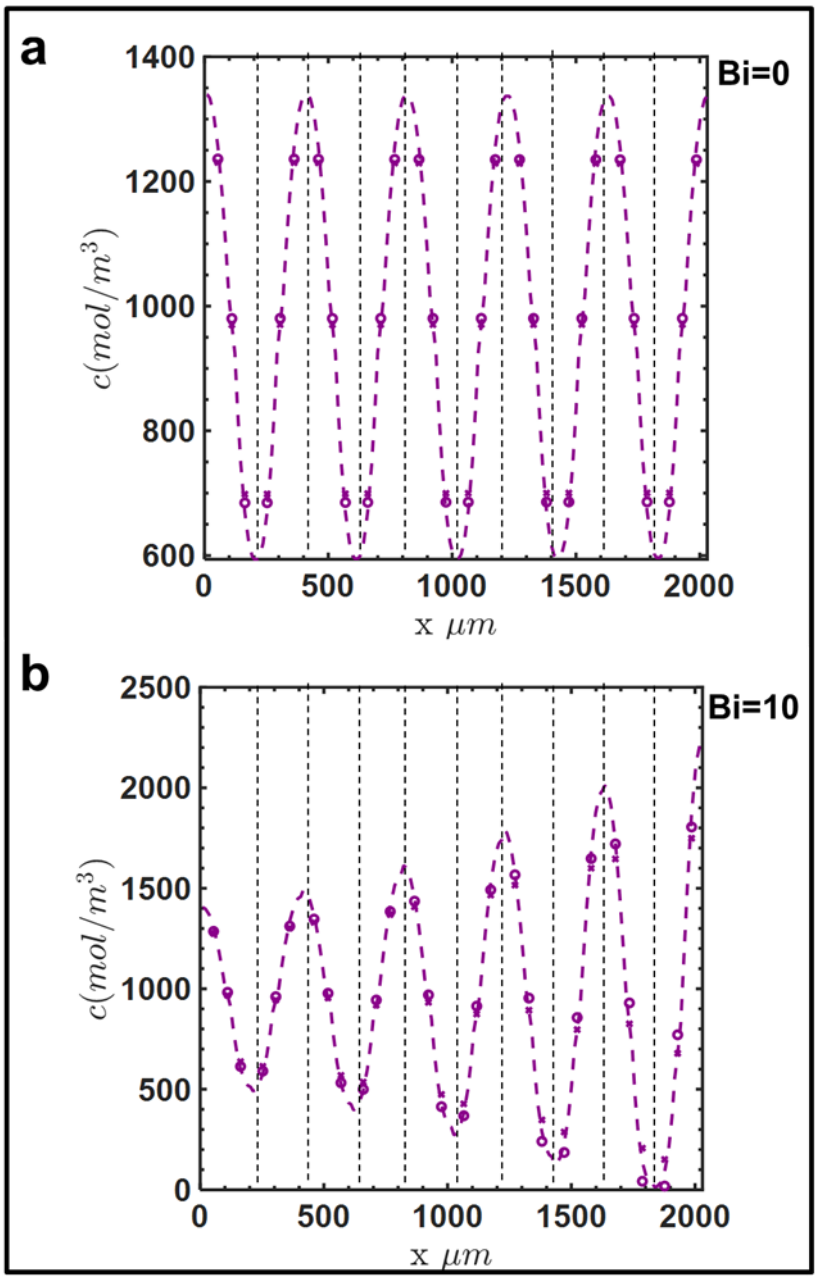

Figure 3.17. Representative spatial profiles of electrolyte concentration for a 10-cell stack and 4C discharge at a typical t=300 s, for two cases of **(a)** Bi=0.01 and **(b)** Bi=10 showing the x-profile from the sp2D model (dashes), the sp2D average (circles), and the Tank Average (crosses). The vertical dotted lines are intended to demarcate the individual cells.

Temperature profiles for the two cases are illustrated in **Figure 3.18**. From **Figure 3.18 (a)**, for *Bi*=0.01, the temperature decreases across the cell-stack, leading to a total $\Delta T \sim 20K$. The sTTM predictions match closely with that of the sp2D model, indicating the accuracy of the Thermal Tank Model approximations for heat flux and generation rates. The difference between the cold end and the ambient temperatures ($T_{amb} = 263K$) corresponds to the value of the convective flux for the given heat transfer coefficient. For the large *Bi*=10, the temperature drop is expectedly higher, as seen in **Figure 3.18 (b)**. The average $\overline{T_i}$ reduces from 298 K at the hot end to nearly 267 K at the cold end, corresponding to a temperature drop of approximately 3 K per cell. The substantial temperature inhomogeneity thus explains the trends in concentration gradients discussed previously. The value of ambient heat transfer coefficient h is 1000-fold higher than the *Bi*=0.01 case, which explains the smaller temperature difference required sustain the convective flux at the right surface. The marginally higher temperature drop across the separator domains is consistent with its significantly higher thermal resistance relative to the more conductive electrode and collector domains. It is also worth noting that even at 4C, for the high *Bi* case the heat dissipation rate by convection from the cold end, combined with the constant temperature boundary condition at the leftmost end, dominates the internal heat generation rates, giving rise to the observed temperature levels.

Even for a high *Bi=10*, where the temperature drop is clearly discernible, the sTTM predictions of $\overline{T_i}$ match closely with the full sp2D model, indicating the suitability of the Thermal Tank Model to capture the temperature variations within a given domain, even for a 4C discharge rate. It must

be noted that these trends may change for different parameter combinations. For example, for the same *Bi* value, the performance of the sTTM may deteriorate for a cell-stack in which the individual cells have much thicker electrodes. However, this is more likely to be to the inherently higher cell polarizations that the Tank Model is unable to account for, as discussed previously. For an expected 'baseline error' based on the parameters of the single cell, it is possible to determine the upper limit of *Bi* based on acceptable error metrics of stack-level V_{cell} and temperature predictions, which can help define performance limits of BMS and TMS.

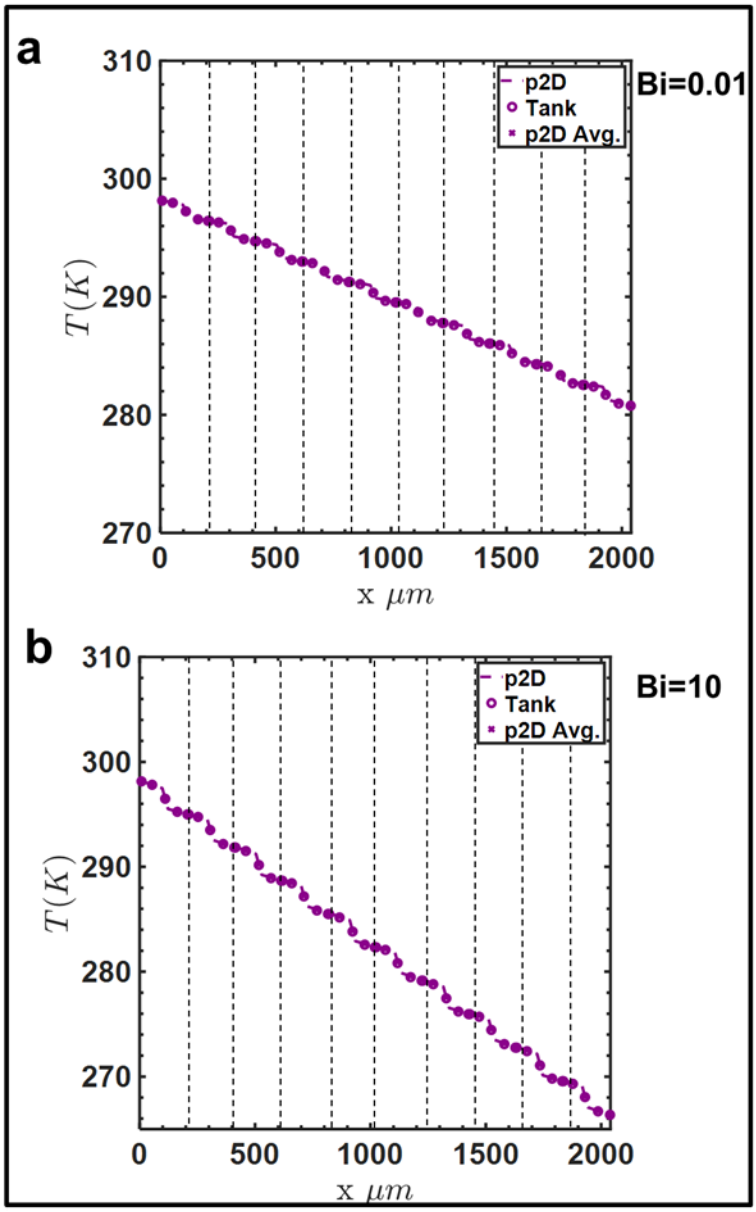

Figure 3.18. Spatial profiles of Temperature for a 10-cell stack and 4C discharge at a typical t=300 s, for two cases of **(a)** Bi=0.01 and **(b)** *Bi*=10. The averages across each porous domain are plotted at the corresponding midpoint for convenience. As with the concentration profiles, vertical dotted lines are used to denote the boundaries between adjacent cells. Unlike $\overline{c_i}$, $\overline{T_i}$ is modeled in the collector domains as well, and is indicated accordingly.

The temperature profiles in **Figure 3.18 (b)** suggest that the errors in the electrochemical variables,

which contribute to the errors in V_{cell} through the estimates of various polarization contributions, do not significantly affect the predictions of the heat generation rates and fluxes. These trends are further emphasized through the error profiles in **Figure 3.19**, which compares errors in $\overline{c_i}$ and $\overline{T_i}$ for the two cases. For both the *Bi*=0.01 and *Bi*=10 cases, the maximum error in $\overline{T_i}$ does not exceed 0.12 K. It is also noteworthy that the maximum error in $\overline{T_i}$ is marginally higher for lower *Bi* than the less homogenous *Bi*=10 case. In addition, the error in $\overline{T_i}$ is highest towards the center of the cell stack ($x \sim 1300 \mu m$) for the *Bi*=10 case, as opposed to **Figure 3.19 (a)**, where the error maximum is attained at the right extreme. The profiles in **Figure 3.19 (b)** for *Bi*=0.01 indicate $\overline{c_i}$ errors in the 5 – 25 mol/m^3 range, with expectedly lower errors in the separator domains. The error levels in the respective domains are nearly constant across the stack in the x - direction. This is consistent with typical temperature levels and variations across the stack. The minimum temperature in the stack is ~281 K, which appears to be high enough for the Tank Model approximations to capture the liquid phase and kinetic polarizations. In **Figure 3.17 (b)**, we can observe the increasing concentration gradient as temperatures decrease along the x direction. For the fast external heat transfer case of *Bi*=10, the performance of the overall stack is essentially limited by the increased polarization in the low temperature cells due to electrolyte depletion. The difference between the tank and sp2D model averages is also clear, sometimes as high as two-fold, as seen in the error plots of **Figure 3.19**. The errors in $\overline{c_i}$ in the respective domains can be seen to increase away from the 'hot' end. The Tank Model, by its very nature reduces in accuracy as the liquid phase non-uniformities increase in magnitude, as is the case at lower temperatures characterized by slower kinetics and transport. The study of these profiles thus indicates that, for

the given set of cell parameters, the error in V_{cell} due to non-uniform temperature profile is not due to errors in predictions of $\overline{T_i}$ by the sTTM. It is primarly due to the interplay between temperature and other electrochemical variables. Inhomogeneous temperature distributions and low temperatures produce kinetic polarizations and liquid phase gradients that are not adequately captured by the Tank Model approximations, even though the temperatures themselves are well-approximated.

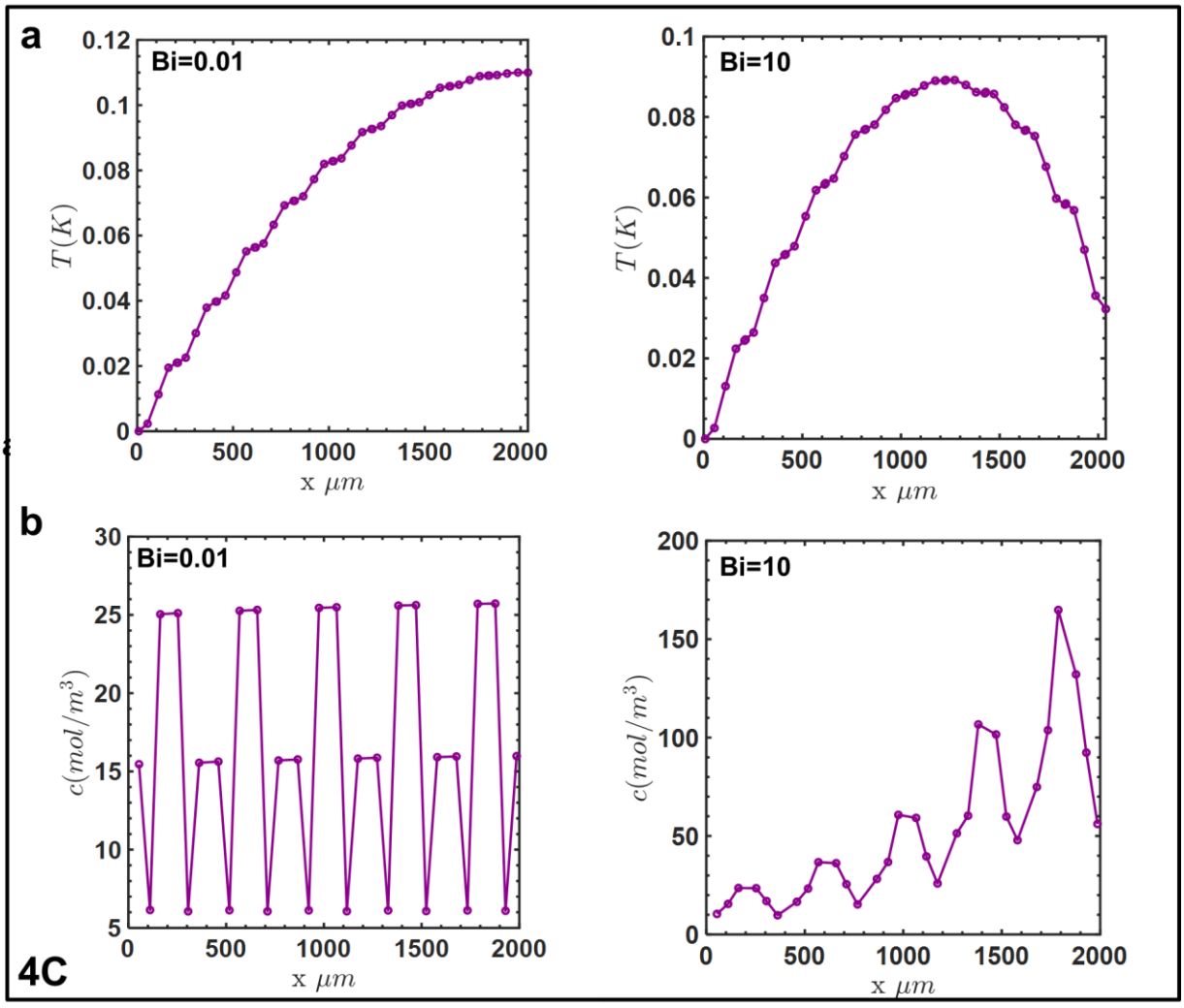

Figure 3.19. Comparison errors in **(a)** average temperature and **(b)** average concentration across a 10-cell stack for a 4C discharge for the two extreme cases of *Bi*. The averages across each porous domain are

plotted at the corresponding midpoint for convenience.

The temperature-dependent limitations may be circumvented by refining the Tank Model approximations via a temperature-dependent diffusion length, i.e. $\delta_{i,ij}$ may be replaced by $\delta_{i,ij}(T_{ij})$. This is reasonable since the characteristic boundary layers are a function of the temperature-dependent transport properties. The sTTM can be parameterized using experimental data to determine these adjustable values. During real-time operation, a BMS may be able to vary these diffusion lengths for each individual cell based on predictions or measurements of instantaneous temperatures, refining the flux approximations on the fly, thus improving predictions of V_{cell}.

3.8.3. *Effect of Bi*

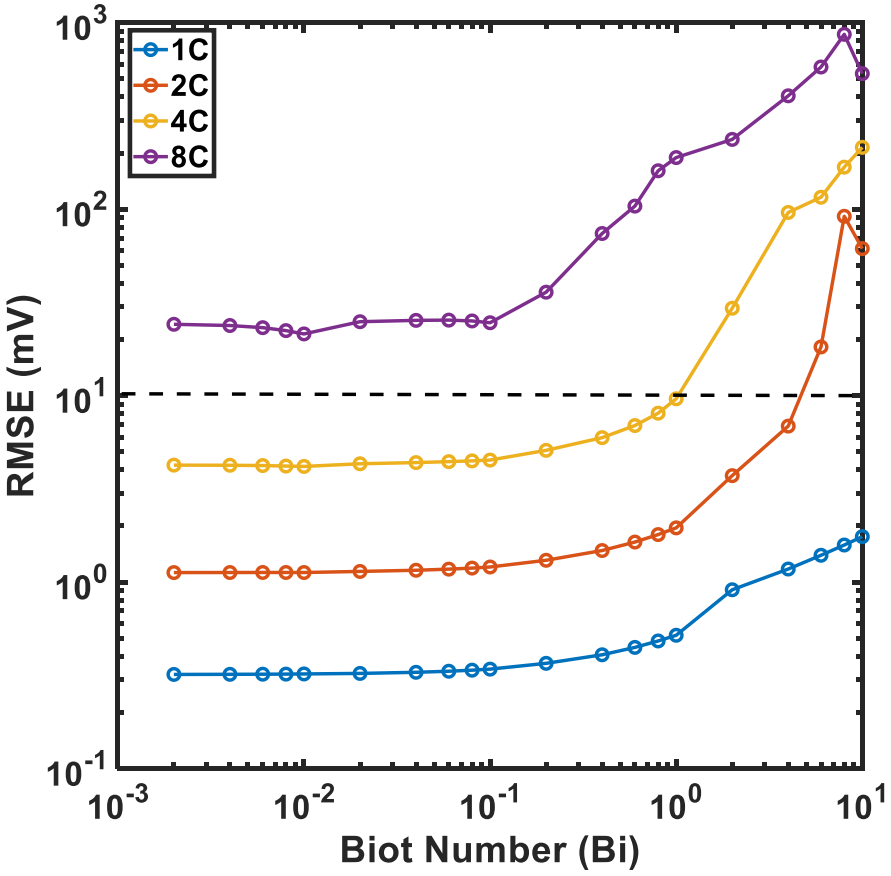

Figure 3.20 . Comparison of Root Mean Square Error (RMSE) as a function of Biot Number at different discharge rate. For simulations which terminated prematurely, the discharge curves were extrapolated to the cutoff voltage (2.8 V) to simplify error calculation.

Given the dependence of the accuracy of the sTTM on the effective Biot number and operating conditions, it is worthwhile to determine approximate performance limits for the sTTM as a means of providing guidance for model selection. This can be done by comparing error metrics with respect to the sp2D model for simulations over a range of relevant parameter combinations. For example, we can vary the operating current density in conjunction with parameters pertaining to

the external heat transfer conditions, such as h, T_{amb} and the terminal temperature boundary conditions (**Figure 3.3**). We can also test the accuracy of the sTTM for V_{cell} as a function of N_{cell}. To illustrate such a 'performance chart', we vary the N_{cell}, the effective current density $i_{app,stack}$, and the ambient heat transfer coefficient h. Errors from these simulation runs can then be plotted as a function of the calculated values of *Bi* and C-rate for each case. The results from one such study are illustrated in **Figure 3.20**, which shows the Root Mean Square Error (RMSE) for the sTTM against the benchmark stack sp2D model. Inspection of **Figure 3.20** reveals an interesting trend of RMSE as a function of *Bi*. For a given C-rate, the RMSE remains almost constant for a large range of *Bi*. However, beyond a certain threshold value, there is a sharp increase of nearly an order of magnitude, which indicates the increasing effect due to the polarization in the 'weaker' cells, which are at lower temperature. Temperature gradients in turn result in non-uniform current density distributions across individual cells. The temperature variation also affects the accuracy of the other electrochemical variables due to higher overall polarization and the non-linear dependence of temperature on transport and kinetic properties, which is only partially captured by the approximations of the Tank Model. Expectedly, this threshold *Bi* reduces by approximately an order of magnitude with increasing discharge rate, from *Bi~1* for 4C to *Bi~0.1* at 8C. The horizontal dotted line indicates the 10 mV threshold, which is typically the acceptable error in onboard estimation, optimization and control applications. It can be seen that the RMSE for the sTTM is below this value up to 4C and *Bi ~0.7*. This indicates a wide range of applicability of the Tank Model, even for the asymmetric temperature boundary conditions considered herein. The region of applicability can be further extended if we relax the acceptable error, for instance a threshold of 20 mV will would also envelope certain *Bi* values at 8C. We would also expect the

specific values of errors and error thresholds to change with the temperature boundary conditions and cell parameters, although the qualitative trend is expected to be identical. Varying the cell parameters will alter the 'baseline error' due to the electrochemical variables at a given C-rate, an estimate of which can be obtained by extrapolating the curves in **Figure 3.20** towards $Bi \to 0$. This value may also be obtained by simulating the insulated cold end case where $h = 0$, as was shown in previous sections. For the range of *Bi* considered in this study (10^{-4} – 10), we do not observe the sharp increase in RMSE for the 1C case due to the cell parameters considered herein. However, the RMSE for an aggressive *Bi=1000* case was found to be ~800 mV, pointing to a threshold at an intermediate value of *Bi*. An important caveat in interpreting this result is that the numerical convergence for the sp2D models may be compromised beyond *Bi>10*, but the qualitative trend still holds. In addition, the three-parameter model for the solid phase may also require reexamination at lower temperatures, as discussed previously, and efficient higher-order methods from our group may be explored for this and other aggressive cases.[55] It must be noted that at a given C-rate, the nominal current density per individual cell in the stack, i.e. $i_{app,avg} = \frac{i_{app,stack}}{N_{cell}}$ is independent of N_{cell}. This justifies the direct comparison of the RMSE values for cell stacks of different N_{cell}.

3.9. Predicting cell-level quantities

We can now use the results of the stack simulations to illustrate the ability of the Tanks-in-Series approach to predict current distributions and the SoCs of individual cells. Importantly, we compare the sTTM against the full sp2D models by examining the time-dependent profiles for the individual

layers in the stack.

3.9.1. *Current Distribution*

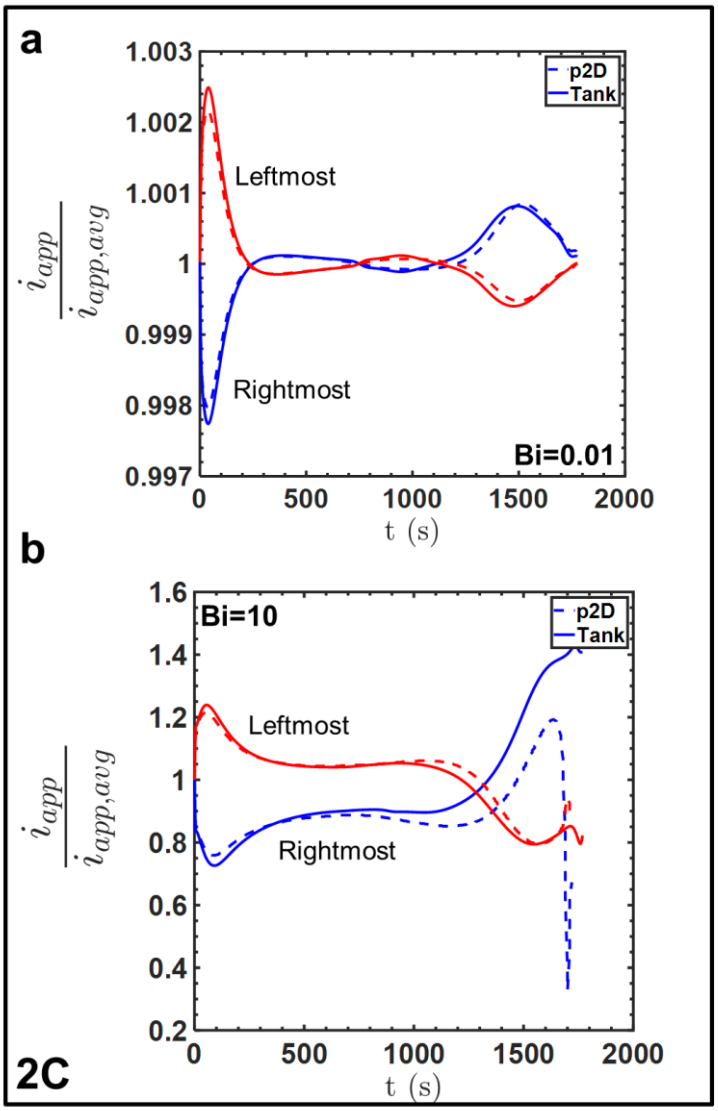

Figure 3.21. Representative current density split through the extremum cells in a 10-cell stack for a 2C discharge, for two cases of **(a)** *Bi*=0.01 and **(b)** *Bi*=10.

Figure 3.21 represents current density profiles through the two end cells at 2C. The current density split is illustrated by plotting the ratio of the actual current density to the nominal value, $\beta_k = \frac{i_{app,k}}{i_{app,avg}}$ for cell k . Given the boundary conditions used in the previous study, the end cells also represent temperature extrema, and thus may reasonably be expected to have different effective dynamic resistances. Useful insight into the current distribution may thus be obtained by examining the currents and SoCs in these cells. **Figure 3.21 (a)** depicts these profiles for *Bi=0.01*. The β profiles for the two cells are nearly symmetric about the y-axis. Additionally, the variations in instantaneous current density are negligible, with the maximum deviation about the average only ~0.002. The overall current distribution is thus rather uniform. The increase in the current density for the hot cell at short times is consistent with its higher temperature (298 K). In contrast, the effective resistance of the 'colder' cell increases as its temperature reduces to its pseudo steady-state value. Thereafter, β vary based on the instantaneous cell resistances. The symmetric β profiles indicate nearly equal cell utilization over the entire discharge process (which can also be seen by examining the area under the respective curves, a measure of the total charge drawn). The close agreement of the sTTM in predicting these trends is expected given the relatively uniform temperature profiles and suggests its ability in accurately predicting the current distributions in large multi-cell configurations. The observed β profiles are in qualitative agreement with experimental data from similar studies on parallel configurations of cylindrical cells.[113]

For the *Bi=10* case, **Figure 3.21 (b**) indicates substantial non-uniformity in the current density distribution, suggesting a significant effect due to the nearly 30 K temperature difference. As with the previous case, the sharp temperature drop in the cold cell (298K at t=0 to 267K) increases its

instantaneous resistance, reducing the amount of current drawn (it must be remembered that the cells are connected in parallel, and thus experience the same V_{cell}). In contrast, β for the 'hot' cell sharply increases to over 20% of the average value. This indicates an overloading of the higher temperature cells because of their lower resistance, especially during the initial portions of the discharge. The 'cold' cell remains underutilized until t~1200 s due to its higher overall resistance arising out of slower kinetics and transport processes. Around t~1200 s, the decrease in β for the 'hot' cell is accompanied by a concomitant increase for the colder cell. The decrease is likely due to the increased kinetic overpotential in the electrodes associated with the saturation and depletion of active material in the overloaded cell. This increases the cell resistance above that of the colder cells, causing the currents to now be drawn predominantly from the latter. This 'overloading' of the colder cells, in order to maintain the total current density $i_{app,stack}$, substantially increases the polarization. From the previous section, this is chiefly concentration polarization due to diffusion limitations. Slow electrolyte diffusion leads to electrolyte depletion, which explains the sudden drop in V_{cell} due to the consequent spike in concentration overpotential. In **Figure 3.21 (b)**, this is reflected in the sudden decrease in β as the rightmost cell is no longer able to sustain the same level of current.

Around t~800 s, the predicted value of β predicted by the sTTM prediction also starts to diverge from the benchmark sp2D model. This is consistent with the errors observed in $\overline{c_1}$, due to the inability of the Tank Model to capture the increasing concentration gradients as the current density drawn from the cold cell starts to increase. As observed previously, the sTTM substantially overpredicts the electrolyte concentration in the positive electrode, thereby underestimating the

concentration overpotential, and thus the effective cell resistance. This causes the mismatch to increase as the discharge progresses, since the sTTM predicts that the cell can now sustain even higher currents, and the sTTM predicts an increase over the average value of over 40% at the end of discharge. Such errors may become even more significant for higher current densities, dynamic load currents as in drive cycles, and high-current pulsed operation, during which large transients and instantaneous spatial non-uniformities may be neglected by volume-averaged representations. This indicates the limitation of the Tank Model approximations and the need for their refinement for such cases. For instance, in a multi-cell stack or a large battery pack in which each individual cell is represented by the Thermal Tank Model, the objective function in a parameter estimation strategy may also incorporate error metrics between predicted and measured currents in each cell. The adjustable parameters may then be determined to minimize the errors observed in **Figure 3.21 (b)**, in addition to errors in V_{cell} .

3.9.2. *State of Charge (SoC) Prediction*

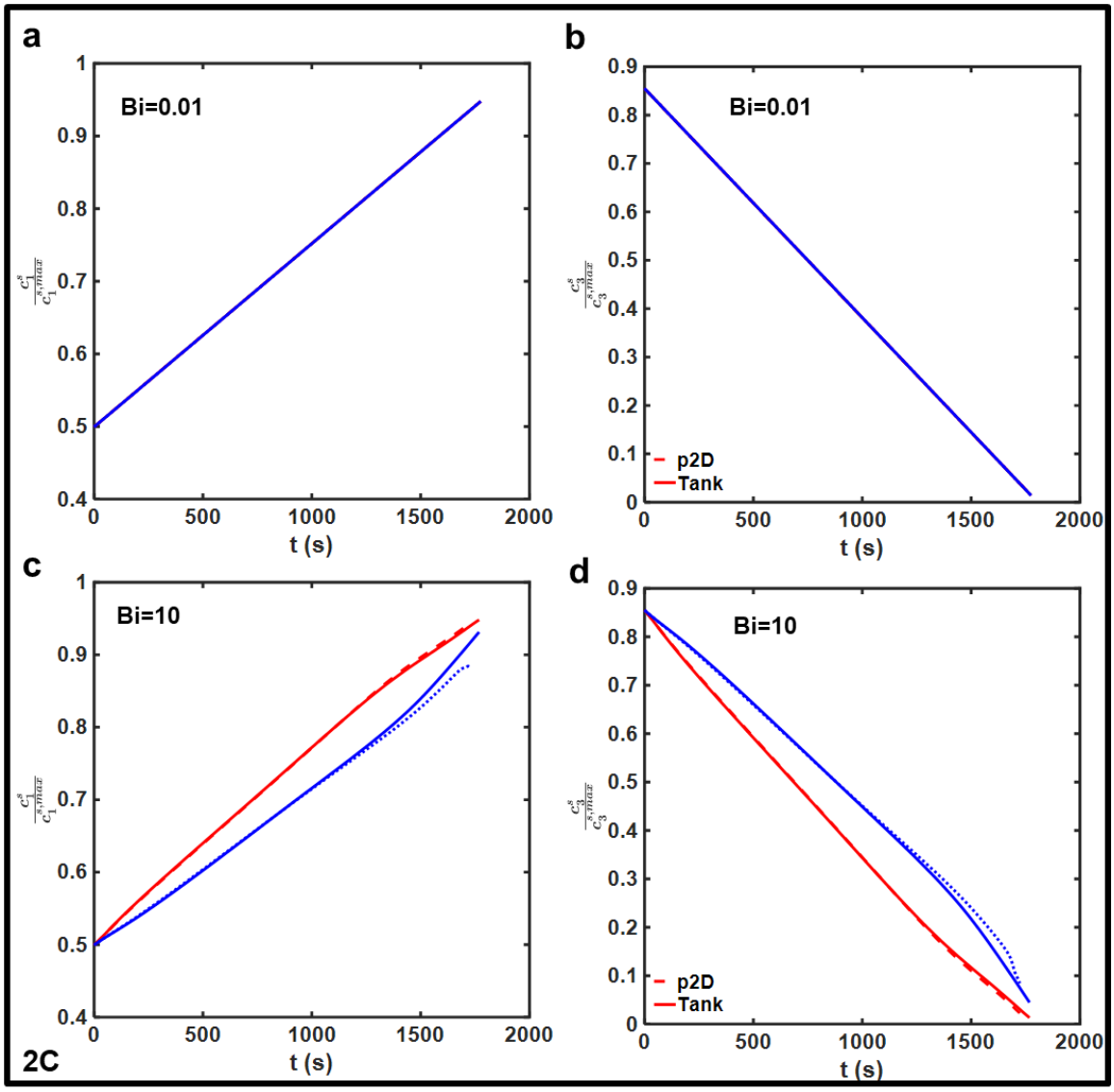

Figure 3.22. Electrode stoichiometry profiles at a typical 2C discharge rate for the 'hot' (red) and 'cold' (blue) cells for *Bi*=0.01 ((**a)** and **(b)**) and *Bi*=10 (**(c)** and **(d)**) respectively.

The mismatch in current density distribution is expected to result in errors in the predictions of the State of Charge (SoC) of individual cells. This can be observed in **Figure 3.22 (c)** and **(d)**, which

compares the cell-averaged degree of lithiation (i.e., $\overline{\theta}_i = \frac{\overline{c_i^s}}{c_i^{s,\max}}$). These quantities are directly proportional to the effective SoC of the cell.[16,104,119] For the *Bi=10*, the Tank Model deviates by approximately 10% for the 'cold' cell. Errors in cell SoC will accumulate over the discharge process, given the substantial variations in instantaneous β, the integral of which determines SoC. This is despite its ability to predict the broad qualitative trends, including the change in slope of the SoC curves for both the over and under-utilized cells at t~1200 s. A more uniform current distribution means that these deviations are not observed at the more practical *Bi*=0.01 case, which thus indicates the ability of the sTTM to accurately predict current and SoC distributions for cell stacks over a wide range of operating conditions. This indicates substantial potential for use in predicting the effect of non-uniform utilization and degradation, and in integration into a BMS compared to the full sp2D model. While the sTTM is unable to predict the granular details that affect performance under aggressive conditions, these results suggest substantial utility in predicting SoC for cell-balancing and other BMS objectives. As with the dynamic currents in individual cells, the instantaneous SoC errors may also be incorporated into the objective function in parameter estimation applications. In addition, cell-level $\overline{\theta}_i$ can be directly obtained from the DAE system of the sTTM, due to the three-parameter models for solid phase transport, which directly solve for $\overline{\theta}_i$ that can then be incorporated into control problem formulations.[41,49] In contrast, the SoC of the individual cells (or $\overline{\theta}_i$) have to be computed from the sp2D model by way of volume-integrals and averaging, which will add to the computational cost. The sTTM is thus competitive with reformulated sp2D models in terms of both accuracy and computational efficiency, quantitative measures of which are presented in the next section.

At this point, it is also worthwhile to reexamine the original 2C discharge curves of **Figure 3.16 (b)**. It can be seen that the predictions of cell voltage exhibit close agreement, with only a slight mismatch in the final discharge time. **Figure 3.20** suggests that the RMSE for the sTTM relative to the sp2D model is about ~20 mV. However, as this discussion shows, the agreement in voltage masks significant underlying variations in the individual cells, which are a result of the complex interplay of electrochemical and thermal phenomena. This indicates the value of a physics-based model to compute emergent cell-level properties, since the subtle electrochemical variations that give rise to complex trends in cell-level quantities can be adequately captured. These variations have clear implications for BMS and TMS, in terms of cell-balancing, monitoring individual cell SoH, preventing non-uniform degradation, and preventing overtemperature.[10,21,113] The sTTM approach also provides a simpler means relative to the sp2D model to include detailed models for capacity degradation and integrating the resulting insights into stack-level operation.[113] The level of electrochemical detail retained by the model also makes its parameterization materially superior to equivalent circuit models[11] for studying current imbalances in parallel configurations of cells. While the sTTM is illustrated for a case of a multi-layer pouch cell, the same formulation can also be applied to battery packs consisting of multiple cells. The model can be extended to account for interfacial and inter-cell resistances (both electrical and thermal), and the modification of the Thermal Tank Model approximations to include interfacial resistances is included in the Appendix A (**Section 6.2**).

3.10. Computational Performance

Table 3-VIII. Representative computational performance metrics for the Thermal Tank Model.

Model and Implementation	Number of DAEs	Computation time for Bi=10(ms)*
p2D - Reformulated (10-cell stack sp2D) n=(2,7,3,7,2)	1800-2000	12383±312.6
Stack Thermal Tank Model (10-cell stack)**	251**	22±0.6

* Average of N=3 simulation runs for a 1C discharge. It must be noted that the simulation time and memory consumption is a strong function of the computing environment as well as error tolerances for both initialization and simulation.

**Including the equation for cell voltage

Representative computation times for the two models are shown in **Table 3-VIII**. For a 10-cell stack, the reformulated sp2D model computes a 1C discharge curve is ~12 s. The sTTM is able to compute the same in ~20 ms, corresponding to a reduction of nearly 500*x*. Of note, preliminary results suggest computation times of ~700 ms even for a large 50-cell stack. Beyond 1C, the accuracy of the sTTM is substantially compromised for the aggressive *Bi=10* cases as discussed previously. In addition, it is important to note that the computation time of the benchmark

reformulated sp2D model is affected by the choice of the model used for solid phase transport. In this work, we used an error-free collocation approach to model the solid phase transport. Using computationally simple two and three-parameter models will cause a significant reduction in the computation time of the benchmark models.[46,49,54,55,78] However, the competitiveness of the sTTM is evident, caused by the replacement of each conservation law in the sp2D model by its volume-averaged counterpart. Based on the results obtained in the previous chapter[41], we expect a standard Finite-Difference implementation for the p2D stack model to result in ~10000 DAEs, and in computation times of ~10 min, indicating the superiority of both the state-of-the-art sp2D models and the sTTM.

In this work the Tank Models were obtained by the reduction of the p2D model in one spatial dimension (x). The use of a one-dimensional model instead of a 2-D model in the $x-y$ plane is justified by the aspect ratios of most practical cells. The height (vertical y dimension in **Figure 3.3**) is usually about three orders of magnitude higher than the thickness of the assembly, which justifies the consideration of heat transfer through the thickness dimension alone.[105,109,120,121] However, having discussed the importance of variations in the $y-z$ plane for large format cells, such models must be used as electrode-scale submodel in an MSMD approach, for which the ~ms computation times of the sTTM suggests substantial potential. It is worth noting that despite the computation time metrics achieved, the sTTM does not require additional simplifying assumptions on heat generation rates or temperature profiles.[100,101,108] This means that the exact configuration of the cell along the thickness dimension may be directly and efficiently simulated, without assuming uniform intra-cell temperatures or electrochemically identical layers as is often done for multiple electrode pairs.[96,100,108]

3.11. Summary

A simplified electrochemical-thermal model for lithium-ion batteries is generated using the Tanks-in-Series methodology. The flux approximations and volume-averaged representations notwithstanding, the Thermal Tank Model is able to achieve errors below 10 mV relative to the p2D model for galvanostatic discharge rates of up to 5C. Internal electrochemical variables and temperature predictions are accurate within 1% error. The ease of implementation of the methodology is demonstrated by extending the single cell formulation to a multi-cell stack and simulated for a large parameter space corresponding to various conditions of discharge and external heat transfer. This Stack Thermal Tank Model also results in prediction errors of <10 mV up to 4C discharge rates and $Bi \sim 0.7$. Even for aggressive conditions where $Bi > 1$, the predictions of temperature profiles across the stack agree within 1 K, with the chief source of errors in cell voltage being mismatches in electrolyte phase variables for $T < 280\ K$. Predictions of emergent cell-level quantities such as current density splits and SoC are in close agreement (<1% error) for practical operating conditions, and are in qualitative agreement for more extreme cases. As with the isothermal model, the performance of the thermal models at single-cell and stack levels can be improved by parameter estimation techniques. The computational speed up over two orders of magnitude indicates the potential for real-time applications. The models can serve as replacement for SPM-like and empirical models for advanced BMS. The access to electrochemical quantities means that the models can also be used in the study of fast-charging effects on cell degradation and temperature, and incorporated into optimal-charging problems. Additionally, the models can be used to simulate performance under cycling and investigate the effects of inhomogeneities in multi-cell stacks and large battery packs. The ~ms computation time of the multi-cell models

suggests promise for use in algorithms for advanced BMS functions such as SoC estimation, cell balancing, temperature control, and SoH monitoring in conjunction with physics-based degradation models.

3.12. List of Symbols

3.12.1. *Dependent Variables*

c Electrolyte Concentration

c^s Solid Phase Concentration

ϕ_l Liquid Phase Potential

ϕ_s Solid Phase Potential

T Temperature

3.12.2. *Other Symbols*

V_{cell} Cell Voltage

j Pore-wall flux

N Electrolyte molar flux

q Heat flux

Q_{rev} Reversible volumetric heat generation rate

Q_{irrev} Irreversible volumetric heat generation rate due to interfacial polarization

Q_{ohmic} Volumetric heat generation rate due to ohmic drop

β Ratio of the instantaneous current density to the nominal average for a given cell in a multi-cell system

h Ambient heat transfer coefficient

3.12.3. *Other Superscripts*

surf Pertaining to the surface of the particle in the solid phase

$\bar{}$ Pertaining to the average over the volume of a porous domain

s, avg Pertaining to the average over the volume of the solid particle

3.12.4. *Other Subscripts*

i Pertaining to region *i* where $i \in \{0,1,2,3,4\}$

ij Pertaining to the interface between regions *i* and *j*, where $i, j \in \{0,1,2,3,4\}$

i,ij Pertaining to the interface between regions *i* and *j* on the side of region *i* where $i, j \in \{0,1,2,3,4\}$

i,k Pertaining to the region *i* of the k^{th} cell in an N-cell stack, where $i \in \{0,1,2,3,4\}$ and $1 \leq k \leq N_{cell}$

4. Analysis and Robust Simulation of Lithium Symmetric Cells

4.1. Lithium Symmetric Cells

.Symmetric cells represent a convenient model system for the study of Lithium metal electrodes. Instead of studying the lithium anode in a full cell configuration, they consist of identical materials for both electrodes (**Figure 4.1**).[122] This enables the study of lithium anode operation and electrodeposition dynamics sans compound interactions with other cell components. Symmetric cells are also useful for the evaluation of new electrolytes, additives, and separator materials. They can also be used in experiments for property measurements and electrochemical model validation.[123,124]

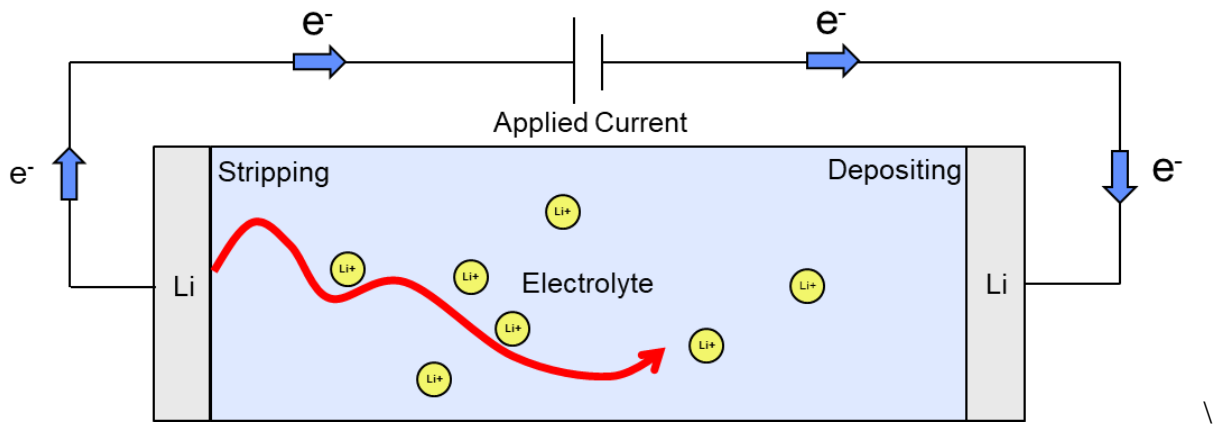

Figure 4.1. Schematic of a lithium symmetric cell. The open circuit potential of the system is zero. When a potential difference is applied, lithium ions are stripped from one electrode and are reduced to metallic lithium at the other 'deposition' electrode. The transport model considers the transport of a binary electrolyte, such as LiPF6 by diffusion and migration.

4.2. Review of Models and Solution Methods

The choice of the computational scheme used for charged transport models can greatly limit the

utility of physics-based models in extended cycling simulations for aging studies or parameter estimation. Efficient and elegant solutions of the bulk ion transport equations greatly simplify the coupling of kinetic models to ultimately predict cell-level voltage response. This entails the careful consideration of the computational aspects of these models in order to determine the optimal simulation method.

Two common transport models for charged species transport, based on the Nernst-Planck flux laws, are Poisson and Nernst-Planck (PNP) equations and the Electroneutrality and Nernst-Planck (EN-NP) equations. These models chiefly differ in the form of the charge conservation laws. Although the PNP model is the more complete treatment of charged species transport and better describes transitions in the boundary layers near electrodes (typically 1 ~ 10 nm), obtaining the desired numerical convergence is non-trivial due to the very large coefficients (6.8×10^{14}) resulting from the $F/\varepsilon_0\varepsilon_s$ factor in Poisson's equation, where F is Faraday's constant (96485 C/mol), ε_0 is the vacuum permittivity (8.85×10^{-12} A^2s^2/Nm^2), and ε_s represents the dielectric constant of the solvent (~15 for a typical organic solvent). These factors necessitate the use of appropriate dimensionless groups, scaling factors, and numerical discretization schemes.

The literature on the computational aspects of the PNP equations is extensive, beginning with the work of Cohen and Cooley, and that of Brumleve and Buck.[125,126] Modified finite difference schemes have been employed for spatial discretization, with various implicit and semi-implicit schemes used for time integration.[127–131] Spectral methods have also been exploited to achieve improved resolution of double layers for certain steady-state problems.[132,133] In addition, some researchers have attempted to find analytical solutions. Golovnev[134] found the analytical form of

PNP solutions in the linear regime under applied direct current. Pabst[135] also derived the analytical solution of the PNP equations for a system close to electroneutrality by introducing two different time constants. Analytical solutions for PNP can only be found under specific operating conditions and limiting assumptions.

In this study, we present an analytical solution for the concentration profiles in the EN-NP case**.** Using bulk electroneutrality is a common simplification in battery modeling, for example, in the porous electrode pseudo-two-dimensional (P2D) models of Newman and co-workers.[45,79] We then present finite volume method (FVM) numerical schemes for dimensionless forms of both EN-NP and PNP models for a binary electrolyte**.** Furthermore, we compare EN-NP with PNP for galvanostatic operating conditions and the typical length and time scales encountered in lithium symmetric cells. In summary, we can use the FVM scheme to solve PNP and EN-NP models efficiently in a robust manner. For typical design parameters, we can further approximate PNP with EN-NP, leveraging the easy implementation of analytical solutions for the concentration profile to enhance simulation efficiency.

4.2.1. *1-D Nernst-Planck system for binary electrolytes*

Assuming a symmetric binary electrolyte with a constant diffusivity completely dissociating in a non-ionized solvent in the presence of uncharged background components, the 1-D Nernst-Planck [79] constitutive relations are be used in species conservation laws, considering the transport equations in the absence of chemical reactions. For a common electrolyte ion pair, such as Li^+ and PF_6^-, these conservation equations can be written as:

$$\frac{\partial c_1}{\partial t} = -\frac{\partial N_1}{\partial x} \tag{95}$$

$$\frac{\partial c_2}{\partial t} = -\frac{\partial N_2}{\partial x} \tag{96}$$

where c is the concentration (mol/m^3), t is the time (s), N represents the total flux (mol/m^2 s), and x is the position along the cell (m). For convenience, subscript 1 represents Li^+ and 2 denotes PF_6^-.

In the absence of convection, the Nernst-Planck (NP) constitutive equations for the fluxes are given by

$$N_1 = -D_1 \frac{\partial c_1}{\partial x} - z_1 c_1 u_1 F \frac{\partial \phi}{\partial x} \tag{97}$$

$$N_2 = -D_2 \frac{\partial c_2}{\partial x} - z_2 c_2 u_2 F \frac{\partial \phi}{\partial x} \tag{98}$$

where D is the diffusivity (m^2/s), z is the electric charge of the ion, u is the ionic mobility (mol m^2/J s), F is the Faraday's constant (96485 C/mol), and ϕ is the mean-field electrostatic potential (V).

In the equation, the first term (diffusive flux) denotes the diffusion contribution due to the concentration gradient, and the second term represents the migration of charged ions under an electric field. u is the ionic mobility which gives the average migration velocity of the species under a unit electric field, and zF is charge per mole of the species. In the dilute solution formulation, ion-ion interactions are neglected. A description based on the 'Onsager-Stefan-Maxwell' (OSM) flux laws will consider the complete set of pairwise interactions for all species.[79,136] However, the computational methods outlined herein are applicable to the full OSM equations as well. In particular, for electroneutral systems comprising a binary electrolyte, both

the EN-NP and the OSM equations reduce to a similar mathematical form, indicating direct extensibility to the mathematical treatment of concentrated binary electrolytes.

We can further link the ionic mobility (u) and diffusivity (D) by the Nernst-Einstein relation

$$u_1 = \frac{D_1}{RT} \tag{99}$$

$$u_2 = \frac{D_2}{RT} \tag{100}$$

where R is the gas constant (8.3143 J/mol K), and T is the absolute temperature (K).

Hence, the mass transport equations can be written as:

$$\frac{\partial c_1}{\partial t} = -\frac{\partial}{\partial x}\left(-D_1 \frac{\partial c_1}{\partial x} - z_1 c_1 \frac{D_1 F}{RT}\frac{\partial \phi}{\partial x}\right) \tag{101}$$

$$\frac{\partial c_2}{\partial t} = -\frac{\partial}{\partial x}\left(-D_2 \frac{\partial c_2}{\partial x} - z_2 c_2 \frac{D_2 F}{RT}\frac{\partial \phi}{\partial x}\right) \tag{102}$$

The boundary conditions for both species are listed in **Table 4-I**.

Table 4-I. Boundary conditions for Nernst-Planck equations

I	Species	*x* = 0	*x* = *L*
1	Li^+	$N_1\big\vert_{x=0} = \frac{I_{app}}{z_1 F}$	$N_1\big\vert_{x=L} = \frac{I_{app}}{z_1 F}$
2	PF_6^-	$N_2\big\vert_{x=0} = 0$	$N_2\big\vert_{x=L} = 0$

The boundary conditions for all the species in our model are specified in terms of the normal component of their fluxes at each electrode. The flux of the electroactive Li^+ species is related to the applied current density. The negatively charged PF_6^- ions are assumed not to react at either electrode. In the following sections, we will present solutions for the ion concentration and electrostatic potential profiles, beginning with EN-NP.

4.2.2. *Electroneutrality and Nernst-Planck (EN-NP)*

Electroneutrality is generally an accurate assumption except in the 1-10 nm charged interfacial double layer region. Although the Poisson's equation (equation (140)) in PNP describes a system with a uniform dielectric constant more accurately than EN-NP, the presence of thin double layers with respect to characteristic system dimensions poses both modeling and computational challenges.[137] For the symmetric cell modeled here, this quantity, given by the ratio of the characteristic Debye length to the characteristic system dimension, ε, is of the order of 10^{-7}. In general, EN-NP is substantially easier to solve numerically compared to the PNP system. Coupled with the increasing validity of the EN approximation as $\varepsilon \to 0$, this motivates the use of the

electroneutrality assumption to avoid the computational difficulties associated with thin boundary layers.[130,138] Chu and Bazant[132] commented that Levich[139] was probably the first to notice that the assumption of bulk electroneutrality yields approximate solutions to the Poisson-Nernst-Planck (PNP) equations. Additionally, the double layer structure at the electrode interface can often be implicitly considered in the boundary conditions.[79] The electroneutrality condition is expressed as:

$$\sum_i z_i c_i = 0 \tag{103}$$

where z_i represents the charge of each ion and c_i represents the concentration of each ion species.

For a binary electrolyte, the electroneutrality relation provides:

$$z_1 c_1 + z_2 c_2 = 0 \tag{104}$$

Under this assumption, we obtain $c_1 = c_2$ and we can further define them as c when $z_1 = 1$ and $z_2 = -1$. Therefore, we can get the Nernst-Planck equations for both species from equations (101) and (102).

$$\frac{\partial c}{\partial t} = -\frac{\partial}{\partial x}\left(-D_1 \frac{\partial c}{\partial x} - c\frac{D_1 F}{RT}\frac{\partial \phi}{\partial x}\right) \tag{105}$$

$$\frac{\partial c}{\partial t} = -\frac{\partial}{\partial x}\left(-D_2 \frac{\partial c}{\partial x} + c\frac{D_2 F}{RT}\frac{\partial \phi}{\partial x}\right) \tag{106}$$

During galvanostatic operation, the constant current density (I_{app}) can be related to the species flux balance as:

$$F\sum_{i}^{n} z_i N_i = F\left(z_1 N_1 + z_2 N_2\right) = I_{app} \tag{107}$$

In this case, we have:

$$F\left(\left(-D_1\frac{\partial c}{\partial x} - c\frac{D_1 F}{RT}\frac{\partial \phi}{\partial x}\right) - \left(-D_2\frac{\partial c}{\partial x} + c\frac{D_2 F}{RT}\frac{\partial \phi}{\partial x}\right)\right) = I_{app} \tag{108}$$

Therefore, from equation (108), we can get

$$\frac{\partial \phi}{\partial x} = \frac{RT}{cF}\left(\frac{D_2 - D_1}{D_1 + D_2}\right)\frac{\partial c}{\partial x} - \frac{RT}{cF^2}\left(\frac{I_{app}}{D_1 + D_2}\right) \tag{109}$$

If we substitute equation (109) back into equation (105), we can get:

$$\frac{\partial c}{\partial t} = \left(\frac{2D_1 D_2}{D_1 + D_2}\right)\frac{\partial^2 c}{\partial x^2} = D\frac{\partial^2 c}{\partial x^2} \tag{110}$$

where D can be defined as a binary electrolyte diffusivity:

$$D = \frac{2D_1 D_2}{D_1 + D_2} \tag{111}$$

We introduce the following dimensionless variables:

$$C = \frac{c}{c_0},\quad X = \frac{x}{L},\quad \tau = \frac{D}{L^2}t,\ \text{and}\quad \delta = \frac{I_{app} L}{F c_0 D_1} \tag{112}$$

The governing equation in equation (110), boundary conditions in **Table 4-I** and initial conditions become:

$$\frac{\partial C}{\partial \tau} = \frac{\partial^2 C}{\partial X^2} \tag{113}$$

$$C\left(X,0\right) = 1 \tag{114}$$

$$\frac{\partial C}{\partial X}\left(0,\tau\right) = -\frac{\delta}{2} \tag{115}$$

$$\frac{\partial C}{\partial X}\left(1,\tau\right) = -\frac{\delta}{2} \tag{116}$$

The dimensionless governing equation for electrolyte concentration is essentially a parabolic partial differential equation (PDE) with two non-homogenous flux boundary conditions.

4.3.Analytical solution of EN-NP model

We obtain an analytical solution for $C(X, \tau)$ using the separation of variables (SOV) approach.[140] First, we assume the solution of the concentration as follows:

$$C\left(X,\tau\right) = g\left(X,\tau\right) + w\left(X\right) \tag{117}$$

In equation (117), $g(X, \tau)$ satisfies the homogeneous part of boundary conditions, while $w(X)$ satisfies the non-homogeneous part.[141]

The boundary conditions are therefore expressed as:

$$\frac{\partial g}{\partial X}\left(0,\tau\right) = 0 \text{, and } \frac{\partial g}{\partial X}\left(1,\tau\right) = 0 \tag{118}$$

$$\frac{dw}{dX}\left(0\right) = -\frac{\delta}{2} \text{, and } \frac{dw}{dX}\left(1\right) = -\frac{\delta}{2} \tag{119}$$

By substituting equation (117) into equation (113), we get:

$$\frac{\partial g}{\partial \tau} = \frac{\partial^2 g}{\partial X^2} + \frac{d^2 w}{dX^2} \tag{120}$$

It can be separated as the following two equations.

$$\frac{\partial g}{\partial \tau} = \frac{\partial^2 g}{\partial X^2} \tag{121}$$

$$\frac{d^2 w}{dX^2} = 0 \tag{122}$$

We can first solve $\frac{d^2 w}{dX^2} = 0$ with the boundary conditions listed in equation (119) and obtain:

$$w(X) = -\frac{\delta}{2} X + B \tag{123}$$

where *B* is an arbitrary constant for integration, which cannot be found using the flux boundary conditions for *w*(*X*).

So far, the solution is:

$$C(X,\tau) = g(X,\tau) + w(X) = g(X,\tau) - \frac{\delta}{2} X + B \tag{124}$$

The next step is to solve for *g*(*X*, *τ*) by the SOV approach, assuming $g(X,\tau) = \theta(X) T(\tau)$, where $\theta(X)$ is a function of *X* and $T(\tau)$ is a function of *τ* alone.

$$g(X,\tau)=\sum_{n=1}^{\infty}A_n\cos(n\pi X)\exp(-n^2\pi^2\tau) \tag{125}$$

The solution is mostly complete from equations (124) and (125), except for the constant *B*.

$$C(X,\tau)=\sum_{n=1}^{\infty}A_n\cos(n\pi X)\exp(-n^2\pi^2\tau)-\frac{\delta}{2}X+B \tag{126}$$

Now, we can use the initial condition in the equation (114) to solve the constant *B* and A_n. When $\tau=0$, the equation (126) becomes:

$$\sum_{n=1}^{\infty}A_n\cos(n\pi X)-\frac{\delta}{2}X+B=1 \tag{127}$$

According to the Sturm-Liouville theory, we can obtain the solution of A_n from equation (128), where *IC* is the initial condition, ω_n represents the eigenfunction, and *r*(*X*) represents the weighting function. In this example, $\omega_n=\cos(n\pi X)$ and *r*(*X*) = 1.

$$A_n=\frac{\int_0^1(IC-w(X))\omega_n r(X)dX}{\int_0^1\omega_n^2 r(X)dX} \tag{128}$$

Therefore:

$$A_n=\frac{\int_0^1(IC-w(X))\omega_n r(X)dX}{\int_0^1\omega_n^2 r(X)dX}=\frac{\delta(-1+\cos(n\pi))}{n^2\pi^2} \tag{129}$$

For even *n*, $\cos(n\pi)=1$, and A_n vanishes. Thus, the infinite series of equation (125) only consists of odd-numbered terms.

To get the constant *B*, we can multiply the weighting function *r*(*X*) on both sides in equation (127) and integrate over *X* from 0 to 1.

$$\sum_{n=1}^{\infty} A_n \int_0^1 \cos\left(n\pi X\right) dX - \int_0^1 \frac{\delta}{2} X dX + \int_0^1 B dX = \int_0^1 1 dX \tag{130}$$

Since the first term $\sum_{n=1}^{\infty} A_n \int_0^1 \cos\left(n\pi X\right) dX$ goes to zero, we get:

$$B = 1 + \frac{\delta}{4} \tag{131}$$

Hence, the full analytical solution of the dimensionless concentration profile is:

$$C\left(X,\tau\right) = \left[\sum_{n=1}^{\infty} \frac{\delta\left(-1+\cos\left(n\pi\right)\right)}{n^2\pi^2} \cos\left(n\pi X\right) \exp\left(-n^2\pi^2\tau\right)\right] - \frac{\delta}{2} X + 1 + \frac{\delta}{4} \tag{132}$$

The steady-state concentration profile is:

$$C\left(X,\infty\right) = -\frac{\delta}{2} X + 1 + \frac{\delta}{4} \tag{133}$$

The infinite series in equation (132) can be reasonably approximated by its first *n =5* terms except for short times. Of note, for cycling simulations, the coefficients A_n need to be updated for each change in the galvanostatic boundary conditions, corresponding to the reversal of polarity, but the steady-state term remains unchanged. In simulating cell cycling, since the values of the coefficients A_n are arrived at using the initial concentration profile in equation (128), the concentration profile at the end of a given cycle must be used as the initial concentration profile for the succeeding one. In other words, the coefficients for two successive cycles are mathematically related and establish

the relationship between the concentration profiles.[140]

It is also worth noting that the electrostatic potential profile given in equation (109) has to be solved numerically due to the presence of the infinite series in $C(X, \tau)$ and the nonlinearity of the potential equation. A Gaussian quadrature numerical integration can be applied to get the terminal potential at $x = 0$. This method is illustrated in the Appendix B (**Section 7.1**). Alternatively, $C(X, \tau)$ can be solved numerically using FVM.

4.4. Finite Volume Formulation of EN-NP

Unlike FDM, which evaluates the variables at the nodes, the FVM discretization method uses finite volumes around the nodes and explicitly considers the fluxes of each variable through each finite volume. Since the discretization involves the summation of the fluxes entering and leaving each finite volume, the FVM scheme is conservative, which is a major advantage. It is also easier to extend to unstructured grids compared to FDM.

The computational domain can be divided into n elements, each of size h (n thus denotes the number of internal nodes). To apply the finite volume method, a (discrete) flux balance for each control volume need to be elucidated. We integrate equation (95) from *(j-1)h* to *jh*, giving us the dimensionless FVM formulation as:

$$\frac{dC_{j-1/2}}{d\tau} = -\frac{N_j - N_{j-1}}{h} \tag{134}$$

where the subscript j represents the spatially discretized variable index and varies from 1 to $n + 1$.

The first-order approximation can be applied for the flux:

$$N_j = -\frac{C_{j+1/2} - C_{j-1/2}}{h} \tag{135}$$

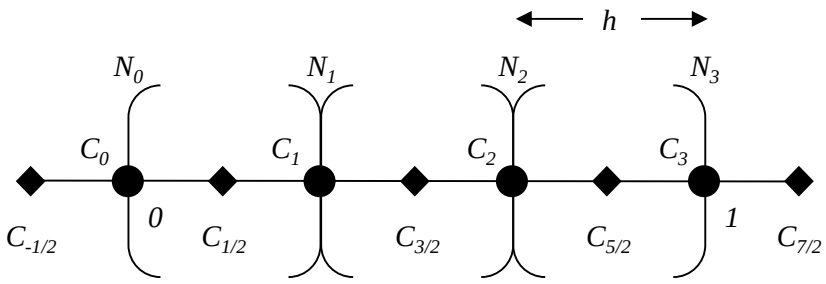

Figure 4.2. A two-internal-node (three-element) FVM scheme.

Figure 4.2 shows a schematic drawing of a cell-centered three-element (two internal nodes) FVM scheme and ghost points. Previous applications of FVM methods for lithium-ion batteries have been reported elsewhere.[142] FVM approach with *n* elements provides the discretized equations for the original PDE as given below

$$\frac{dC_{1/2}}{d\tau} = -\frac{\left(-\frac{C_{3/2} - C_{1/2}}{h}\right) - \left(\frac{\delta}{2}\right)}{h} \tag{136}$$

$$\frac{dC_{j-1/2}}{d\tau} = -\frac{\left(-\frac{C_{j+1/2} - C_{j-1/2}}{h}\right) - \left(-\frac{C_{j-1/2} - C_{j-3/2}}{h}\right)}{h},\ j = 2\ldots n \tag{137}$$

$$\frac{dC_{n+1/2}}{d\tau} = -\frac{\left(\frac{\delta}{2}\right) - \left(-\frac{C_{n+1/2} - C_{n-1/2}}{h}\right)}{h} \tag{138}$$

A simple averaging procedure is used to approximate the concentrations at the boundaries ($X = 0$ and $X = 1$ respectively) as:

$$C_0 = \frac{C_{1/2} + C_{-1/2}}{2} \text{ and } C_3 = \frac{C_{5/2} + C_{7/2}}{2} \tag{139}$$

Higher order approximations can also be used to find the values at the boundaries.

4.5.Poisson Nernst-Planck Model

The Poisson Nernst-Planck (PNP) equations represent a mean-field continuum approximation of the dynamics of ionized electrolyte under the influence of the electrostatic field in a dilute system. The PNP model is restricted to the dilute solution regime. The electrolyte acts as a conducting liquid, and the ions create a continuous concentration profile across the system. The PNP model provides quantitative predictions, and it is useful for relating system-level experimental data to the local electrochemistry.

Poisson's equation relates the charge density and the Laplacian of the electric potential (ϕ). For the binary electrolyte considered for lithium symmetric cells, it is represented in 1-D as:

$$\frac{\partial^2 \phi}{\partial x^2} = -\frac{F}{\varepsilon_0 \varepsilon_s}\left(z_1 c_1 + z_2 c_2\right) \tag{140}$$

where the boundary conditions for ϕ are listed in **Table 4-II**.

Table 4-II. Boundary conditions for Poisson's equation

$x = 0$	$x = L$
$\frac{\partial \phi}{\partial x} = 0$	$\phi = 0$

The explicit specification of the potential distribution now necessitates additional boundary conditions for ϕ. For simplicity, the "zero-field" condition of Streeter and Compton[127,133] is used at the electrode, $x = 0$. A reference value for electrostatic potential is taken at $x = L$.

The full PNP system is comprised of (101), (102), (140), and the boundary conditions listed in **Table 4-I** and **Table 4-II**. When $t = 0$, the bulk concentrations of both ions are such that $c_1 = c_2 = c_0$.

For computational convenience and analysis, the PNP equations can be scaled and transformed by the following dimensionless variables and scale factors:

$$C_i = \frac{c_i}{c_0},\ X = \frac{x}{L},\ \Phi = \frac{z_1 F}{RT}\phi, \text{ and } \tau = \frac{D_1}{L^2}t \tag{141}$$

$$\varepsilon = \sqrt{\frac{RT\varepsilon_s\varepsilon_0}{z_1^2 F^2 c_0 L^2}},\ \delta = \frac{I_{app} L}{z_1 F c_0 D_1}, \text{ and } \xi = \frac{D_2}{D_1} \tag{142}$$

The dimensionless PNP system and the boundary conditions are listed in **Table 4-III**.

Table 4-III. Dimensionless PNP system ($z_1 = 1$, $z_2 = -1$)

i	Governing Equations	*X* = 0	*X* = *1*
1	$\frac{\partial C_1}{\partial \tau} = \frac{\partial^2 C_1}{\partial X^2} + C_1 \frac{\partial^2 \Phi}{\partial X^2} + \frac{\partial C_1}{\partial X}\frac{\partial \Phi}{\partial X}$	$-\frac{\partial C_1}{\partial X}\Big\|_{X=0} - C_1 \frac{\partial \Phi}{\partial X}\Big\|_{X=0} = \delta$	$-\frac{\partial C_1}{\partial X}\Big\|_{X=1} - C_1 \frac{\partial \Phi}{\partial X}\Big\|_{X=1} = \delta$
2	$\frac{\partial C_2}{\partial \tau} = \xi\left(\frac{\partial^2 C_2}{\partial X^2} - C_2 \frac{\partial^2 \Phi}{\partial X^2} - \frac{\partial C_2}{\partial X}\frac{\partial \Phi}{\partial X}\right)$	$-\frac{\partial C_2}{\partial X}\Big\|_{X=0} + C_2 \frac{\partial \Phi}{\partial X}\Big\|_{X=0} = 0$	$-\frac{\partial C_2}{\partial X}\Big\|_{X=1} + C_2 \frac{\partial \Phi}{\partial X}\Big\|_{X=1} = 0$
	$\frac{\partial^2 \Phi}{\partial X^2} = -\frac{1}{\varepsilon^2}(C_1 - C_2)$	$\frac{\partial \Phi}{\partial X}\Big\|_{X=0} = 0$	$\Phi\Big\|_{X=1} = 0$

For the symmetric cell, we assume the anion flux is zero at each electrode, thus the average concentration of the PF_6^- ions in the cell remains unchanged with time. In addition, since we have the same current density at both electrodes, the rate of stripping and deposition of lithium at the electrodes will be the same. Therefore, the average ion concentration across the cell remains the same as the initial concentration and we can integrate microscopic PDEs, equations (95) and (96) , in space from 0 to *L* and get:

$$\frac{\partial \int_0^L c_1 dx}{\partial t} = L\frac{\partial c_{1,avg}}{\partial t} = -\left(N_1\Big|_{x=L} - N_1\Big|_{x=0}\right) = -\left(\frac{I_{app}}{z_1 F} - \frac{I_{app}}{z_1 F}\right) = 0 \tag{143}$$

$$\frac{\partial \int_0^L c_2 dx}{\partial t} = L\frac{\partial c_{2,avg}}{\partial t} = -\left(N_2\Big|_{x=L} - N_2\Big|_{x=0}\right) = -(0-0) = 0 \tag{144}$$

Thus, after applying the dimensionless groups (equation (141)) and integrating the equations (143) and (144) in time with the initial condition, we can get:

$$C_{1,\,avg} = \int_0^1 C_1 dX = 1 \text{ and } C_{2,\,avg} = \int_0^1 C_2 dX = 1 \tag{145}$$

Microscopic PDEs and macroscopic balances (equations (143) and (144)) are thus always related, and the reduction is obvious for Neumann boundary conditions.

With this knowledge of average ion concentrations, we can integrate the Poisson's equation in X from 0 to 1 and obtain:

$$\left.\frac{\partial \Phi}{\partial X}\right|_{X=1} - \left.\frac{\partial \Phi}{\partial X}\right|_{X=0} = -\frac{1}{\varepsilon^2}\left(C_{1,\,avg} - C_{2,\,avg}\right) = 0 \tag{146}$$

Therefore, when the potential gradient at one end is defined, its value at the other boundary is automatically determined from equation (146). In our analysis, the zero-field assumption at X=0 leads to the same condition at X=1. This is exactly satisfied for conservative discretization schemes. For non-conservative convergent numerical schemes, it might result in a finite but small non-zero value, which approaches zero as the computational grid is refined.

4.6.Finite Volume Formulation of PNP

Similar to EN-NP model, FVM scheme is used for the PNP model. It inherits the advantages in simplicity as shown in the EN-NP model. The domain can be divided into *n* elements (*n* denotes the number of internal nodes) with constant grid spacing *h.* To apply the FVM, we integrate equations (95) and (96) over a single volume element, from *(j-1)h* to *jh*, giving us the FVM formulation for species 1 and 2 as:

$$\frac{dC_{1,\,j-1/2}}{d\tau} = -\left(\frac{N_{1,\,j} - N_{1,\,j-1}}{h}\right) \tag{147}$$

$$\frac{dC_{2,j-1/2}}{d\tau} = -\left(\frac{N_{2,j} - N_{2,j-1}}{h}\right) \tag{148}$$

where *j* represents the spatial discretization and *j* is from 1 to *n*.

The first-order approximation can be applied for the flux:

$$N_{1,j} = -\frac{\partial C_1}{\partial X} - C_1\frac{\partial \Phi}{\partial X} = -\frac{C_{1,j+1/2} - C_{1,j-1/2}}{h} - C_{1,j}\frac{\Phi_{j+1/2} - \Phi_{j-1/2}}{h} \tag{149}$$

$$N_{2,j} = -\frac{\partial C_2}{\partial X} + C_2\frac{\partial \Phi}{\partial X} = -\frac{C_{2,j+1/2} - C_{2,j-1/2}}{h} + C_{2,j}\frac{\Phi_{j+1/2} - \Phi_{j-1/2}}{h} \tag{150}$$

In contrast to the simpler flux expression in EN-NP (equation (135)), the PNP flux discretization requires concentration at the ends of each element (equations (149) and (150)). If the concentration is defined at the midpoint of the element, the face concentrations ($C_{1,j}$) , ($C_{2,j}$) are also needed. A strict FVM solves concentration as a piecewise continuous function, and the value $C_{i,j}$ is not known. The flux is calculated based on the local velocity. In this work, we assume that $C_{1,j}$ is the average of $C_{1,j-1/2}$ and $C_{1,j+1/2}$ as equation (151).

$$C_{1,j} = \frac{C_{1,j-1/2} + C_{1,j+1/2}}{2} \tag{151}$$

This will introduce errors and oscillations in strongly convective PDEs, but this approximation appears to work for the PNP case. In order to avoid approximating the $C_{i,j}$, a piecewise linear profile can be assumed to arrive at a control-volume scheme as demonstrated earlier by Zeng et al.[143] However, this will result in a tri-diagonal mass matrix for the accumulation terms.

The FVM form of the equations (147) and (148) become

$$\frac{dC_{1,1/2}}{d\tau} = -\frac{\left(-\frac{C_{1,3/2}-C_{1,1/2}}{h} - C_{1,1}\frac{\Phi_{3/2}-\Phi_{1/2}}{h}\right)-\delta}{h} \tag{152}$$

$$\frac{dC_{1,j-1/2}}{d\tau} = -\frac{\left(-\frac{C_{1,j+1/2}-C_{1,j-1/2}}{h} - C_{1,j}\frac{\Phi_{j+1/2}-\Phi_{j-1/2}}{h}\right)-\left(-\frac{C_{1,j-1/2}-C_{1,j-3/2}}{h} - C_{1,j-1}\frac{\Phi_{j-1/2}-\Phi_{j-3/2}}{h}\right)}{h}, j = 2\ldots n \tag{153}$$

$$\frac{dC_{1,n+1/2}}{d\tau} = -\frac{\delta-\left(-\frac{C_{1,n+1/2}-C_{1,n-1/2}}{h} - C_{1,n}\frac{\Phi_{n+1/2}-\Phi_{n-1/2}}{h}\right)}{h} \tag{154}$$

Similarly, the dimensionless concentration expressions for species 2 are:

$$\frac{dC_{2,1/2}}{d\tau} = -\xi\frac{\left(-\frac{C_{2,3/2}-C_{2,1/2}}{h} + C_{2,1}\frac{\Phi_{3/2}-\Phi_{1/2}}{h}\right)-0}{h} \tag{155}$$

$$\frac{dC_{2,j-1/2}}{d\tau} = -\xi\frac{\left(-\frac{C_{2,j+1/2}-C_{2,j-1/2}}{h} + C_{2,j}\frac{\Phi_{j+1/2}-\Phi_{j-1/2}}{h}\right)-\left(-\frac{C_{2,j-1/2}-C_{2,j-3/2}}{h} + C_{2,j-1}\frac{\Phi_{j-1/2}-\Phi_{j-3/2}}{h}\right)}{h}, j = 2\ldots n \tag{156}$$

$$\frac{dC_{2,n+1/2}}{d\tau} = -\xi\frac{0-\left(-\frac{C_{2,n+1/2}-C_{2,n-1/2}}{h} + C_{2,n}\frac{\Phi_{n+1/2}-\Phi_{n-1/2}}{h}\right)}{h} \tag{157}$$

Also, the FVM discretization for dimensionless electrostatic potential can be expressed as:

$$-\frac{\left(-\frac{\Phi_{3/2}-\Phi_{1/2}}{h}\right)-0}{h} = -\frac{1}{\varepsilon^2}\left(C_{1,1/2}-C_{2,1/2}\right) \tag{158}$$

$$-\frac{\left(-\frac{\Phi_{j+1/2}-\Phi_{j-1/2}}{h}\right)-\left(-\frac{\Phi_{j-1/2}-\Phi_{j-3/2}}{h}\right)}{h}=-\frac{1}{\varepsilon^2}\left(C_{1,j-1/2}-C_{2,j-1/2}\right),\ j=2\ldots n \tag{159}$$

$$-\frac{\left(-\frac{-2\Phi_{n+1/2}}{h}\right)-\left(-\frac{\Phi_{n+1/2}-\Phi_{n-1/2}}{h}\right)}{h}=-\frac{1}{\varepsilon^2}\left(C_{1,n+1/2}-C_{2,n+1/2}\right) \tag{160}$$

The PNP DAE system has the initial conditions given by

$$C_{1,j-1/2}=1,\ j=1..n+1 \tag{161}$$

$$C_{2,j-1/2}=1,\ j=1..n+1 \tag{162}$$

$$\Phi_{j-1/2}=0,\ j=1..n+1 \tag{163}$$

We can obtain equations at $x = 0$ as:

$$C_{1,0}=\frac{C_{1,1/2}+C_{1,-1/2}}{2}=C_{1,1/2}+\frac{\delta}{2}h \tag{164}$$

$$C_{2,0}=\frac{C_{2,1/2}+C_{2,-1/2}}{2}=C_{2,1/2} \tag{165}$$

$$\Phi_0=\frac{\Phi_{1/2}+\Phi_{-1/2}}{2}=\Phi_{1/2} \tag{166}$$

Higher order approximations can be used to find the values at X = 0 and 1, but the observed order of convergence remains the same for the PNP model.

In previous work from our group, we had performed reformulation to increase the computational efficiency which primarily has relevance for estimation and real-time control for Battery Management Systems. In this work, reformulation was not performed. Some possible directions

for computationally efficient methods for PNP-type models are outlined below. These will be pursued in future work.

(1) For a FVM or FDM formulations, the equation for the potential is linear and the values for the potential at different node points (or elements can) be written in terms of the species concentrations C1 and C2. This involves finding the eigenvalues and eigenvectors for any number of node points/elements, N.[50]

(2) As opposed to FVM, Galerkin or orthogonal collocation approach results in faster convergence. The best possible approach for applying spectral methods for PNP was presented earlier.[52,54,144]

(3) Both (1) and (2) assume the use of adaptive integrators in time. It is possible to arrive at higher order methods in both space and time using the model equations.

(4) For this particular model, steep gradients are confined to the thin double layers in the vicinity of the electrodes. We can thus solve the model as a 3-region problem, (i.e., as three domains given by [0,δ], [δ,1-δ], and [1-δ,1]) where δ is of order of the double layer thickness. This will help achieve greater efficiency through optimal resolution of the bulk and boundary regions, even though the three PDEs are solved individually in the three regions.[144,145]

4.7. Results and Discussion

4.7.1. *Analytical and Numerical Solutions of EN-NP*

In this study, we chose the parameters listed in **Table 4-IV**, which are a reasonable representation of experimental conditions. Some of the values may be found in Wood et al.[32]

Table 4-IV. Base case simulation parameters

Symbol	Physical meaning	Value	Units
c_0	Initial concentration of the electrolyte	500	mol/m^3
D_1	Diffusivity of Li^+	4×10^{-10}	m^2/s
D_2	Diffusivity of PF_6^-	4×10^{-9}	m^2/s
I_{app}	Applied current density	10.0	A/m^2
L	Cell dimension in x	7.5×10^{-4}	m
T	Temperature	298.15	K
ε_0	Vacuum permittivity	8.85×10^{-12}	$kg^{-1}m^{-3}s^4A^2$
ε_s	Dielectric constant of the solvent	16.8	-

We used separation of variables techniques to find the analytical form of solutions in concentration, and the analytical solution of the dimensionless concentration profile as equation (132). The spatial concentration profiles at a given instant can be obtained by substituting dimensionless time into the equation.

We solved the discretized equations in time using IDA, an Implicit Differential-Algebraic solver in ANSI-standard C language under BSD license. Developed by Hindmarsh et al. IDA is an efficient solver for initial value problems (IVP) for systems of DAEs, which is part of the SUNDIALS (SUite of Nonlinear and DIfferential/ALgebraic equation Solvers) package.[86] We chose an absolute solver tolerance of 1×10^{-8} and relative tolerance of 1×10^{-7}, which we expect to be sufficiently stringent accuracy conditions for relevant situations in experiments and control.

In addition, we limited the maximum order of the BDF (Backward Differentiation Formulae) to 2 to ensure numerical '*A*-stability' .[146] We simulated the model for an hour and demonstrated the transitions in concentration and potential profiles. Since the electrodes are the location of the greatest variation of electrochemical variables, and we are interested in their influence on electrode kinetics, the values of the concentration and potential are examined at $X = 0$. The number of internal nodes was chosen to ensure accuracy up to 6 decimal places.

After substitution of the boundary conditions into the internal governing equations, the EN-NP model yields an initial value problem for a system of ODEs (DAEs if we solve for ϕ as well). The numerical solutions exhibit agreement with the analytical solutions as in **Figure 4.3** and **Figure 4.4**. At short times, we observe a boundary layer near the electrodes in the concentration and potential profiles, while for longer times, the variables attain the linear profile described by the steady-state solution of equation (133). Hence, at longer times, convergence is achieved with relatively fewer node points.

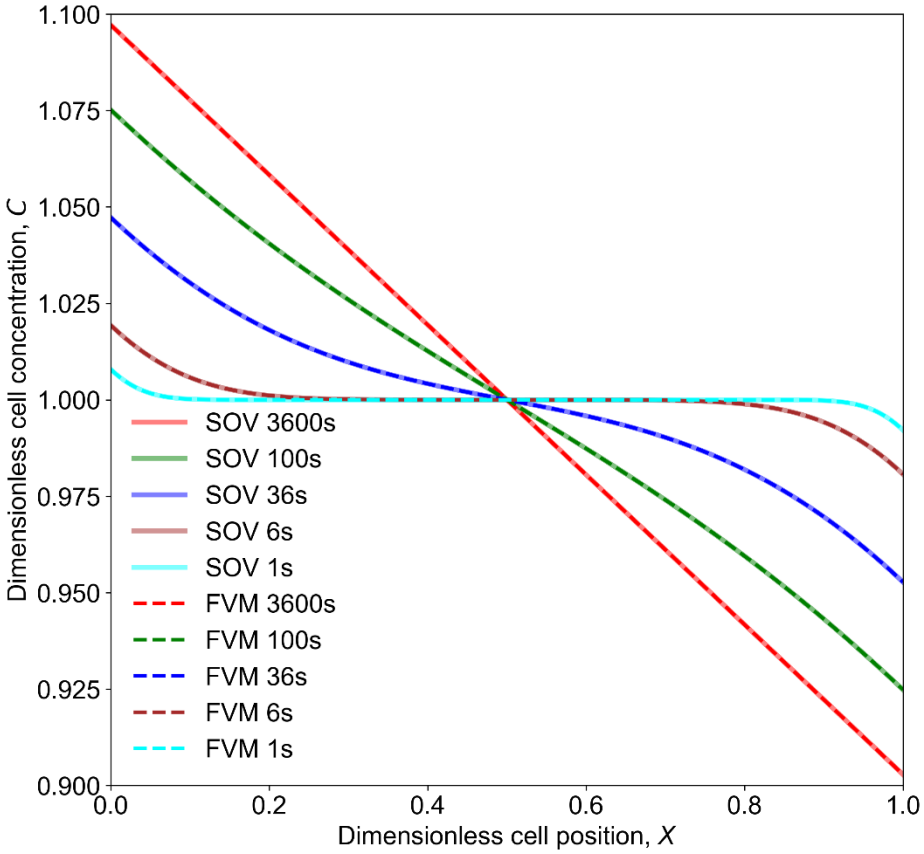

Figure 4.3. Solutions of the EN-NP system for spatial concentration profiles. The agreement of our analytical solution (SOV) with converged numerical solutions establishes its accuracy. The concentration profile is characterized by a gradual increase in electrolyte concentration at the stripping electrode, which generates Li+ ions, with a corresponding decrease in Li+ concentration due to consumption at the deposition electrode.

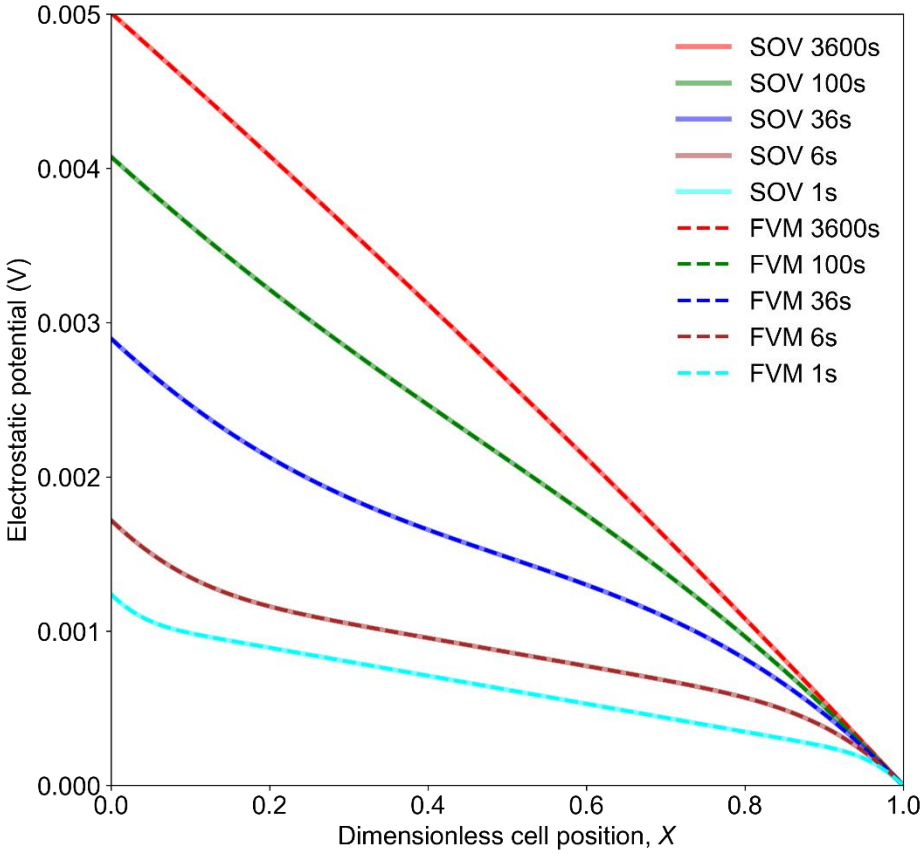

Figure 4.4. Solutions of EN-NP system for electrostatic potential. The profiles predicted using the SOV solution agree with that obtained by numerical methods. The electrostatic potential is set to a reference value of $\phi = 0$ at X=1.

Table 4-V.The EN-NP solutions for C_0 when t = 1 s by FVM scheme

Analytical solution: C_0 = 1.00788467719606.

Spacing (h)	FVM
1/4	1.02528612650271
1/8	1.01407707486321
1/16	1.00954921773040
1/32	1.00826831827022
1/64	1.00797894991306
1/128	1.00790870306024
1/256	1.00789114377750
1/512	1.00788687365799
1/1024	1.00788569105244
1/2048	1.00788557426487

Table 4-V reports the simulated dimensionless concentration solution by FVM scheme at x = 0 and t = 1 s. The convergence rate of the method was evaluated by using the data listed in **Table 4-V** and comparing it with the analytical solution. To facilitate the convergence analysis, grid spacing values ranging from to $h = 1/4$ to $h = 1/512$ (eight values) were used. We avoid using grid sizes below $h = 1/2048$ because they are close to the saturation of the accuracy due to the tolerance settings. In obtaining convergence rate estimates, we used least-squares regression to find the slope of the logarithm of the absolute error (the difference between numerical and analytical solutions) versus log(h). For FVM, the slope is 1.911269, respectively, indicating nearly second order

convergence even at short times.

4.7.2. *Comparison of EN-NP and PNP Results*

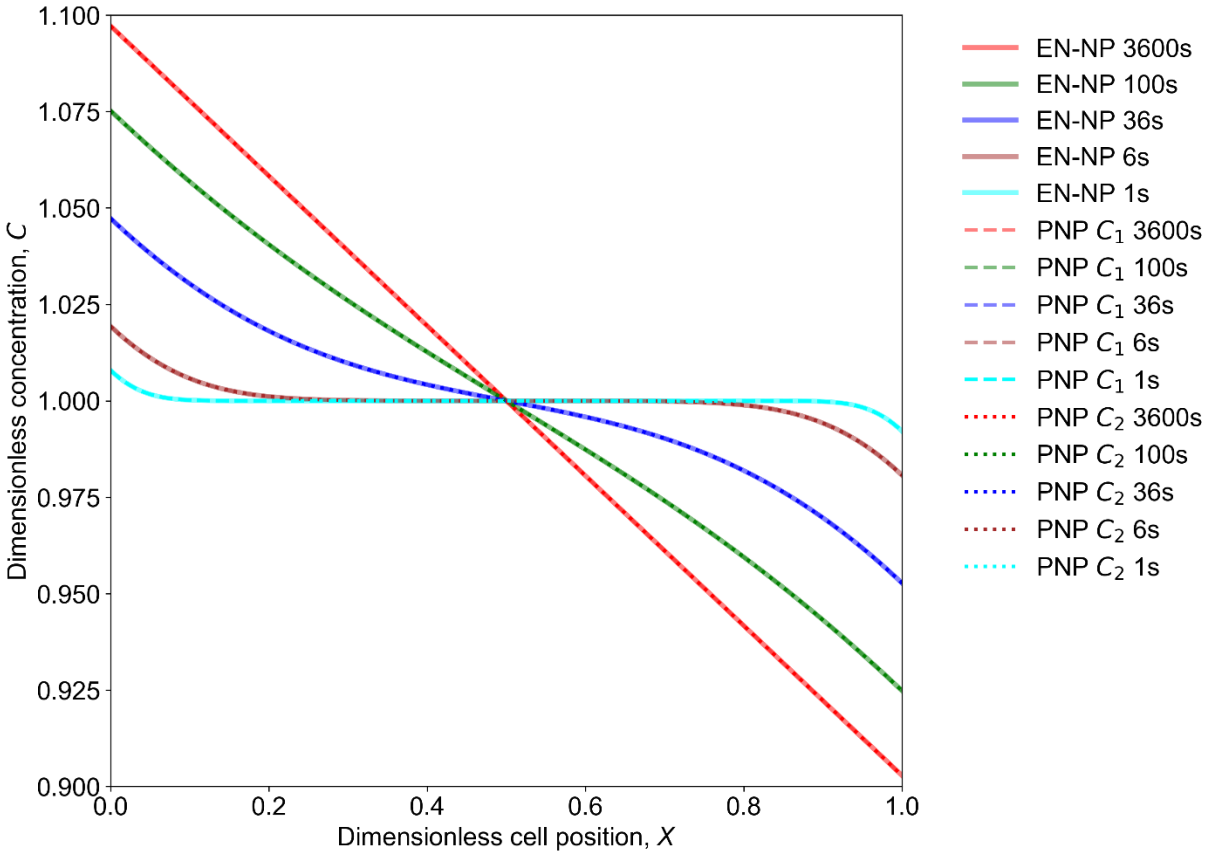

Figure 4.5. Comparison of the concentration profiles obtained from the different methods illustrating the expected agreement between both models.

Table 4-VI reports the difference of the values between EN-NP (analytical solutions) and PNP using 2000 internal nodes, at $x = 0$. We observed that the solutions of EN-NP at $x = 0$ were roughly the average of C_1 and C_2. From **Figure 4.5**, and **Figure 4.6**, it is reasonable to use EN-NP to replace the PNP to achieve efficient simulation because the differences of concentration and potential at $x = 0$ up to an hour are mostly negligible for practical applications. While a scaling analysis based

on model parameters can determine the applicability of EN-NP a priori, a goal of this work is to provide a robust code with the ability to simulate the PNP model for a wide range of parameter combinations and regimes where the departure from electroneutrality may become significant.

Table 4-VI. The deviation between EN-NP and PNP solutions

Time (s)	$\left\|C_{1,0}^{PNP}-C_{1,0}^{EN-NP}\right\|$	$\left\|C_{2,0}^{PNP}-C_{2,0}^{EN-NP}\right\|$	$\left\|\phi_0^{PNP}-\phi_0^{EN-NP}\right\|$ **(V)**
3600	4.855842×10^{-5}	4.855843×10^{-5}	3.544208×10^{-6}
100	4.982804×10^{-5}	$4.728882\text{e}\times10^{-5}$	2.449541×10^{-6}
36	4.933402×10^{-5}	4.778283×10^{-5}	2.480222×10^{-6}
6	4.956565×10^{-5}	4.755120×10^{-5}	2.439985×10^{-6}
1	4.946024×10^{-5}	4.765661×10^{-5}	2.437030×10^{-6}

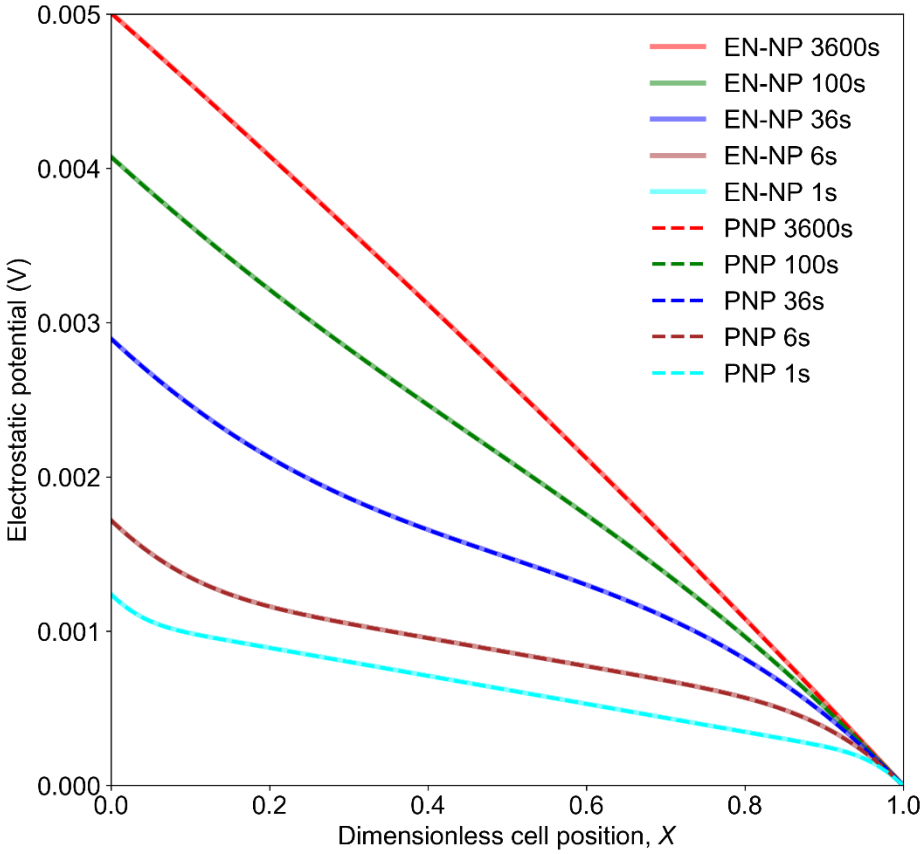

Figure 4.6. Comparison of PNP and EN-NP model in electrostatic potential.

Table 4-VII. The PNP solutions at x = 0 when t = 1 s by FVM scheme

h	C_1 (dimensionless)	C_2 (dimensionless)	ϕ (V)
1/4	1.049577	1.000995	0.720212×10^{-3}
1/8	1.026223	1.001931	0.876889×10^{-3}
1/16	1.015622	1.003477	0.996921×10^{-3}
1/32	1.011305	1.005232	0.109930×10^{-2}
1/64	1.009497	1.006461	0.116515×10^{-2}
1/128	1.008668	1.007150	0.120131×10^{-2}
1/256	1.008271	1.007512	0.122018×10^{-2}
1/512	1.008077	1.007697	0.122974×10^{-2}
1/1024	1.007981	1.007791	0.123452×10^{-2}
1/2048	1.007933	1.007838	0.123692×10^{-2}

The convergence analysis is repeated to examine the solution $x = 0$ when $t = 1$ s. The numerical results are shown in **Table 4-VII**. We used the results with $h = 1/2048$ as the benchmark to conduct the analysis. Taking spacing from 1/16 to 1/1024, the slope for C_1, C_2, and the potential are 1.189440, 1.074816 and 1.091390, respectively. Thus, only first order convergence is found for PNP, as opposed to the second order obtained for the EN-NP model. A detailed examination of the utility of a numerical scheme and its convergence characteristics for the PNP model is beyond the scope of this work. However, while the use of the PNP model may be tempting for greater physical detail, the faster convergence of the EN-NP model may result in more accurate and

meaningful solutions compared to the PNP model if the user can use only small number of node points or elements.

4.7.3. *Effect of ε*

Table 4-VIII reports solutions of the PNP model at relatively short times (1 s), as a function of the parameter ε. ε is a measure of the ratio of double-layer thickness to the characteristic system size, and it is useful to examine its effect on the solution. The results indicate a negligible change (~0.5%) in the dimensionless solutions below a certain lower threshold of ε. From a simulations standpoint, this means that for systems with ε values below this threshold, the solution obtained using the threshold ε may be used as an adequate approximation of that with the actual parameter set. This is because it is easier to treat larger values of ε numerically. The concept is similar to perturbation methods. It must be noted that even though the dimensionless solutions are nearly equal, the corresponding solutions obtained after transformation back to dimensional variables may differ in value depending on the specific set of parameters used. In addition, the specific value of this threshold is likely to vary with the design and transport parameters.

Table 4-VIII. PNP solutions at X = 0 and t =1 s for different values of ε

The base case value: $\varepsilon_0 = 3.76\times10^{-7}$ **;** $\delta = 0.38$

ε	C_1 **(dimensionless)**	C_2 **(dimensionless)**	**ϕ (V)**
ε_0	1.008885	1.006961	1.191527×10^{-3}
$\varepsilon_0\times10$	1.008885	1.006961	1.191479×10^{-3}
$\varepsilon_0\times10^2$	1.008885	1.006961	1.191470×10^{-3}
$\varepsilon_0\times10^3$	1.008886	1.006960	1.191401×10^{-3}
$\varepsilon_0\times10^4$	1.008986	1.006839	1.184991×10^{-3}
$\varepsilon_0\times10^5$	1.010807	1.003693	1.001104×10^{-3}
$\varepsilon_0\times10^6$	1.011778	1.000093	4.713492×10^{-5}

4.7.4. *Case Study: Comparing the model with experimental Li||Cu in situ cell data:*

To illustrate the application of the above computational models to inform our understanding of cell voltage response dynamics, we compare model predictions with experimental data. The experimental voltage response has been generated from a Lithium-Copper (Li-Cu) electrochemical cell. The detailed description and experimental set-up may be found in the Appendix B (**Section 7.3**). In particular, we use the conservative FVM model for transport, along with an electrode kinetic model to calculate the cell-voltage response. **Figure 4.7** depicts representative voltage-time data. In Phase 1, Li is stripped from the bulk Li electrode and deposited on the initially bare Cu substrate. In Phase 2, Li is stripped back from the Cu side (active Li is limited) and deposited at

the Li end. The direction of the applied current density is reversed in Phase 3, and the stripping and deposition switch back to the Li and Cu ends respectively. After Phase 1, sufficient Li is regarded to have deposited on Cu to approximate a Li||Li cell. In particular, a drop in voltage may be observed in Phase 3, which may be a signature of transitions in electrodeposition and electro-dissolution pathways, as determined by Wood et al. via *operando* studies. [32]

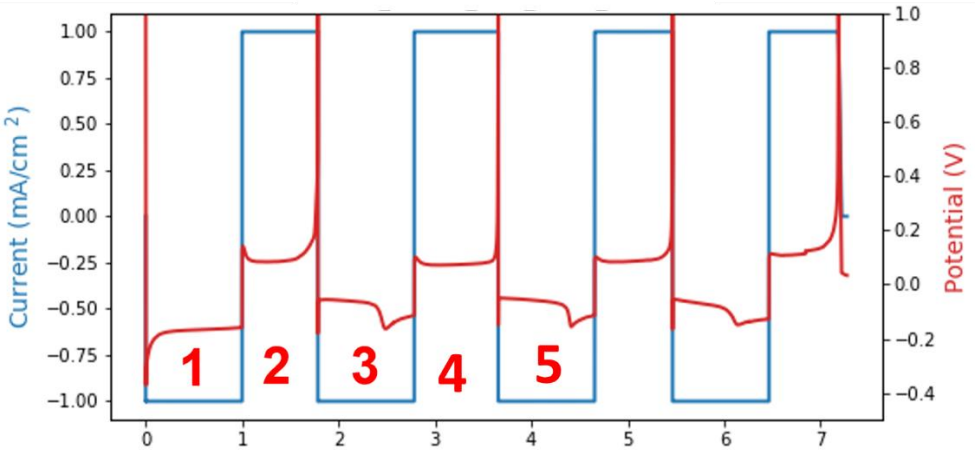

Figure 4.7. Experimental current and voltage profiles for the Li-Cu electrochemical cell at an applied current density of 1 mA/cm^2. The polarization spike in Phase 2 is attributed to the lack of electrochemically active Li remaining on the Cu electrode due to inefficiencies such as side reactions, corrosion, and electrically disconnected 'dead' Li.

In Wood et al., the transition between deposition and dissolution mechanisms is considered via a lumped, parallel pathway mechanism. Each reaction pathway is modeled as an electrode reaction described by a Butler-Volmer (BV)-type expression. The kinetic model equation at both stripping and deposition electrodes is given by[147]:

$$i = i_{0,ref}\left(\frac{c_{Li+}(x,t)}{c_{ref}}\right)^{\alpha_a}\left\{\left[\exp\left(\frac{\alpha_a F\eta(t)}{RT}\right)-\exp\left(-\frac{\alpha_c F\eta(t)}{RT}\right)\right]\right\} \quad (167)$$

Here, $i_{0,ref}$ is an 'effective' exchange current density that includes the contributions of the 'fast' and 'slow' reactions. α_a and α_c are anodic and cathodic charge transfer coefficients, and the other symbols have their usual meaning. The lithium-ion concentration at the electrode is denoted by $c_{Li^+}(x,t)$. $i_{0,ref}$ may be written as $i_{0,ref} = \theta i_{0,fast} + (1-\theta) i_{0,slow}$, where $i_{0,fast}$ and $i_{0,slow}$ are reference exchange current densities proportional to the rate constants of the slow and fast reactions respectively These parameters are lumped quantities that encode differences in deposit morphology, surface reactivity, inhomogeneities in the Solid Electrolyte Interphase (SEI), local ion transport effects and other complexities. The quantity θ denotes the surface coverage of the kinetically fast deposits.

The electrode potentials $\phi_s(t)$ are determined using the relation

$$\eta(t) = \phi_s^c - \phi \tag{168}$$

assuming zero open-circuit potential for the Li-metal reaction .

The cell voltage is thus defined as the difference between the computed $\phi_s(t)$ at each electrode:

$$V_{cell} = \phi_s^c - \phi_s^a \tag{169}$$

The calculation of the surface area fractions θ as a function of time, thus $i_{0,ref}$ necessitates assumptions about the morphology of the electrodeposits.[32,131] In this study, we circumvent the need for assumptions on deposit morphology and instead attempt the direct fitting of $i_{0,ref}$ at each electrode as a function of time. Thus:

$$i = i_{0,ref}(t)\left(\frac{c_{Li+}(x,t)}{c_{ref}}\right)^{\alpha_a}\left\{\left[\exp\left(\frac{\alpha_a F\eta(t)}{RT}\right)-\exp\left(-\frac{\alpha_c F\eta(t)}{RT}\right)\right]\right\} \tag{170}$$

The parameterization problem is thus the determination of $i_{0,ref}(t)$ profiles that minimize the error between the simulated and experimental values of the voltage response. We refer to these by $i_{0,effa}$ and $i_{0,effc}$ for the stripping and deposition electrodes respectively. In this example, the Mean Absolute Error (MAE) between model and experiment is used as the objective function, which is minimized. In addition, we focus solely on the Phases 3 and 5 in **Figure 4.7** in an attempt to capture the sharp voltage transition therein, and verify our predictions against data and literature reports.

In the systems approach, the effective exchange current density at each electrode is assumed as a piecewise quadratic profile in Lagrange form with two stages. Mathematically this is illustrated as:

$$i_{0,ref}(t) = \begin{cases} i_1\dfrac{t-t_1}{0-t_1}\cdot\dfrac{t-2t_1}{0-2t_1}+i_2\dfrac{t-0}{t_1-0}\cdot\dfrac{t-2t_1}{t_1-2t_1}+i_3\dfrac{t-0}{2t_1-0}\cdot\dfrac{t-t_1}{2t_1-t_1} & 0\le t\le 2t_1 \\ i_3\dfrac{T-t_2}{0-t_2}\cdot\dfrac{T-2t_2}{0-2t_2}+i_4\dfrac{T-0}{t_2-0}\cdot\dfrac{T-2t_2}{t_2-2t_2}+i_5\dfrac{T-0}{2t_2-0}\cdot\dfrac{T-t_2}{2t_2-t_2} & 2t_1\le t\le 2t_1+2t_2 \end{cases}$$
$$t_1=\frac{2500-0}{2},\ t_2=\frac{3600-2500}{2},\ T=t-2t_1 \tag{171}$$

This mathematical form is assumed for both $i_{0,effa}$ and $i_{0,effc}$. The experimental data is divided into two sets, before and after the voltage transition (t ~ 2500 s). This results in 5 parameters (i_1 - i_5) for $i_{0,ref}(t)$ at each electrode. The experimental data were sampled every 5 seconds over the whole half-cycle, and the upper and lower bound for exchange current densities were set at 0.1 and 100

A/m^2 respectively. The Global Optimization package in *Maple 2018* was used which uses a differential evolution approach for optimization. Results were also verified using gradient-based algorithms.

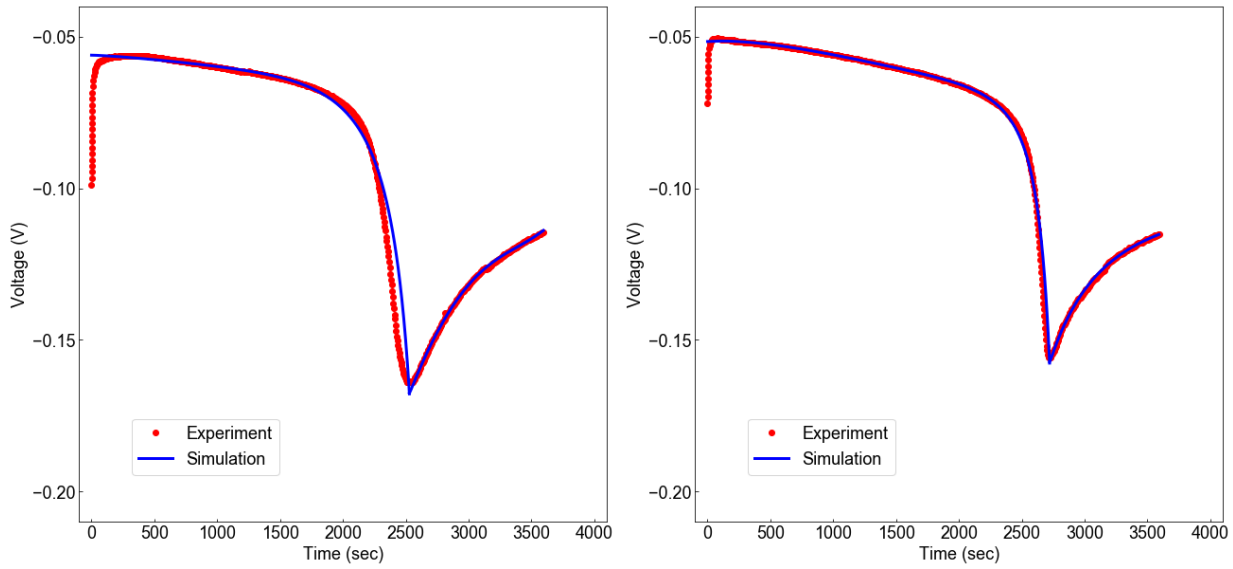

Figure 4.8. Comparison between model prediction and experimental voltage response for Phase 3(a) and Phase 5(b).

Figure 4.8 illustrates the agreement between the simulated voltage response and experimental data, even with this simplified model of exchange current density variation. The use of quadratic polynomials provides better fits compared to a piecewise linear approximation for the current density, but higher order polynomials provided only marginal reduction in error. In this case, the MAE corresponding to the optimal values of the coefficients i_j of equation (171) is approximately 5 mV.

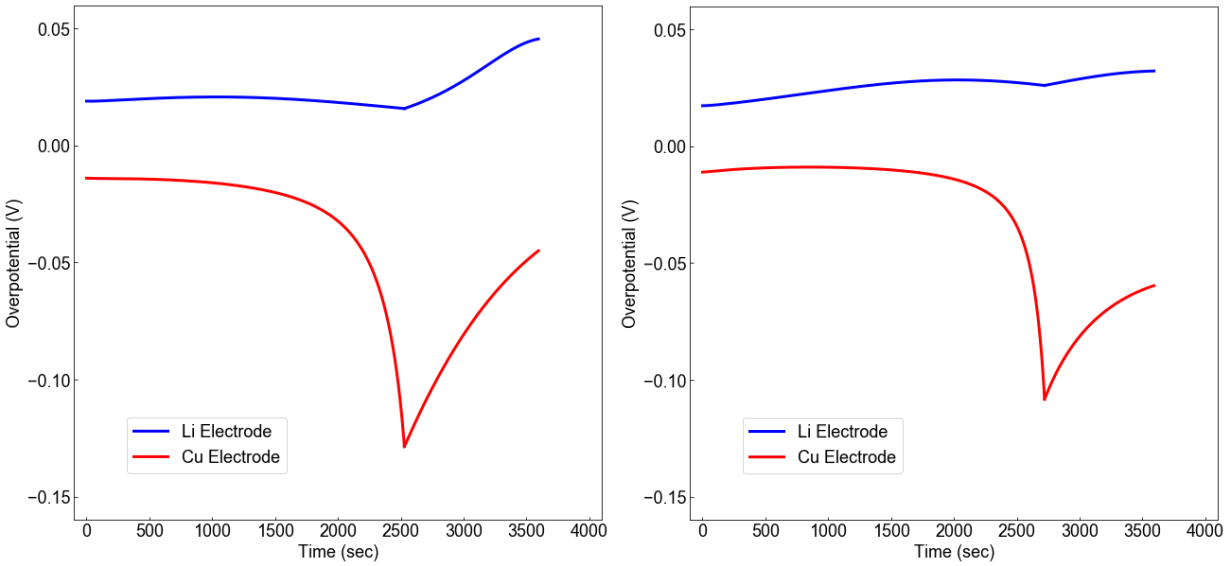

Figure 4.9. Simulated electrode overpotentials as a function of time for Phase 3 (a) and Phase 5 (b).

Figure 4.9 shows the variation of overpotentials as a function of time. It can be seen that the fitted polynomials predict a sharp drop in overpotential at the Cu electrode, in addition to a smaller increase at the Li electrode. The anodic signature is likely due to the transition between 'fast' and 'slow' pathways. At the Li electrode, this may be the exhaustion of electrochemically deposited Li and their associated faster kinetics, and the gradual transition to stripping from the bulk. The sharp drop at the Cu electrode is more pronounced and suggests a transition in which Li deposits via the formation of new nuclei as opposed to growing on existing deposits, possibly due to passivation by SEI formation. This likely explains the sudden drop followed by a gradual rise in overpotential. The fitted profiles were verified by simulation and comparison with multiple data sets and exhibited adequate agreement for each case. The trends in electrode polarization track the variations in fitted exchange current density of **Figure 4.10**. The increase in polarization of both electrodes is due to the reduction in effective exchange current densities, and this is borne out in

the profiles of **Figure 4.10**, establishing the self-consistency of the model.

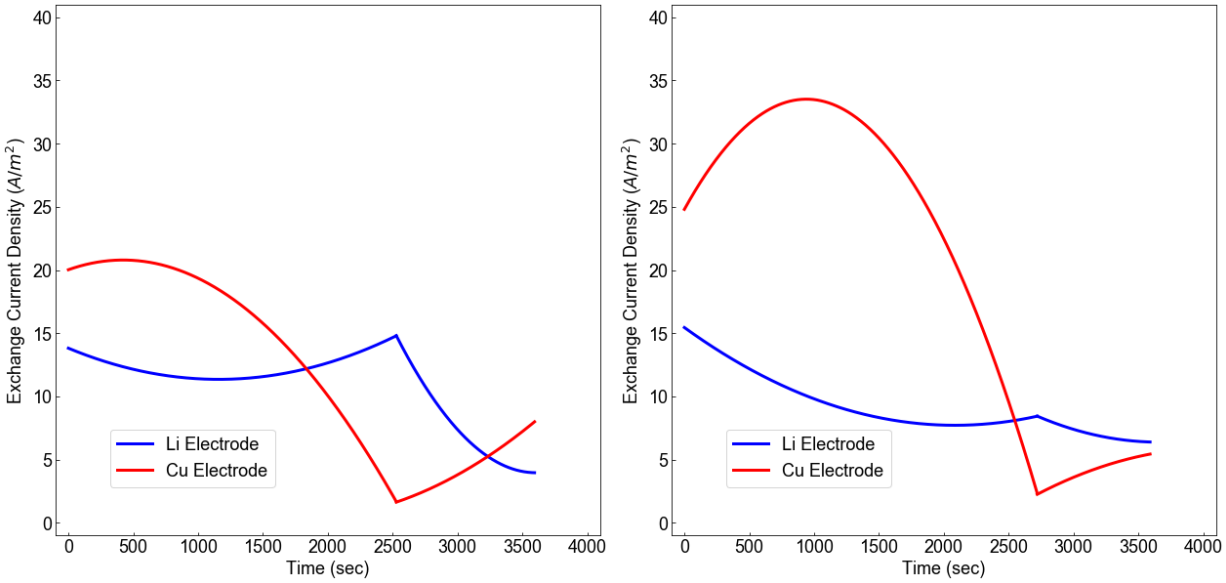

Figure 4.10. Temporal variation of the fitted exchange current densities for Phase 3 (a) and Phase 5 (b).

The above approach used an unconstrained approach which allowed the $i_{0,ref}(t)$ to vary freely within a physically acceptable range. We now consider a different mechanism for the observed voltage transition reported in literature. In particular, the exhaustion of kinetically fast deposits at the stripping electrodes has been reported as the dominant cause of the voltage transition of Phase 3, and nucleation events at the deposition electrodes are not observed.[32] A gradual increase in polarization at the Cu electrode is expected due to continually reducing Li^+ concentration. In addition, the surface area of deposits is expected to reduce as the initial deposits grow in size and eventually merge. This effect is expected to manifest in in the gradual reduction of $i_{0,effc}$ with time. However, it is possible that the reduction in $i_{0,effa}$ due to the unavailability of the electrochemically

deposited Li, with its substantially enhanced kinetics is more significant and has a greater contribution to the voltage drop. This mechanism may be expressed in the optimization problem formulation through an additional constraint on the exchange current density at the Cu electrode. We can specify that the exchange current density can only decrease with time. Mathematically, this is expressed as:

$$i_{j+1,c} \le i_{j,c};\ j = 1...5 \tag{172}$$

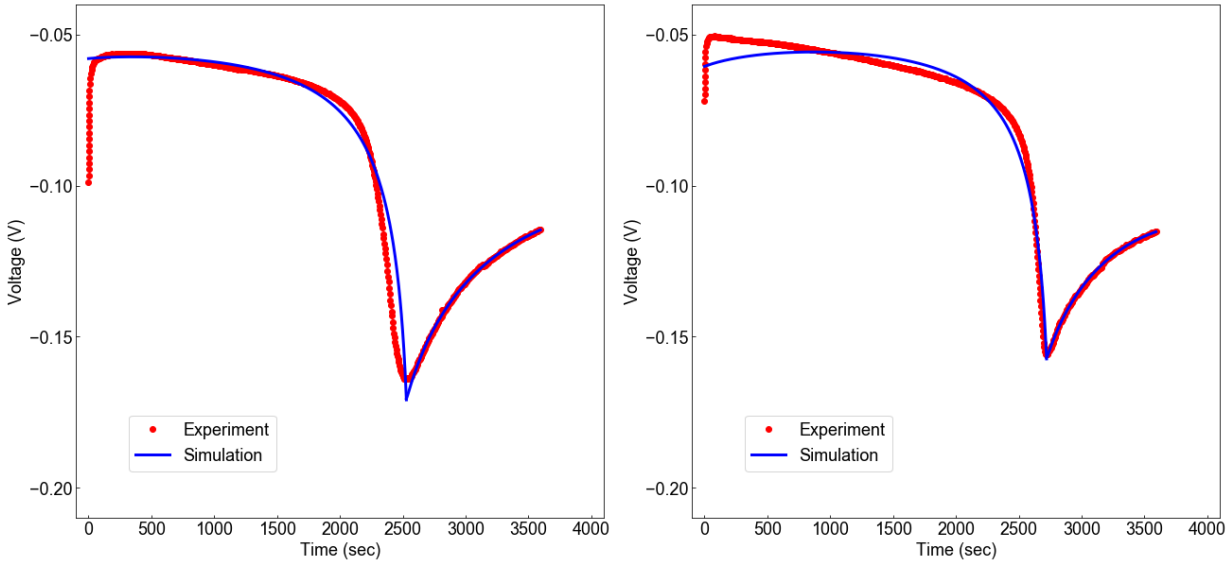

Figure 4.11. Comparison between model prediction and experimental voltage response for Phase 3 (a) and Phase 5 (b) with constraints at Cu electrode.

Figure 4.11 shows the voltage profiles obtained for this constrained case and indicates reasonable agreement between simulation and experimental data. Despite the disagreement in the initial part of Phase 5, the voltage transition is adequately captured. **Figure 4.12** shows the simulated temporal

evolution of electrode overpotentials. In contrast to the profiles of **Figure 4.10**, the overpotential of Li electrode is a dominant cause of voltage drop, while the Cu electrode overpotential increases much more slowly. The MAE between the model and data is only marginally higher compared to the previous unconstrained case (~ 6 mV vs 5 mV).

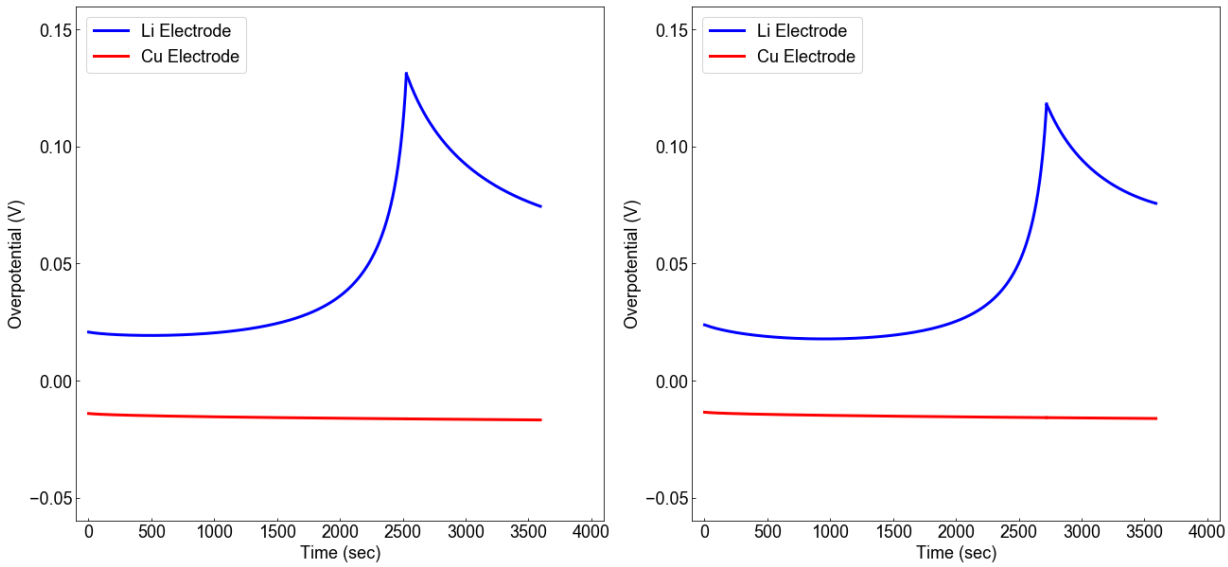

(a) (b)

Figure 4.12. Simulated electrode overpotentials as a function of time for Phase 3(a) and Phase 5(b) with constraints at Cu electrode.

The behavior of overpotential at both electrodes is a result of the dynamics of the effective exchange current densities, as shown in **Figure 4.13**. While the exchange current density at Cu electrode is almost constant, the Li electrode shows the drop and recovery of exchange current density over time. The variation of the exchange current density is over 15 A/m^2, and it results in the increase in overpotential in **Figure 4.12**. This result is consistent with the mechanism of transition from fast to slow stripping. The constrained optimization suggests that mechanisms

reported previously for Li-Li symmetric cells are able to match the voltage signatures for the experimental cell considered here. A more detailed model of Li deposition on Cu surfaces will help identify the precise mechanism underlying the voltage transitions and better explain the trends in the estimated parameters.

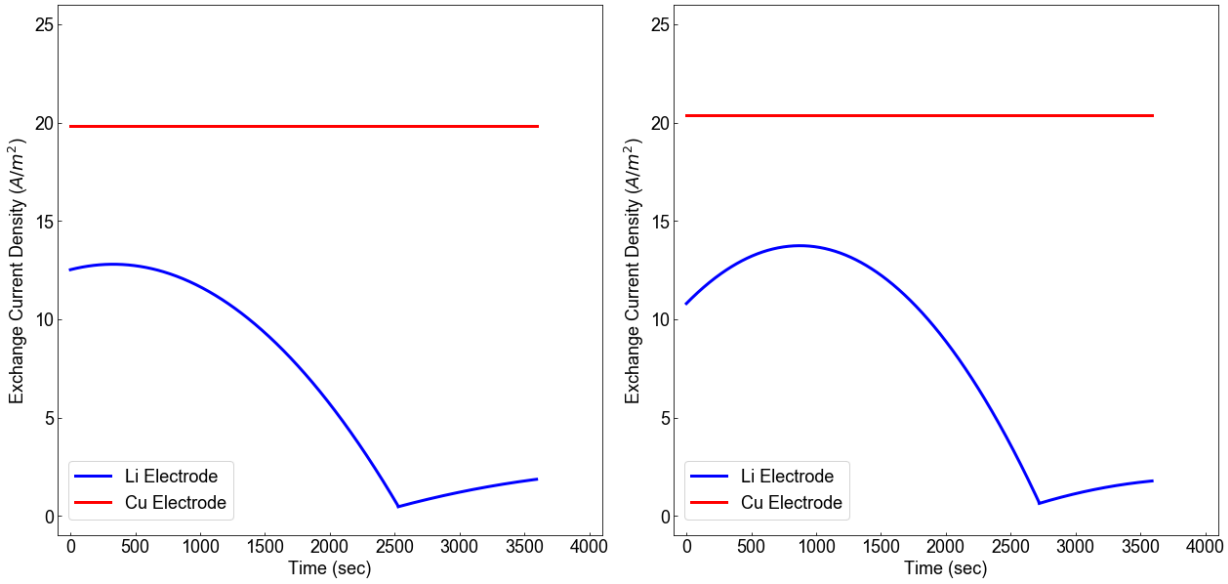

(a) (b)

Figure 4.13. Temporal variation of the fitted exchange current densities for Phase 3(a) and Phase 5(b) with constraints at Cu electrode.

The systems-level approach is thus able to predict the key signatures in voltage response and can potentially provide useful insights into the relationship between voltage response and internal electrochemistry. The analysis is substantially enabled by the fast transport model, which makes possible the simulation and parameterization over multiple cycles.

4.8. Conclusion

Transport models based on the Nernst-Planck (NP) flux laws were analyzed in the context of

lithium symmetric cells. Both EN-NP and PNP models were considered for a binary electrolyte. The EN-NP model (with electroneutrality assumption) was found to capture the concentration and electrostatic potential dynamics reasonably well compared to the full PNP model, but a robust and efficient simulation algorithm was demonstrated for the full PNP model. An analytical solution was reported for the EN-NP system. The validity of the model and the simulation approach in explaining the experimental behavior are also examined. This was done by coupling the efficient transport models with electrode kinetics models and employing a systems-level parameterization approach to obtain time-dependent exchange current densities. The systems-level approach is able to achieve quantitative agreement with the transitions in experimental voltage data, though the analysis suggests that more detailed physics are required in order to provide mechanistic explanations for the trends in the estimated parameters. However, the fast transport model allows the quick evaluation of different candidate parameter profiles by efficiently simulating the resulting voltage response, complementing experiments and helping achieve an improved understanding of lithium metal anodes.

5. Directions for Future Research

5.1. Tanks-in-Series Models

5.1.1. *Tank Models for Parameter Estimation*

Recalling the volume-averaged electrolyte equations (46) - (48) of the Tank Model, we have

$$\frac{d\overline{c_1}}{dt} = \frac{\dfrac{2D(c_{12})(\overline{c_2}-\overline{c_1})}{\dfrac{l_1}{\varepsilon_1^{b_1}}+\dfrac{l_2}{\varepsilon_2^{b_2}}}}{\varepsilon_1 l_1} + \left(1-t_+^0\right)\frac{i_{app}}{\mathrm{F}\varepsilon_1 l_1} \tag{173}$$

$$\frac{d\overline{c_2}}{dt} = \frac{\dfrac{-2D(c_{12})(\overline{c_2}-\overline{c_1})}{\dfrac{l_1}{\varepsilon_1^{b_1}}+\dfrac{l_2}{\varepsilon_2^{b_2}}} + \dfrac{2D(c_{23})(\overline{c_3}-\overline{c_2})}{\dfrac{l_2}{\varepsilon_2^{b_2}}+\dfrac{l_3}{\varepsilon_3^{b_3}}}}{\varepsilon_2 l_2} \tag{174}$$

$$\frac{d\overline{c_3}}{dt} = \frac{\dfrac{-2D(c_{23})(\overline{c_3}-\overline{c_2})}{\dfrac{l_2}{\varepsilon_2^{b_2}}+\dfrac{l_3}{\varepsilon_3^{b_3}}}}{\varepsilon_3 l_3} - \left(1-t_+^0\right)\frac{i_{app}}{\mathrm{F}\varepsilon_3 l_3} \tag{175}$$

The above equations may be conveniently written as

$$\frac{d\overline{c_1}}{dt} = \frac{K_{12}}{V_{l,1}}(\overline{c_2}-\overline{c_1}) + \left(1-t_+^0\right)\frac{i_{app}}{\mathrm{F}V_{l,1}} \tag{176}$$

$$\frac{d\overline{c_2}}{dt} = \frac{-K_{12}(\overline{c_2}-\overline{c_1}) + K_{23}(\overline{c_3}-\overline{c_2})}{V_{l,2}} \tag{177}$$

$$\frac{d\overline{c_3}}{dt} = \frac{-K_{23}}{V_{l,3}}(\overline{c_3} - \overline{c_2}) - \left(1 - t_+^0\right)\frac{i_{app}}{\mathrm{F}V_{l,3}} \tag{178}$$

Where the governing equations have been expressed in terms of equivalent 'mass transfer' coefficients, volume and source terms. In the above equations, the $K_{ij} = \dfrac{2D(c_{ij})}{\dfrac{l_i}{\varepsilon_i^{b_i}} + \dfrac{l_j}{\varepsilon_j^{b_j}}}$ have units of mass transfer coefficient (m/s), and $V_{l,i}$ denotes the electrolyte volume (per unit area) in region i with units of length. The transport parameters in the electrolyte current balance (56) may also be grouped similarly

$$\begin{aligned} i_{app} &= -S_{12}\left(\overline{\phi_{l,2}} - \overline{\phi_{l,1}}\right) + \frac{2RT(1-t_+^0)}{F}S_{12}\left(\frac{\overline{c_2} - \overline{c_1}}{c_{12}}\right) \\ i_{app} &= -S_{23}\left(\overline{\phi_{l,3}} - \overline{\phi_{l,2}}\right) + \frac{2RT(1-t_+^0)}{F}S_{23}\left(\frac{\overline{c_3} - \overline{c_2}}{c_{23}}\right) \end{aligned} \tag{179}$$

Where, the thermodynamic factor $\nu(c_{ij}) = 1$ for simplicity. Here, $S_{ij} = \dfrac{2\kappa(c_{ij})}{\dfrac{l_i}{\varepsilon_i^{b_i}} + \dfrac{l_j}{\varepsilon_j^{b_j}}}$ have units of S/m^2. The lengths used in the flux approximation, which for this case is $\frac{l_i}{2}$, are present in the expressions for K_{ij} and S_{ij}. Estimating these quantities is equivalent to deriving a suitable flux or gradient approximation. For constant diffusivity, the electrolyte concentration equations constitute a coupled linear system of Ordinary Differential Equations with constant coefficients. The form of these equations suggests a possible parameter estimation strategy in which the Tank

Model is matched against experimental data by direct estimation of the 'consolidated' transfer coefficients. Variations due to concentration-dependent transport properties, or transients in which the 'steady state layer' is attained over a characteristic timescale comparable to the total discharge time can potentially be handled by estimating average values over the course of the process. The similarity of the mathematical model to conventional Continuous Stirred Tank Reactor (CSTR) systems is noteworthy and suggests scope for exploiting the extensive control theory developed for CSTR systems.

5.1.2. *Extensions and Future Work*

The generalized methodology developed herein can be applied to electrochemical models for more complex systems, including conversion chemistries such as Li-sulfur and lead-acid batteries. The application of this technique for a PDE model for Li-sulfur batteries has also been accomplished.[148] Future work also includes developing approximate analytical and perturbation solutions for this model, and integration with capacity degradation models. The above formulation can also be tested using standard parameter estimation techniques.

In this work, we defined the scope of our work as the detailed development of the Tanks-in-Series model, and evaluation of its predictions against the full p2D model in terms of accuracy and computational speed. Some comparisons against SPM were provided to illustrate the improvement over the most common electrochemical models for advanced BMS. While conceptual differences between this model and other methodologies in literature were touched upon, a detailed comparison was avoided to maintain focus on the details of the generalized Tanks-in-Series methodology. The literature on reduced-order p2D models is vast with each technique possessing

its advantages, limitations, and conditions for applicability. Future work will involve more detailed analyses of the differences in the Tanks-in-Series approach and other methods, and their impact on key performance measures and model predictions.

The ~ms computation time of the multi-cell models suggests promise for use in algorithms for advanced BMS functions such as SoC estimation, cell balancing, temperature control, and SoH monitoring in conjunction with physics-based degradation models. Future work will thus attempt to demonstrate the single-cell and stack Thermal Tank models for these applications, especially for practically relevant cell and pack designs and parameters. A key focus is on demonstrating these efficient models for parameter estimation and optimal charging. Additionally, we intend to evaluate the models against other classes of reduced-order thermal models for accuracy and efficiency metrics. A third goal is the integration of the Thermal Tank Model into MSMD frameworks, which can study more realistic temperature distribution scenarios, for the design and safety analyses of large format cells.

From a model development standpoint, interfacial thermal resistances are likely to increase the magnitude of stack temperature gradients, leading to inaccuracies in the Tank Model approximations. Additionally, while briefly touched upon, the influence of temperature and cell-level geometric, kinetic and transport parameters on the accuracy of stack-level predictions needs systematic evaluation. The derivation of the temperature approximations in the presence of interfacial resistances may be found in **Section 6.2**, and its implementation is a key extension of current work. An additional extension is the application of the Tanks-in-Series methodology to cylindrical coordinates, characterizing accuracy and computational performance vis-à-vis both full-order and lumped models for cylindrical Li-ion cells. Combined with efficient two-

dimensional schemes for the current and potential distributions[51,96], it may be possible to develop an efficient MSMD model for entire large-format cells that can be integrated into real-time frameworks. The feasibility of such an extension is worth examining in future work.

5.2. Lithium Metal Modeling

5.2.1. *Electrochemical-Mechanical Models for Lithium Metal Batteries - Theory*

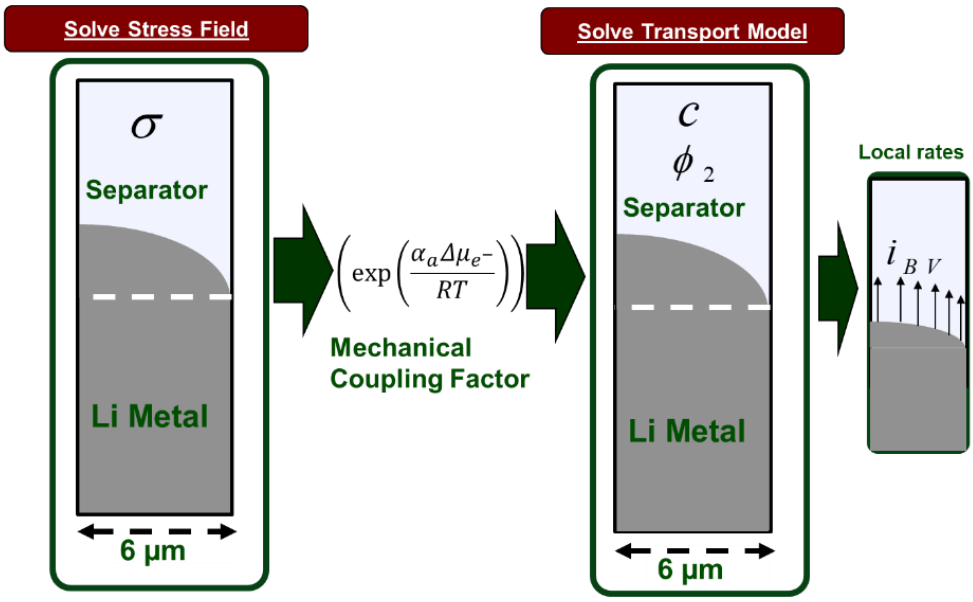

Figure 5.1. Proposed localized modeling approach.

In order to explore the effect of external pressure on Li electrodeposition, models must be able to capture the effect of pressure on the mechanical deformation and evolution of the electrode-electrolyte interface. To this end, the first objective is the development of a localized electrodeposition model that incorporates mechanical effects. The deformation of the interface between the Li metal and the separator results in the generation of stresses, which in turn modify the electrochemical potentials of the species at the interface. This is then manifested in variations

in local electrode kinetics parameters across the interface. **Figure 5.1** illustrates the proposed coupled modeling approach. In the first step, the stress and displacement fields around a representative metal-separator interface are solved. With the computed stress field, during postprocessing, the hydrostatic and deviatoric components of the stresses are computed and used to compute the BV enhancement factor, and thus the local reaction rate. In combination with the solution of the electrolyte field, this sequential solution approach is expected to give the variation of a deformed electrode-electrolyte interface as a function of time. In particular, this aims to build on existing literature by extending the approaches for determining initial deposition rates to predict temporal evolution.[149] This objective deals with the first step, i.e. solution of the stress field and computation of the BV enhancement factor for a *given state* of the interface.

The theory of Monroe and Newman links the stress distributions generated due to pressure, surface tension, and other electrochemical variables is through a modification of the exchange current density in the Butler-Volmer equation. This factor, hereafter referred to as the 'BV enhancement factor', rigorously corrects for the energetic effects of mechanical deformation.[34] Thus

$$i_{loc} = i_{0,ref}\left(\frac{c_{Li+}(x,y,t)}{c_{ref}}\right)^{\alpha_a}\left(\exp\left(\frac{\alpha_c \Delta\mu_{e^-}}{RT}\right)\right)\left\{\left[\exp\left(\frac{\alpha_a F\eta_{loc}(t)}{RT}\right)-\exp\left(-\frac{\alpha_c F\eta_{loc}(t)}{RT}\right)\right]\right\} \tag{180}$$

Where the BV enhancement factor is given by

$$\Delta\mu_{e^-} = -\frac{1}{2}\left(\overline{V_{Li}}+(1-t_+^0)\overline{V_{LiX}}\right)\times\left\{\vec{e_n}\cdot[\vec{e_n}\cdot(\underline{\underline{\tau_d^{Li}}}-\underline{\underline{\tau_d^{s}}})]\right\}+\frac{1}{2}\left(\overline{V_{Li}}-(1-t_+^0)\overline{V_{LiX}}\right)\times\left\{\Delta p^{s}+\Delta p^{Li}\right\} \tag{181}$$

Where the symbols above have the same meaning as in equation (170) and the subscript *loc* denotes local quantities.

Where the superscripts pertain to the separator and Li metal domains, respectively. Δp denotes the hydrostatic component of the stress tensor at the interface, and $\underline{\underline{\tau}}$ denotes the shear or deviatoric portion. The parameter depends on the transport number t_+^0 of the Li-salt used in the electrolyte, as well as thermodynamics, through the component partial molar volumes $\bar{V}$. $\vec{e_n}$ is the normal vector at the interface. The components of the stress tensor are obtained by the solution of the steady-state equation of motion, neglecting viscoelastic effects, which is deemed reasonable for the mechanical properties of a typical separator. In the first iteration, we also neglect plastic deformation, which is to be included in future iterations of the model. Thus

$$\vec{\nabla}\cdot\left(\underline{\underline{\sigma}}\right)=\vec{0} \tag{182}$$

Where the theory of linear elasticity relates the stresses in the two domains as

$$\begin{aligned}
&\underline{\underline{\sigma}}=\underline{\underline{\tau_d}}+p\underline{\underline{I}}\\
&\underline{\underline{\sigma}}=\frac{2\nu_i G_i}{1-2\nu_i}tr(\underline{\underline{\varepsilon_i}})-2G_i\underline{\underline{\varepsilon_i}}\\
&\underline{\underline{\varepsilon_i}}=\frac{1}{2}\left(\vec{\nabla}\vec{u_i}+\left(\vec{\nabla}\vec{u_i}\right)^T\right) \qquad i\in\{Li,s\}
\end{aligned} \tag{183}$$

Here, ν_i and G_i denote the Poisson's ratio and shear modulus in a given domain. $\vec{u_i}$ denotes the displacement vector, which is the basis for computation of the stress distributions.

5.2.2. *Preliminary Electrochemical-Mechanical Model*

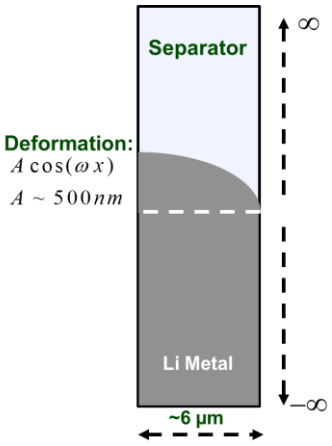

Figure 5.2. Modeling schematic for the electrochemical-mechanical model.

Figure 5.2 shows the computational domain and boundary conditions used in the first iteration. In the preliminary model, we apply linear elasticity theory following Monroe and Newman.[44] In order to simulate an initial Li metal deposit, a sinusoidal shape is applied to the electrode-separator interface. A semi-infinite domain is assumed in the vertical direction as a first approximation. This assumption is justified by the original authors as well as by numerical investigations, which show that non-zero deformations are restricted to a few hundred nanometers of the interface.[44,150] Periodic boundary conditions are applied in the horizontal direction, and tangential forces are balanced at interfaces, where continuity is also imposed.[44] With these boundary conditions, an analytical solution for displacement is obtained. The unknown constants in the solutions were rigorously obtained by numerical solution of the boundary conditions, in contrast to the Monroe approach, which derived approximate values assuming small-amplitude deformations.[34,44]

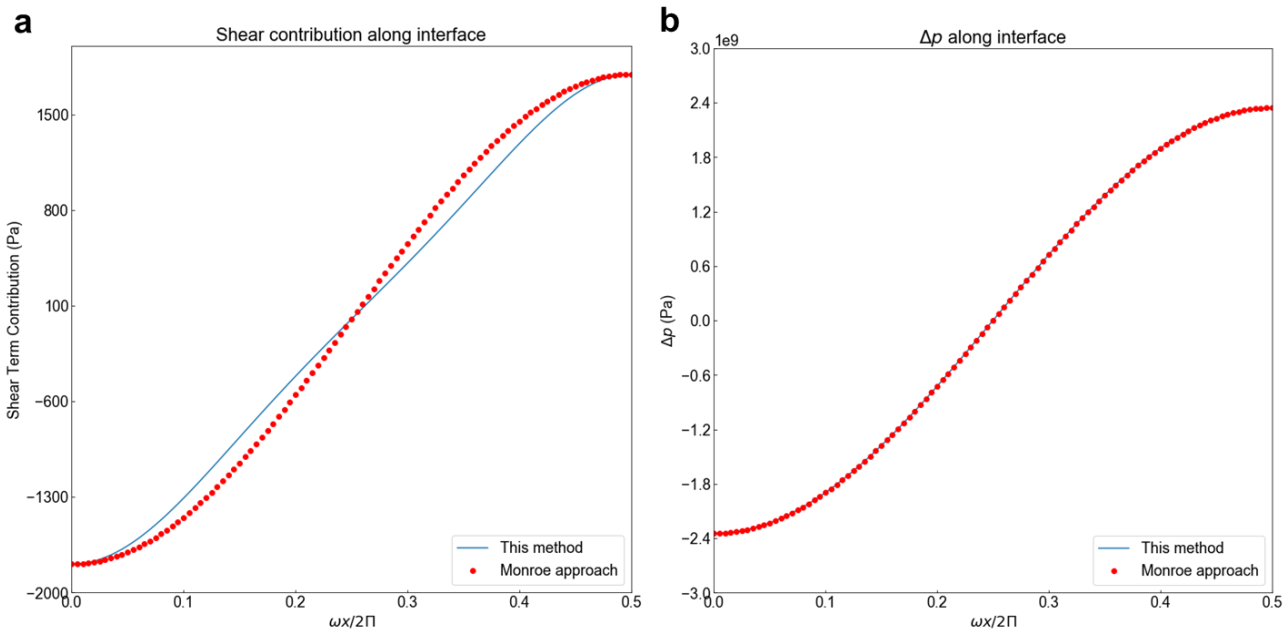

Figure 5.3. Profiles of the (a) tangential and (b) normal contributions to the BV enhancement factor for a soft separator, $G_s \sim 10^{-6} G_{Li}$. A Poisson's ratio of $\nu_s = \nu_{Li} = 0.33$ is used for the simulation.

As depicted in equation The BV enhancement factor is characterized by two chief contributions, each associated with normal and tangential forces along the interface. The relative stiffness moduli of the electrode G_{Li} versus the separator G_s is a parameter that affects this value, and thus the mechanical enhancement of electrode kinetics. **Figure 5.3** illustrates the profiles for $G_s / G_{Li} \sim 10^{-6}$,a value typical for liquid or soft-solid electrolytes. The profiles are compared against the more approximate solution of Monroe et al., with the agreement providing verification of our preliminary model. Similar profiles are illustrated in **Figure 5.4** for the case of a very stiff separator, $G_s / G_{Li} \sim 2$. In particular, a significant difference in the tangential contributions is observed as a result of increasing separator modulus. This effect is additionally reflected in **Figure 5.5**, illustrating the variation of the BV enhancement term along the electrode-separator interface. The stiff separator results in a more uniform profile of the enhancement factor, predicting more

uniform local deposition rates, in contrast to the soft separator case, for which the predicted enhancement factor at the protrusion tip is orders of magnitude higher than elsewhere along the interface. The predicted results agree well with the solutions reported in literature, which serves as verification of the preliminary model. It is interesting to note the maximum in rate constant at an intermediate point for the stiff separator case, where the local rate constant is substantially higher than that predicted by the approximate model. The numerical solution thus predicts greatly enhanced rate constant in the 'valley' region, which might have implications for the structure of the interface during evolution, due to the rapid initial filling up of the valley region.

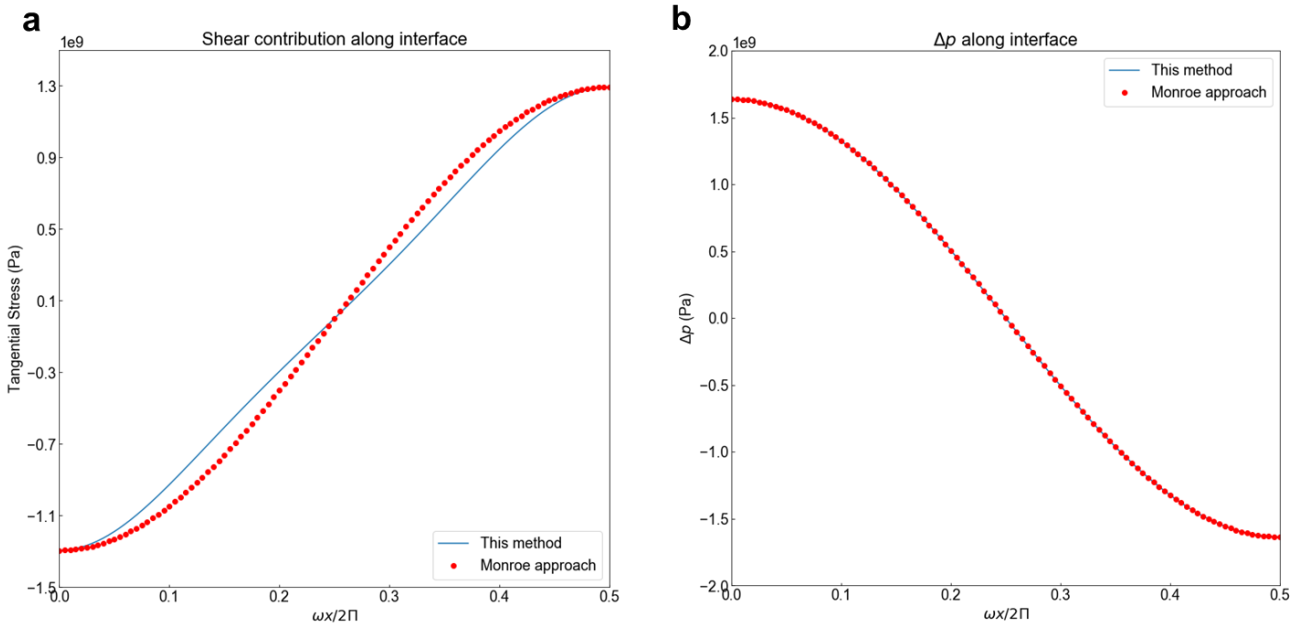

Figure 5.4. Profiles of the (a) tangential and (b) normal contributions to the BV enhancement factor for a stiff separator, $G_s \sim 2G_{Li}$.

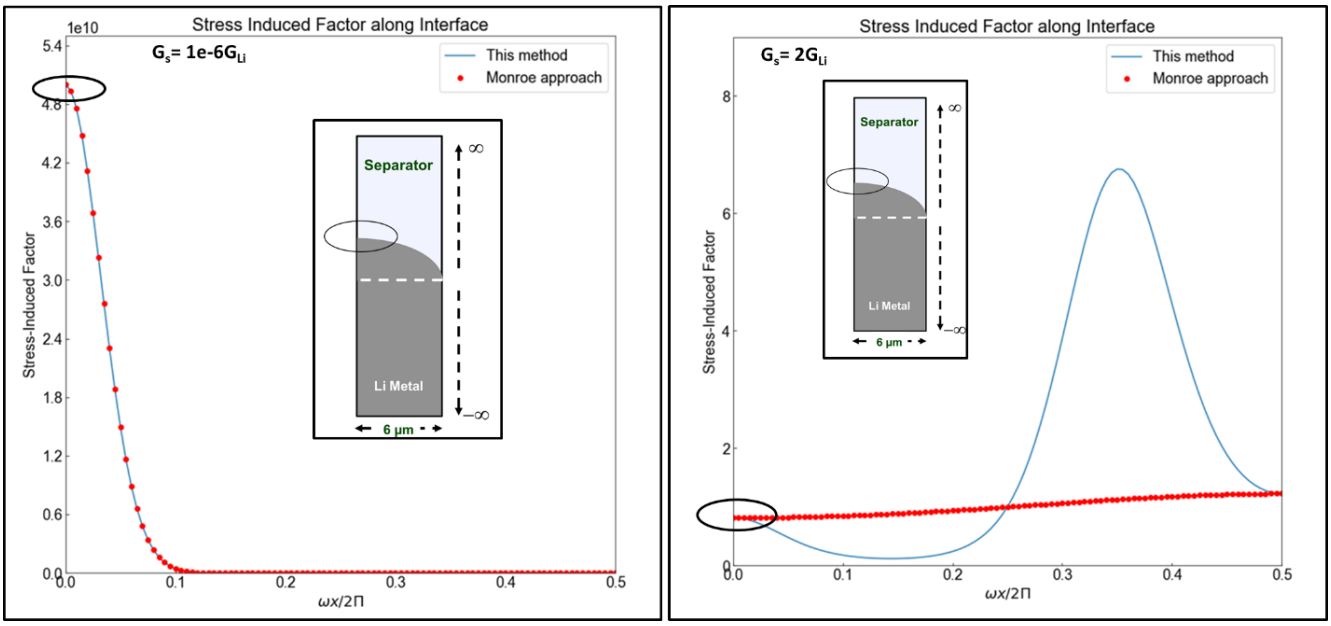

Figure 5.5. Butler-Volmer enhancement factor profiles along the electrode interface

5.2.3. *Extensions and Future Work*

The calculated values of the BV enhancement factor, and the substantial enhancement at the protrusion tips (~10^{10}), suggests that unstable deposition will occur for all but the most stiff separators. This is in direct contradiction with experimental data, however, where stable cell operation is observed even for typical Li metal batteries, albeit with substantially reduced coulombic efficiency. This is in part because the models based on linear elasticity tend to ignore plastic deformation effects, which are significant for Li metal anodes on account of their low yield strengths relative to other metals. Indeed, plastic flows have the ability to physically suppress dendritic protrusions, thereby smoothening Li electrolyte interfaces.[30,149,151] These considerations are the motivation for augmenting the current model with more realistic theories for the mechanical response of Li metal. Recent work has focused on the development of theories for the plastic response for Li metal.[40,151,152] . In addition, as mentioned, the precise coupling mechanism for the

simultaneous evolution of the deformed interface and other electrochemical engineering models needs to be determined. To achieve this, we intend to leverage past work in two-dimensional modeling for cathode architectures. We are evaluating finite-element techniques, spectral methods, and phase-field techniques. [51,153,154] A substantial research effort in past work involved the two-dimensional modeling using spectral methods and finite-element softwares, which makes us well-positioned to complete this refinement. A recent perspective article outlined the expected computational challenges associated with the simulation of moving Li metal interfaces.[155] These models need to be coupled with realistic deformation models to achieve the unified multiscale continuum simulation framework.

The modified electrode-kinetics parameters obtained thus will be fed into a classical, macrohomogeneous pseudo two-dimensional (p2D) model,[45] which can be combined with a one-dimensional moving boundary formulation for the Li anode.[39] The modified kinetic parameters from the basic mechanical model can be used to study the manifestation of these mechanical effects on the cell-voltage response. This is the ultimate integration envisaged, i.e. predicting the emergent cell-level voltage response arising out of predictions from the localized models coupled with reformulated electrochemical engineering models. The voltage response from this 'pressure-aware p2D model' will be studied for full Li metal cells under pressure for experimentally relevant conditions and cycling.[156,157] In the first iteration, in addition to the averaged parameters from the mechanical model, a simple one-dimensional cell-level model has also been developed to study the modified kinetics on overall voltage response. These models leverage modifications of p2D-type models developed in past work with Li-ion batteries.[41,42] A secondary aspect relates to the modification of the two-dimensional interface model by the addition of localized transport models

based on electrochemical engineering principles.[154] This in turn will introduce the ability to simulate the dynamic evolution of the anode-electrolyte interface, with attendant improvements in understanding morphological evolution during practical operation.

6. Appendix A: Additional Derivations for the Thermal Tank Model

6.1. Derivation of Volume-averaged Heating Terms in The Thermal Tank Model

In region 1, the volumetric ohmic heat generation term is given by

$$Q_{ohmic,1} = -i_{s,1}\frac{\partial \phi_{s,1}}{\partial x} - i_{l,1}\frac{\partial \phi_{l,1}}{\partial x} \tag{184}$$

This expression is based on the assumption of Rao and Newman[110], namely that the ohmic heat dissipation is due to potential gradients in both solid and liquid phases, and concentration effects are ignored.

Following the general Tanks-in-Series averaging procedure in one-dimension, we have

$$\overline{Q_{ohmic,1}} = \left(\frac{1}{l_1}\right)\int_{x=0}^{x=l_1} Q_{ohmic,1}dx = \left(\frac{1}{l_1}\right)\left(\int_{x=0}^{x=l_1} -i_{s,1}\frac{\partial \phi_{s,1}}{\partial x}dx - \int_{x=0x}^{x=l_1} i_{l,1}\frac{\partial \phi_{l,1}}{\partial x}dx\right) \tag{185}$$

As mentioned previously, the solid phase ohmic drop is generally negligible compared to that of the liquid phase.[41] Therefore, the solid phase ohmic contribution may also be neglected, and Equation (185) becomes

$$\overline{Q_{ohmic,1}} \approx -\left(\frac{1}{l_1}\right)\int_{x=0x}^{x=l_1} i_{l,1}\frac{\partial \phi_{l,1}}{\partial x}dx \tag{186}$$

Integrating by parts, we have

$$\overline{Q_{ohmic,1}} = -\left(\frac{1}{l_1}\right)\left(i_{l,12}\phi_{l,1,x=l_1} - i_{l,01}\phi_{l,1,x=0}\right) + \left(\frac{1}{l_1}\right)\int_{x=0}^{x=l_1} \frac{\partial i_{l,1}}{\partial x}\phi_{l,1}dx \tag{187}$$

From **Figure 3.2**, we have, $i_{l,12} = i_{app}$, and $i_{l,12} = 0$. Using these relations, and the standard notation, we obtain

$$\overline{Q_{ohmic,1}} = -\left(\frac{1}{l_1}\right)\left(i_{app}\phi_{l,12}\right) + \left(\frac{1}{l_1}\right)\int_{x=0}^{x=l_1} \frac{\partial i_{l,1}}{\partial x}\phi_{l,1}dx \tag{188}$$

Now, we can simplify the integral in the above equation by using Equation (49) in Ref. 41

$$\overline{Q_{ohmic,1}} = -\left(\frac{1}{l_1}\right)\left(i_{app}\phi_{l,12}\right) + \left(\frac{1}{l_1}\right)\int_{x=0}^{x=l_1} Fa_1 j_1\phi_{l,1}dx \tag{189}$$

Furthermore, using the volume-averaged relation, we have

$$\overline{Q_{ohmic,1}} = -\left(\frac{1}{l_1}\right)\left(i_{app}\phi_{l,12}\right) + \left(Fa_1\,\overline{j_1\phi_{l,1}}\right) \tag{190}$$

Using the standard Tank Model assumption ($\overline{j_1\phi_{l,1}} \approx \overline{j_1}\,\overline{\phi_{l,1}}$), and the relation for volume-averaged pore-wall flux $\overline{j_1} = \frac{i_{app}}{Fl_1a_1}$, the equation reduces to

$$\overline{Q_{ohmic,1}} = -\left(\frac{1}{l_1}\right)\left(i_{app}\phi_{l,12}\right) + \left(Fa_1\left(\frac{i_{app}}{Fa_1l_1}\right)\overline{\phi_{l,1}}\right) = \left(\frac{i_{app}}{l_1}\right)\left(\overline{\phi_{l,1}} - \phi_{l,12}\right) \tag{191}$$

Thus, we have obtained a simple expression for the ohmic heating terms, similar to the work of Rao and Newman.[110] The form of $\overline{Q_{ohmic,1}}$ in Equation (191) may be interpreted as the product of

the applied current density i_{app} and an 'average' electrolyte potential gradient $\left(\frac{\overline{\phi_{l,1}} - \phi_{l,12}}{l_1}\right)$.

An analogous expression may be derived for the separator and negative electrodes as

$$\overline{Q_{ohmic,3}} = \left(\frac{i_{app}}{l_3}\right)\left(\phi_{l,23} - \overline{\phi_{l,3}}\right) \tag{192}$$

$$\overline{Q_{ohmic,2}} = \left(\frac{i_{app}}{l_2}\right)\left(\phi_{l,12} - \phi_{l,23}\right) \tag{193}$$

The ohmic heating term for the separator is slightly modified due to the lack of a reaction term, i.e. $\frac{\partial i_{l,1}}{\partial x} = 0$. Thus, a constant current density i_{app} is carried entirely by the liquid phase.

6.2. Accounting for interfacial thermal resistances

In the presence of thermal resistances at the interfaces, there is an interfacial temperature discontinuity which must be accounted for, and which changes the *Bi* further. This example is illustrated for the positive electrode, and may be identically applied to the other domains.

The thermal resistance boundary conditions are given by

$$q_{1,x=l_1} = q_{2,x=l_2} = \frac{(T_{1,x=l_1} - T_{2,x=l_1})}{R_{it,12}} \tag{194}$$

Given the requirement for flux continuity. Using the Tank Model flux approximations gives us two relations for determination of Temperature on either side of the interface

$$T_{1,x=l_1} - T_{2,x=l_1} = \left(\frac{1}{R_{it,12}} \right) \left(\frac{-\lambda_1 \left(T_{1,x=l_1} - \overline{T_1} \right)}{\delta_{T1,12}} \right)$$
$$T_{1,x=l_1} - T_{2,x=l_1} = \left(\frac{1}{R_{it,12}} \right) \left(\frac{-\lambda_2 \left(\overline{T_2} - T_{2,x=l_1} \right)}{\delta_{T2,12}} \right) \tag{195}$$

Solving these two equations yields the interfacial values as

$$T_{1,x=l_1} = \left(\frac{2R_{it,12}\overline{T_1} + \frac{l_2\overline{T_1}}{\lambda_2} + \frac{l_1\overline{T_2}}{\lambda_1}}{2R_{it,12} + \frac{l_2}{\lambda_2} + \frac{l_1}{\lambda_1}} \right)$$
$$T_{2,x=l_1} = \left(\frac{2R_{it,12}\overline{T_2} + \frac{l_2\overline{T_1}}{\lambda_2} + \frac{l_1\overline{T_2}}{\lambda_1}}{2R_{it,12} + \frac{l_2}{\lambda_2} + \frac{l_1}{\lambda_1}} \right) \tag{196}$$

Where the standard film thickness approximation, $\delta_{Ti,ij} = \frac{l_i}{2}$ has been applied. In the absence of interfacial resistance, $R_{it,12} = 0$, and we recover the original condition $T_{12,x=l_1} = T_{12,x=l_2} = T_{12}$.

Equations (196) and analogous expressions for the other domains can now be substituted into the volume-averaged heat balances of equations (36) - (38) to yield the augmented energy balances.

7. Appendix B: Additional Derivations and Experimental Details for the Li||Cu Symmetric Cells

7.1. General Analytical Solutions for EN-NP

For finding coefficient A_n for any cycle, we still follow the idea of equation (128). The difference is that the initial dimensionless concentration is no longer uniform across the cell. The simplified $A_{n,j}$ (j^{th} galvanostatic cycle) can be expressed by the following recurrence relation:

$$A_{n,1} = \frac{\delta_1\left(-1+\cos\left(n\pi\right)\right)}{n^2\pi^2} \tag{197}$$

$$A_{n,j+1} = A_{n,j}\exp\left(-n^2\pi^2\tau_j\right)+\left(\delta_{j+1}-\delta_j\right)\frac{\cos\left(n\pi\right)-1}{n^2\pi^2} \tag{198}$$

The dimensionless concentration profile can be also expressed as:

$$C_j\left(X,\tau_j\right)=\left[\sum_{n=1}^{\infty}A_{n,j}\cos\left(n\pi X\right)\exp\left(-n^2\pi^2\tau_j\right)\right]-\frac{\delta_j}{2}X+1+\frac{\delta_j}{4} \tag{199}$$

7.2. Obtaining Electrostatic Potential Value at x = 0 by Gaussian Quadrature

If we are particularly interested in the potential at the boundaries rather than the profile across the cell, we can evaluate the potential at x = 0 (because we defined $\phi = 0$ at x = L) by Gaussian quadrature approximation. **Table 7-I** shows the results of using a different number of integration points at x = 0 using Gaussian-Legendre quadrature approximation. When the operation time is longer, the profile is more linear (approach to steady-state), so fewer integration points are needed to achieve the designated accuracy.

Table 7-I. The potential at x = 0 by Gaussian-Legendre approximation using different integration points

m	t = 1 s	t = 6 s	t = 36 s	t = 100 s	t = 3600 s
1	9.077964×10^{-4}	9.082839×10^{-4}	1.735120×10^{-3}	3.541051×10^{-3}	4.992880×10^{-3}
2	9.079289×10^{-4}	1.274546×10^{-3}	2.943894×10^{-3}	4.104423×10^{-3}	5.008643×10^{-3}
3	9.683264×10^{-4}	1.737706×10^{-3}	2.900398×10^{-3}	4.075433×10^{-3}	5.008683×10^{-3}
4	1.152398×10^{-3}	1.749635×10^{-3}	2.896741×10^{-3}	4.076097×10^{-3}	5.008683×10^{-3}
5	1.252632×10^{-3}	1.716824×10^{-3}	2.897312×10^{-3}	4.076087×10^{-3}	
6	1.263696×10^{-3}	1.718749×10^{-3}	2.897272×10^{-3}	4.076087×10^{-3}	
7	1.246675×10^{-3}	1.720205×10^{-3}	2.897274×10^{-3}		
8	1.237110×10^{-3}	1.719912×10^{-3}	2.897274×10^{-3}		
9	1.237268×10^{-3}	1.719905×10^{-3}			
10	1.239157×10^{-3}	1.719915×10^{-3}			
11	1.239606×10^{-3}	1.719914×10^{-3}			
12	1.239377×10^{-3}	1.719914×10^{-3}			
13	1.239263×10^{-3}				
14	1.239282×10^{-3}				
15	1.239301×10^{-3}				
16	1.239300×10^{-3}				
17	1.239297×10^{-3}				
18	1.239297×10^{-3}				

7.3. Experimental Set-Up and Details: Li||Cu operando X-ray diffraction cell

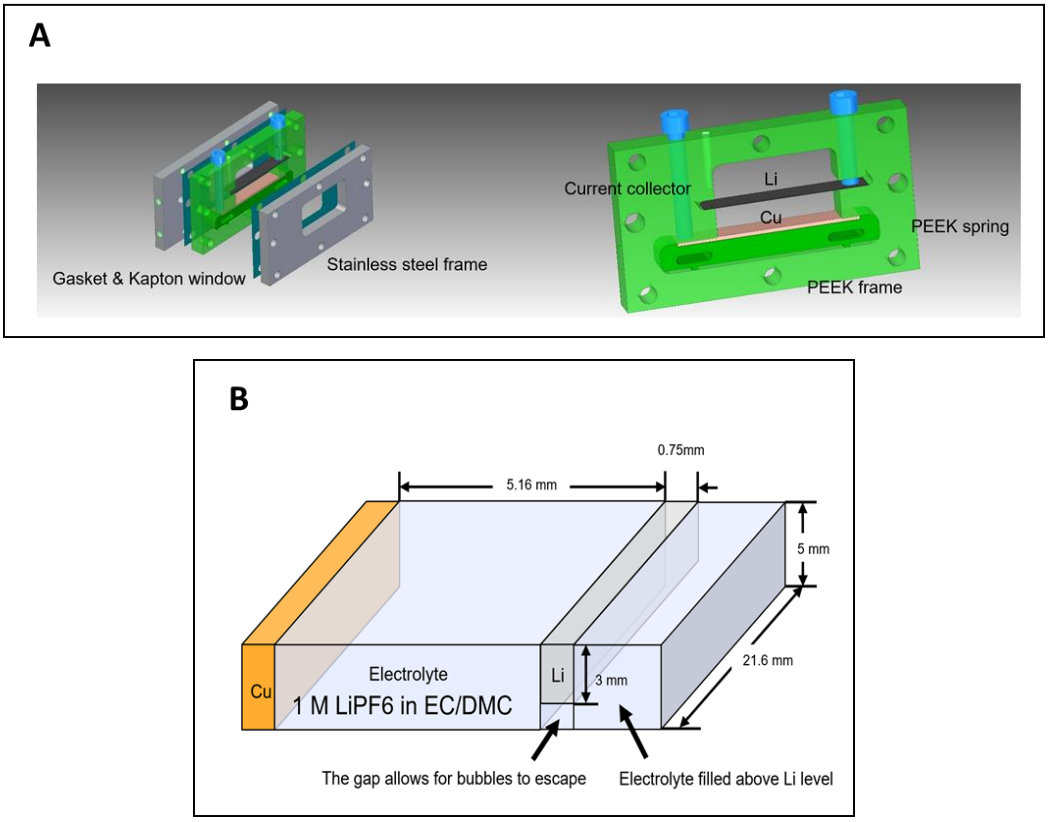

Figure 7.1 A: Diagram of the Li-Cu cell. **B**: A schematic representation indicating relevant dimensions of the electrode and electrolyte region. The relevant computational domain length for the electrochemical modeling is the separation between the two electrodes (L = 5.16 mm). The large electrode separation relative to the thicknesses of lithium plated and stripped is expected to eliminate the need for moving-boundary formulations to track the motion of the electrode interfaces.

The experimental Li||Cu electrochemical cell, which enables us to quantify dead (inactive) lithium formation on the copper substrate by X-ray diffraction, is depicted in **Figure 7.1**. This is a modification of the cell we used in Cao et al.[158] Specifically, the experimental set-up helps quantify the loss of capacity/lithium into SEI and electrically disconnected "dead" lithium deposits in addition to understanding SEI inhomogeneity and effects on lithium plating morphology and

reversibility. Copper is used as a deposition substrate instead of lithium to distinguish between ”dead” lithium and uncycled lithium. To allow the X-ray beam to pass through the cell, a Kapton window is used. The PEEK spring and frame also ensures that the electrodes are connected well to the current collectors. The lithium foil is intentionally designed to be slightly narrower than the cell width to allow bubbles to escape and the 1 M $LiPF_6$ in Ethylene Carbonate/Dimethyl Carbonate (EC/DMC) electrolyte is filled above the lithium counter electrode. Since this is an open cell design with no applied pressure as in a typical coin cell, the columbic efficiency of the *operando* cell is somewhat lower.

8. References

1. P. Hertzke, N. Muller, P. Schaufuss, S. Schenk, and T. Wu, *McKinsey Co.*, https://www.mckinsey.com/industries/automotive-and-assembly/our-insights/expanding-electric-vehicle-adoption-despite-early-growing-pains/, last accessed: April 2021.

2. L. Goldie-Scot, *BloombergNEF*, https://about.bnef.com/blog/behind-scenes-take-lithium-ion-battery-prices/, last accessed: April 2021.

3. J. Wandt, P. Jakes, J. Granwehr, R.-A. Eichel, and H. A. Gasteiger, *Mater. Today*, **21**, 231 (2018).

4. J. M. Reniers, G. Mulder, and D. A. Howey, *J. Electrochem. Soc.*, **166**, A3189 (2019).

5. T. M. Bandhauer, S. Garimella, and T. F. Fuller, *J. Electrochem. Soc.*, **158**, R1 (2011).

6. S. Tippmann, D. Walper, L. Balboa, B. Spier, and W. G. Bessler, *J. Power Sources*, **252**, 305 (2014).

7. A. M. Colclasure, T. R. Tanim, A. N. Jansen, S. E. Trask, A. R. Dunlop, B. J. Polzin, I. Bloom, D. Robertson, L. R. Flores, M. Evans, E. J. Dufek, and K. Smith, *Electrochim. Acta*, **337**, 135854 (2020).

8. S. Ahmed, I. Bloom, A. N. Jansen, T. Tanim, E. J. Dufek, A. Pesaran, A. Burnham, R. B. Carlson, F. Dias, K. Hardy, M. Keyser, C. Kreuzer, A. Markel, A. Meintz, C. Michelbacher, M. Mohanpurkar, P. A. Nelson, D. C. Robertson, D. Scoffield, M. Shirk, T. Stephens, R. Vijayagopal, and J. Zhang, *J. Power Sources*, **367**, 250 (2017).

9. M. T. Lawder, P. W. C. Northrop, and V. R. Subramanian, *J. Electrochem. Soc.*, **161**, A2099

(2014).

10. E. Hosseinzadeh, J. Marco, and P. Jennings, *J. Energy Storage*, **22**, 194 (2019).

11. W. Shi, X. Hu, C. Jin, J. Jiang, Y. Zhang, and T. Yip, *J. Power Sources*, **313**, 198 (2016).

12. K. J. Lee, K. Smith, A. Pesaran, and G. H. Kim, *J. Power Sources*, **241**, 20 (2013).

13. N. A. Chaturvedi, R. Klein, J. Christensen, J. Ahmed, and A. Kojic, *IEEE Control Syst.*, **30**, 49 (2010).

14. X. Lin, Y. Kim, S. Mohan, J. B. Siegel, and A. G. Stefanopoulou, *Annu. Rev. Control. Robot. Auton. Syst.*, **2**, 393 (2019).

15. T. R. Tanim, C. D. Rahn, and C.-Y. Wang, *J. Dyn. Syst. Meas. Control*, **137**, 011005 (2014).

16. H. E. Perez, S. Dey, X. Hu, and S. J. Moura, *J. Electrochem. Soc.*, **164**, A1679 (2017).

17. M. F. Samadi and M. Saif, *Proc. Am. Control Conf.*, 2924 (2014).

18. S. Santhanagopalan and R. E. White, *J. Power Sources*, **161**, 1346 (2006).

19. M. Pathak, D. Sonawane, S. Santhanagopalan, R. D. Braatz, and V. R. Subramanian, *ECS Trans.*, **75**, 51 (2017).

20. N. Ganesan, S. Basu, K. S. Hariharan, S. M. Kolake, T. Song, T. Yeo, D. K. Sohn, and S. Doo, *J. Power Sources*, **322**, 57 (2016).

21. B. Wu, V. Yufit, M. Marinescu, G. J. Offer, R. F. Martinez-Botas, and N. P. Brandon, *J. Power Sources*, **243**, 544 (2013).

22. P. Albertus, S. Babinec, S. Litzelman, and A. Newman, *Nat. Energy*, **3**, 16 (2018).

23. J. Qian, W. A. Henderson, W. Xu, P. Bhattacharya, M. Engelhard, O. Borodin, and J. G. Zhang, *Nat. Commun.*, **6**, 6362 (2015).

24. M. D. Tikekar, S. Choudhury, Z. Tu, and L. A. Archer, *Nat. Energy*, **1**, 16114 (2016).

25. D. Lin, Y. Liu, and Y. Cui, *Nat. Nanotechnol.*, **12**, 194 (2017).

26. K. N. Wood, M. Noked, and N. P. Dasgupta, *ACS Energy Lett.*, **2**, 664 (2017).

27. C. Fang, J. Li, M. Zhang, Y. Zhang, F. Yang, J. Z. Lee, M. H. Lee, J. Alvarado, M. A. Schroeder, Y. Yang, B. Lu, N. Williams, M. Ceja, L. Yang, M. Cai, J. Gu, K. Xu, X. Wang, and Y. S. Meng, *Nature*, **572**, 511 (2019).

28. X. Yin, W. Tang, I. D. Jung, K. C. Phua, S. Adams, S. W. Lee, and G. W. Zheng, *Nano Energy*, **50**, 659 (2018).

29. L. Gireaud, S. Grugeon, S. Laruelle, B. Yriex, and J.-M. Tarascon, *Electrochem. commun.*, **8**, 1639 (2006).

30. Y. Mikhaylik, I. Kovalev, R. Schock, K. Kumaresan, J. Xu, and J. Affinito, *ECS Trans.*, **25**, 23 (2010).

31. P. Bai, J. Li, F. R. Brushett, and M. Z. Bazant, *Energy Environ. Sci.*, **9**, 3221 (2016).

32. K. N. Wood, E. Kazyak, A. F. Chadwick, K. H. Chen, J. G. Zhang, K. Thornton, and N. P. Dasgupta, *ACS Cent. Sci.*, **2**, 790 (2016).

33. P. Barai, K. Higa, and V. Srinivasan, *J. Electrochem. Soc.*, **164**, A180 (2017).

34. C. Monroe and J. Newman, *J. Electrochem. Soc.*, **151**, A880 (2004).

35. Z. Ahmad and V. Viswanathan, *Phys. Rev. Lett.*, **119**, 1 (2017).

36. D. R. Ely, A. Jana, and R. E. García, *J. Power Sources*, **272**, 581 (2014).

37. L. Liang, Y. Qi, F. Xue, S. Bhattacharya, S. J. Harris, and L. Q. Chen, *Phys. Rev. E - Stat. Nonlinear, Soft Matter Phys.*, **86**, 1 (2012).

38. Z. Hong and V. Viswanathan, *ACS Energy Lett.*, **3**, 1737 (2018).

39. K. Yoo, S. Banerjee, and P. Dutta, *J. Power Sources*, **258**, 340 (2014).

40. A. Ferrese and J. Newman, *J. Electrochem. Soc.*, **161**, 1350 (2014).

41. A. Subramaniam, S. Kolluri, C. D. Parke, M. Pathak, S. Santhanagopalan, and V. R. Subramanian, *J. Electrochem. Soc.*, **167**, 013534 (2020).

42. A. Subramaniam, S. Kolluri, S. Santhanagopalan, and V. R. Subramanian, *J. Electrochem. Soc.*, **167**, 113506 (2020).

43. A. Subramaniam, J. Chen, T. Jang, N. R. Geise, R. M. Kasse, M. F. Toney, and V. R. Subramanian, *J. Electrochem. Soc.*, **166**, A3806 (2019).

44. C. Monroe and J. Newman, *J. Electrochem. Soc.*, **152**, A396 (2005).

45. M. Doyle, T. F. Fuller, and J. Newman, *J. Electrochem. Soc.*, **140**, 1526 (1993).

46. P. W. C. Northrop, V. Ramadesigan, S. De, and V. R. Subramanian, *J. Electrochem. Soc.*, **158**, A1461 (2011).

47. A. M. Bizeray, S. Zhao, S. R. Duncan, and D. A. Howey, *J. Power Sources*, **296**, 400 (2015).

48. A. Jokar, B. Rajabloo, M. Désilets, and M. Lacroix, *J. Power Sources*, **327**, 44 (2016).

49. V. R. Subramanian, V. D. Diwakar, and D. Tapriyal, *J. Electrochem. Soc.*, **152**, A2002 (2005).

50. V. R. Subramanian, V. Boovaragavan, V. Ramadesigan, and M. Arabandi, *J. Electrochem. Soc.*, **156**, 260 (2009).

51. P. W. C. Northrop, M. Pathak, D. Rife, S. De, S. Santhanagopalan, and V. R. Subramanian, *J. Electrochem. Soc.*, **162**, A940 (2015).

52. V. Ramadesigan, P. W. C. Northrop, S. De, S. Santhanagopalan, R. D. Braatz, and V. R. Subramanian, *J. Electrochem. Soc.*, **159**, R31 (2012).

53. V. Ramadesigan, K. Chen, N. A. Burns, V. Boovaragavan, R. D. Braatz, and V. R. Subramanian, *J. Electrochem. Soc.*, **158**, A1048 (2011).

54. P. W. C. Northrop, B. Suthar, V. Ramadesigan, S. Santhanagopalan, R. D. Braatz, and V. R. Subramanian, *J. Electrochem. Soc.*, **161**, E3149 (2014).

55. V. Ramadesigan, V. Boovaragavan, J. C. Pirkle, and V. R. Subramanian, *J. Electrochem. Soc.*, **157**, A854 (2010).

56. S. Atlung, K. West, and T. Jacobsen, *J. Electrochem. Soc.*, **126**, 1311 (1979).

57. S. Santhanagopalan, Q. Guo, P. Ramadass, and R. E. White, *J. Power Sources*, **156**, 620 (2006).

58. M. Doyle and J. Newman, *J. Appl. Electrochem.*, **27**, 846 (1997).

59. T. F. Fuller, M. Doyle, and J. Newman, *J. Electrochem. Soc.*, **141**, 1 (1994).

60. S. G. Marquis, V. Sulzer, R. Timms, C. P. Please, and S. J. Chapman, *J. Electrochem. Soc.*, **166**, A3693 (2019).

61. G. Richardson, I. Korotkin, R. Ranom, M. Castle, and J. M. Foster, *arXiv Preprint.*, **arXiv:1907**, 1 (2019).

62. Z. Deng, L. Yang, H. Deng, Y. Cai, and D. Li, *Energy*, **142**, 838 (2018).

63. S. K. Rahimian, S. Rayman, and R. E. White, *J. Power Sources*, **224**, 180 (2013).

64. S. K. Rahimian, S. Rayman, and R. E. White, *J. Power Sources*, **241**, 295 (2013).

65. A. K. Sharma, S. Basu, K. S. Hariharan, S. P. Adiga, S. M. Kolake, T. Song, and Y. Sung, *J. Electrochem. Soc.*, **166**, A1197 (2019).

66. W. Luo, C. Lyu, L. Wang, and L. Zhang, *J. Power Sources*, **241**, 295 (2013).

67. X. Han, M. Ouyang, L. Lu, and J. Li, *J. Power Sources*, **278**, 814 (2015).

68. S. J. Moura, F. B. Argomedo, R. Klein, A. Mirtabatabaei, and M. Krstic, *IEEE Trans. Control Syst. Technol.*, **25**, 453 (2017).

69. A. Guduru, P. W. C. Northrop, S. Jain, A. C. Crothers, T. R. Marchant, and V. R. Subramanian, *J. Appl. Electrochem.*, **42**, 189 (2012).

70. N. Baba, H. Yoshida, M. Nagaoka, C. Okuda, and S. Kawauchi, *J. Power Sources*, **252**, 214 (2014).

71. T. R. Tanim, C. D. Rahn, and C.-Y. Wang, *J. Dyn. Syst. Meas. Control*, **137**, 011005 (2014).

72. Y. Shi, G. Prasad, Z. Shen, and C. D. Rahn, *Proc. 2011 Am. Control Conf.*, 356 (2011).

73. P. Kemper, S. E. Li, and D. Kum, *J. Power Sources*, **286**, 510 (2015).

74. V. Senthil Kumar, *J. Power Sources*, **222**, 426 (2013).

75. J. Newman and W. Tiedemann, *AIChE J.*, **21**, 25 (1975).

76. Y. Zeng and M. Z. Bazant, *SIAM J. Appl. Math.*, **74**, 980 (2014).

77. D. R. Baker and M. W. Verbrugge, *J. Electrochem. Soc.*, **159**, A1341 (2012).

78. V. R. Subramanian, J. A. Ritter, and R. E. White, *J. Electrochem. Soc.*, **148**, E444 (2001).

79. J. Newman and K. E. Thomas-Alyea, *Electrochemical Systems*, 3rd ed., John Wiley and Sons, Inc., Hoboken, NJ, (2004).

80. L. O. Valøen and J. N. Reimers, *J. Electrochem. Soc.*, **152**, A882 (2005).

81. W. B. Gu, C. Y. Wang, and B. Y. Liaw, *J. Electrochem. Soc.*, **145**, 3418 (1998).

82. P. Kemper and D. Kum, *2013 9th IEEE Veh. Power Propuls. Conf. IEEE VPPC 2013*, 158 (2013).

83. V. R. Subramanian, V. Boovaragavan, and V. D. Diwakar, *Electrochem. Solid-State Lett.*, **10**, A255 (2007).

84. M. T. Lawder, V. Ramadesigan, B. Suthar, and V. R. Subramanian, *Comput. Chem. Eng.*, **82**, 283 (2015).

85. *Maple Product Information*, https://www.maplesoft.com/products/maple/, last accessed: April 2021.

86. A. C. Hindmarsh, R. Serban, and A. Collier, *Cent. Appl. Sci. Comput. LLNL* (2018).

87. T. F. Fuller, M. Doyle, and J. Newman, *J. Electrochem. Soc.*, **141**, 982 (1994).

88. T. Ohzuku, Y. Iwakoshi, and K. Sawai, *J. Electrochem. Soc.*, **140**, 2490 (1993).

89. T. Danner, M. Singh, S. Hein, J. Kaiser, H. Hahn, and A. Latz, *J. Power Sources*, **334**, 191 (2016).

90. M. Singh, J. Kaiser, and H. Hahn, *J. Electrochem. Soc.*, **162**, A1196 (2015).

91. F. Jiang and P. Peng, *Sci. Rep.*, **6**, 32639 (2016).

92. C. Y. Wang and V. Srinivasan, *J. Power Sources*, **110**, 364 (2002).

93. M. Guo, G. Sikha, and R. E. White, *J. Electrochem. Soc.*, **158**, A122 (2011).

94. C. Forgez, D. Vinh Do, G. Friedrich, M. Morcrette, and C. Delacourt, *J. Power Sources*, **195**, 2961 (2010).

95. S. Kosch, A. Rheinfeld, S. V. Erhard, and A. Jossen, *J. Power Sources*, **342**, 666 (2017).

96. S. Kosch, Y. Zhao, J. Sturm, J. Schuster, G. Mulder, E. Ayerbe, and A. Jossen, *J. Electrochem. Soc.*, **165**, A2374 (2018).

97. S. J. Bazinski and X. Wang, *J. Electrochem. Soc.*, **161**, A2168 (2014).

98. Y. Ye, L. H. Saw, Y. Shi, K. Somasundaram, and A. A. O. Tay, *Electrochim. Acta*, **134**, 327 (2014).

99. G.-H. Kim, K. Smith, K.-J. Lee, S. Santhanagopalan, and A. Pesaran, *J. Electrochem. Soc.*, **158**, A955 (2011).

100. N. T. Tran, T. Farrell, and M. Vilathgamuwa, *J. Electrochem. Soc.*, **166**, 3059 (2019).

101. M. Guo and R. E. White, *J. Power Sources*, **221**, 334 (2013).

102. R. E. Gerver and J. P. Meyers, *J. Electrochem. Soc.*, **158**, A835 (2011).

103. K. A. Smith, C. D. Rahn, and C. Y. Wang, *Energy Convers. Manag.*, **48**, 2565 (2007).

104. K. Smith and C. Y. Wang, *J. Power Sources*, **160**, 662 (2006).

105. J. Li, Y. Cheng, M. Jia, Y. Tang, Y. Lin, Z. Zhang, and Y. Liu, *J. Power Sources*, **255**, 130 (2014).

106. Y. Ji, Y. Zhang, and C. Y. Wang, *J. Electrochem. Soc.*, **160**, 636 (2013).

107. C. R. Pals and J. Newman, *J. Electrochem. Soc.*, **142**, 3274 (1995).

108. C. R. Pals and J. Newman, *J. Electrochem. Soc.*, **142**, 3282 (1995).

109. M. G. Hennessy and I. R. Moyles, *Appl. Math. Model.*, **80**, 724 (2020).

110. L. Rao and J. Newman, *J. Electrochem. Soc.*, **144**, 2697 (2006).

111. D. Bernardi, E. Pawlikowski, and J. Newman, *J. Electrochem. Soc.*, **132**, 5 (1985).

112. K. Kumaresan, G. Sikha, and R. E. White, *J. Electrochem. Soc.*, **155**, A164 (2008).

113. N. Yang, X. Zhang, B. Shang, and G. Li, *J. Power Sources*, **306**, 733 (2016).

114. Z. Lei, C. Zhang, J. Li, G. Fan, and Z. Lin, *J. Mod. Power Syst. Clean Energy*, **3**, 289 (2015).

115. D. Ouyang, Y. He, J. Weng, J. Liu, M. Chen, and J. Wang, *RSC Adv.*, **9**, 9053 (2019).

116. T. F. Fuller, M. Doyle, and J. Newman, *J. Electrochem. Soc.*, **141**, 1 (1994).

117. Y. Lai, S. Du, L. Ai, L. Ai, Y. Cheng, Y. Tang, and M. Jia, *Int. J. Hydrogen Energy*, **40**, 13039 (2015).

118. J. Mao, W. Tiedemann, and J. Newman, *J. Power Sources*, **271**, 444 (2014).

119. T. R. Tanim, C. D. Rahn, and C. Y. Wang, *Energy*, **80**, 731 (2015).

120. I. R. Moyles, M. G. Hennessy, T. G. Myers, and B. R. Wetton, *SIAM J. Appl. Math.*, **74**, 1528 (2019).

121. P. Amiribavandpour, W. Shen, D. Mu, and A. Kapoor, *J. Power Sources*, **284**, 328 (2015).

122. J. C. Burns, L. J. Krause, D.-B. Le, L. D. Jensen, A. J. Smith, D. Xiong, and J. R. Dahn, *J. Electrochem. Soc.*, **158**, A1417 (2011).

123. D. M. Pesko, Z. Feng, S. Sawhney, J. Newman, V. Srinivasan, and N. P. Balsara, *J. Electrochem. Soc.*, **165**, A3186 (2018).

124. S.-L. Wu, A. E. Javier, D. Devaux, N. P. Balsara, and V. Srinivasan, *J. Electrochem. Soc.*, **161**, A1836 (2014).

125. H. Cohen and J. W. Cooley, *Biophys. J.*, **5**, 145 (1965).

126. T. R. Brumleve and R. P. Buck, *J. Electroanal. Chem.*, **90**, 1 (1978).

127. I. Streeter and R. G. Compton, *J. Phys. Chem. C*, **112**, 13716 (2008).

128. T. Sokalski, P. Lingelfelter, and A. Lewenstam, *J. Phys. Chem. B*, **107**, 2443 (2003).

129. D. Britz and J. Strutwolf, *Electrochim. Acta*, **137**, 328 (2014).

130. M. Z. Bazant, K. Thornton, and A. Ajdari, *Phys. Rev. E - Stat. Physics, Plasmas, Fluids, Relat. Interdiscip. Top.*, **70**, 021506 (2004).

131. A. F. Chadwick, G. Vardar, S. DeWitt, A. E. S. Sleightholme, C. W. Monroe, D. J. Siegel, and K. Thornton, *J. Electrochem. Soc.*, **163**, A1813 (2016).

132. K. T. Chu and M. Z. Bazant, *SIAM J. Appl. Math.*, **65**, 1485 (2005).

133. E. J. F. Dickinson and R. G. Compton, *Chem. Phys. Lett.*, **497**, 178 (2010).

134. A. Golovnev and S. Trimper, *J. Chem. Phys.*, **134**, 154902 (2011).

135. M. Pabst, *J. Chem. Phys.*, **140**, 224113 (2014).

136. A. M. Bizeray, D. A. Howey, and C. W. Monroe, *J. Electrochem. Soc.*, **163**, E223 (2016).

137. Z. Song, X. Cao, and H. Huang, *Phys. Rev. E*, **97**, 012411 (2018).

138. E. J. F. Dickinson, J. G. Limon-Petersen, and R. G. Compton, *J. Solid State Electrochem.*, **15**, 1335 (2011).

139. V. G. Levich, *Physicochemical Hydrodynamics*, Prentice-Hall, Englewood Cliffs, NJ, (1962).

140. T. R. Rosebrugh and W. L. Miller, *J. Phys. Chem.*, **14**, 816 (1910).

141. R. E. White and V. R. Subramanian, *Computational Methods in Chemical Engineering with Maple*, Springer-Verlag, Berlin, (2010).

142. M. Torchio, L. Magni, R. B. Gopaluni, R. D. Braatz, and D. M. Raimondo, *J. Electrochem. Soc.*, **163**, A1192 (2016).

143. Y. Zeng, P. Albertus, R. Klein, N. Chaturvedi, A. Kojic, M. Z. Bazant, and J. Christensen, *J. Electrochem. Soc.*, **160**, A1565 (2013).

144. A. Subramaniam, J. Chen, and V. R. Subramanian, *Meet. Abstr.*, **MA2018-02**, 520 (2018).

145. G. F. Carey and B. A. Finlayson, *Chem. Eng. Sci.*, **30**, 587–596 (1974).

146. E. Hairer and G. Wanner, *Solving Ordinary Differential Equations II: Stiff and Differential - Algebraic Problems*, Springer-Verlag, Berlin, (1996).

147. C. Monroe and J. Newman, *J. Electrochem. Soc.*, **150**, A1377 (2003).

148. C. D. Parke, A. Subramaniam, S. Kolluri, D. T. Schwartz, and V. R. Subramanian, *J.*

Electrochem. Soc., **167**, 163503 (2020).

149. P. Barai, K. Higa, and V. Srinivasan, *J. Electrochem. Soc.*, **165**, A2654 (2018).

150. P. Barai, K. Higa, and V. Srinivasan, *J. Electrochem. Soc.*, **164**, A180 (2017).

151. W. S. LePage, Y. Chen, E. Kazyak, K.-H. Chen, A. J. Sanchez, A. Poli, E. M. Arruda, M. D. Thouless, and N. P. Dasgupta, *J. Electrochem. Soc.*, **166**, A89 (2019).

152. L. Anand and S. Narayan, *J. Electrochem. Soc.*, **166**, A1092 (2019).

153. L. Chen, H. W. Zhang, L. Y. Liang, Z. Liu, Y. Qi, P. Lu, J. Chen, and L. Q. Chen, *J. Power Sources*, **300**, 376 (2015).

154. R. Alkire, T. Bergh, and R. L. Sani, *J. Electrochem. Soc.*, **125**, 1981 (1978).

155. K. Shah, A. Subramaniam, L. Mishra, T. Jang, M. Z. Bazant, R. D. Braatz, and V. R. Subramanian, *J. Electrochem. Soc.*, **167** (2020).

156. X. Yin, W. Tang, I. D. Jung, K. C. Phua, S. Adams, S. W. Lee, and G. W. Zheng, *Nano Energy*, **50**, 659 (2018).

157. A. J. Louli, M. Genovese, R. Weber, S. G. Hames, E. R. Logan, and J. R. Dahn, *J. Electrochem. Soc.*, **166**, A1291 (2019).

158. C. Cao, H. G. Steinrück, B. Shyam, K. H. Stone, and M. F. Toney, *Nano Lett.*, **16**, 7394 (2016).